Anthropomimetic Control Synthesis: Adaptive Vehicle Traction Control

William T. Kirchner

Dissertation submitted to the Faculty of the
Virginia Polytechnic Institute and State University
in partial fulfillment of the requirements for the degree of

Doctor of Philosophy
in
Mechanical Engineering

Steve C. Southward, Chair
Mehdi Ahmadian
Alfred L. Wicks
Corina Sandu
Craig A. Woolsey

March 22, 2012
Blacksburg, Virginia

Keywords: Vehicle Dynamics, Traction Control, Anthropomimetic, Human in the Loop, Adaptive Control, Gradient Estimation, Discrete Adaptive Filter

Anthropomimetic Control Synthesis: Adaptive Vehicle Traction Control

William T. Kirchner

(ABSTRACT)

Human expert drivers have the unique ability to build complex perceptive models using correlated sensory inputs and outputs. In the case of longitudinal vehicle traction, this work will show a direct correlation in longitudinal acceleration to throttle input in a controlled laboratory environment. In fact, human experts have the ability to control a vehicle at or near the performance limits, with respect to vehicle traction, without direct knowledge of the vehicle states; speed, slip or tractive force. Traditional algorithms such as PID, full state feedback, and even sliding mode control have been very successful at handling low level tasks where the physics of the dynamic system are known and stationary. The ability to learn and adapt to changing environmental conditions, as well as develop perceptive models based on stimulus-response data, provides expert human drivers with significant advantages. When it comes to bandwidth, accuracy, and repeatability, automatic control systems have clear advantages over humans; however, most high performance control systems lack many of the unique abilities of a human expert. The underlying motivation for this work is that there are advantages to framing the traction control problem in a manner that more closely resembles how a human expert drives a vehicle. The fundamental idea is the belief that humans have a unique ability to adapt to uncertain environments that are both temporal and spatially varying. In this work, a novel approach to traction control is developed using an anthropomimetic control synthesis strategy. The proposed anthropomimetic traction control algorithm operates on the same correlated input signals that a human expert driver would in order to maximize traction. A gradient ascent approach is at the heart of the proposed anthropomimetic control algorithm, and a real-time implementation is described using linear operator techniques, even though the tire-ground interface is highly non-linear. Performance of the proposed anthropomimetic traction control algorithm is demonstrated using both a longitudinal traction case study and a combined mode traction case study, in which longitudinal and lateral accelerations are maximized simultaneously. The approach presented in this research should be considered as a first step in the development of a truly anthropomimetic solution, where an advanced control algorithm has been designed to be responsive to the same limited input signals that a human expert would rely on, with the objective of maximizing traction. This work establishes the foundation for a general framework for an anthropomimetic control algorithm that is capable of learning and adapting to an uncertain, time varying environment. The algorithms developed in this work are well suited for efficient real time control in ground vehicles in a variety of applications from a driver assist technology to fully autonomous applications.

Acknowledgments

I would like to thank my family for being supportive of my efforts to pursue my Ph.D at Virginia Tech, they have never wavered in their support and encouragement. Always understanding that I couldn't make it home for every holiday and family gathering, regardless of how much I would have liked to. They were even kind enough to break with tradition to make several trips to Virginia and enjoy some of the east coast during their vacation time. With out the foundation that they laid over the first 28 years of my life, none of this would have been possible. I am forever in debt to all of them; Tom, Kay, Mike and Claire Kirchner. I would also like to thank all my fellow graduate students that have made my time in Virginia quite enjoyable and enriched my life in countless ways. I will always remember the hiking and camping trips. The diversity of cooking skills my many roommates have demonstrated was also a source of great enjoyment. Their critical thinking and challenging questions have undoubtedly improved the quality of this work. Lastly, I would like to thank my advisor, Dr. Steve Southward, for providing incredible advice over the course of 4 years. His advice, guidance and knowledge has undoubtedly helped improve and develop not only this work but also my personal character and future career path.

Contents

List of Figures

List of Tables

Chapter 1

Introduction

This chapter starts by elaborating on the motivation for this work. A review of past research and the state of the art technology, followed by a summary of what to expect through the rest of the paper.

1.1 Motivation

Human expert drivers are able to control their vehicles at high performance traction levels without direct sensing of speed, slip, or traction forces. Clearly human drivers rely on indirect inputs such as visual, audible, inertial, and tactile cues, along with some form of internal representation of the dynamics developed through reinforcement learning. The primary motivation for this research begins with a fundamental belief that human experts possess valuable behavioral traits, which can be applied to the synthesis of high performance control solutions, and more specifically, vehicle traction control. This work considers high performance traction control as either getting from point A to point B in a minimum amount of time or maximizing the distance travelled in a fixed amount of time, barring engine power limitations. The solution to this problem for ground vehicles is controlling the vehicle such that it operates at the maximum of the vector sum of longitudinal and lateral tractive forces, along a specified path, and subsequently the maximum of acceleration. This is not a trivial task even for expert human drivers for which a model of the vehicle and tire ground interface are unknown or only crudely understood. This is especially true considering the significant variability in the terrain and the general lack of knowledge about the tire-ground interface that even expert humans possess. The human ability to learn and adapt to spatially and temporally changing environments is a significant advantage when compared to a vast number of automatic control systems. The ability to construct and exploit intuitive, albeit often crude, models of the environment, differentiates humans from most automatic control systems. By combining a human's superiority when operating in uncertain and changing environments, with a machines superiority of higher bandwidths and greater precision, it is possible to create a controller that

features the best from both worlds.

1.2 Literature Review

Several solutions to the traction control problem exist in both industry and academia. The motorsports community has reaped the benefits of traction control for years. While commercial vehicle applications have used anti-lock brake systems since the early 1970's, with the addition of traction control and stability control becoming more prevalent in the last decade. The unmanned ground vehicle community has yet to fully embrace technologies that have been mainly used in a driver assist application for ground vehicles. There is a great deal of technology that can be used, but more importantly improved upon in developing a more robust traction control algorithm capable of adaptation in both time and space.

1.2.1 Motorsports Applications

Motorsports applications have reaped the most value from automatic traction control, largely because the tire-ground interface in these applications has less variability [3], and is relatively better understood through extensive testing [4]. Some form of automatic traction control system (TCS), or its more prevalent complement, an anti-lock braking system (ABS), is also available on a wide range of passenger cars and trucks [5, 2]. In fact, in the past decade there has been an increase in available solutions to traction control with in the motorsports community. Well developed solutions are offered through a variety of companies; Motec [58], EFI Technology [59], and Pectel [60]. With the use of drive by wire engine control there are two different methods to decrease the torque being applied to the wheel; reduce engine torque and/or increase braking force. In a fuel injected engine, reducing the engine torque typically requires cutting ignition spark or cutting fuel [6]. Motec, a supplier of one of the more popular engine management systems, uses a slip control system that measures individual wheel speeds (undriven and driven) and compares them to a table of allowable amounts of slip (differences in wheel speeds) versus engine speed. This is similar to existing traction control and anti-lock brake control algorithms that regulate slip to an acceptable range [7, 8], often sacrificing performance to do so. The Motec system then uses a combination of cutting ignition spark and fuel to decrease the engine torque. This method breaks down as the velocity of vehicle approaches zero and for this reason, the traction control is either run in a mode analogous to open loop control where a minimum engine speed is specified before cutting ignition spark or fuel is allowed. Once the vehicle has exceeded this predetermined speed the slip control algorithm takes over [6].

1.2.2 Commercial Vehicle Applications

Even commercially available automatic traction control systems are designed with restrictive assumptions such as relative uniformity in the ground surface, which ultimately limits the operational envelope [9, 10, 11, 12, 5, 8, 2]. Many traction control methods track a desired slip ratio using linear control theory or more advanced non-linear approaches such as sliding mode control [9]. In fact, sliding mode control is a popular choice to control the slip seen at the tire-ground interface [9]. The work of Lee and Tomizuka [9] develops two approaches, one which assumes explicit knowledge of vehicle parameters and traction curve to calculate the friction coefficient of the road and subsequently track the desired slip ratio [9]. The second approach is a fuzzy logic approach to control the slip ratio with crudely defined fuzzy sets over the interval $\kappa \in [-2,2]$ with labels: Negative Big, Negative Small, Zero, Positive Small, and Positive Big. The second approach of Lee and Tomizuka [9] can be summed up in three steps: 1. Estimate the local value of $\partial F_t/\partial \kappa$, 2. Move the target slip towards the peak value. 3. Steer the wheel slip toward the new target slip via sliding mode or fuzzy logic slip control, and return to 1.

Fuzzy logic model based approaches are also very popular when developing traction control solutions [9, 11]. Following the work of Colli et. al. [11] a Fuzzy Adherence Gradient Approach is developed in which a fuzzy logic set is developed to estimate the gradient of the traction curve $\partial F_t/\partial \kappa$. However, as Colli et. al point out there is a singularity in this gradient at steady state conditions, which includes the peak of the traction curve. To get around this issue the gradient estimation is only updated when an appreciable change in vehicle operating conditions is seen [11], where the appreciable change is a predetermined threshold. Even the fuzzy logic approach of Colli et. al. is model based with respect to the friction estimation [11].

Kazemi et. al. have developed a 7-DOF model, and applied a sliding mode controller to create an anti-lock brake system that is able to maximize tractive forces on each individual wheel, and in doing so prevents unwanted yaw accelerations [8]. Similar to the aforementioned work on sliding mode control a model based expression of the sliding manifold and its derivative are developed as the slip ratio and the derivative of slip ratio [8]. An equation governing each wheel is developed using the general sliding manifold. However, the control algorithm explicitly limits the longitudinal force of all the wheels to the minimum value seen across all four wheels, eliminating unwanted yaw moments. The algorithm also assumes explicit knowledge of the road surface and the location of the peak tractive force [8]. This method is limited in the sense that it requires explicit knowledge of the tire-ground interface and is also sensitive to model uncertainties.

1.2.3 Defense and UGV Applications

Defense and civil applications of Unmanned Ground Vehicle (UGV) technology are rapidly progressing to the point where high-performance traction control systems for both acceleration and braking will be necessary to achieve future mobility and mission needs [13]. Existing UGV platforms are typically restricted to operate within a conservative performance envelope relative to

traction at the tire-ground interface. The majority of research in this area has focused on the path planning and associated perception challenges. Performance is commonly sacrificed in favor of stability as a mechanism for accommodating the interface uncertainties. Traction control solutions that offer higher levels of performance than what is currently available today will provide significant value for a wide range of ground vehicle applications, provided they can adapt in a manner similar to that of a human expert.

1.2.4 Friction Model and Estimation

The majority of tire-ground interface models used in simulation are highly non-linear. The most commonly used model in high performance racing simulations is that of Pacejka [1, 14]. The Pacejka model is a semi-empirical model which can be used to model pure longitudinal motion, pure lateral motion or combined mode friction (longitudinal and lateral).

Many vehicle control algorithms such as anti-lock brake systems and traction control can benefit from real-time knowledge of the tire-ground interface properties [15]. As a result, a popular area of research in the last decade has been estimation techniques to determine the tractive force at the tire-ground interface [3, 16, 17], which can then be exploited in more sophisticated traction control algorithms. In fact, models have been developed to estimate the tractive forces in real time for both manned and unmanned ground vehicles by Li et al [3], Tran et al [13] and Pasterkamp et al [17]. In some cases these algorithms estimate the entire friction curve [15], while some simply estimate the peak of the curve [18]. The popular slip-slope method does exactly this, it estimates the slip in the linear region of the friction curve, the offset in the curve at zero slip and the variance in the error, where the error is the difference between the actual data and the linear approximation in the least squares sense. This information is then used in a classifier to estimate the location of μ_{max} or the location of the peak tractive force [18]. A key drawback to this method is the necessary training of the classifier, the use of a classifier is also restrictive in the sense that it constrains the estimation to known surfaces. Rajamani et. al. developed a slightly more robust process to use the slip-slope method, by using a recursive least squares estimate of the linear portion of the traction curve [19]. This method provides a control engineer with the option of tuning a forgetting factor, allowing for the adjustment between fast convergence and immunity to noise. All of this work is focused on generating a more robust friction model that allows the control engineer to push the limits of the more traditional traction control algorithms.

Rajamani et. al. have also developed a suite of friction estimation techniques to estimate the tractive forces [19, 18] in real time. The drawback of these methods is that they are all model based and are therefore sensitive to model uncertainties. Even the mass of a vehicle can vary drastically due to changes in fuel loads and varying numbers of passengers. However, as Rajamani et al. [19, 18] show, given explicit knowledge of the vehicle model, it is possible to obtain accurate measurements of the tractive forces.

Ray has used an extended Kalman filter (EKF) to show that it is possible to estimate the tractive forces of the vehicle using onboard sensors (vehicle speed, wheel speed and yaw rate) and

knowledge of the system inputs [20, 21]. Provided the filter is tuned correctly, it is possible for this estimation algorithm to accurately track discrete changes in tractive forces and the respective coefficients of friction [20, 21]. The work of Wilkin et. al. [22] can be considered an extension of Ray's to practice where a fully instrumented race car is used with wheel force transducers to assess the accuracy of the extended Kalman filter. In fact Ray and Wilkin et. al. model each tractive force as a random walk output of a dynamic system comprised of rigid body modes [20, 22], which is very similar to the way disturbance accommodating control algorithms attempt to model the disturbance [23, 24].

1.2.5 Adaptive Filtering and Number Guessing Games

The adaptive signal processing community has a variety of techniques to address non-stationary signals ranging from the Filtered X LMS algorithm [25] to FIR filters used in noise cancellation [26]. To illustrate the basis for many adaptive algorithms a numbers guessing game using a finite impulse response (FIR) filter is considered. The FIR filter or linear combiner is the building block for many learning systems [26, 27]. To illustrate the basis for the adaptation of the parameters in such a filter a simple guessing game is defined similar to that of Treichler et. al. [27]. There exists a non-linear function $f(x)$ that has a unique, but time varying, maximum on the interval $x \in [-1,1]$. The game participant is asked to guess the location x_k at which the maximum occurs. After each successive guess the only information that the game participant is given is the value of $f(x)$ at that location. The strategy becomes immediately apparent. After at least two successive choices, the participant formulates an estimate of the gradient $\partial f/\partial x$ and makes a new guess. The objective of the user is to track the value of x at which the maximum value of $f(x)$ is observed. Mathematically the user needs to design a function that will update the guess x_{k+1} based on information at the current time step k. As Widrow and Stearns show, Equation 1.1 will accomplish exactly this [26], where μ is the adaptive step size.

$$x_{k+1} = x_k + \mu \frac{\partial f}{\partial x_k} \tag{1.1}$$

The underlying approach here is that the control algorithm, or human expert, uses knowledge of the system output in terms of the gradient of a performance surface to make updates to the control input. This generalization is the motivation for the core of the algorithms developed in this work.

1.2.6 Simulator Validation

For completeness, the validity in using motion platforms to perform Human In the Loop (HIL) simulations must also be addressed. The airline industry has used 6-DOF motion platforms for years to train pilots [28]. However, for years engineers and psychologists have struggled with what makes a simulator successful or have a realistic feel. To this end NATO's (North Atlantic Treaty Organi-

zation) Advisory Group for Aerospace Research & Development distinguishes between objective (physical) and perceptual fidelity. The objective fidelity of a simulator and its motion cueing platform is a measure of how closely the accelerations on the simulator motion platform match those of a high-fidelity vehicle model or the accelerations of the true vehicle [28]. While, the more relevant perceptual fidelity, is a measure not only of a pilot (or drivers) perception of the vehicle and simulator but also of his performance and resulting control strategies in the vehicle and simulator [28]. A simulator with a finite displacement will have finite limits on the duration of sustained accelerations that are achievable. In fact, 'tilt coordination' is widely used in most 6-DOF motion platforms as a result of the perceptual ambiguity between sustained translational accelerations and rotations of the human body [29]. Because the vestibular system is primarily responsible for the perception of self-motion (angular velocity and linear acceleration) the center of rotation of the tilting occurs near the drivers head, whereas natural vehicle rotations occur around the center of gravity of the motion platform itself [29]. It is then possible for the simulator to perform a type of motion cueing [29] to provide the driver with the perception of sustained accelerations despite a relatively small and finite displacement envelope. It has been confirmed both informally and in controlled experiments with pilots, that vestibular motion cues are preferable and improve perceptual fidelity of a simulator [28]. The Cruden 6-DOF driving simulator enables human drivers to experience sight, sound, tactile feedback as well as vestibular motion; pitch, roll, yaw, heave, surge and sway accelerations [61]. The driver inputs include throttle, steering, braking and gear selection as well as terrain inputs to the tires. Based on feedback from expert/professional drivers we believe that the perceptual fidelity of the Cruden 6-DOF simulator is quite high, although admittedly difficult to prove.

1.3 Summary

The motivation for the proposed research work has been presented along with a review of the technology currently available as a solution to traction control. The next chapter discusses a series of laboratory experiments that were performed using a 6-DOF motion simulator in order to study the human response when given the task of performing traction control with out any driver assist technology. Chapter 1 is devoted presenting a series of HIL tests that were performed to analyze the behavior of a human expert driver. Meanwhile, Chapter 2 presents the necessary physical models for both vehicle and the tire-ground interface that are used in this work. Once the physical models have been introduced Chapter 3 synthesizes the anthropomimetic control architecture; including development of a gradient filter, simulations using the gradient filter, and comparison of the results to the HIL data from Chapter 1. Chapter 4 is devoted to an approximation of the gradient filter, with simulations comparing the exact gradient filter and its approximation. The necessary estimation algorithms to complement the filters developed in Chapters 3 and 4 are developed and presented in Chapter 5. The next chapter, Chapter 6, describes the implementation of the complete control architecture (Chapters 2-5) on a Cruden 6-DOF driving simulator. The work is completed by Chapters 7 and 8 were the conclusions of this research are presented and its future direction is

discussed.

Chapter 2

HIL Control - Case Study

Literally translated, *anthropomimetic* refers to the direct copying of desirable human behavior. A necessary obstacle in designing control solutions that are anthropomimetic in nature is the distillation of human behavioral responses. By studying human control of dynamic systems in a laboratory environment it is possible to gather the necessary sensory feedback and response signals to do just that. Even human experts are not infallible and there can be great advantage in using the desirable components of human behavior with the advantages of automatic control systems; greater precision, accuracy and higher bandwidth. It is important to note that desirable human behavior can include but is not limited to adaptation, estimation and prediction. The focus of this work will be centered around the adaptation and estimation. The challenge of vehicle traction control is well studied with in the automotive community.

2.1 HIL Traction Control Case Study

The Cruden 6-DOF full-motion driving simulator located at SoVa Motion [61], was utilized as a Human-In-the-Loop (HIL) test platform to develop a novel approach for synthesizing traction control algorithms designed to mimic the desirable behavior of human expert drivers. For this study, the driving simulator was used to measure human behavioral responses under controlled conditions. The Cruden 6-DOF driving simulator enables human drivers to experience the sight, sound, and tactile feedback at the steering wheel. Drivers also experience the pitch, roll, yaw, heave, surge, and sway motions associated with simulated vehicles in response to steering, braking, throttle, and gear selection commands provided by the driver as well as terrain inputs to the tires.

Figure 2.1 shows the basic simulation-mode operation where a human driver on the driving simulator (LHS of Figure 2.1) commands a virtual vehicle within a virtual terrain environment (RHS of Figure 2.1). This platform also allows for algorithms such as traction control to be integrated into the HIL simulation for prototype evaluation. A large selection of virtual vehicles was available for use in a variety of virtual environments, where each vehicle model is a full multi-body dynamic

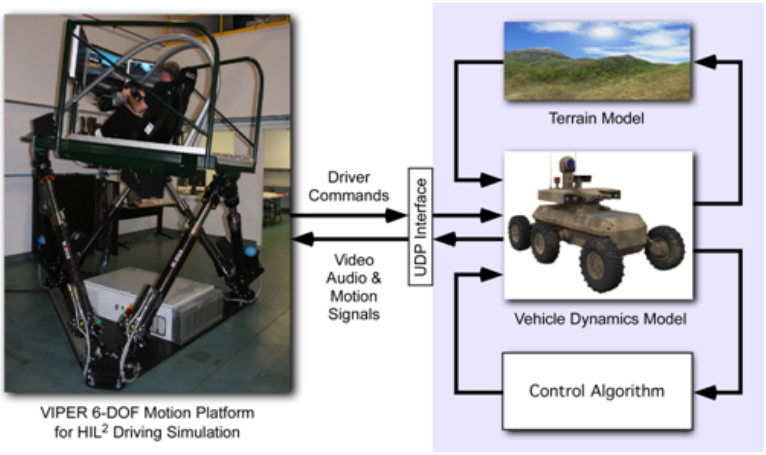

Figure 2.1: A HIL driving simulator platform was used to collect behavioral data from human expert drivers.

system including suspension kinematics, non-linear tire dynamics, engine torque curves, and aero maps. Table 2.1 lists the physical performance specifications associated with the SoVa Motion Labs driving simulator.

Table 2.1: Performance Specifications for the SoVa Motion Labs HIL Driving Simulator

	Displacement			
DOF	Single DOF	Maximum	Velocity	Acceleration
Surge	$-0.46/+0.57m$	$\pm 0.57m$	$\pm 0.7m/s$	$\pm 7m/s^2$
Sway	$\pm 0.47m$	$\pm 0.5m$	$\pm 0.7m/s$	$\pm 7m/s^2$
Heave	$\pm 0.39m$	± 0.39	$\pm 0.5m/s$	$\pm 10m/s^2$
Roll	$\pm 23.2^\circ$	$\pm 23.8^\circ$	$\pm 34^\circ/s$	$> 225^\circ/s^2$
Pitch	$-23.2/+25.5^\circ$	$-27.4/+31.6^\circ$	$\pm 35^\circ/s$	$> 225^\circ/s^2$
Yaw	$\pm 24.3^\circ$	$\pm 27.6^\circ$	$\pm 35^\circ/s$	$> 225^\circ/s^2$

Since the primary purpose of this study was to establish the feasibility of an anthropomimetic approach to control system synthesis, a simple HIL driving task was designed with only one pertinent human command input in order to isolate one key aspect of traction control. This driving task was designed to study how human drivers "find" the optimal throttle position, and thus the wheel torque, to maximize longitudinal traction performance. This task was intentionally simplified for a number of reasons. First, numerical simulation results were easily compared with the experimental HIL test results from a driving simulator, and second, minimizing the number of input and output variables was expected to lead to a more concise understanding of how human experts operate at the uncertain limits of performance. Even with the restrictions associated with this simple driving task, the non-linear traction dynamics at the tire-ground interface were more than sufficient to make this a challenging yet highly instructive case study.

2.2 HIL Testing Specifications

For this HIL case study, formal test protocols were developed instructing the human expert to drive a particular ground vehicle along a straight line on a flat dry paved surface starting from a resting condition. In addition to minimizing the steering input, the driver was also instructed not to switch gears and not to apply the brakes during any test run. These additional degrees of freedom are quite interesting and may play a role when considering both longitudinal and lateral traction control; however, their inclusion would have compromised the ability to isolate desired human behavior in this case study. Mathematically, if we define T_{25} to be the time it takes the simulated vehicle to reach a distance of twenty-five meters, then the formal objective was to control only the throttle input, or wheel torque, to minimize T_{25}. Since the driver was intentionally not provided with direct feedback on the T_{25}time, they were required to rely on internal motivation, or to simply "drive as fast as possible for each run."

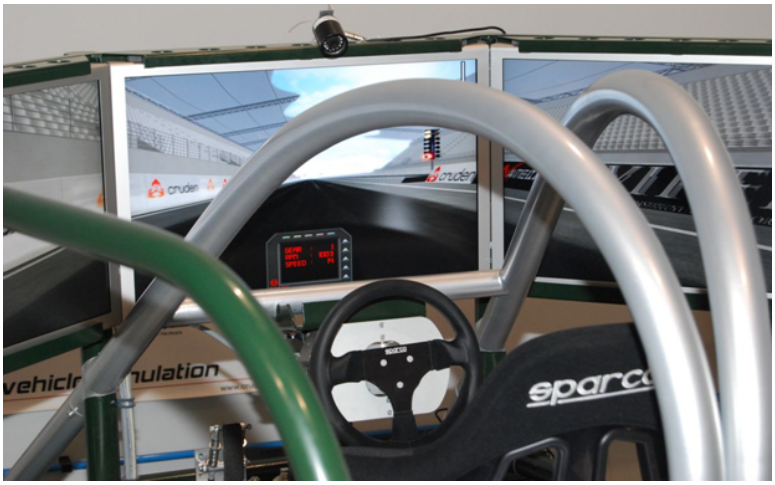

Figure 2.2: View of the virtual track used for HIL testing on the driving simulator.

In order to make this HIL case study more challenging and realistic, a virtual car was selected with enough wheel torque to quickly reach a tire burnout slip condition at any point within the 25 meter test track. The virtual car model parameters and the track surface friction properties were chosen to provide the human driver with a realistic driving experience. During the test, the driver experienced visual cues, audio, platform motion, and steering force feedback, although little or no steering was actually required for this study. The photo in Figure 2 shows an over-the-shoulder view of the simulated track as seen by a driver on the simulator. During the HIL testing, the human driver attempted fifty-one consecutive runs within the same test period without any "warm-up" trials. All driver inputs and vehicle dynamic responses were recorded during the experimental HIL testing. False starts and otherwise corrupted runs were removed from the data during post-processing, leaving a total of forty-seven usable runs.

2.3 HIL Testing Results

The four time series plots in Figure 2.3 summarize the key signals for each of the usable runs. In each plot below, the "best" run, i.e. minimum T_{25} time, is highlighted in green and the "worst" run is highlighted in red. The remaining forty-five runs were sorted by T_{25}, and are shaded from light gray (second best) to dark gray (second worst). Figure 2.3(a) is a plot of the displacement x of the vehicle. Note that reference grid lines have been drawn on this plot as displacement trajectories associated with constant accelerations. For the HIL testing, the best T_{25} time was 2.39 seconds and the worst T_{25} time was 2.99 seconds. Figure 2.3(b) is a plot of the control input torque T_E, and Figure 2.3(c) is the corresponding slip ratio, k. These simulation results confirm that the best T_{25} solution requires the torque to quickly reach a level where the slip ratio maximizes the traction force.

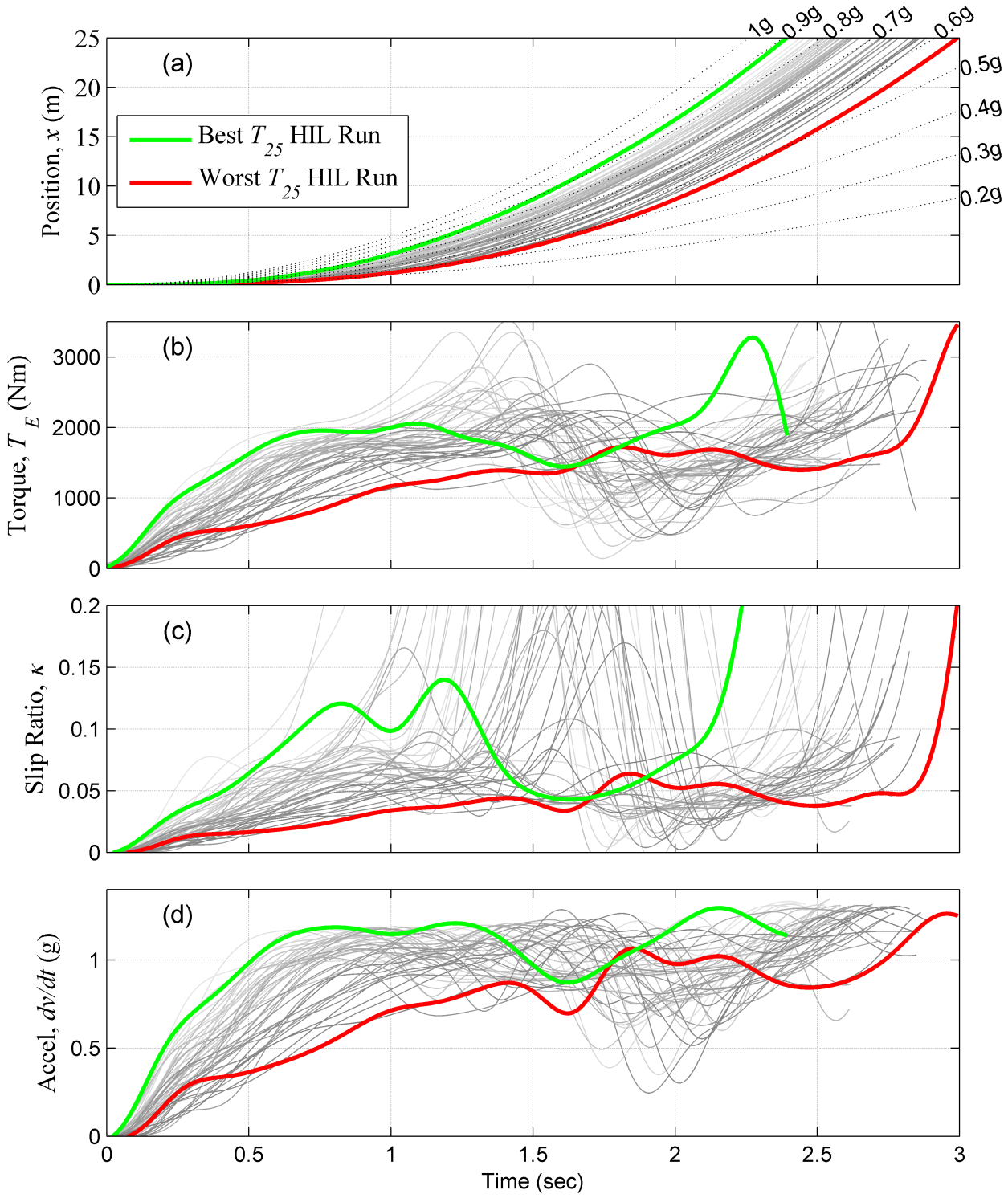

Figure 2.3: HIL experimental data; (a) position, (b) wheel torque, (c) slip ratio, and (d) acceleration.

Even with this limited set of runs, the human driver was able to demonstrate an ability to learn. This is depicted more clearly in Figure 2.4 where the T_{25} times are plotted against sequential run number. The shaded region in Figure 2.4 is an admittedly subjective estimate of an envelope centered around the data, showing a generally downward trend. The best T_{25} time occurred during run 36, and after making significant progress up to run 30, the human driver consciously began a series of even more aggressive trials (runs 32, 34, 39, 46, and 47) which were each immediately followed by one or more good runs.

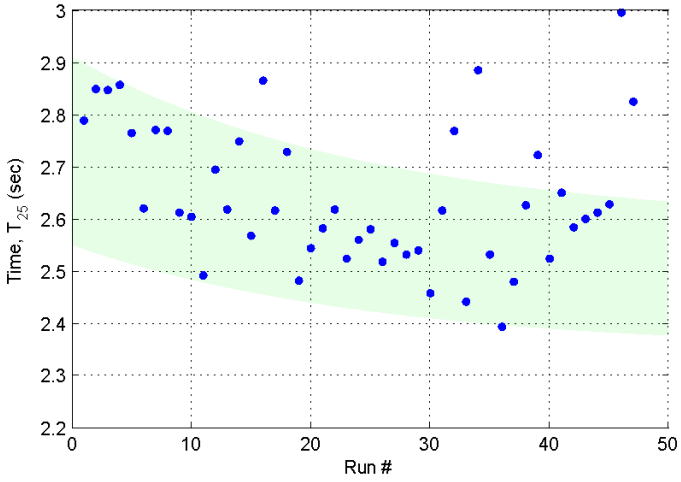

Figure 2.4: Learning trend from HIL consecutive run testing.

These HIL test results raise a fundamental question: How does the human driver learn to improve his or her performance without direct knowledge of the traction force or wheel slip? The human driver receives feedback from multiple sources such as visual, audible, tactile, and motion. For this simple task, the visual and tactile feedback is very likely negligible by design; however, the audible feedback of tire squeal as well as the longitudinal acceleration of the platform are well correlated to the traction force being generated. From the HIL acceleration data in Figure 2.3(d), it is clear that longitudinal acceleration is reduced whenever the wheel enters a burnout condition. To confirm this relationship numerically, cross-correlations were computed from the HIL test data between key driver inputs and acceleration response outputs. The normalized cross-correlation between any two sampled-data signals was calculated as

$$\rho(n) \equiv \frac{\sum_k signal_1(k)\, signal_2(k-n)}{\sqrt{\sum_k signal_1^2(k)}\sqrt{\sum_k signal_2^2(k)}}, \tag{2.1}$$

where k is the sample index and n is the delay or lag between signals. Table 2.2 shows the results of a zero-lag ($n = 0$) correlation study between the driver input (throttle and resulting wheel torque) and the pertinent acceleration responses sensed by the driver, with the exception of visual and audible feedback. The data in Table 2.2 shows the mean correlation across all 47 runs, as well as the associated standard deviation.

Table 2.2: Correlation between driver input and acceleration responses.

	Throttle		Wheel Torque	
	Mean	STD	Mean	STD
Throttle	1.000	0.0002	0.989	0.0041
Wheel Torque	0.989	0.0041	1.000	0.0004
Surge Accel	0.981	0.0157	0.981	0.0235
Sway Accel	0.218	0.4145	0.236	0.4441
Heave Accel	−0.803	0.2170	−0.806	0.2209
Pitch Accel	0.088	0.2370	0.085	0.2433
Roll Accel	−0.138	0.2204	−0.149	0.2341
Yaw Accel	0.145	0.4031	0.130	0.3846

In the HIL simulation, the throttle is the primary input from the driver; however, Table 2.2 confirms that the throttle and wheel torque are highly correlated. As expected from inspection of Figure 2.3(b) and 2.3(d), and as clearly demonstrated in Table 2.2, the longitudinal acceleration (i.e. Surge Accel) has a significantly higher level of correlation to both the throttle and the wheel torque, than any of the other five accelerations sensed by the driver. Note that the relatively high negative correlation in Table 2.2 between either the throttle or the wheel torque and the heave acceleration is physically due to the linear relationship between aerodynamic downforce and vehicle speed.

2.4 Summary

In this chapter the results of the HIL testing, performed to study a human solution to traction control, was presented. The task of travelling 25 m in the shortest amount of time was given to the human subject and a series of test runs were subsequently conducted on a 6-DOF motion platform that included a virtual vehicle environment. The human subject showed the desirable behavioral trait of being able to learn the location of the peak tractive force through repetitive learning. Analysis of the results showed a direct correlation between the sensed longitudinal (Surge) acceleration and the throttle input. This correlation is the motivation behind the development of a filter designed to estimate the gradient of the dynamic system with respect to the input, which is presented in Chapter 4. The next chapter is devoted to the development of the physical models and definitions used in the remainder of the work.

Chapter 3

Model Development

This chapter develops the vehicle, tire and system models used in the remainder of this work. The vehicle models used include a 1-DOF longitudinal model and a 3-DOF bicycle model. The tire models include the Pacejka semi-empirical model for pure longitudinal slip as well as combined slip (longitudinal and lateral).

3.1 Definitions: Tire Slip and Traction Force Generation

One of the most widely accepted tire models is the Magic Formula developed by Pacejka [30, 14, 1]. The family of Pacejka models are semi-empirical formulas expressed with a set of coefficients that are unique to each tire-ground interface. The values of these coefficients are derived from a non-linear curve fit of experimental tire force and moment data collected over a range of operating conditions. The lateral and longitudinal traction forces at each tire-ground interface are functions of the following four generally time-varying states.

- $\alpha =$ *Slip Angle* (radians)
- $\gamma =$ *Camber Angle* (radians)
- $\kappa =$ *Slip Ratio* (non-dimensional)
- $F_z =$ *Normal Force* (Newtons)

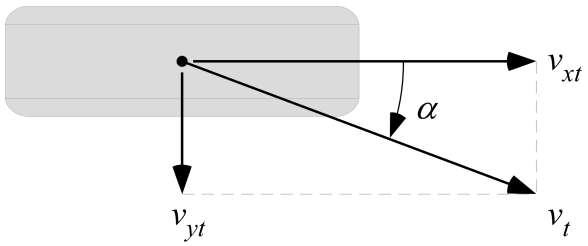

Figure 3.1: Top view of slip angle definition using SAE coordinate system convention.

Following the definition in Figure 3.1, the slip angle α is measured from the longitudinal (x) axis of the wheel toward the actual net velocity of the wheel, and is defined by Equation 3.1.

$$\alpha\left(v_{xt}, v_{yt}\right) = \arctan\left(\frac{v_{yt}}{|v_{xt}|}\right) \tag{3.1}$$

Using the SAE J670 definition [2, 14, 1], the slip ratio represents the longitudinal slip, which is defined by Equation 3.2 [31].

$$\kappa\left(\omega, v_{xt}\right) = \left(\frac{\omega R - v_{xt}}{v_{xt}}\right) \tag{3.2}$$

where ω is the angular velocity of the wheel, and R is the effective rolling radius of the wheel. Note that $\omega R > v_{xt} \rightarrow \kappa > 0$ during acceleration, and $\omega R < v_{xt} \rightarrow \kappa < 0$ when braking [4]. The general form of the Magic Formula is based on a common nonlinear function given by Equation 3.3.

$$Y\left(s; \mathbf{p}\right) = D \sin\left[C \arctan\left(Bs\left[1 - E\right] + E \arctan\left[Bs\right]\right)\right] + S \tag{3.3}$$

When the general slip state s is the slip angle α, then Equation 3.3 represents the pure lateral traction force. When the general slip state s is the slip ratio κ, then Equation 3.3 represents the pure longitudinal traction force. The coefficients B, C, D, and E are respectively referred to as the stiffness, shape, peak, and curvature coefficients for a given tire-ground interface [14, 1]. These coefficients and S are explicit functions of the time-varying normal force F_N, the camber angle γ, and a vector of constant parameter values $\mathbf{p}$ that are empirically derived from experimental test data [31]. The constant values of $\mathbf{p}$ used in this work for both the 1-DOF model and 3-DOF model as well as wet and dry pavement are listed in the Appendix F.3. For pure longitudinal slip, the longitudinal tractive force is given by F_{xo} in Equation 3.4, and for pure lateral slip, the lateral tractive force is given by F_{yo} in Equation 3.5. The change in sign in Equation 3.5 is needed to accommodate for the difference between the reference frames used in the development of Pacejka's Magic Formula of Equation 3.3 and those seen in this work, specifically Figure 3.1.

$$F_{xo}\left(\kappa, \gamma, F_z\right) = Y\left(\kappa, \gamma, F_z; \mathbf{p_x}\right) \tag{3.4}$$

$$F_{yo}\left(\alpha, \gamma, F_z\right) = -Y\left(\alpha, \gamma, F_z; \mathbf{p_y}\right) \tag{3.5}$$

In the more common case where the tire simultaneously experiences combined longitudinal and lateral slip, the pure slip forces defined by Equations 3.4 and 3.5 are modified according to Genta [32] using Equations 3.6 and 3.7. The method developed by Genta [32] is empirical and is designed to accommodate for the fact that a tire has some limit when it comes to tractive capacity and

according to Genta produces better results than those obtained through the elliptical approximation [32].

$$F_x(\alpha,\kappa,\gamma,F_z) = \frac{\sigma_x^*}{\sigma^*}\left|F_{xo}(\kappa,\gamma,F_z)\right| \tag{3.6}$$

$$F_y(\alpha,\kappa,\gamma,F_z) = \frac{\sigma_y^*}{\sigma^*}\left|F_{yo}(\alpha,\gamma,F_z)\right| \tag{3.7}$$

The terms $F_{xo}(\kappa,\gamma,F_z)$ and $F_{yo}(\alpha,\gamma,F_z)$, in Equations 3.6 and 3.7, are defined according to Genta [32] as Equations 3.4 and 3.5, which are the values obtained from the Pacejka's empirical tire model [14, 1]. While σ_x^*, σ_y^* and σ^* are defined according to Equations 3.8-3.10, where κ^* and α^* are locations of peak longitudinal and lateral forces [32].

$$\sigma_x^* = \kappa/\kappa^* \tag{3.8}$$

$$\sigma_y^* = \alpha/\alpha^* \tag{3.9}$$

$$\sigma^* = \sqrt{(\sigma_x^*)^2+(\sigma_y^*)^2} \tag{3.10}$$

An example family of pure longitudinal traction curves is shown in Figure 3.2 for a tire on three different but uniform terrain surfaces with a constant normal force and a constant camber angle. This plot shows the longitudinal traction curves for acceleration (i.e. $\alpha = 0, \kappa > 0$). The traction curve is typically antisymmetric about $(0,0)$ when braking is included (i.e. $\kappa < 0$); however, in most real tire-ground interfaces, the braking region is similar in shape to the acceleration region of the curve. The dashed line region of the curves in Figure 3.2 represent the regions of longitudinal wheel slip where the traction force remains high, but not at the peak value. High performance traction control systems must be able to operate at or near and preferably below the peak point in the traction curve.

An approximation that differs from the SAE J670 definition [4] of slip ratio κ is used at low vehicle speeds, according to Equation 3.11 for pure longitudinal slip and both Equations 3.11 and 3.12 for combined slip, to avoid a singularity in the solution.

$$\kappa = \begin{cases} \frac{\omega R - v_{xt}}{v_{xt}} & v_{xt} \geq v_o \\ \frac{\omega R - v_{xt}}{v_o} & v_{xt} < v_o \end{cases} \tag{3.11}$$

$$\alpha = \begin{cases} \arctan\left(\frac{v_{yt}}{|v_{xt}|}\right) & v_{xt} \geq v_o \\ \arctan\left(\frac{v_{yt}}{v_o}\right) & v_{xt} < v_o \end{cases} \tag{3.12}$$

$$\tag{3.13}$$

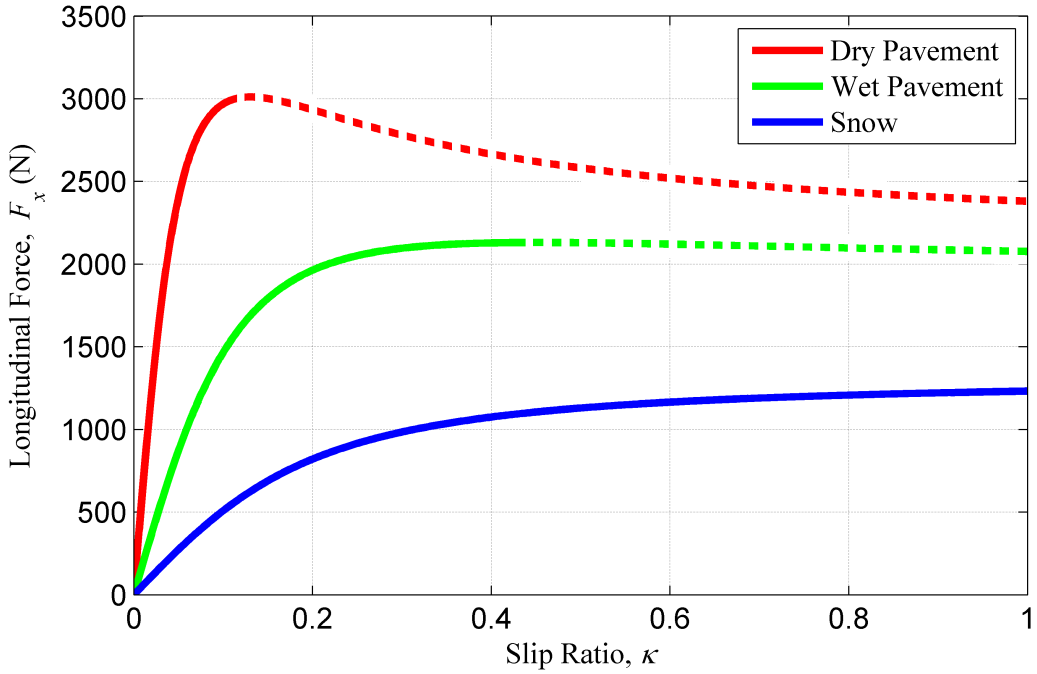

Figure 3.2: Example pure longitudinal traction curves from the Pacejka Magic Formula.

Figures 3.3 and 3.4 are the plots of the longitudinal and lateral forces in combined slip according to Equations 3.6 and 3.7 for both dry and wet pavement. These plots clearly illustrate the saturation of both lateral and longitudinal forces in combined slip, in much the same manner as the Figure3.2 clearly shows the saturation of longitudinal forces for a variety of surfaces. Figure 3.5 is an example plot of the resultant magnitude of the traction force $((F_r) = \sqrt{F_{xt}^2 + F_{yt}^2})$ for a single tire as a function of the slip angle and the slip ratio at a constant camber angle and a constant normal force condition. Notice that the interval defined by $\alpha = 0$ and $\kappa \geq 0$, presented in Figure 3.3, defines the pure longitudinal force magnitude as a function of slip ratio that is similar to the Dry Pavement traction curve plotted in Figure 3.2. Similarly, the interval defined by $\kappa = 0$ and $\alpha \geq 0$, presented in Figure 3.4, defines the pure lateral force magnitude as a function of slip angle for a left turn.

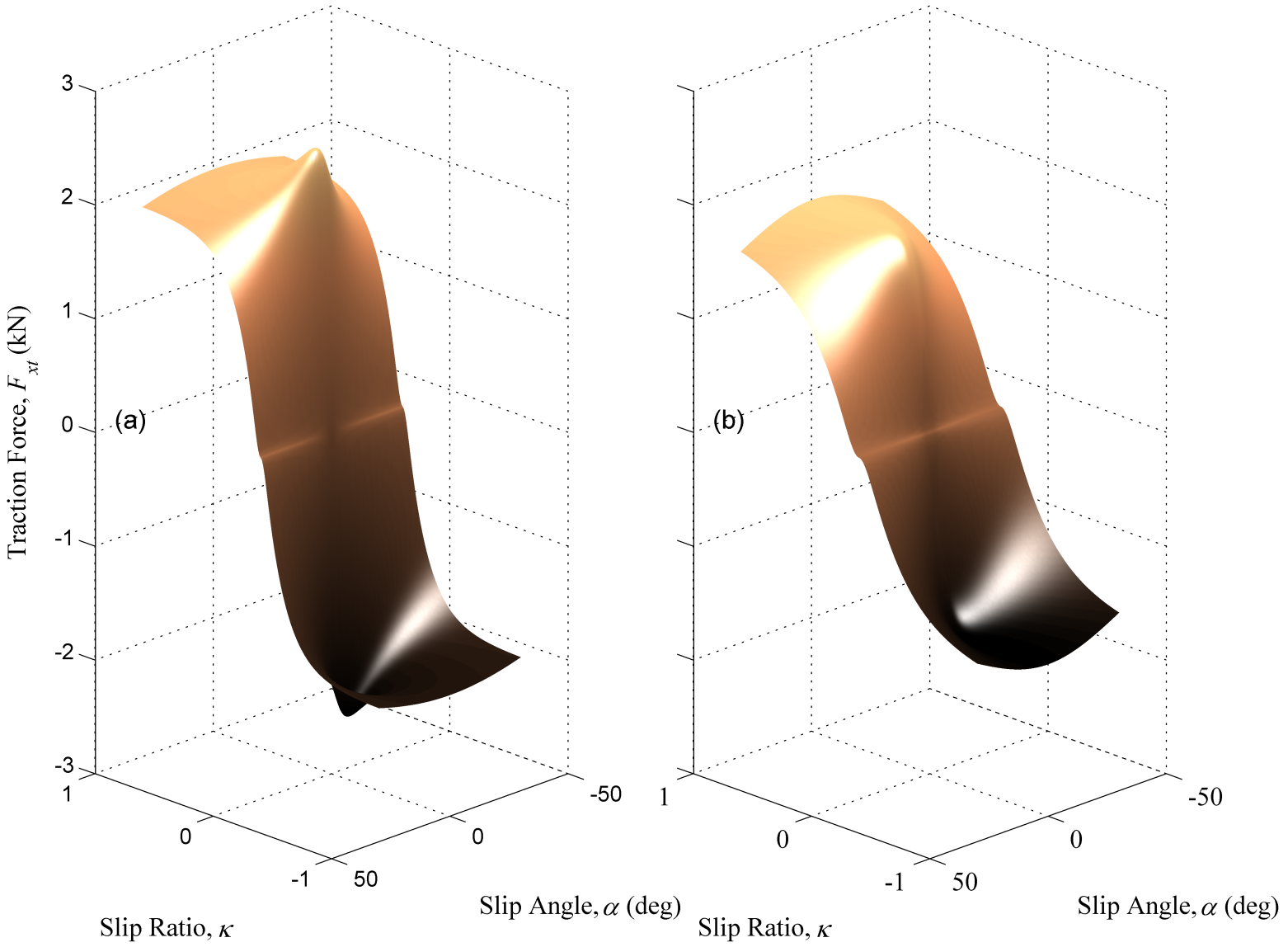

Figure 3.3: Typical longitudinal force values when operating in combined mode friction regime: (a) Dry Pavement (b) Wet Pavement.

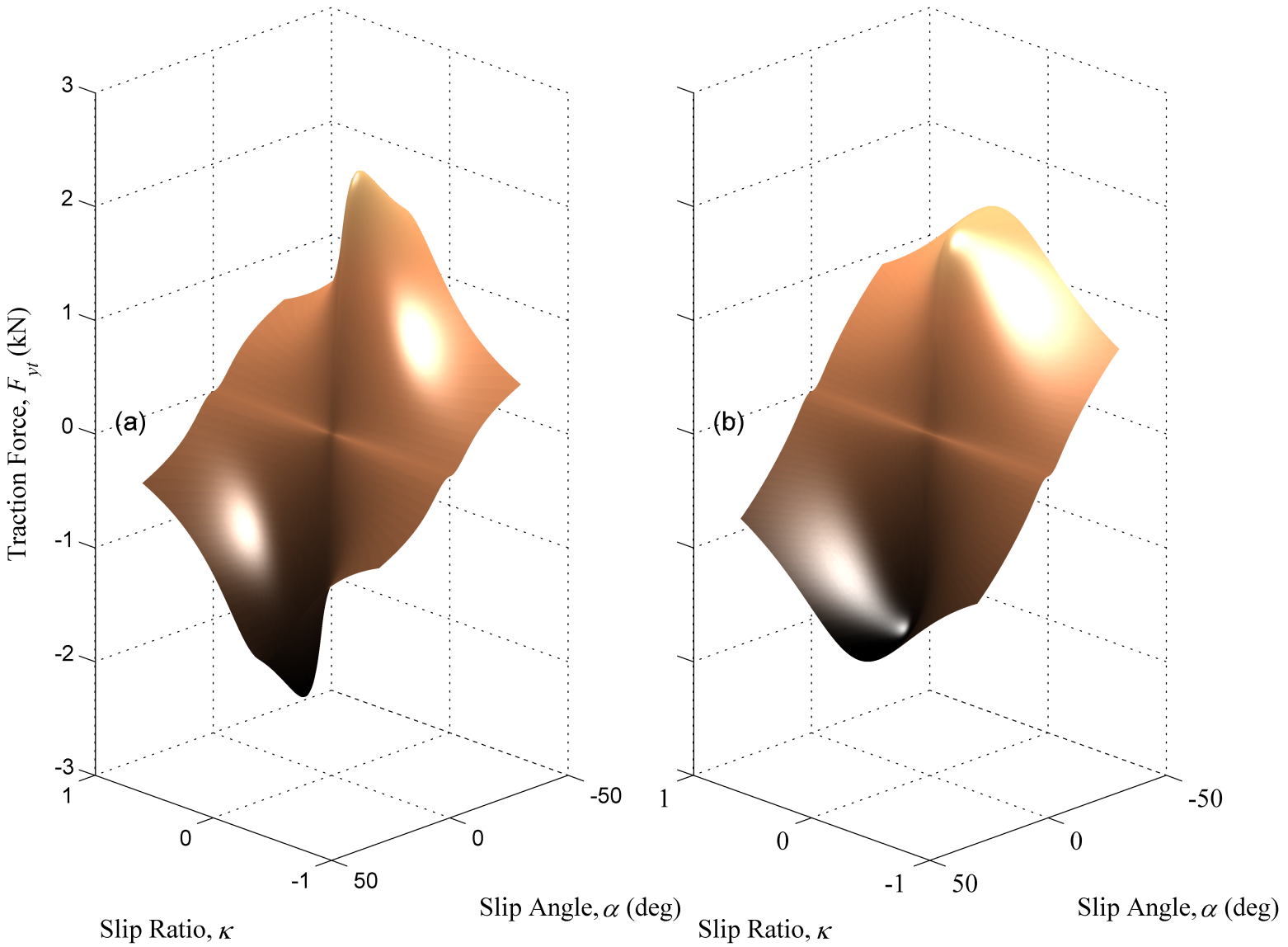

Figure 3.4: Typical lateral force values when operating in combined mode friction regime: (a) Dry Pavement (b) Wet Pavement.

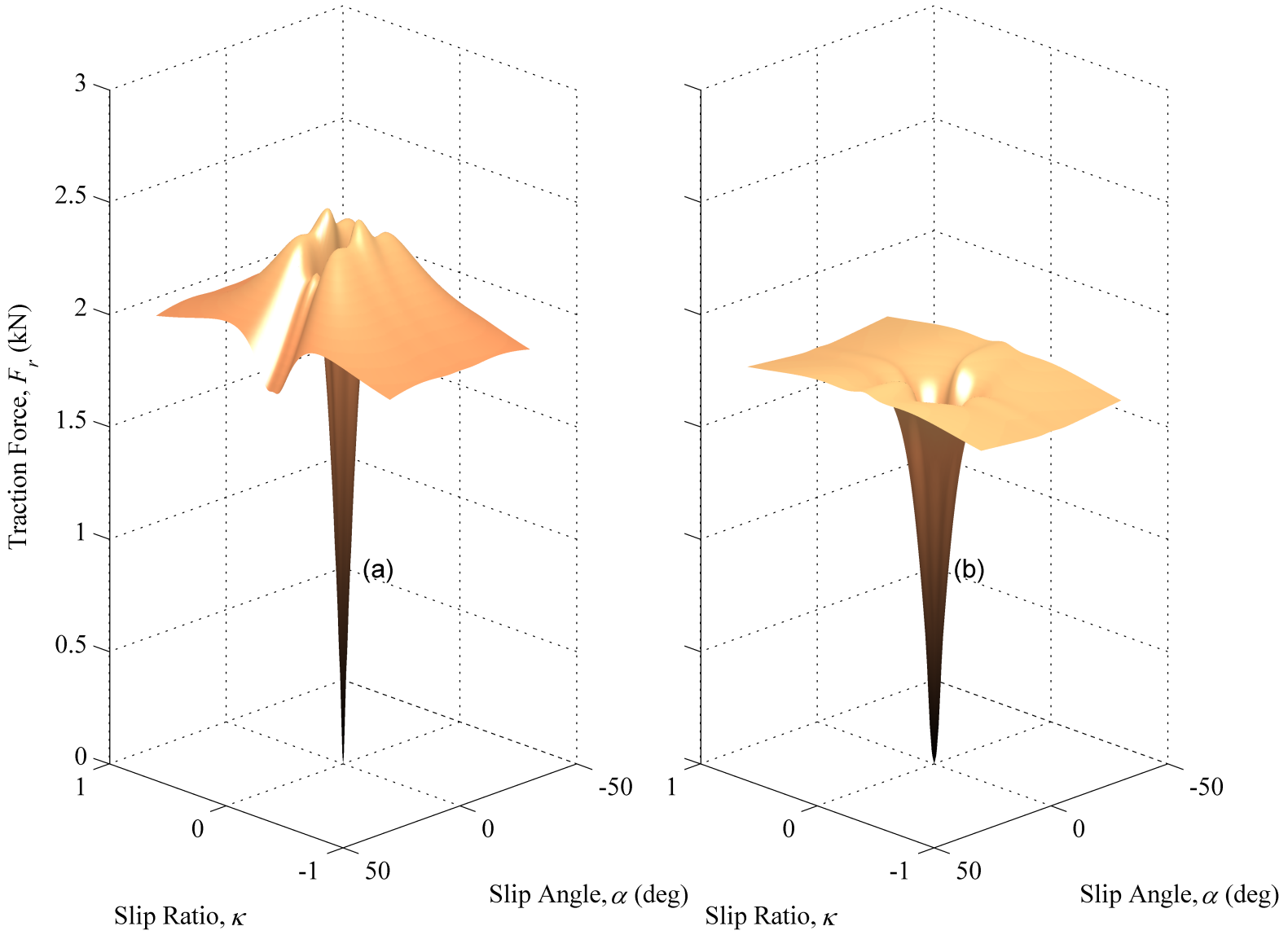

Figure 3.5: The magnitude (vector sum of longitudinal and lateral forces) of the traction force at one wheel as a function of slip ratio κ and slip angle α: (a) Dry Pavement (b) Wet Pavement.

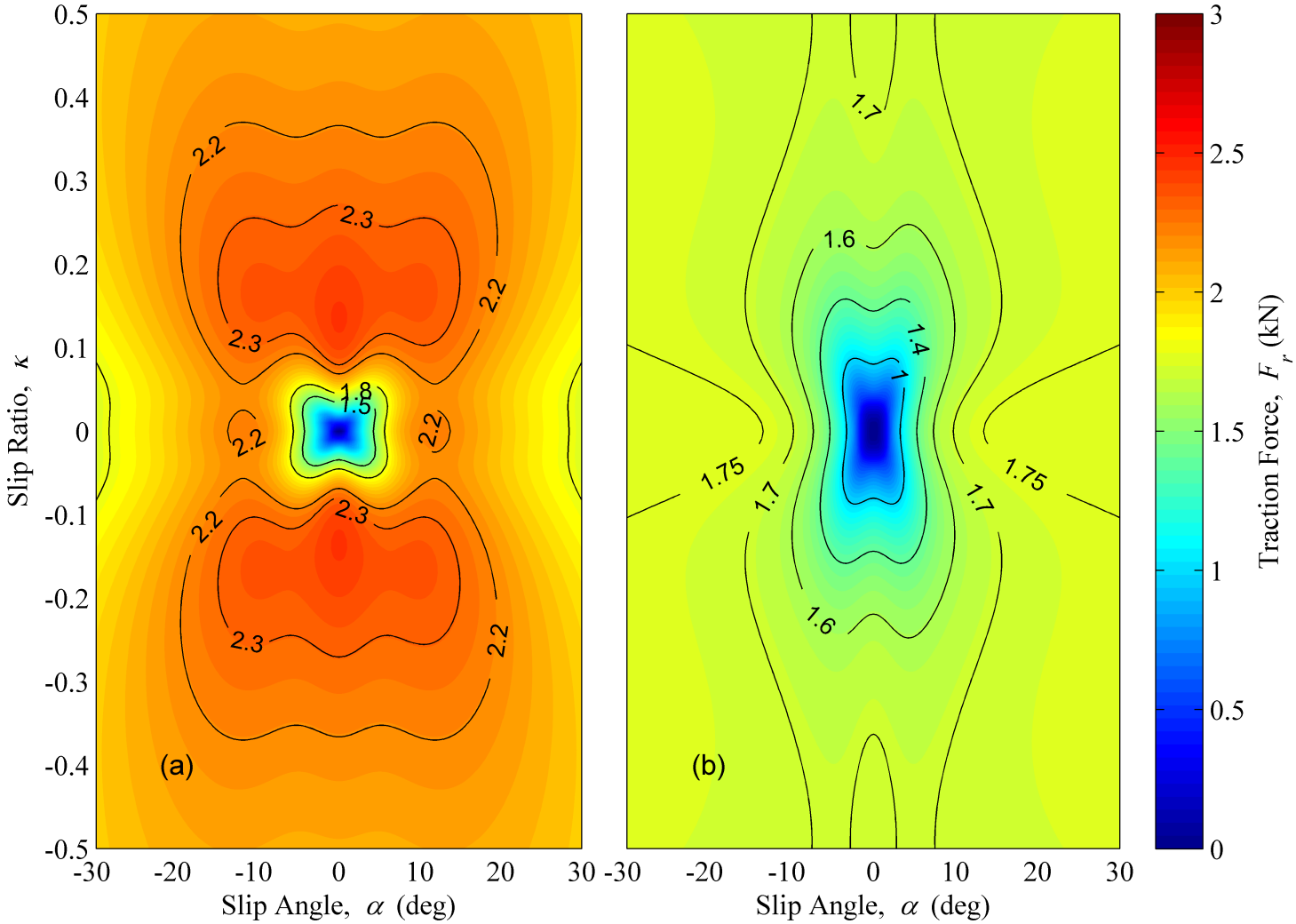

Figure 3.6: Contour plot of the magnitude (vector sum of longitudinal and lateral forces) of the traction force at one wheel as a function of slip ratio κ and slip angle α: (a) Dry Pavement (b) Wet Pavement.

Notice from Figure 3.5 that at a fixed slip ratio, e.g. $\kappa = 0.15$, as the slip angle is increased, the traction force magnitude actually decreases. In order to maximize the traction force as the slip angle is increased, the slip ratio must be reduced in this case. Figure 3.5 clearly indicates the existence of a ridge of maxima, not necessarily at the same level, which generally has an elliptical shape in the α-κ plane.

Another more instructive way to interpret Figure 3.5 is to imagine a radial line emanating outward from the origin of the plot. Along any radial line, the force magnitude starts at zero, then it monotonically increases to a maximum force, after which it monotonically decreases. A human driver will generally always have complete control of the steering angle(s), even in a vehicle with traction control. In an autonomous vehicle, the autonomous control algorithm will also have complete control over the steering angle(s). If we interpret this to be a hard constraint, then we must accept the fact that the slip angle is not a quantity that can generally be used by a traction control algorithm as a controlled signal. The slip angle will be completely determined by the steering angle and the individual tire velocity. The traction control algorithm will however, have the authority to command the slip ratio in any driven wheel through applied engine torque and braking, much like conventional traction control algorithms. The algorithm will display a limited amount of control authority over the slip angle, as the slip angle is dynamically linked to the states that are directly controlled by the engine torque. As clearly indicated by Figure 3.5, the problem of combined lateral and longitudinal traction control is, in essence, equivalent to the problem of pure longitudinal traction control. This fact enables the proposed adaptive traction control algorithm outlined for 1-DOF longitudinal case to be applied directly to the combined traction condition for the 3-DOF dynamic bicycle model.

3.2 Longitudinal Vehicle Model (1-DOF)

Initial simulation studies for this work were performed using the 1-DOF vehicle model of Figure 3.7. Similar models have been utilized for studying the non-linear longitudinal dynamics of traction control [33, 34], as well as alternative traction control algorithms [8, 9, 35, 36, 37]. While clearly not representative of an actual car, the model does illustrate the pertinent non-linear dynamics associated with wheeled vehicle traction. The vehicle mass m is constrained to move along displacement x with velocity v. Energy is applied through the control torque T_C to a single wheel of radius R and rotational inertia J_W, producing an angular velocity ω. The viscous wheel damping is assumed to be linear with respect to wheel velocity, $T_W = \beta\omega$. Similarly, the aerodynamic drag force and down force are defined as $F_D = \gamma_x v$ and $F_A = a_D v$, respectively. The non-linear tractive force F_x is a function of the normal force F_N and slip ratio κ.

The net horizontal force is the sum of the non-linear traction force F_x and aerodynamic drag force F_D. Combining these results, the complete linear dynamics are given by Equation 3.14.

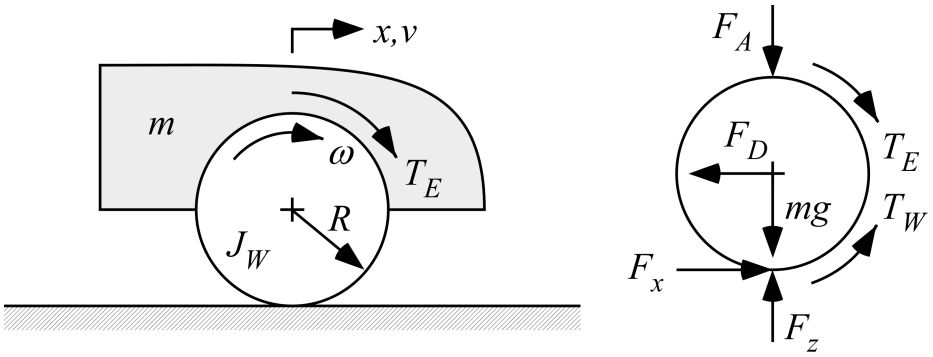

Figure 3.7: 1-DOF longitudinal car model.

$$\begin{bmatrix} \dot{v} \\ \dot{\omega} \\ \dot{T}_E \end{bmatrix} = \begin{bmatrix} -\left(\frac{\alpha}{m}\right) & 0 & 0 \\ 0 & -\left(\frac{\beta}{J_W}\right) & \left(\frac{1}{J_W}\right) \\ 0 & 0 & -(2\pi f_E) \end{bmatrix} \begin{bmatrix} v \\ \omega \\ T_E \end{bmatrix} + \begin{bmatrix} 0 & \left(\frac{1}{m}\right) \\ 0 & -\left(\frac{R}{J_W}\right) \\ (2\pi f_E) & 0 \end{bmatrix} \begin{bmatrix} T_C \\ F_x \end{bmatrix}, \quad (3.14)$$

where T_C is the commanded input torque and T_E is the actual applied wheel torque. In this model, the actual applied torque state is assumed to be the output of a first-order unity-gain low-pass filter with break frequency f_E (Hz). Note that the dynamics for this simple single-wheel model are linear except for the constitutive Equation for the traction force. The non-linear traction force, F_x, is given by the semi-empirical "Magic Formula" of Pacejka and discussed in Section 3.1. It is convenient to define a generic continuous time system as Equation 3.15, where N is the number of states, P is the number of outputs, M is the number of inputs and Q is the number of non-linear feedback terms. This allows us to define $\mathbf{x} \in \Re^N$, $\mathbf{y} \in \Re^P$, $\mathbf{u} \in \Re^M$ and $\mathbf{u}' \in \Re^Q$.

$$\dot{\mathbf{x}} = \mathbf{A_c x} + \mathbf{B_c u} + \mathbf{F_c u}' \quad (3.15)$$
$$\mathbf{y} = \mathbf{C_c x} + \mathbf{D_c u} + \mathbf{G_c u}' \quad (3.16)$$

The non-linear dynamics of Equation 3.15 are split into a set of linear dynamics with non-linear feedback according to Figure 3.8.

The non-linear feedback terms $\mathbf{u}' \in \Re^Q$ and $\mathbf{y}' \in \Re^{N+M}$ are defined according to Equations. 3.17 and 3.18.

$$\mathbf{y}' = \begin{bmatrix} \mathbf{I}_N \\ \mathbf{0} \end{bmatrix} \mathbf{x} + \begin{bmatrix} \mathbf{0} \\ \mathbf{I}_M \end{bmatrix} \mathbf{u} = \begin{bmatrix} \mathbf{x} \\ \mathbf{u} \end{bmatrix} \quad (3.17)$$

$$\mathbf{u}' = \begin{bmatrix} f_1(\mathbf{y}') \\ \vdots \\ f_Q(\mathbf{y}') \end{bmatrix} = \mathbf{f}(\mathbf{y}') \quad (3.18)$$

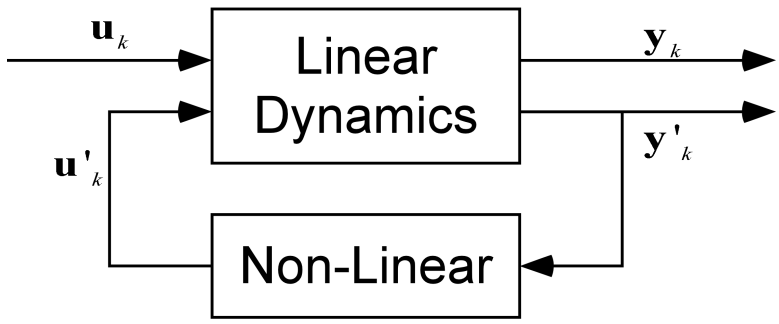

Figure 3.8: Block diagram of linear system with non-linear feedback.

When using the vehicle model of Figure 3.7, this results in $\mathbf{u}' = [F_T]$, $\mathbf{u} = [T_C]$, $\mathbf{x} = \begin{bmatrix} v & \omega & T_E \end{bmatrix}^T$ and $\mathbf{y} = [\dot{v}]$.

3.3 Kinematic Bicycle Model (3-DOF)

The kinematic model of lateral vehicle motion developed by Rajamani [38] is shown in Figure 3.9. The front and rear steering angles are represented as δ_f and δ_r, respectively. The distances between the front and rear axles to the center of gravity are represented as L_f and L_r and when added together will equal the wheelbase of the vehicle, L. The vehicles' velocity, represented by v in Figure 3.9, is a vector quantity composed of the longitudinal velocity v_{xc} and lateral velocity v_{yc} of the vehicle. The yaw rate $\dot{\psi}$ is measured about the vehicles' center of gravity, while the yaw angle ψ is an absolute value. The tire forces are developed in the reference frame of each tire using Pacejka's Magic Formula [30, 14, 1] for combined mode friction. The longitudinal forces are defined as F_{xtf} and F_{xtr}, while the lateral forces are defined as F_{ytf} and F_{ytr}. It is important to emphasize that the tire forces are developed in the local coordinate frame of the tire(s) as seen in Figure 3.9.

The Equations of motion, Equations 3.19-3.21, for Figure 3.9 are developed by summing the forces and torques for the three degrees of freedom of the vehicle through its center of mass. The three degrees of freedom for this particular model are referred to as the longitudinal, lateral and yaw degrees of freedom.

$$m\dot{v}_x = F_{xtf}\cos(\delta_f) - F_{ytf}\cos(90-\delta_f) + F_{xtr}\cos(\delta_r) - F_{ytr}\cos(90-\delta_r) \quad (3.19)$$

$$m\dot{v}_y = F_{xtf}\sin(\delta_f) + F_{ytf}\sin(90-\delta_f) + F_{xtr}\sin(\delta_r) + F_{ytr}\sin(90-\delta_r) \quad (3.20)$$

$$J_m\ddot{\psi} = L_f\left[F_{xtf}\sin(\delta_f) + F_{ytf}\sin(90-\delta_f)\right] - L_r\left[F_{xtr}\sin(\delta_r) + F_{ytr}\sin(90-\delta_r)\right] \quad (3.21)$$

The non-linear tire forces are functions of the instantaneous values of the normal forces F_{ztf} and

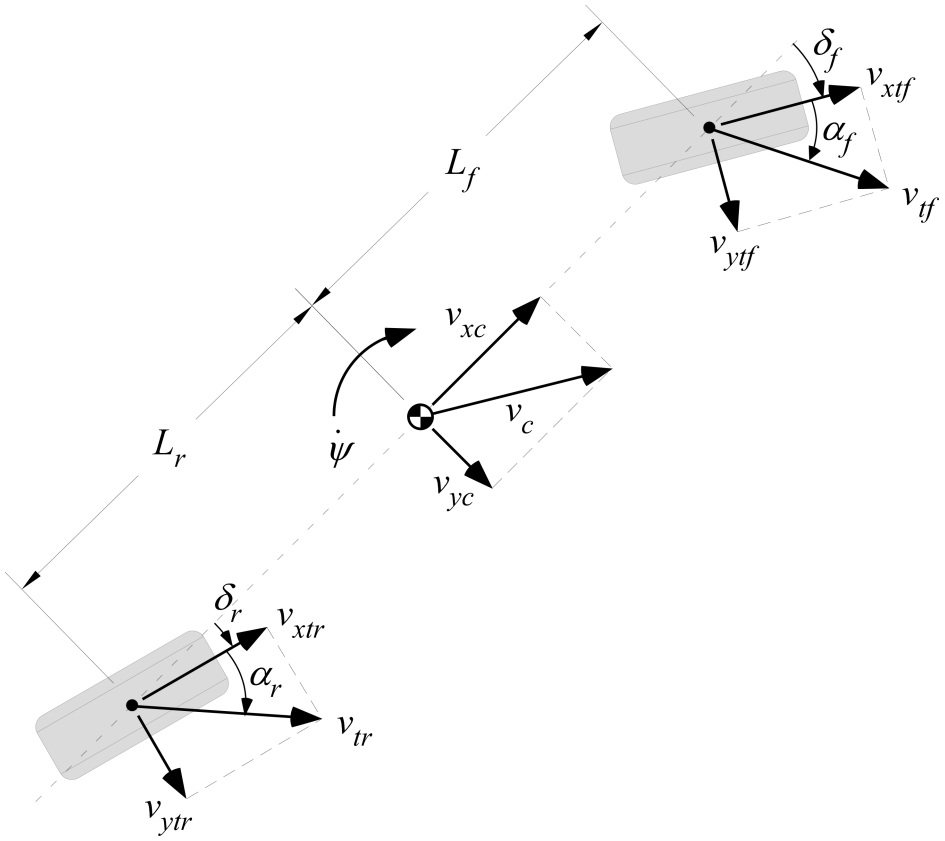

Figure 3.9: Bicycle model used to include lateral dynamics.

F_{ztr} as well as the tire slip angle α_f and α_r and tire slip ratio κ_f and κ_r [1, 14, 39]. The slip angle α, defined in Equation 3.1, is defined according to Pacejka et. al. [14, 1, 31], as Equations 3.22 and 3.23 for the front and rear tires respectively.

$$\alpha_f = arctan\left(\frac{v_{ytf}}{|v_{xtf}|}\right) \tag{3.22}$$

$$\alpha_r = arctan\left(\frac{v_{ytr}}{|v_{xtr}|}\right) \tag{3.23}$$

The tire slip ratio κ of Equation 3.2 is defined by Pacejka et. al. [14, 1, 31] as Equations 3.24 and 3.25, for the front and rear tires respectively.

$$\kappa_f = \frac{\omega_f R - v_{xtf}}{v_{xtf}} \tag{3.24}$$

$$\kappa_r = \frac{\omega_r R - v_{xtr}}{v_{xtr}} \tag{3.25}$$

The velocities v_{xtf}, v_{ytf}, v_{xtr}, and v_{ytr} refer to the velocity in the wheel reference frame at the front and rear wheels, respectively. The values from the vehicle reference (v_x, v_y, $\dot{\psi}$) can be transformed to the wheel reference (v_{xtf}, v_{ytf}, v_{xtr}, v_{ytr}) using Equations 3.26 and 3.26.

$$\begin{bmatrix} v_{xtf} \\ v_{ytf} \end{bmatrix} = \begin{bmatrix} cos(\delta_f) & sin(\delta_f) \\ -sin(\delta_f) & cos(\delta_f) \end{bmatrix} \begin{bmatrix} v_{xc} \\ v_{yc} + L_f \dot{\psi} \end{bmatrix} \tag{3.26}$$

$$\begin{bmatrix} v_{xtr} \\ v_{ytr} \end{bmatrix} = \begin{bmatrix} cos(\delta_r) & sin(\delta_r) \\ -sin(\delta_r) & cos(\delta_r) \end{bmatrix} \begin{bmatrix} v_{xc} \\ v_{yc} - L_r \dot{\psi} \end{bmatrix} \tag{3.27}$$

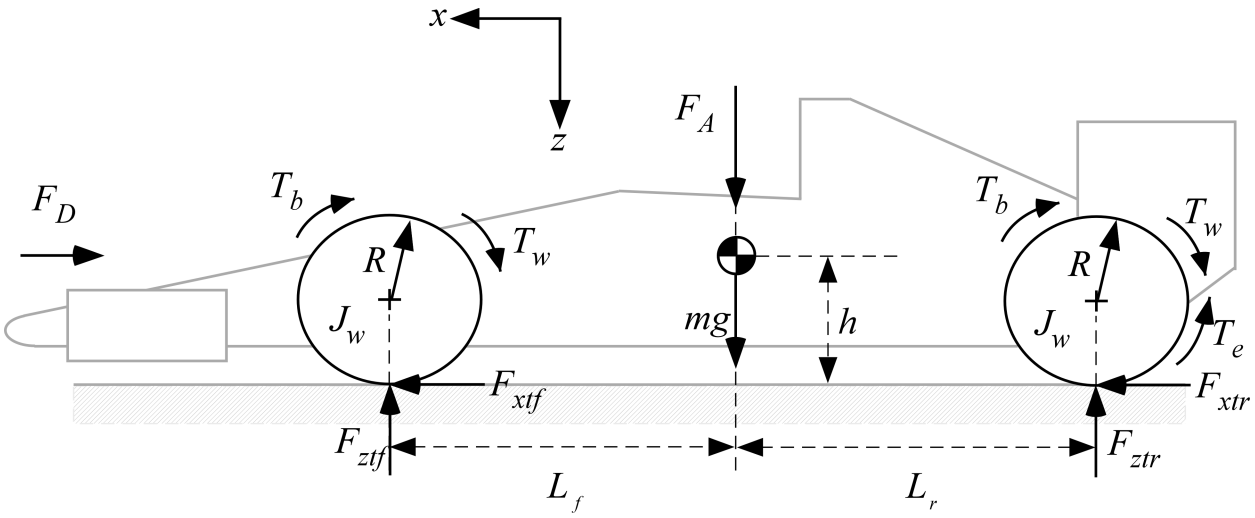

Figure 3.10: Longitudinal dynamics of the planar bicycle model

The instantaneous normal forces are F_{zf} and F_{zr} are developed by summing the moments about the front and rear contact patches and are considered to be static and given by Equations 3.28 and 3.29, respectively. It is important to note that the front and rear wheels shown in Figures 3.10 and 3.9 are treated as two tires at the identical slip ratio and slip angle each having a normal load described by either Equation 3.28 or 3.29.

$$F_{ztf} = \left(mgL_r + F_A L_r - F_D h - m\ddot{x}h\right) / \left(L_f + L_r\right) \tag{3.28}$$

$$F_{ztr} = \left(mgL_f + F_A L_f + F_D h + m\ddot{x}h\right) / \left(L_f + L_r\right) \tag{3.29}$$

3.4 Dynamic Bicycle Model (3-DOF)

The kinematic bicycle model of Figure 3.9, and the longitudinal vehicle model of Figure 3.7 are combined to form the complete model which can be represented as a single dynamic system in

continuous time by Equation 3.15. In order to approximate the engine dynamics the commanded torque T_c is filtered to get the engine torque T_e using a first order low pass filter with break frequency equal to f_E (Hz). Using these additional definitions and Equations 3.19, 3.20, and 3.21 make it possible to represent the complete model as Equation 3.15, where N is the number of states, P is the number of outputs, M is the number of inputs and Q is the number of non-linear feedback terms. The structure of Equation 3.15 separates the dynamic system into a set of linear states and inputs combined with a set of non-linear feedback terms $\mathbf{u}' \in \Re^Q$ as has been done in previous work [121, 122, 123]. It is possible to define the non-linear feedback terms $\mathbf{u}' \in \Re^Q$ and $\mathbf{y}' \in \Re^{N+M}$, according to Equation 3.31. The vector quantity $f(\mathbf{y}')$ is a static non-linear mapping from $\mathbf{y}'$ to $\mathbf{u}'$. For our particular problem the state space system is defined according to Equations 3.30-3.44.

$$\mathbf{y}' = \left[\ \mathbf{I}_N\mathbf{0}\ \right]\mathbf{x} + \left[\ \mathbf{0}\mathbf{I}_M\ \right]\mathbf{u} = \begin{bmatrix} \mathbf{x} \\ \mathbf{u} \end{bmatrix} \tag{3.30}$$

$$\mathbf{u}' = \begin{bmatrix} f_1(\mathbf{y}') \\ \vdots \\ f_Q(\mathbf{y}') \end{bmatrix} = \mathbf{f}(\mathbf{y}') \tag{3.31}$$

$$\mathbf{A_c} = \begin{bmatrix} \frac{-\gamma_x}{m} & 0 & 0 & 0 & 0 & 0 \\ 0 & \frac{-\gamma_y}{m} & 0 & 0 & 0 & 0 \\ 0 & 0 & 0 & 0 & 0 & 0 \\ 0 & 0 & 0 & \frac{-\beta}{J_w} & 0 & 0 \\ 0 & 0 & 0 & 0 & \frac{-\beta}{J_w} & \frac{1}{J_w} \\ 0 & 0 & 0 & 0 & 0 & -2\pi f_e \end{bmatrix} \tag{3.32}$$

$$\mathbf{B_c} = \left[\ 0 \quad 0 \quad 0 \quad 0 \quad 0 \quad 2\pi f_e\ \right]^T \quad (acceleration) \tag{3.33}$$

$$\mathbf{B_c} = \begin{bmatrix} 0 & 0 & 0 & \frac{-1}{J_w} & 0 & 0 \\ 0 & 0 & 0 & 0 & \frac{-1}{J_w} & 0 \end{bmatrix}^T \quad (braking) \tag{3.34}$$

$$\mathbf{F_c} = \begin{bmatrix} \frac{1}{m}\cos(\delta_f) & \frac{1}{m} & \frac{-1}{m}\cos(90-\delta_f) & 0 \\ \frac{1}{m}\sin(\delta_f) & 0 & \frac{1}{m}\sin(90-\delta_f) & \frac{1}{m} \\ \frac{L_f}{J_m}\sin(\delta_f) & 0 & \frac{L_f}{J_m}\sin(90-\delta_f) & -\frac{L_r}{J_m} \\ \frac{-R}{J_w} & 0 & 0 & 0 \\ 0 & \frac{-R}{J_w} & 0 & 0 \\ 0 & 0 & 0 & 0 \end{bmatrix} \tag{3.35}$$

$$\mathbf{C_c} = \begin{bmatrix} \frac{-\gamma_x}{m} & 0 & 0 & 0 & 0 & 0 \\ 0 & \frac{-\gamma_y}{m} & 0 & 0 & 0 & 0 \end{bmatrix} \tag{3.36}$$

$$\mathbf{D_c} = \begin{bmatrix} 0 \\ 0 \end{bmatrix} \quad (acceleration) \tag{3.37}$$

$$\mathbf{D_c} = \begin{bmatrix} 0 & 0 \\ 0 & 0 \end{bmatrix} \quad (braking) \tag{3.38}$$

$$\mathbf{G_c} = \begin{bmatrix} \frac{1}{m}\cos(\delta_f) & \frac{1}{m} & \frac{-1}{m}\cos(90-\delta_f) & 0 \\ \frac{1}{m}\sin(\delta_f) & 0 & \frac{1}{m}\sin(90-\delta_f) & \frac{1}{m} \end{bmatrix} \tag{3.39}$$

$$\mathbf{x} = \left[\ v_x \quad v_y \quad \dot{\psi} \quad \omega_f \quad \omega_r \quad T_e\ \right]^T \tag{3.40}$$

$$\mathbf{y} = \left[\ \dot{v}_x \quad \dot{v}_y\ \right]^T \tag{3.41}$$

$$\mathbf{u} = \left[\ T_c\ \right] \quad (acceleration) \tag{3.42}$$

$$\mathbf{u} = \left[\ T_{b,f} \quad T_{b,r}\ \right]^T \quad (braking) \tag{3.43}$$

$$\mathbf{u}' = \left[\ F_{xtf} \quad F_{xtr} \quad F_{ytf} \quad F_{ytr}\ \right]^T \tag{3.44}$$

3.5 Summary

This chapter presented the physical models used in the latter portions of the work: a combined-mode tire-ground interface model (Pacejka), a 1-DOF longitudinal car model, and a dynamic bicycle model. While both models neglect suspension dynamics as well as weight transfer, and are very simplistic in nature, they capture all the necessary dynamics to simulate a traction control solution. The dynamic bicycle model is a model that is proposed for the continuation of this work considering combined (lateral/longitudinal) mode maneuvers. These models are also similar to the models used in literature when studying traction control and ABS solutions.

Chapter 4

Gradient Ascent Adaptive Control

This chapter develops the mathematics to implement the basic algorithm introduced as a numbers guessing game in the introduction. The algorithm, or more specifically, a filter that is used to estimate the gradient of vehicle acceleration with respect to throttle input (or commanded wheel torque) is developed. The gradient filter and adaptive control algorithms design, motivated by the analysis performed in Chapter 2, are such that they use the same sensory inputs and outputs that a human expert does. The gradient filter developed in this chapter is model based and requires knowledge of tire-ground interface properties as well as a vehicle model. A simple study of longitudinal traction is designed to prove the utility of the exact gradient filter. Simulations using a 1-DOF model are performed on a flat and uniform section of dry pavement as well as through a non-uniform surface that includes a discrete transition from dry to wet pavement. The simulations also compare the adaptive approach to a more conventional PID tracking loop as well as the HIL testing. The adaptive controller is shown to track the peak tractive force in both cases. The purpose of this section is to develop the necessary mathematics and control architecture.

4.1 Controller Architecture

The first generation of the controller is based on a gradient filter that uses the same sensory inputs and outputs that human would use to perform traction control. The controller uses the acceleration output from the plant as a feedback signal. The acceleration signal is passed through a dynamic filter, defined in a subsequent section, which provides an estimate of the gradient with respect to the control variable. The controller then uses the estimate of the gradient in an adaptive update (Least Mean Squares) to generate a new control signal. The closed loop system of Figure 4.1 is presented as a solution for a driver assist application or the autonomous application where the controller consists of the series combination of the Gradient Estimation and Adaptive Update blocks.

A more detailed block diagram is presented in Figure 4.2, where explicit knowledge of the vehicle model and tire ground interface are initially assumed to be known. Advanced knowledge of these

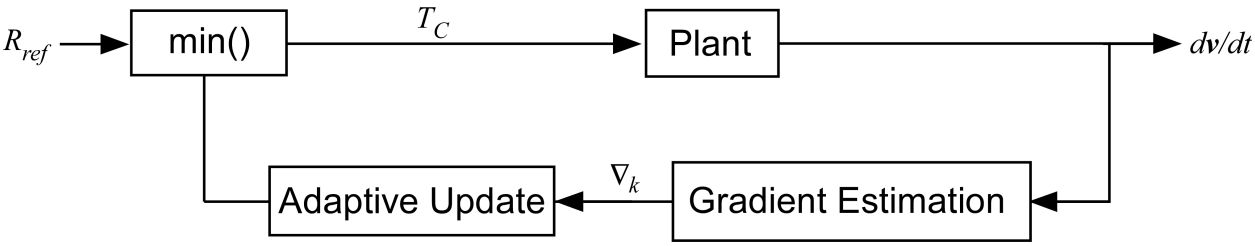

Figure 4.1: Block diagram of control structure for gradient filter used in a driver assist application. Applicable to fully autonomous vehicles provided R_{ref} is always larger than the output of the controller.

quantities can be quite restrictive, and approximations and estimation techniques that eliminate this requirement are presented in subsequent chapters. The block diagram of Figure 4.2 is a more detailed version of the Gradient Filter block in Figure 4.1.

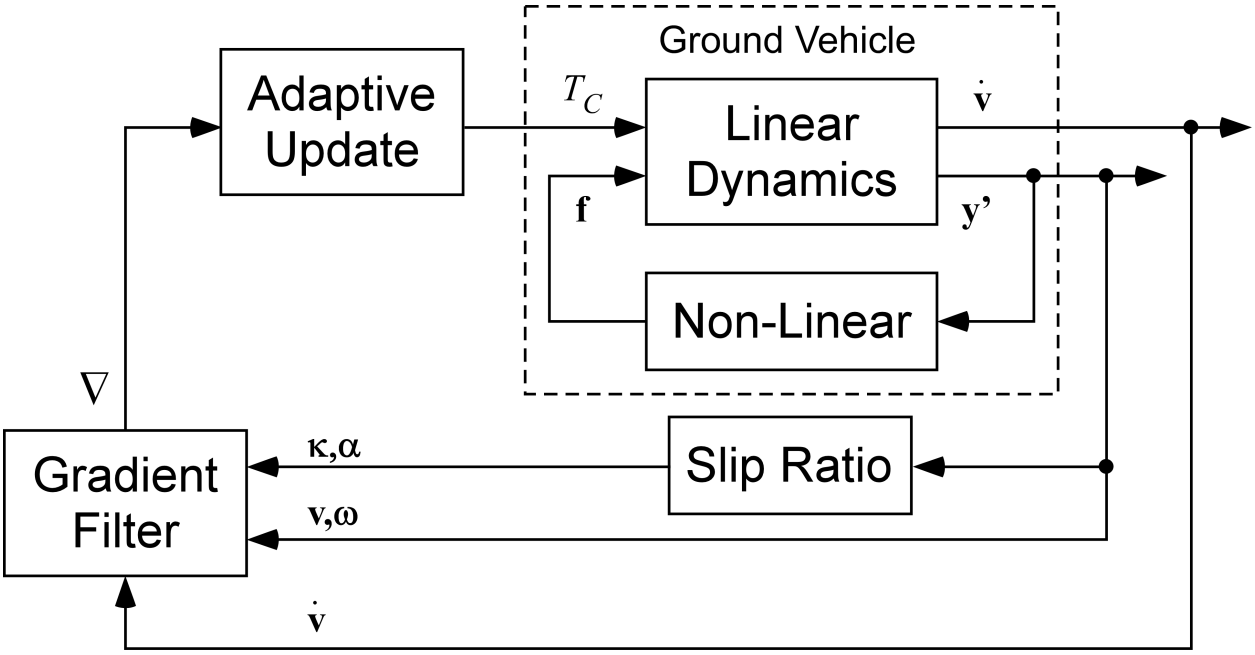

Figure 4.2: Detailed block diagram of control structure using the gradient filter and requisite knowledge of the vehicle model and tire-ground interface properties.

4.2 Indirect Adaptation Law for SISO and MISO Systems

HIL test results provided both qualitative and quantitative evidence that the human driver relies on directly sensed longitudinal acceleration as the key feedback to determine the optimal time-varying throttle position for the simple driving task of getting from point A to B as quickly as

possible. The HIL experimental test results also indicate that the driver occasionally commands the throttle to exceed the peak traction force. One plausible explanation for this is that the driver is attempting to construct a perceptive model of the relationship between the input (throttle or wheel torque) and the output (longitudinal acceleration). Our primary objective is to develop a traction control method that commands throttle position (wheel torque) based only on sensed longitudinal acceleration. Since it is also an objective to implement the method on a digital controller, we will first discretize the dynamic vehicle model while retaining the non-linearities. The block diagram in Figure 3.8 indicates that the linear dynamic system has two outputs and two inputs. This particular structure, i.e. continuous LTI dynamics coupled with a non-linear feedback path, is a generalized non-linear dynamic system representation. The control algorithm development will proceed using the general formulation in order to enable a wider scope of applicability than the simple task in this case study. Based on observations from the HIL test data and the correlation study (Table 2.2), a gradient-based approach is proposed as a candidate solution for determining the optimal throttle position to maximize longitudinal acceleration. There are many possible gradient-based approaches that can be employed; however, for this study, a steepest ascent approach was chosen.

Assuming an appropriate method is chosen to discretize the system of Equations 3.15 and 3.16, it is possible to arrive at the system of Equations 4.1 and 4.2.

$$\mathbf{x}_{k+1} = \mathbf{A}\mathbf{x}_k + \mathbf{B}\mathbf{u}_k + \mathbf{F}\mathbf{u'}_k \tag{4.1}$$

$$\mathbf{y}_k = \mathbf{C}\mathbf{x}_k + \mathbf{D}\mathbf{u}_k + \mathbf{G}\mathbf{u'}_k \tag{4.2}$$

In this chapter, the output $\mathbf{y}_k$ is the scalar longitudinal acceleration of the vehicle. This particular method is referred to as the indirect adaptation law because the outputs of the dynamic system are being used as the inputs to the gradient filter as opposed to directly using the states. To develop the necessary mathematics, we start with the objective function $J(\mathbf{u}_k)$ defined as Equation 4.3.

$$J(\mathbf{u}_k) = \frac{1}{2}\mathbf{y}_k^T\mathbf{y}_k \tag{4.3}$$

Mathematically, maximizing longitudinal acceleration will yield a minimum time solution. This can be accomplished using a gradient based adaptive algorithm such as Equation 4.4.

$$\mathbf{u}_{k+1} = \mathbf{u}_k + \mu\nabla_k \tag{4.4}$$

The gradient of the objective function ∇_k is defined according to Equation 4.5.

$$\begin{aligned}\nabla_k \equiv \frac{\partial J(\mathbf{u}_k)}{\partial \mathbf{u}_k} &= \frac{1}{2}\frac{\partial J_k(\mathbf{u}_k)}{\partial \mathbf{u}_k} = \frac{1}{2}\frac{\partial\left(\mathbf{y}_k^T\mathbf{y}_k\right)}{\partial \mathbf{u}_k} \\ &= \frac{1}{2}\frac{\partial \mathbf{y}_k^T}{\partial \mathbf{u}_k}\mathbf{y}_k + \frac{1}{2}\left(\mathbf{y}_k^T\frac{\partial \mathbf{y}_k}{\partial \mathbf{u}_k}\right)^T \\ &= \frac{\partial \mathbf{y}_k^T}{\partial \mathbf{u}_k}\mathbf{y}_k. \end{aligned} \tag{4.5}$$

After formulating the gradient as the discrete time process of Equation 4.5, it is necessary to develop $\partial \mathbf{y}_k/\partial \mathbf{u}_k$ as a discrete time filter. This is similar to Filtered-X LMS algorithm implementations [25], where the gradient term is represented by a dynamic filtering operation. To begin, it is possible to represent the state equation of Equations 4.1 and 4.2 as Equation 4.6, where z is the unit advance operator.

$$\mathbf{x} = [z\mathbf{I} - \mathbf{A}]^{-1}\left[\mathbf{B}\mathbf{u} + \mathbf{F}\mathbf{u}'\right] \tag{4.6}$$

Substituting Equation 4.6 into the output equation Equations 4.1 and 4.2 results in Equation 4.7, which is exactly what would be expected from linear systems theory with the addition of the nonlinear feedback term(s) $\mathbf{u}'$.

$$\mathbf{y} = \left[\mathbf{C}[z\mathbf{I} - \mathbf{A}]^{-1}\mathbf{B} + \mathbf{D}\right]\mathbf{u} + \left[\mathbf{C}[z\mathbf{I} - \mathbf{A}]^{-1}\mathbf{F} + \mathbf{G}\right]\mathbf{u}' \tag{4.7}$$

Using the definition, $\mathbf{H} \equiv [z\mathbf{I} - \mathbf{A}]^{-1}$, combined with the system of Equations 4.6 and 4.7, it is possible to define an equivalent system in the form of Equation 4.8.

$$\begin{bmatrix} \mathbf{x}(z) \\ \mathbf{y}(z) \end{bmatrix} = \begin{bmatrix} \mathbf{H}(z)\mathbf{B} & \mathbf{H}(z)\mathbf{F} \\ \mathbf{C}\mathbf{H}(z)\mathbf{B} + \mathbf{D} & \mathbf{C}\mathbf{H}(z)\mathbf{F} + \mathbf{G} \end{bmatrix} \begin{bmatrix} \mathbf{u}(z) \\ \mathbf{u}'(\mathbf{y}'(z)) \end{bmatrix} \tag{4.8}$$

Again, it is important to note that there is no loss in generality from linear systems theory, for the case when $\mathbf{u}'(\mathbf{y}'(z)) = \mathbf{0}$ or $\mathbf{F} = \mathbf{G} = \mathbf{0}$, the system reduces to a traditional linear time invariant system. In order to evaluate the gradient term in Equation 4.5 the output of Equation 4.8 can be differentiated, resulting in an expression for $\partial \mathbf{y}(z)/\partial \mathbf{u}(z)$.

$$\frac{\partial \mathbf{y}(z)}{\partial \mathbf{u}(z)} = [\mathbf{C}\mathbf{H}(z)\mathbf{B} + \mathbf{D}]\frac{\partial \mathbf{u}(z)}{\partial \mathbf{u}(z)} + [\mathbf{C}\mathbf{H}(z)\mathbf{F} + \mathbf{G}]\frac{\partial \mathbf{f}(\mathbf{y}'(z))}{\partial \mathbf{u}(z)} \tag{4.9}$$

By definition, the non-linear feedback term $\mathbf{f}(\mathbf{y}'(z))$ is a function of both the states $\mathbf{x}(z)$ and the inputs $\mathbf{u}(z)$. Expanding the partial derivative of this term results in Equation 4.10.

$$\frac{\partial \mathbf{f}(\mathbf{y}'(z))}{\partial \mathbf{u}(z)} = \frac{\partial \mathbf{f}(z)}{\partial \mathbf{x}(z)} \frac{\partial \mathbf{x}(z)}{\partial \mathbf{u}(z)} \tag{4.10}$$

Substituting Equation 4.10 into the output equation, Equation 4.9, results in an expanded expression for $\partial \mathbf{y}(z)/\partial \mathbf{u}(z)$ in Equation 4.11.

$$\frac{\partial \mathbf{y}(z)}{\partial \mathbf{u}(z)} = [\mathbf{CH}(z)\mathbf{B}+\mathbf{D}]+[\mathbf{CH}(z)\mathbf{F}+\mathbf{G}]\left[\frac{\partial \mathbf{f}(z)}{\partial \mathbf{x}(z)} \frac{\partial \mathbf{x}(z)}{\partial \mathbf{u}(z)}\right] \tag{4.11}$$

The partial derivative of the state vector, which shows up in Equation 4.11, can be expressed as Equation 4.12.

$$\frac{\partial \mathbf{x}(z)}{\partial \mathbf{u}(z)} = \mathbf{H}(z)\mathbf{B}+\mathbf{H}(z)\mathbf{F}\left[\frac{\partial \mathbf{f}(z)}{\partial \mathbf{x}(z)} \frac{\partial \mathbf{x}(z)}{\partial \mathbf{u}(z)}\right] \tag{4.12}$$

Equation 4.12 is recursive and it is necessary to break the loop, which leads to Equation 4.13.

$$\frac{\partial \mathbf{x}(z)}{\partial \mathbf{u}(z)} = \left[\mathbf{I}-\mathbf{H}(z)\mathbf{F}\frac{\partial \mathbf{f}(z)}{\partial \mathbf{x}(z)}\right]^{-1}\mathbf{H}(z)\mathbf{B} \tag{4.13}$$

Substituting Equation 4.13 back into Equation 4.11, results in Equation 4.14, where the unit advance operator z has been dropped for ease in notation.

$$\frac{\partial \mathbf{y}}{\partial \mathbf{u}} = [\mathbf{CHB}+\mathbf{D}]+[\mathbf{CHF}+\mathbf{G}]\left\{\frac{\partial \mathbf{f}}{\partial \mathbf{x}}\left[\mathbf{I}-\mathbf{HF}\frac{\partial \mathbf{f}}{\partial \mathbf{x}}\right]^{-1}\mathbf{HB}\right\} \tag{4.14}$$

Equation 4.14 appears to be difficult to implement in real time. In practice it is more robust and efficient to express Equation 4.14 as a discrete state space system. To simplify the notation one additional definition is made.

$$\mathbf{\Omega} = \mathbf{F}\frac{\partial \mathbf{f}}{\partial \mathbf{x}} \tag{4.15}$$

Substituting Ω into the portion of Equation 4.14 contained inside the curly brackets results in Equation 4.16.

$$\frac{\partial \mathbf{f}}{\partial \mathbf{x}}\left[\mathbf{I}-\mathbf{HF}\frac{\partial \mathbf{f}}{\partial \mathbf{x}}\right]^{-1}\mathbf{HB} \;=\; \frac{\partial \mathbf{f}}{\partial \mathbf{x}}\left[\mathbf{I}-\mathbf{H}\Omega\right]^{-1}\mathbf{HB} \tag{4.16}$$

The dynamic system of Equation 4.16 can be given a set of input and output vectors defined as $\mathbf{q}(z)$ and $\mathbf{r}(z)$, respectively. Using these vectors Equation 4.16 can be reformulated as Equation 4.17.

$$\begin{aligned}\mathbf{r}^{(1)}(z) &= \left[\frac{\partial \mathbf{f}}{\partial \mathbf{x}}\left[\mathbf{I}-\mathbf{H}\Omega\right]^{-1}\mathbf{HB}\right]\mathbf{q}^{(1)}(z)\\ &= \frac{\partial \mathbf{f}}{\partial \mathbf{x}}\left[\mathbf{I}-\mathbf{H}\Omega\right]^{-1}\mathbf{HBq}^{(1)}(z)+\left[\mathbf{0}\right]\mathbf{q}^{(1)}(z)\end{aligned} \tag{4.17}$$

At this point it is convenient to define the state vector $\mathbf{w}^{(1)}(z)$ according to Equation 4.18.

$$\mathbf{w}^{(1)}(z) \;=\; \left[\mathbf{I}-\mathbf{H}\Omega\right]^{-1}\mathbf{HBq}^{(1)}(z) \tag{4.18}$$

Using Equation 4.18 it is possible to express Equation 4.17 as Equation 4.19.

$$\mathbf{r}^{(1)}(z) \;=\; \frac{\partial \mathbf{f}}{\partial \mathbf{x}}\mathbf{w}^{(1)}(z)+\left[\mathbf{0}\right]\mathbf{q}^{(1)}(z) \tag{4.19}$$

With a little algebra it is possible to formulate the state equation according to Equation 4.20.

$$\left[\mathbf{I}-\mathbf{H}\Omega\right]\mathbf{w}^{(1)}(z) \;=\; \mathbf{HBq}^{(1)}(z) \tag{4.20}$$

We can now substitute the previous definition of $\mathbf{H}\equiv\left[z\mathbf{I}-\mathbf{A}\right]^{-1}$ back into Equation 4.18 and arrive at Equation 4.21.

$$\left[\mathbf{I}-\left[z\mathbf{I}-\mathbf{A}\right]^{-1}\Omega\right]\mathbf{w}^{(1)}(z) \;=\; \left[z\mathbf{I}-\mathbf{A}\right]^{-1}\mathbf{Bq}^{(1)}(z) \tag{4.21}$$

With some more algebra we arrive at Equation 4.22.

$$[z\mathbf{I}-\mathbf{A}-\Omega]\,\mathbf{w}^{(1)}(z) \;=\; \mathbf{B}\mathbf{q}^{(1)}(z) \tag{4.22}$$

Equations 4.22 and 4.19 can be expressed as a state space system according to Equation 4.23. The transfer function corresponding to the state space system of Equation 4.23 will be referred to as $\mathbf{P}^{(1)}(z)$.

$$\begin{array}{rcl} \mathbf{w}_{k+1}^{(1)} & = & [\mathbf{A}+\Omega]\,\mathbf{w}_k^{(1)}+\mathbf{B}\mathbf{q}_k^{(1)} \\ \mathbf{r}_k^{(1)} & = & \left[\frac{\partial \mathbf{f}_k}{\partial \mathbf{x}_k}\right]\mathbf{w}_k^{(1)}+[\mathbf{0}]\,\mathbf{q}_k^{(1)} \end{array} \tag{4.23}$$

Using similar algebra and notation it is possible to define the remaining two components of Equation 4.14 as the systems defined in Equations 4.24 and 4.25. As before, the transfer functions corresponding to the systems of Equations 4.24 and 4.25 are defined as $\mathbf{P}^{(2)}(z)$ and $\mathbf{P}^{(3)}(z)$, respectively.

$$[\mathbf{CHB}+\mathbf{D}] \Longrightarrow \begin{array}{rcl} \mathbf{w}_{k+1}^{(2)} & = & \mathbf{A}\mathbf{w}_k^{(2)}+\mathbf{B}\mathbf{q}_k^{(2)} \\ \mathbf{r}_k^{(2)} & = & \mathbf{C}\mathbf{w}_k^{(2)}+\mathbf{D}\mathbf{q}_k^{(2)} \end{array} \tag{4.24}$$

$$[\mathbf{CHF}+\mathbf{G}] \Longrightarrow \begin{array}{rcl} \mathbf{w}_{k+1}^{(3)} & = & \mathbf{A}\mathbf{w}_k^{(3)}+\mathbf{F}\mathbf{q}_k^{(3)} \\ \mathbf{r}_k^{(3)} & = & \mathbf{C}\mathbf{w}_k^{(3)}+\mathbf{G}\mathbf{q}_k^{(3)} \end{array} \tag{4.25}$$

It is now possible to express $\partial \mathbf{y}_k/\partial \mathbf{u}_k$ in block diagram form as Figure 4.3.

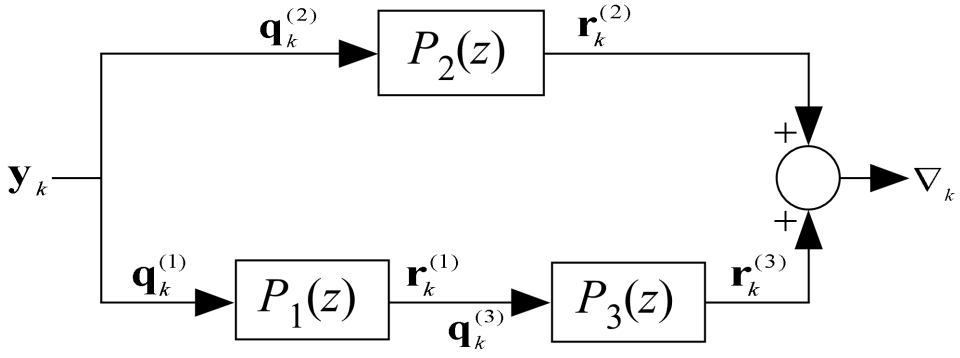

Figure 4.3: Block Diagram of discrete filter used to calculate the gradient.

For the path with $\mathbf{P}^{(1)}(z)$ and $\mathbf{P}^{(3)}(z)$ in series, we define an equivalent system as $\mathbf{P}^{(13)}(z)$ according to Equation 4.26.

$$\mathbf{P}^{(13)}(z) = \mathbf{P}^{(3)}(z) \times \mathbf{P}^{(1)}(z) \tag{4.26}$$

Using Equations 4.23 and 4.25 it is possible to define the equivalent system $\mathbf{P}^{(13)}(z)$ according to Equations. 4.27 and 4.28.

$$\mathbf{w}_{k+1}^{(13)} = \begin{bmatrix} \mathbf{A} & \mathbf{F}\frac{\partial \mathbf{f}_k}{\partial \mathbf{x}_k} \\ \mathbf{0} & \mathbf{A}+\Omega \end{bmatrix} \mathbf{w}_k^{(13)} + \begin{bmatrix} \mathbf{0} \\ \mathbf{B} \end{bmatrix} \mathbf{q}_k^{(1)} \tag{4.27}$$

$$\mathbf{r}_k^{(3)} = \begin{bmatrix} \mathbf{C} & \mathbf{G}\frac{\partial \mathbf{f}_k}{\partial \mathbf{x}_k} \end{bmatrix} \mathbf{w}_k^{(13)} + [\mathbf{0}]\, \mathbf{q}_k^{(1)} \tag{4.28}$$

The state vector is defined as $\mathbf{w}^{(13)} \equiv [\mathbf{w}^{(1)}\ \mathbf{w}^{(3)}]^T$. Combining $\mathbf{P}^{(2)}(z)$ in parallel to the series combination resulting in Equation 4.28, the single dynamic system can be represented as Equation 4.29 for $\mathbf{P}(z)$. This dynamic system represents the discrete filter of Figure 4.3.

$$\mathbf{P}(z) = \mathbf{P}^{(2)}(z) + \left[\mathbf{P}^{(3)}(z) \times \mathbf{P}^{(1)}(z)\right] \tag{4.29}$$

The corresponding state vector is defined as $\mathbf{w} \equiv [\mathbf{w}^{(13)}\ \mathbf{w}^{(2)}]^T$. This single dynamic system, which is linear time varying, is expanded to the system described by Equations 4.31 and 4.30. This system is well suited for real time application provided the apriori knowledge necessary to calculate $\partial \mathbf{f}_k / \partial \mathbf{x}_k$ and $\partial \mathbf{f}_k / \partial \mathbf{u}_k$ is available.

$$\mathbf{w}_{k+1} = \begin{bmatrix} \begin{bmatrix} \mathbf{A} & \mathbf{F}\frac{\partial \mathbf{f}_k}{\partial \mathbf{x}_k} \\ \mathbf{0} & \mathbf{A}+\Omega \end{bmatrix} & \mathbf{0} \\ \mathbf{0} & \mathbf{A} \end{bmatrix} \mathbf{w}_k + \begin{bmatrix} \mathbf{0} \\ \mathbf{B} \\ \mathbf{B} \end{bmatrix} \mathbf{y}_k \tag{4.30}$$

$$\nabla_k = \begin{bmatrix} \mathbf{C} & \mathbf{G}\frac{\partial \mathbf{f}_k}{\partial \mathbf{x}_k} & \mathbf{C} \end{bmatrix} \mathbf{w}_k + [\mathbf{D}]\, \mathbf{y}_k \tag{4.31}$$

The $\partial \mathbf{f}_k / \partial \mathbf{x}_k$ term in Equations 4.30 and 4.31 involving partial derivatives of the non-linear function of Equation 3.3 with respect to states and inputs, represent quasi-constant transformation matrices. To illustrate this fact using the quarter-car model defined by Equations 3.14, 3.15 and 4.1, these partial derivatives are simply given by Equations 4.32 and 4.33.

$$\frac{\partial \mathbf{f_k}}{\partial \mathbf{u}_k} = [0] \tag{4.32}$$

$$\frac{\partial \mathbf{f_k}}{\partial \mathbf{x}_k} = \begin{bmatrix} \frac{\partial F_x(v_k,\omega_k)}{\partial \kappa_k}\frac{\partial \kappa_k}{\partial v_k}, & \frac{\partial F_x(v_k,\omega_k)}{\partial \kappa_k}\frac{\partial \kappa_k}{\partial \omega_k}, & \frac{\partial F_x(v_k,\omega_k)}{\partial \kappa_k}\frac{\partial \kappa_k}{\partial T_{C,k}} \end{bmatrix} \tag{4.33}$$

The partial derivative of the traction curve with respect to slip for the 1-DOF quarter car model $\partial F_x / \partial \kappa$ used in Equation 4.33 is presented in Figure 4.4.

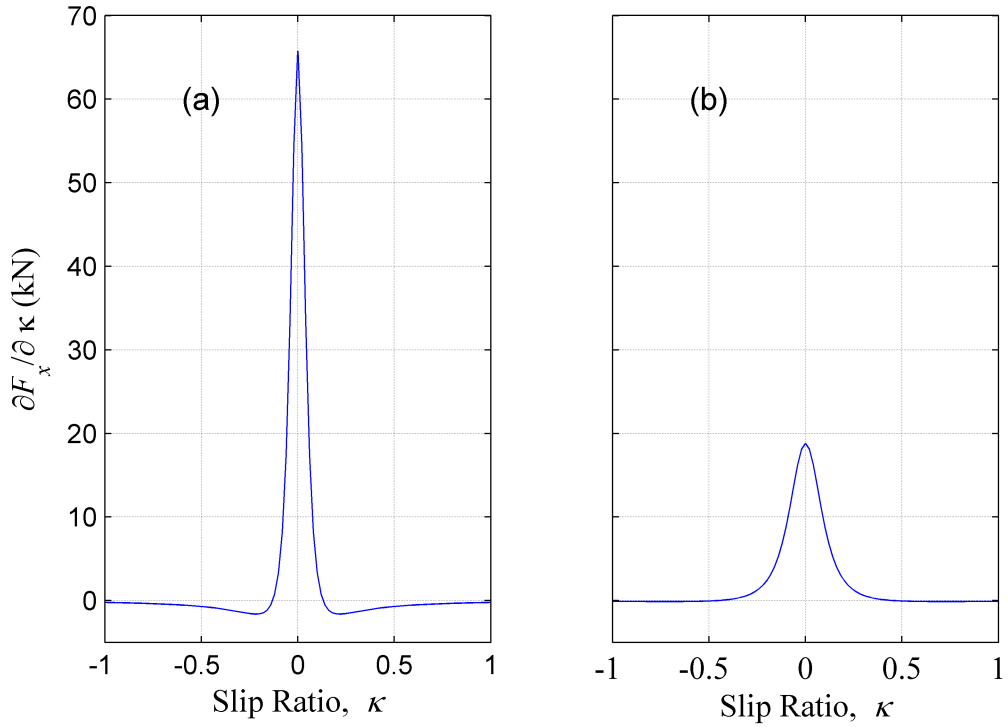

Figure 4.4: Partial derivative of F_x with respect to slip ratio κ for pure longitudinal slip: (a) Dry Pavement (b) Wet Pavement.

The partial $\partial \mathbf{f_k} / \partial \mathbf{x}_k$ for the 3-DOF dynamic bicycle model of Section 3.4 is quite tedious and a complete derivation of this partial derivative can be found in Appendix G.2. The more relevant partial derivatives, $(\partial F_{xt}/\partial \kappa, \partial F_{xt}/\partial \alpha, \partial F_{yt}/\partial \kappa, \partial F_{yt}/\partial \alpha)$ are presented, for completeness, in Figures 4.5 and 4.6.

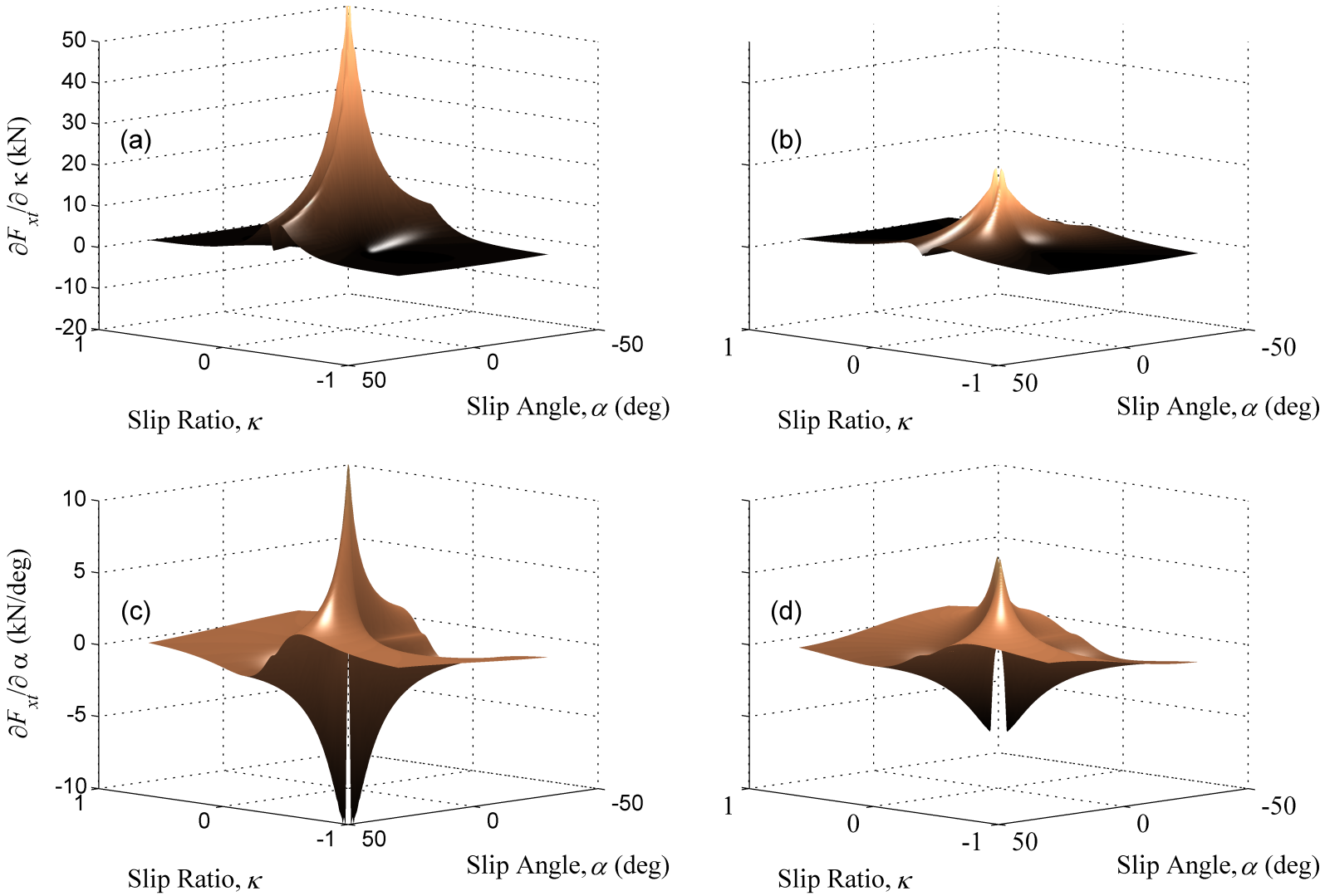

Figure 4.5: Partial derivatives of F_{xt} with respect to slip ratio κ and slip angle α when operating in combined mode friction regime: (a,c) Dry Pavement (b,d) Wet Pavement.

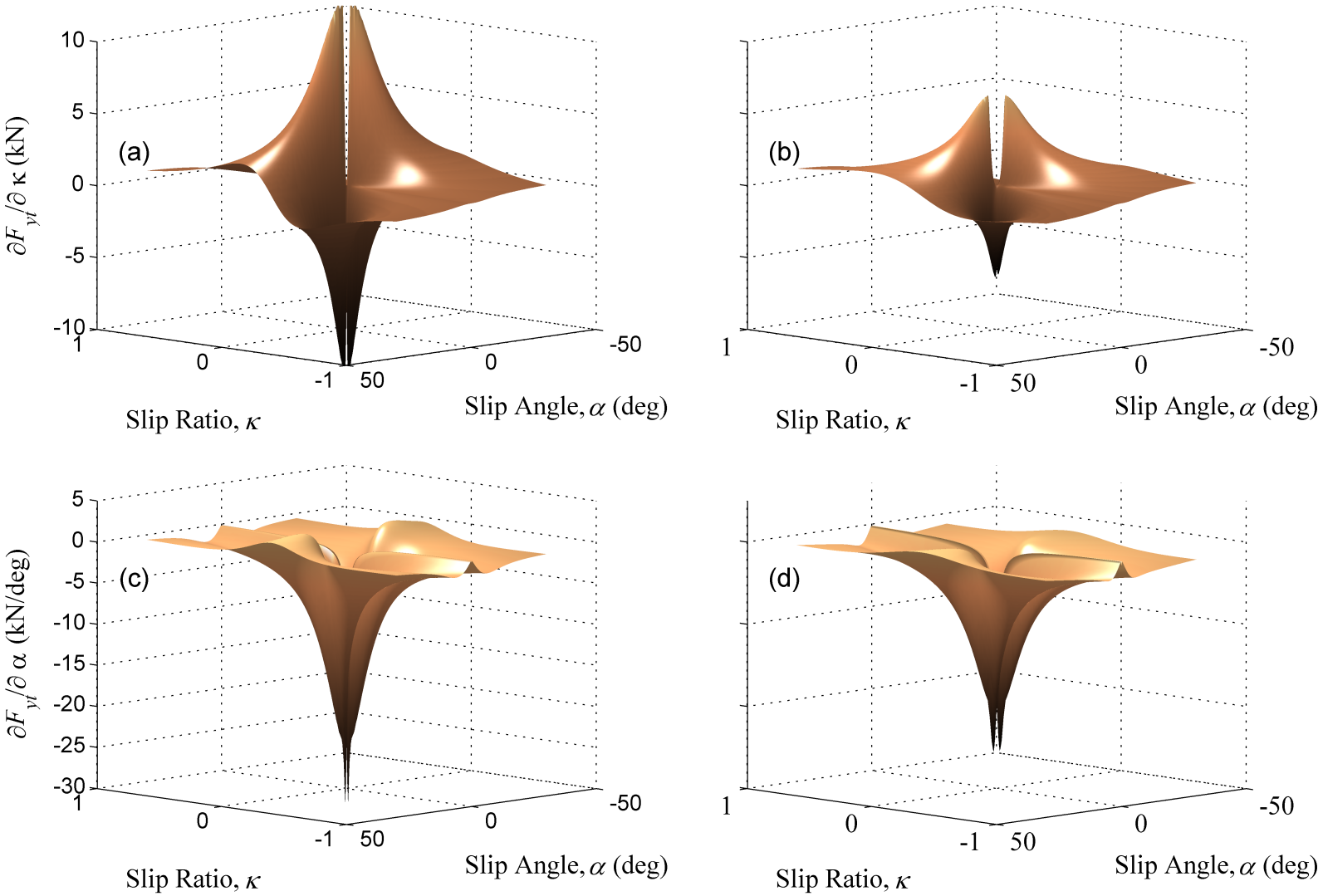

Figure 4.6: Partial derivatives of F_{yt} with respect to slip ratio κ and slip angle α when operating in combined mode friction regime: (a,c) Dry Pavement (b,d) Wet Pavement.

4.3 Indirect Adaptation Law for MIMO and SIMO Systems

The gradient filter has been derived in the previous section in the general sense for SISO (single-input, single-output) and MISO (multi-input, single-output) systems. This section is devoted to the necessary changes to the objective function when extending the algorithm to the MIMO (multi-input, multi-output) and SIMO (single-input, multi-output) cases. The objective function of Equation 4.34 includes the additional term $\mathbf{Q_a} \in \Re^{(PxP)}$, which is a positive definite, symmetric matrix used to weight each component of the objective function, where P is the number of outputs in Equation 3.16.

$$J(\mathbf{u}_k) = \frac{1}{2}\mathbf{y}_k^T \mathbf{Q_a} \mathbf{y}_k \tag{4.34}$$

The adaptation law remains unchanged as Equation 4.35.

$$\mathbf{u}_{k+1} = \mathbf{u}_k + \mu \nabla_k. \tag{4.35}$$

The gradient can then be defined according to Equation 4.36. As previously stated in order for Equation 4.36 to be valid, $\mathbf{Q_a}$ must be symmetric.

$$\begin{aligned} \nabla_k \equiv \frac{\partial J(\mathbf{u}_k)}{\partial \mathbf{u}_k} &= \frac{1}{2}\frac{\partial \left(\mathbf{y}_k^T \mathbf{Q_a} \mathbf{y}_k\right)}{\partial \mathbf{u}_k} \\ &= \frac{1}{2}\frac{\partial \mathbf{y}_k^T}{\partial \mathbf{u}_k}\mathbf{Q_a}\mathbf{y}_k + \frac{1}{2}\left(\mathbf{y}_k^T \mathbf{Q_a}\frac{\partial \mathbf{y}_k}{\partial \mathbf{u}_k}\right)^T \\ &= \frac{\partial \mathbf{y}_k^T}{\partial \mathbf{u}_k}\mathbf{Q_a}\mathbf{y}_k. \end{aligned} \tag{4.36}$$

It is important to note here the structure that this algorithm takes for the multi-input multi-output (MIMO) and single-input multi-output (SIMO) cases. Noting that the model designation as MIMO or SIMO refers to the plant model, where the input refers to $\mathbf{u}_k$ and output refers to $\mathbf{y}_k$. While the single-input single-output (SISO) and multi-input single-output (MISO) case are straight forward and a trivial extensions of the derivation in Section 4.2, the application to MIMO and SIMO cases requires clarification. Using the gradient term defined according to Equation 4.36 requires the use of a filter bank for the MIMO and SIMO cases. Essentially the filter bank is comprised of individual filters that use the same structure as they would for the SISO and MISO cases of Section 4.2. This becomes clear when studying Equation 4.37, and should clear up any ambiguity in the structure of the filter developed in Section 4.2.

$$\frac{\partial J(\mathbf{u}_k)}{\partial \mathbf{u}_k} = \left[\frac{\partial \mathbf{y}_{1,k}}{\partial \mathbf{u}_k} , \frac{\partial \mathbf{y}_{2,k}}{\partial \mathbf{u}_k} , \cdots , \frac{\partial \mathbf{y}_{n,k}}{\partial \mathbf{u}_k} \right] \mathbf{Q_a} \mathbf{y}_k \tag{4.37}$$

Equation 4.37 for the planar vehicle model of Section 3.4 becomes equal to Equation 4.38, where the goal is to maximize the vector sum of longitudinal and lateral acceleration.

$$\frac{\partial J(\mathbf{u}_k)}{\partial \mathbf{u}_k} = \left[\frac{\partial \dot{v}_{x,k}}{\partial T_{c,k}} , \frac{\partial \dot{v}_{y,k}}{\partial T_{c,k}} \right] \mathbf{Q_a} \begin{bmatrix} \dot{v}_{x,k} \\ \dot{v}_{y,k} \end{bmatrix} \tag{4.38}$$

If we define the positive definite matrix $\mathbf{Q_a} = \begin{bmatrix} q_{a,11} & q_{a,12} \; ; \; q_{a,21} & q_{a,22} \end{bmatrix}$, then Equation 4.38 can be expanded and expressed as Equation 4.40. The two partial derivative terms on the right hand side of Equation 4.40 are both filters developed exactly as they were in Section 4.2 for the SISO algorithm. It should now be clear how the discrete filter to estimate the gradient can be used for a generic class of SISO, SIMO, MISO and MIMO systems. A continuous time representation of the filter bank of Equation 4.40 is included in Appendix B.2. For comparison purposes the continuous time representation of the indirect filter for the 1-DOF model is included in Appendix B.1.

$$\frac{\partial J(\mathbf{u}_k)}{\partial \mathbf{u}_k} = \frac{\partial J_x(\mathbf{u}_k)}{\partial \mathbf{u}_k} + \frac{\partial J_y(\mathbf{u}_k)}{\partial \mathbf{u}_k} \tag{4.39}$$

$$\frac{\partial J(\mathbf{u}_k)}{\partial \mathbf{u}_k} = \frac{\partial \dot{v}_{x,k}}{\partial T_{c,k}} \left[q_{a,11} \dot{v}_{x,k} + q_{a,12} \dot{v}_{y,k} \right] + \frac{\partial \dot{v}_{y,k}}{\partial T_{c,k}} \left[q_{a,21} \dot{v}_{x,k} + q_{a,22} \dot{v}_{y,k} \right] \tag{4.40}$$

4.4 Direct Adaptation Law for MIMO and SIMO Systems

The motivation for an alternative objective function will be clear in subsequent sections, however, the alternative formulation is presented here for consistency and is justified later. When considering the models developed in this work, Sections 3.2 and 3.4, it is possible and interesting to define an alternative objective function according to Equation 4.41, where we use the sum of the squares of the forces $\mathbf{f} = \mathbf{u}' = \begin{bmatrix} F_{xtf} & F_{xtr} & F_{ytf} & F_{ytr} \end{bmatrix}^T$. It is important to note that each force is weighted according to the values in matrix $\mathbf{Q_b} \in \Re^{(QxQ)}$ which is constrained to be positive definite, where Q is the number of nonlinear feedback terms from Equation 3.18.

$$J_f(\mathbf{u}_k) = \frac{1}{2} \mathbf{f}_k^T \mathbf{Q_b} \mathbf{f}_k \tag{4.41}$$

The objective is still to maximize the objective function in Equation 4.41. This can be accomplished using the aforementioned gradient based adaptive algorithm of Equation 4.35. To determine the gradient of Equation 4.41 it is necessary to differentiate with respect to the input vector $\mathbf{u}$.

The gradient is then defined according to Equation 4.42, similar to previous gradient definition but in this case the objective function has changed. As before, in order for Equation 4.42 to be valid, $\mathbf{Q_b}$ must also be symmetric in addition to being positive definite.

$$\begin{aligned}\nabla_k \equiv \frac{\partial J_f(\mathbf{u}_k)}{\partial \mathbf{u}_k} &= \frac{1}{2}\frac{\partial\left(\mathbf{f}_k^T\mathbf{Q_b}\mathbf{f}_k\right)}{\partial \mathbf{u}_k} \\ &= \frac{1}{2}\frac{\partial \mathbf{f}_k^T}{\partial \mathbf{u}_k}\mathbf{Q_b}\mathbf{y}_k + \frac{1}{2}\left(\mathbf{f}_k^T\mathbf{Q_b}\frac{\partial \mathbf{f}_k}{\partial \mathbf{u}_k}\right)^T \\ &= \frac{\partial \mathbf{f}_k^T}{\partial \mathbf{u}_k}\mathbf{Q_b}\mathbf{f}_k. \end{aligned} \tag{4.42}$$

To further expand the objective function of Equation 4.42 we return to Equation 4.10 listed here for consistency.

$$\frac{\partial \mathbf{f}(\mathbf{y}'(z))}{\partial \mathbf{u}(z)} = \frac{\partial \mathbf{f}(z)}{\partial \mathbf{x}(z)}\frac{\partial \mathbf{x}(z)}{\partial \mathbf{u}(z)}$$

The derivation continues, as in Section 4.2, starting with Equation 4.10 and continuing to the system of Equation 4.23, repeated here for convenience.

$$\begin{aligned}\mathbf{w}_{k+1}^{(1)} &= [\mathbf{A}+\Omega]\,\mathbf{w}_k^{(1)} + \mathbf{B}\mathbf{q}_k^{(1)} \\ \mathbf{r}_k^{(1)} &= \left[\frac{\partial \mathbf{f}_k}{\partial \mathbf{x}_k}\right]\mathbf{w}_k^{(1)} + [\mathbf{0}]\,\mathbf{q}_k^{(1)}\end{aligned}$$

It should be clear now that the system of Equation 4.23 filters either the acceleration signals, as is the case when using the objective function of Equation 4.3 or 4.34 or the nonlinear forces $\mathbf{f}(\mathbf{y}'(z))$ as is the case when using the objective function of Equation 4.41. This should come as no surprise, as according to Newtons second law, the net force $\mathbf{f}(\mathbf{y}'(z))$ on a body is directly proportional to its acceleration $\mathbf{y}(\mathbf{z})$. When returning to analyze the filter of Figure 4.3 and Equations 4.30 and 4.31, it can be seen that the subsystem characterized by $\mathbf{P}^{(3)}(z)$ and the system of Equation 4.25 merely filters the gradient of the forces with respect to the inputs $\nabla_{f,k}$ into the resulting gradient of the accelerations ∇_k. It is also important to note that the output from the linear path $\mathbf{P}^{(2)}(z)$ of the filter shown in Figure 4.25 is always zero for the models used in this work as the acceleration $\mathbf{y}$ is not a direct function of the input $\mathbf{u}$, but rather, dynamically a function of $\mathbf{u}'$ through the nonlinear functions of $\mathbf{f}$ which is captured in the $\mathbf{P}^{(1)}(z) \rightharpoonup \mathbf{P}^{(3)}(z)$ path. In the case of the 3-DOF bicycle model the filter bank is described according to Equation 4.43. A continuous time representation of the filter bank of Equation 4.43, as applied to the 3-DOF bicycle model is also included in Appendix C.2. For comparison purposes the continuous time representation of the direct filter for the 1-DOF model is included in Appendix C.1.

$$\frac{\partial J_f(\mathbf{u}_k)}{\partial \mathbf{u}_k} = \begin{bmatrix} \frac{\partial f_1}{\partial T_{c,k}} \left(q_{b,11} F_{xtf,k} + q_{b,12} F_{xtr,k} + q_{b,13} F_{ytf,k} + q_{b,14} F_{ytr,k} \right) \\ \frac{\partial f_2}{\partial T_{c,k}} \left(q_{b,21} F_{xtf,k} + q_{b,22} F_{xtr,k} + q_{b,23} F_{ytf,k} + q_{b,24} F_{ytr,k} \right) \\ \frac{\partial f_3}{\partial T_{c,k}} \left(q_{b,31} F_{xtf,k} + q_{b,32} F_{xtr,k} + q_{b,33} F_{ytf,k} + q_{b,34} F_{ytr,k} \right) \\ \frac{\partial f_4}{\partial T_{c,k}} \left(q_{b,41} F_{xtf,k} + q_{b,42} F_{xtr,k} + q_{b,43} F_{ytf,k} + q_{b,44} F_{ytr,k} \right) \end{bmatrix} \tag{4.43}$$

The alternative objective function described in this section is preferable to the original objective function of Sections 4.2 and 4.3 when using the 3-DOF bicycle model, as it provides greater control authority over each component of the forces using the weighting matrix $\mathbf{Q_b}$ There is some additional work that is needed however when using this particular objective function, and that is resolving the forces back to the vehicle reference frame. This transformation is not required of the algorithm described in Sections 4.2 and 4.3, because the derivation is done solely in the vehicle reference frame. The transformation is performed using Equations 4.44 and 4.45 and then the total gradient is computed by the addition of these two terms according to Equation 4.46.

$$\frac{\partial J_{fx}(\mathbf{u}_k)}{\partial \mathbf{u}_k} = \begin{bmatrix} \cos(\delta_f) & 1 & -\cos(90-\delta_f) & 0 \end{bmatrix} \frac{\partial J_f(\mathbf{u}_k)}{\partial \mathbf{u}_k} \tag{4.44}$$

$$\frac{\partial J_{fy}(\mathbf{u}_k)}{\partial \mathbf{u}_k} = \begin{bmatrix} \sin(\delta_f) & 0 & \sin(90-\delta_f) & 1 \end{bmatrix} \frac{\partial J_f(\mathbf{u}_k)}{\partial \mathbf{u}_k} \tag{4.45}$$

$$\nabla_{f,k} = \frac{\partial J_{fx}(\mathbf{u}_k)}{\partial \mathbf{u}_k} + \frac{\partial J_{fy}(\mathbf{u}_k)}{\partial \mathbf{u}_k} \tag{4.46}$$

4.5 Simulation of Adaptive Traction Control

For comparison purposes, Figure 4.7 shows an example traction control system based on a conventional feedback strategy to directly regulate the slip ratio. Indeed, variations of this approach are used in a variety of commercial automobile traction control systems (TCS) [9, 10, 35, 36, 37, 40, 41], anti-slip regulation systems (ASR), and anti-lock braking systems (ABS) [5, 8, 2, 42].

The ground vehicle dynamics in Figure 3.7 are represented by the linear dynamics of Equation 3.14 coupled with the non-linear traction force given by Equations 3.3 for the 1-DOF model and Equations 3.30-3.44 and 3.4 3.5 for the 3-DOF model. Although a human driver does not sense or have any direct perception of slip ratio, the two velocity states can be measured with physical sensors and then used to compute the slip ratio according to Equation 3.2. Using the Dry Pavement example in Figure 3.2, the peak traction force at the nominal normal force occurs near k = 0.133, so regulating the actual slip ratio to this desired value will essentially maximize the traction force, resulting in a minimized T_{25} time. Unfortunately, this approach does not work well in the very common situation where the terrain surface is not uniform since it is difficult if not impossible to specify an appropriate desired slip ratio to cover the wide range of surface possibilities.

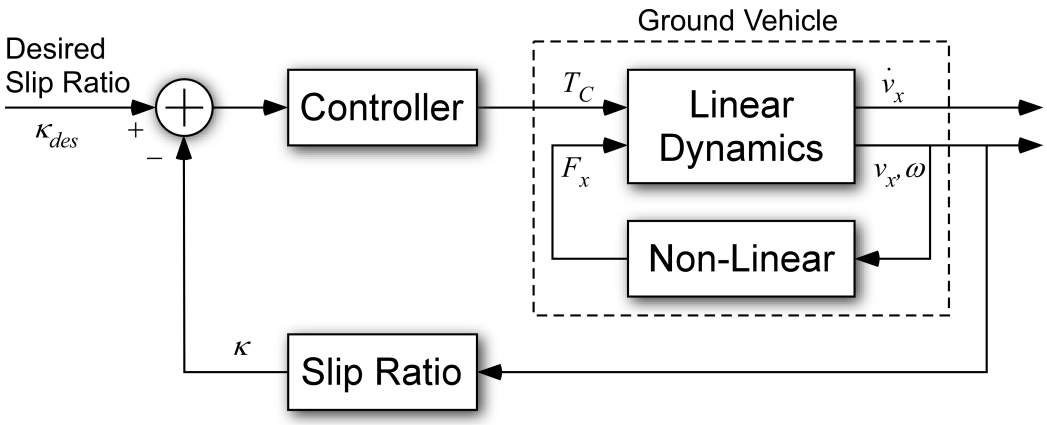

Figure 4.7: Simulation model with conventional feedback loop to regulate longitudinal slip.

Most commercial TCS and ABS systems do not attempt to achieve the peak traction force, typically regulating the slip ratio to sub-optimal levels in order to insure robustness over a wider range of terrain surfaces. In order to evaluate the results from the human-in-the-loop test on the driving simulator, a PID-based traction control simulation was set up as a benchmark for the 1-DOF simulations. The PID controller was tuned to provide a closed-loop response with a bandwidth that approximately matched the nominal bandwidth of a human driver actuating the throttle on the driving simulator. Table 4.1 lists the parameter values used for this simulation study except for the Pacejka coefficients which are included in Appendix F.3. These parameters are equivalent to the actual parameters associated with the virtual vehicle used during the HIL testing on the driving simulator.

Initial evaluation of the anthropomimetic traction control simulation results indicated the need for a minor adjustment to the update law. The modified control law is given by

$$u_{k+1} = u_k + \mu \times \begin{cases} \nabla_k & \nabla_k > 0 \\ -\eta & \nabla_k \leq 0 \end{cases} \tag{4.47}$$

where η is a constant step size when the gradient is negative and μ is positive constant typically used in gradient based search algorithms. The values of these parameters used in the simulations are presented in Table 4.1. With regard to the case study example, a negative gradient physically corresponds to the situation where the slip ratio is beyond the peak point in the traction curve and the update law is effectively attempting to reduce the throttle or wheel torque. Notice from equation 4.47 that when the gradient is positive, the update law is identical to the original control law in equation 4.4. This modification is known in the adaptive signal processing field as a "Signed Regressor" variant [43]. The justification for this modification can be explained with reference to Figure 3.2. Specifically, for the Dry Pavement traction curve at relatively high slip ratios (i.e. dashed line region), the gradient is negative but small and even approaching zero. In order to speed up convergence in this region to push the slip ratio back toward the peak, the magnitude of

Table 4.1: Model Parameters (1-DOF and 3-DOF)

	Model			
Parameter	1-DOF	3-DOF	Units	Description
m	540	540	kg	Mass of vehicle
J_W	1.0	2.0	kgm^2	Rotational inertia of driven wheel
R	0.31	0.31	m	Effective radius of driven wheel
a_D	60	0	Ns/m	Aerodynamic down force constant
β	1.0	1.0	Nms/rad	Viscous friction constant
γ_x	25	0.2	Ns/m	Aerodynamic drag constant
γ_y	10	0.2	Ns/m	Aerodynamic drag constant
f_e	10	5	Hz	Break frequency of low pass filter
J_m	-	1300	kgm^2	Rotational inertia of vehicle (yaw axis)
L_f	-	2	m	Distance from center or gravity to front axle
L_r	-	2	m	Distance from center or gravity to rear axle
h	-	0	m	Height of center of gravity (Pitch DOF)
μ	750	-	-	Step size for adaptive algorithm
η	0.0013	-	-	Negative step size for adaptive algorithm
μ_a	-	500	-	Step size for indirect algorithm (3-DOF)
η_a	-	0.002	-	Negative step size for indirect algorithm (3-DOF)
μ_b	-	166.67	-	Step size for direct algorithm (3-DOF)
η_b	-	0.006	-	Negative step size for direct algorithm (3-DOF)
K_P	800	-	-	Proportional gain for PID
K_I	40000	-	-	Integral gain for PID
κ_{des}	0.133	-	-	Desired slip ratio setpoint for PID
v_0	4	4	m/s	Slip approximation threshold
$q_{a,11}$	-	1	-	Component of weighting matrix $\mathbf{Q_a}$
$q_{a,12}$	-	0	-	Component of weighting matrix $\mathbf{Q_a}$
$q_{a,21}$	-	0	-	Component of weighting matrix $\mathbf{Q_a}$
$q_{a,22}$	-	10	-	Component of weighting matrix $\mathbf{Q_a}$
$q_{b,11}$	-	1	-	Component of weighting matrix $\mathbf{Q_b}$
$q_{b,12}$	-	0	-	Component of weighting matrix $\mathbf{Q_b}$
$q_{b,13}$	-	0	-	Component of weighting matrix $\mathbf{Q_b}$
$q_{b,14}$	-	0	-	Component of weighting matrix $\mathbf{Q_b}$
$q_{b,21}$	-	0	-	Component of weighting matrix $\mathbf{Q_b}$
$q_{b,22}$	-	1	-	Component of weighting matrix $\mathbf{Q_b}$
$q_{b,23}$	-	0	-	Component of weighting matrix $\mathbf{Q_b}$
$q_{b,24}$	-	0	-	Component of weighting matrix $\mathbf{Q_b}$
$q_{b,31}$	-	0	-	Component of weighting matrix $\mathbf{Q_b}$
$q_{b,32}$	-	0	-	Component of weighting matrix $\mathbf{Q_b}$
$q_{b,33}$	-	10	-	Component of weighting matrix $\mathbf{Q_b}$
$q_{b,34}$	-	0	-	Component of weighting matrix $\mathbf{Q_b}$
$q_{b,41}$	-	0	-	Component of weighting matrix $\mathbf{Q_b}$
$q_{b,42}$	-	0	-	Component of weighting matrix $\mathbf{Q_b}$
$q_{b,43}$	-	0	-	Component of weighting matrix $\mathbf{Q_b}$
$q_{b,44}$	-	1	-	Component of weighting matrix $\mathbf{Q_b}$

the actual gradient is replaced by an appropriately chosen constant. All simulations (1-DOF and 3-DOF) were performed with the parameters given in Table 4.1, and also the same Pacejka tire model for Dry Pavement (Figure 3.2) that was used in the HIL testing on the driving simulator.

4.5.1 1-DOF Simulation: Uniform Surface

A simulation study was performed using the generic vehicle model defined according Section 3.2, Appendix A.1 and Table 4.1 along with the control algorithm developed in Section 4.2. The objective in this simulation study was to travel the maximum distance possible in a specific time, which is analogous to traveling a specified distance in a minimum amount of time. The solution to this particular challenge is maximum vehicle acceleration for the duration of the 5 second interval.

Using the results from the gradient based method developed in the previous section, a simulation study was performed with a vehicle on dry pavement. In this particular case the discrete filter, developed in Section 4.2, is slowly time varying as a function of only $\partial \mathbf{f}_k / \partial \mathbf{x}_k$. Using the chain rule it is possible to define the partial derivative of the non-linear function with respect to the states as Equation 4.33. With an efficient method of calculating the gradient, the control law is implemented according to Equations 4.4 and 4.47. The relative difference in the magnitude of the gradient above and below the optimal slip ratio is the motivation behind the asymmetric update of the control law represented by Equation 4.47.

The simulations were performed with the vehicle starting at rest, or with zero initial conditions. The results of the simulations for the proposed anthropomimetic traction control law are plotted as blue curves in Figure 6 for direct comparison with the PID control solution and the HIL data. Figures 4.8(a),(b), and (d) indicate that the PID controller and the anthropomimetic controller both produce similar results, which are very nearly optimal. In fact the results in Figure 4.8(a), position versus time, for both solutions are almost exactly the same. However, the time history of the states, Figure 4.8(b-d) through time are much different for each solution. From the Pacejka tire model of equation 3.3, the tractive force is a function of normal load, which effectively means that the Dry Pavement traction curve in Figure 3.2 will vary with changes in the normal load. For all three simulations in this case study the aerodynamic down force F_A, and therefore the normal load, increases linearly with velocity. Pacejka [14, 1] and Bakker [30] have shown that as the normal load increases, the slip ratio associated with the peak tractive force will decrease slightly in magnitude. This phenomena is clearly seen in Figure 4.8(c) where the anthropomimetic solution automatically tracks this change in optimum slip ratio κ, whereas the PID control solution is not designed to do so. This comparison also confirms that the best T_{25} time for the human driver is not as good as the T_{25} time for the PID simulation because the human driver did not maintain the peak traction force for the same amount of time as the PID simulation. The anthropomimetic traction control response shown in Figure 4.8(c) also indicates what appears to be a hunting behavior around the optimal slip ratio. Although this response is similar to the desirable behavioral response of a human, it was not intentionally designed into the algorithm. The fact that it is occurring can be attributed to the well-known misadjustment behavior of fixed step size gradient-based adaptive algorithms [26].

Although it is possible to "tune" the adaptation process to minimize this hunting behavior, visual inspection of the HIL response data suggests that a certain degree of hunting is desirable and should be retained. In fact, this hunting behavior can prove to be a real asset when performing real-time estimation of the friction at the tire-ground interface [3]. The magnitude of the hunting oscillation can be reduced by choosing a smaller adaptation step size. The simulation is such that the Pacejka curve goes through a slowly time varying change due to the increase in vehicle down force, which is assumed linear with respect to vehicle speed. This change is presented in Figure 4.9, where we can see not only the difference in relative magnitude across the curve but also a small change that occurs in the location of the peak, both of which are a result of increasing normal load.

Figure 4.8(a) shows the position across time where it is evident that the response of the vehicle remains stable for the duration of the simulation. More interesting are the results in Figure 4.8(b-d), where torque, slip ratio and longitudinal acceleration are presented through time, respectively. Inspection of Figure 4.9 shows the existence of a single slip ratio where a peak tractive force is achieved, and it is this slip value that is referred to as the optimal slip ratio. The buildup to the optimal slip ratio on dry pavement can be seen for $t \in [0, 0.5]$ *sec*. The anthropomimetic algorithm then tracks the optimal slip ratio as it decreases as a function of down force for $t \in [0.5, 5.0]$ *sec*. According to Li et. al, a hunting behavior is desirable when using an estimation algorithm similar to the one they developed [3]. The hunting characteristics seen in Figure 4.8 are a function of the gradient, which is defined as Equation 4.5. This simulation is an excellent example of the tradeoff between performance and stability when using a constant step size in an adaptive gradient ascent/descent algorithm.

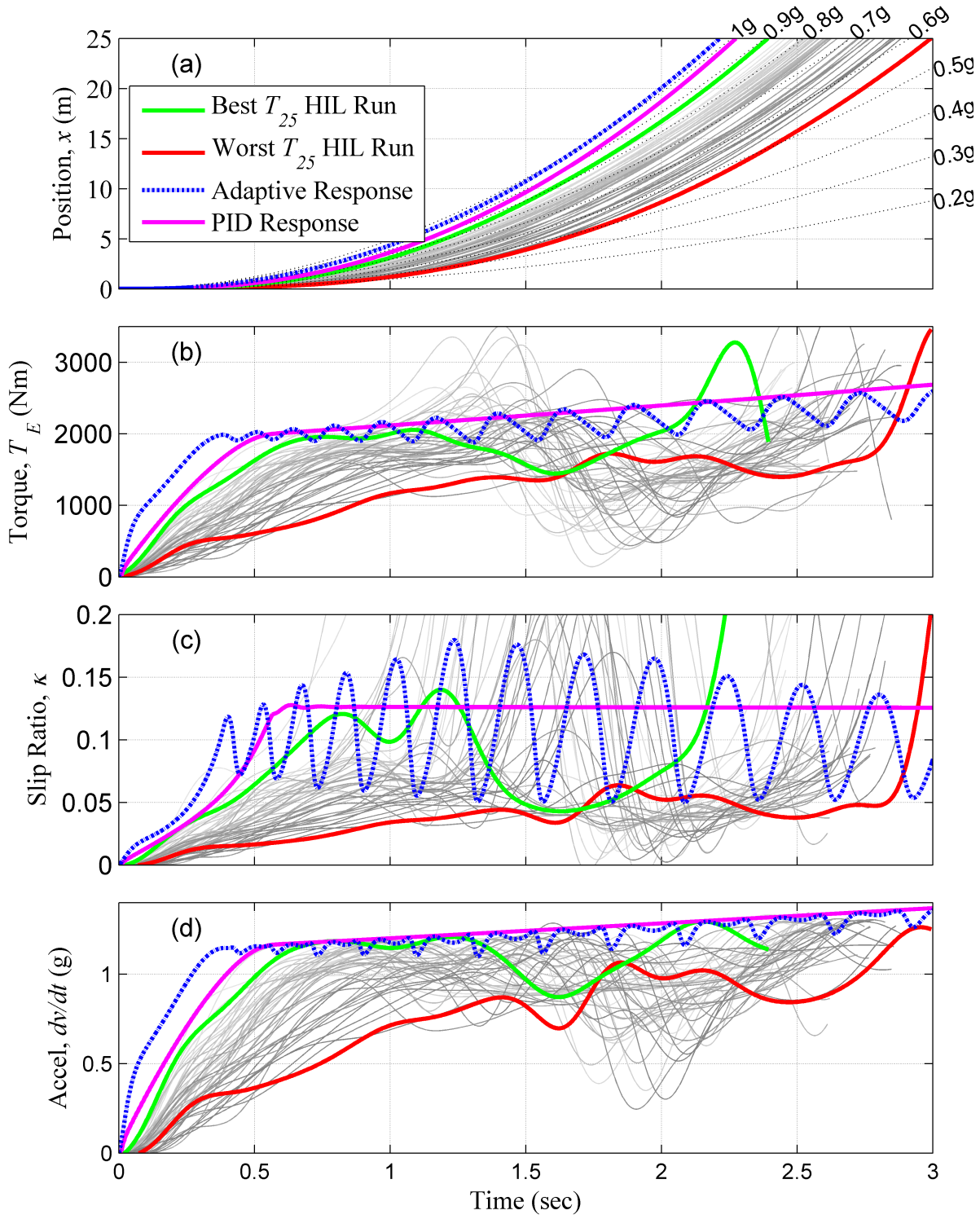

Figure 4.8: Control simulation results with explicit knowledge of the tire-ground interface including results for adaptive control, PID control and HIL testing; (a) position, (b) wheel torque, (c) slip ratio, and (d) acceleration.

4.5.2 1-DOF Simulation: Non-uniform Surface

In the second simulation study, the tire-ground interface properties go through a discrete change from properties that are characteristic of dry pavement to that of wet pavement after the vehicle has travelled five meters. This equates to a discrete change in the Pacejka curve at $x = 5\ m$, simulating the instantaneous transition from dry pavement to wet pavement. It is important to note that the coefficients B, C, D and E are dependent on both the tire-ground interface and down force F_N. This functional dependence is presented in Figure 4.9, where we can see not only the difference between the dry and wet surfaces but also the difference caused as a result of increasing down force.

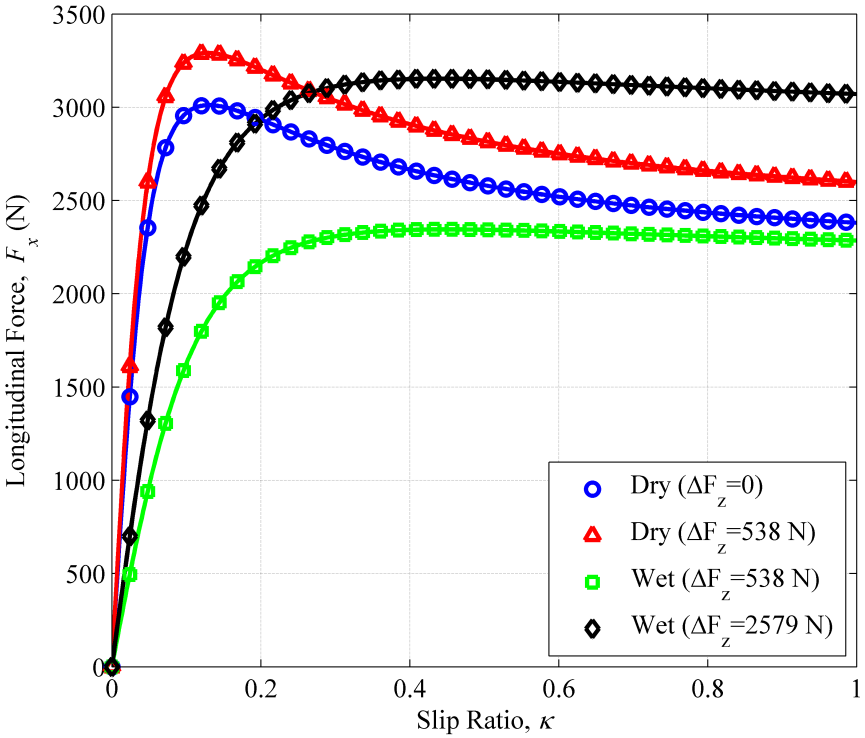

Figure 4.9: The difference in Pacejka curves due to a change in surface properties and increased down force. Typical curves for both dry and wet pavement [1, 2].

Figure 4.10(a) shows the position across time where it is evident that the response of the vehicle remains stable for the duration of the simulation. More interesting are the results in Figure 4.10(b-d), where torque, slip ratio and longitudinal acceleration are presented through time, respectively. Close inspection of Figure 4.10(b) shows the existence of two slip ratios where a peak tractive force is achieved for both dry and wet surfaces respectively. These slip ratios are slowly time varying as a function of down force and are referred to as the peak slip ratios for their respective surfaces. The buildup to the peak slip ratio on dry pavement can be seen for $t \in [0, 0.5]\ sec$. The proposed traction control algorithm then tracks the peak slip ratio for dry pavement as it increases as a

function of down force for $t \in [0.5, 1.0]$ *sec*. There is a discrete change in the surface conditions at $t = 1$ *sec* from dry pavement to wet pavement. The slip ratio then rises abruptly until the proposed traction control algorithm has a chance to recover $t \in [1.0, 2.0]$ *sec*. There is a short period of time where the slip ratio builds up to the peak value for wet pavement and then tracks that value for the remainder of the simulation $t \in [2.0, 5.0]$ *sec*. The gradient is a function of not only the vehicle output, specifically acceleration, but also the discrete time dynamic filter defined as Equation 4.31. Apriori knowledge of the surface conditions is assumed in this simulation. In practice a human has the ability to recognize the difference between dry and wet pavement using a variety of tactile, visual, and audible cues and uses these cues to build a crude model of the tire ground interface and continually adjusts this model based on the correlation between throttle or engine torque and sensed acceleration. Provided that a suitable classification or estimation algorithm is chosen to approximate the Pacejka curve [3, 16], the proposed traction control algorithm is shown to track the peak slip ratio through a spatially and temporally changing environment.

From Equations 4.30-4.32 it is clear that the proposed anthropomimetic traction control algorithm is model-based. Human drivers do not utilize the same types of engineering models such as the model developed in Section 4.2 for the proposed traction control algorithm; however, it is highly likely that humans do construct perceptive models of not only the vehicle dynamics, but also models of the tire-ground interface. While it is reasonable to expect to have a good understanding of the vehicle dynamics model and associated parameter values, the traction curve associated with the tire-ground interface is less likely to be known to the same level of accuracy, and it will usually be spatially varying as the road conditions change. Kazemi et. al. [8], Li et. al. [3], Tan et. al. [36], and Pasterkamp et al. [17] have developed online identification methods that are specifically designed for estimating the tire traction curve in real-time. These algorithms could be incorporated with the proposed anthropomimetic traction control algorithm to enable a fully adaptive solution.

The simulation results shown in Figure 4.10, make use of the aforementioned gradient estimation filter that is updated at the same rate as the simulation. While theoretically we can assume explicit knowledge of the filter parameters and evolution through time, practically it is unreasonable to make use of such a high sample rate, that would be required in discrete time. The results presented in Figure 4.11 were generated using the same approach that was used to generate the results of Figure 4.10 with the exception of the sampling rate of the estimation process. The gradient estimation filter used in these simulations was updated at a rate equal to 1000 Hz compared to a rate of 5000 Hz. These sample rates were determined heuristically with limiting factors being the rates of change in the slip ratio and slip angles near zero velocity as well as the slowly time nonlinear filter that is approximated as the linear time invariant gradient filter.

It is also noticeable, from Figure 4.11, that some degree of the hunting behavior has been lost when changing to a more realistic sampling rate for the estimation process. It should also be emphasized that the hunting behavior was a desirable characteristic of the adaptive approach. Some degree of hunting behavior will be regained by using the control and filter estimation structure developed in Chapter 5.

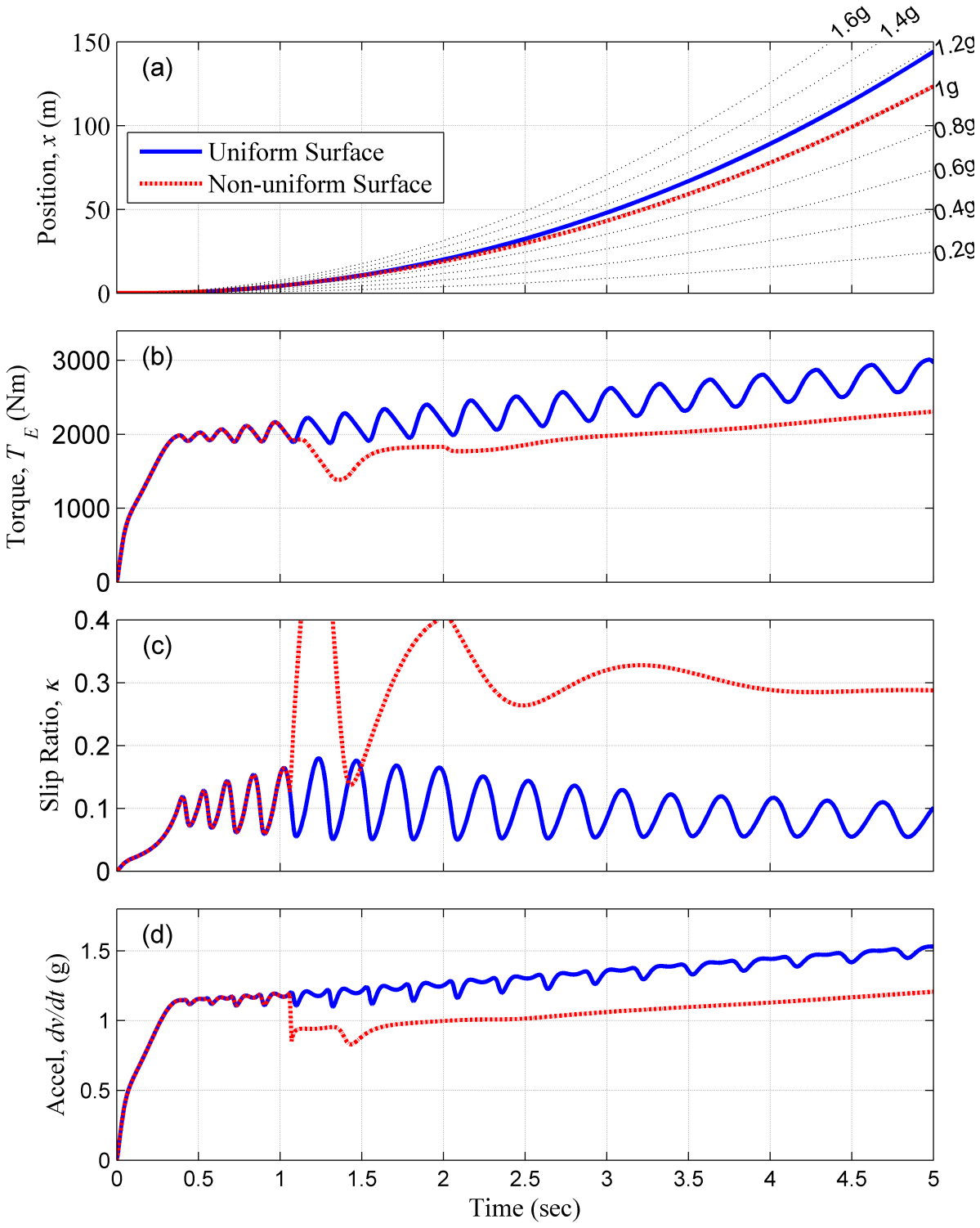

Figure 4.10: Control simulation results with explicit knowledge of the tire-ground interface including results using adaptive control for a uniform surface and non-uniform surface that changes from dry pavement to wet pavement at $x = 5\ m$. The sampling rate of the gradient filter is 5 kHz.

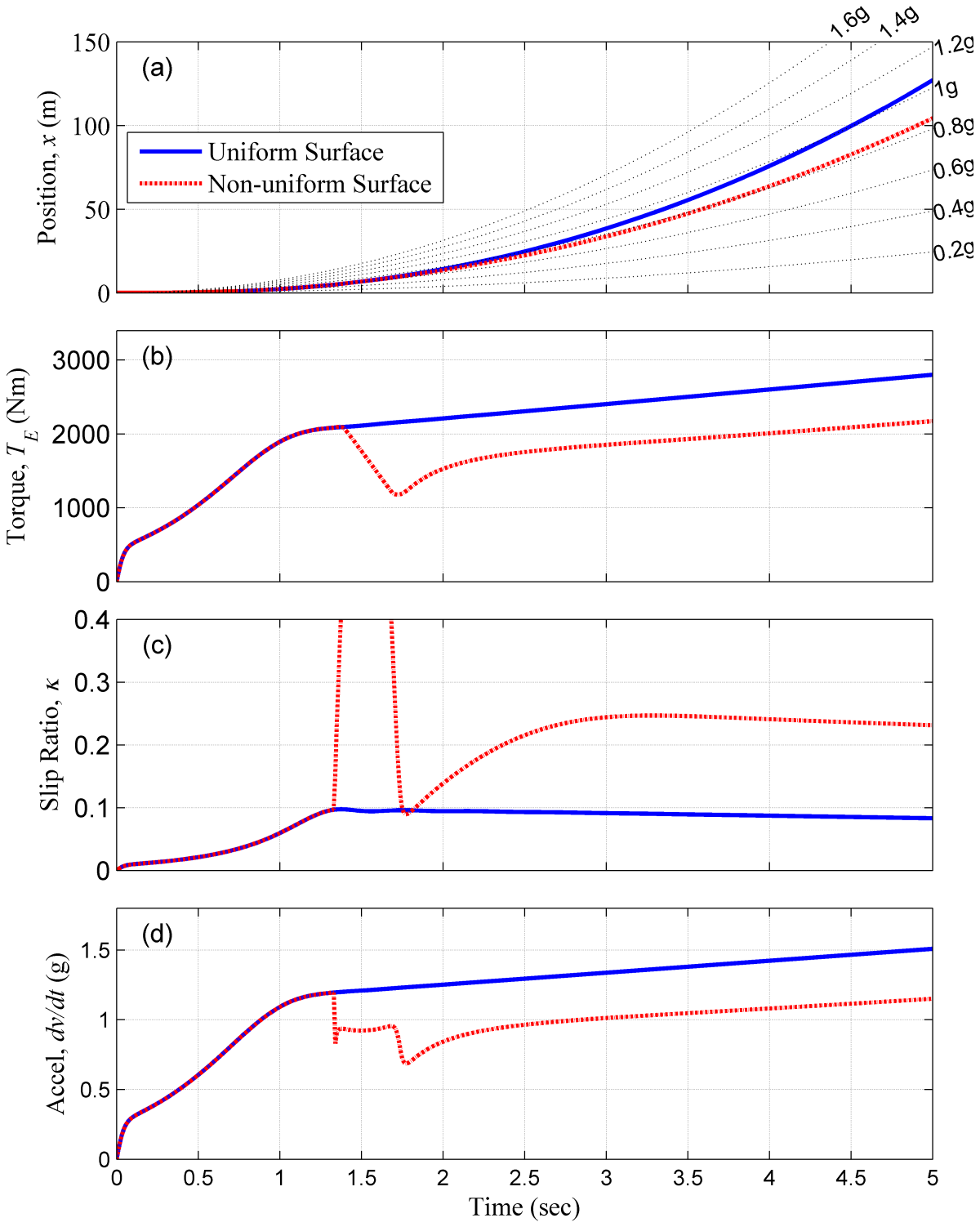

Figure 4.11: Control simulation results with explicit knowledge of the tire-ground interface including results using adaptive control for a uniform surface and non-uniform surface that changes from dry pavement to wet pavement at $x = 5\ m$. The sampling rate of the gradient filter is 1 kHz.

4.5.3 3-DOF Simulation: Uniform Surface

It is desirable to extend the traction control algorithm that has been demonstrated for the longitudinal case (1-DOF) to the bicycle model (3-DOF). Maximizing longitudinal and lateral accelerations simultaneously is not trivial, especially considering the separate but relevant challenge of path planning. As described above, this approach gives the driver (or another automatic control system) complete control of the steering angle, and does not attempt to prescribe requirements for path planning. The objective of this study was to maximize the vector sum of longitudinal and lateral accelerations for a fixed steering input. A total of four circular driving maneuvers were analyzed. In this case the goal was to maximize longitudinal and lateral accelerations simultaneously for the fixed steering angle specified by a driver or another automatic control system. The control algorithm only adjusts the engine output to maximize the vector sum of accelerations. The four driving scenarios studied are outlined in Table 4.2.

Table 4.2: Driving Scenarios

Scenario	Steering Angle δ_f (deg)	Description
1	0	Longitudinal Acceleration Only
2	20	Longitudinal and Lateral Acceleration
3	40	Longitudinal and Lateral Acceleration
4	60	Longitudinal and Lateral Acceleration

Indirect Adaptation Law

The simulations in this section were performed for the 3-DOF bicycle model of Section 3.4 using values in Table 4.1 and the control algorithm of Section 4.3. When using this algorithm a slight modification to the update law of Equation 4.47 is necessary. This modification is performed according to Equation 4.48, which is similar to the signed regressor used in Equation 4.47.

$$u_{k+1} = u_k + \mu_a \times \begin{cases} \nabla_{f,k} & \frac{\partial J_{fx}(\mathbf{u}_k)}{\partial \mathbf{u}_k} > 0 \; and \; \frac{\partial J_{fy}(\mathbf{u}_k)}{\partial \mathbf{u}_k} > 0 \\ -\eta_a & \frac{\partial J_{fx}(\mathbf{u}_k)}{\partial \mathbf{u}_k} < 0 \; or \; \frac{\partial J_{fy}(\mathbf{u}_k)}{\partial \mathbf{u}_k} < 0 \end{cases} \tag{4.48}$$

The weighting matrix used in these four simulations is defined as $\mathbf{Q_a} = \begin{bmatrix} 1 & 0 \; ; \; 0 & 10 \end{bmatrix}$. The position results for all four simulations, presented in Figure 4.12, show exactly what would be expected as steering angle is increased; the circular path of the vehicle decreases in radius. This is a direct result of the effects of slip in generating longitudinal and lateral forces; a larger steering angle will cause a faster buildup in the front slip angle α_f and corresponding lateral force F_{ytr}.

The velocity and acceleration results, presented in Figure 4.13, show the same regions and trends that the 1-DOF simulations displayed. The first region in all of the simulations is the region where

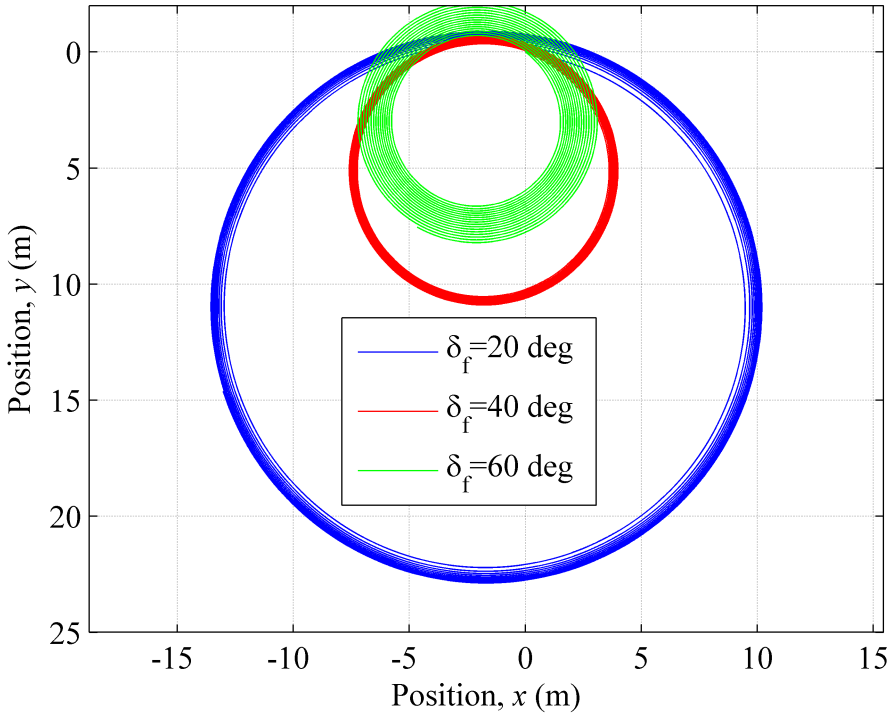

Figure 4.12: Position results for Scenarios 2-4 from Table 4.2 using the Indirect Adaptation Law.

the acceleration builds up to an asymptotic limit, while the second region shows that the algorithm tracks this limit. In the case of the bicycle model of Section 3.4 this asymptotic limit changes as a function of the viscous drag in the undriven wheel. This is exactly what is expected of the algorithm with respect to longitudinal motion. However, what is not expected is the fact that for the simulation where $\delta_f = 60\ deg$, the front slip angle α_f exceeds the value at which the peak lateral force is achieved which is approximately $8-10\ deg$. Figure 4.14(a-d) presents the slip ratios and slip angles of all simulations for comparison. It can readily be seen that the algorithm converges to the value at which the rear slip ratio creates the peak longitudinal force in Figure 4.14(b). This is not true for either the front slip angle α_f or the rear slip angle α_r shown in Figure 4.14(c,d).

The cause of this is two fold. The dominant partial derivative in the gradient filter is $\partial F_{xtr}/\partial \kappa_r$ and this partial derivative is embedded in the state equation of the filter and is not easily isolated by the weighting matrix $\mathbf{Q_a}$. This functional dependence can be seen explicitly when looking at the continuous time representation of the gradient filter from Section 4.3 in Appendix B.1. Additionally, for the same reason that a signed regressor update law was used in the simulations from Sections 4.5.1 and 4.5.2, the relative magnitudes are drastically different when the slip ratio or slip angle at which the peak tractive force is achieved and exceeded. Although not stated at the time, this is proven by returning to Figures 4.4-4.6. This also suggests that if your goal is to maximize the vector sum of accelerations than a valid solution may be to continue to increase the

control torque despite the fact that one or more of the optimal slip ratios or slip angles have been exceeded. This is an incredibly interesting observation as it suggests that maximizing the vector sum of accelerations does not always imply that the algorithm converge on the optimal slip ratios or slip angles.

This conclusion is further supported by Figure 4.15 where the longitudinal component of the gradient $J_{k,x}$ displays the same behavior as that from the 1-DOF case in Section 4.5.1 while the lateral component seems to suggest that the only way to increase the acceleration is to decrease throttle. Regardless of potential changes in the weighting matrix the lateral component of the gradient filter itself retains this behavior due to the mismatch in partial derivative magnitudes.

The control input and steering angles are presented in Figure 4.16. The control torque T_c shows the same behavior that was observed in the 1-DOF simulations of Section 4.5.1 and 4.5.2 and this is to be expected as the algorithm from Section 4.3 has been shown to be biased towards the longitudinal direction.

For comparison purposes in the next section and to reinforce the claim that the peak lateral force is not being achieved, Figure 4.17 is presented. Figure 4.17(c,d) shows that the peak lateral force for the front tire is exceeded for the simulation in which $\delta_f = 60 \ \ deg$ and the peak lateral force for the rear tire is never achieved. While, all simulations track the peak longitudinal force, Figure 4.17(b), quite nicely.

The behavior that has been demonstrated in this section for the gradient filter and control algorithm for Section 4.3, should be seen as a function of the physical system and not a failure of the algorithm itself. No effort was made in this work to determine the true optimal path and subsequent realizable forces necessary to produce maximum lateral and longitudinal accelerations and in some cases the behavior of the Indirect Adaptation Law from Section 4.3 may be desirable. This point will be further discussed at the end of this work in Section 9.3. The results of this section were in fact the motivation for the development of the Direct Adaptation Law, developed in Section 4.5.3.

Direct Adaptation Law

The simulations in this section were performed for the 3-DOF bicycle model of Section 3.4 using values in Table 4.1 and the control algorithm of Section 4.4. When using this algorithm a slight modification to the update law of Equation 4.47 is necessary. This modification is performed according to Equation 4.49, which is similar to the signed regressor used in Equation 4.47.

$$u_{k+1} = u_k + \mu_b \times \begin{cases} \nabla_{f,k} & \frac{\partial J_{fx}(\mathbf{u}_k)}{\partial \mathbf{u}_k} > 0 \ and \ \frac{\partial J_{fy}(\mathbf{u}_k)}{\partial \mathbf{u}_k} > 0 \\ -\eta_b & \frac{\partial J_{fx}(\mathbf{u}_k)}{\partial \mathbf{u}_k} < 0 \ or \ \frac{\partial J_{fy}(\mathbf{u}_k)}{\partial \mathbf{u}_k} < 0 \end{cases} \tag{4.49}$$

It is important to note that if either $\partial J_{fx}(\mathbf{u}_k)/\partial \mathbf{u}_k$ or $\partial J_{fy}(\mathbf{u}_k)/\partial \mathbf{u}_k$ is negative the then the control input T_c is reduced. This was done by design, to ensure that the algorithm does not command the vehicle to excessively overshoot the peak slip ratios κ^* or slip angles α^*. It also opens the door to

investigating the optimal control settings for a variety of paths, which this work does not address explicitly but does mention in Section 9.3. The position results for these simulations are presented in Figure 4.18, with the exception of the case where $\delta_f = 0 \ \ deg$. The position results are rather intuitive, as the steering angle δ_f increases the vehicle converges to a path of decreasing radius.

Somewhat more informative are the velocity and acceleration results of Figure 4.19, where all four sets of results display two distinct regions in the results: a build up to maximum longitudinal acceleration $t \in [0,1]$ *sec* and a tracking of the peak acceleration $t \in [1,20]$ *sec*.

The most informative results are slip ratios κ and slip angles α presented in Figure 4.20. It can be seen, from Figure 4.20(c) and 4.23(c) that the only simulation to reach the slip angle at which the maximum lateral force is achieved was for when $\delta_f = 60 \ \ deg$. There is little difference in the remainder of the simulations as the control input T_c is dominated by the longitudinal forces and accelerations. However, the competing behavior of maximizing both longitudinal acceleration and lateral accelerations is demonstrated for the case when $\delta_f = 60 \ \ deg$. The rear slip ratio κ_r in Figure 4.20 is actually being regulated to a value that is less than the value at which the maximum longitudinal force is created, and this is due to the fact that the front slip angle α_f is tracking the value at which the peak lateral force is created. Careful analysis of the behavior of both of these signals compared to that of the simulations in this section suggests a slower system response when considering the lateral force F_{ytf} and F_{ytr} output relative to the control input T_c, while the longitudinal force F_{xtr} displays a much quicker response to the control input T_c. This makes sense intuitively because the time required to build up a significant longitudinal force in a vehicle is significantly less than that required to build up a significant lateral force when limited to controlling only the input torque T_c. These results also show that the ability of the Direct Adaptation Law of Section 4.4 to isolate both the longitudinal and lateral motion is superior to that of the algorithm developed in Section 4.3.

The results of the individual components of Equation 4.46 are presented in Figure 4.21.

For consistency the control input T_c is presented alongside the specified steering angle δ_f in Figure 4.22. The same two regions prevalent in all the results can be seen readily in this data as well; buildup to peak acceleration, and tracking of that peak acceleration.

The forces, which will be estimated in subsequent Chapters are shown here to reinforce the two separate but distinct regions. All the simulations presented here reach the peak longitudinal force for F_{xtr} while only one simulation, $\delta_f = 60 \ \ deg$ reaches the peak lateral force. Provided the other simulations were allowed to continue past 20 seconds they too would be expected to reach this asymptotic limit as well.

4.6 Summary

In this chapter a filter was developed using a 1-DOF model to calculate the gradient of longitudinal acceleration with respect to engine torque. The filter is a combination of a linear time invariant

system and a system that is non-linear and slowly time varying, but approximated as a linear time invariant system. The filter was then used in an adaptive control algorithm that used a gradient ascent algorithm, causing the vehicle to track the peak tractive force through time. The algorithm was developed in discrete time and is, therefore, well suited for real time control. Simulations were performed on a uniform dry surface as well as a simulation that went through a discrete change from a dry surface to a wet surface. The algorithm was then extended to a 3-DOF model where the objective was to maximize longitudinal and lateral acceleration simultaneously, and an alternative formulation of the filter was presented to accomplish this. Simulations were performed for a set of prescribed steering angles on a uniform surface. In both cases (1-DOF and 3-DOF) the adaptive algorithm(s) were able to track the peak tractive force(s) through time, Even though the Direct Adaptation Law proved to be superior at tracking the peak lateral forces. The superiority of the Direct Adaptation Law can be attributed to the its ability to better isolate the individual forces as opposed to only being able to isolate the translational accelerations, a key limitation of the Indirect Adaptation Law. The filter used in this chapter required knowledge of the vehicle model and the tire-ground interface model. While both the 1-DOF and 3-DOF algorithms successfully showed the ability to maximize both longitudinal as well as lateral acceleration in the case of the 3-DOF algorithm, subsequent chapters are devoted to developing approximations that allow the 1-DOF filter to become model free.

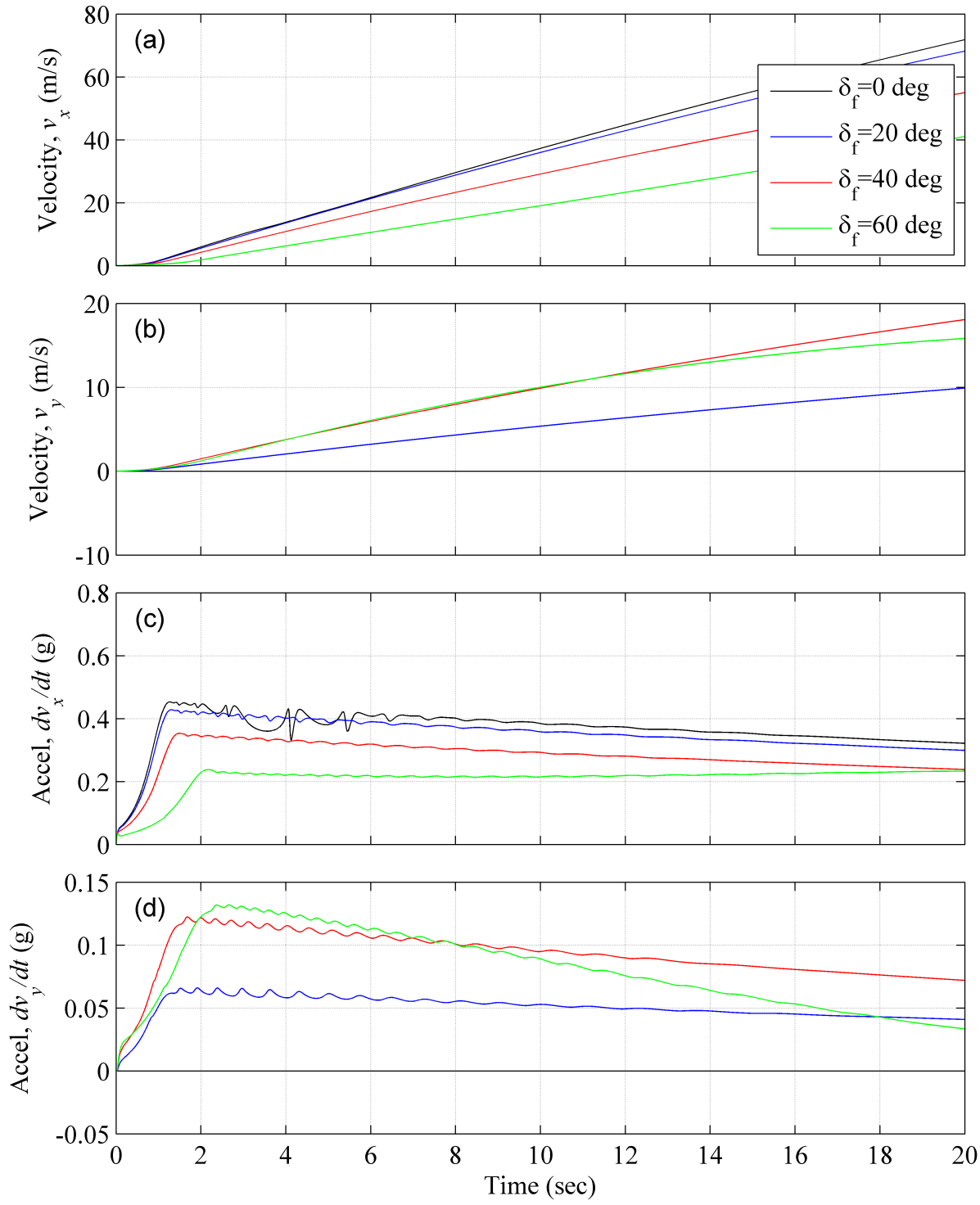

Figure 4.13: Velocity ($\mathbf{v}_k$) and acceleration ($\mathbf{a}_k$) results for Scenarios 1-4 from Table 4.2 using the Indirect Adaptation Law.

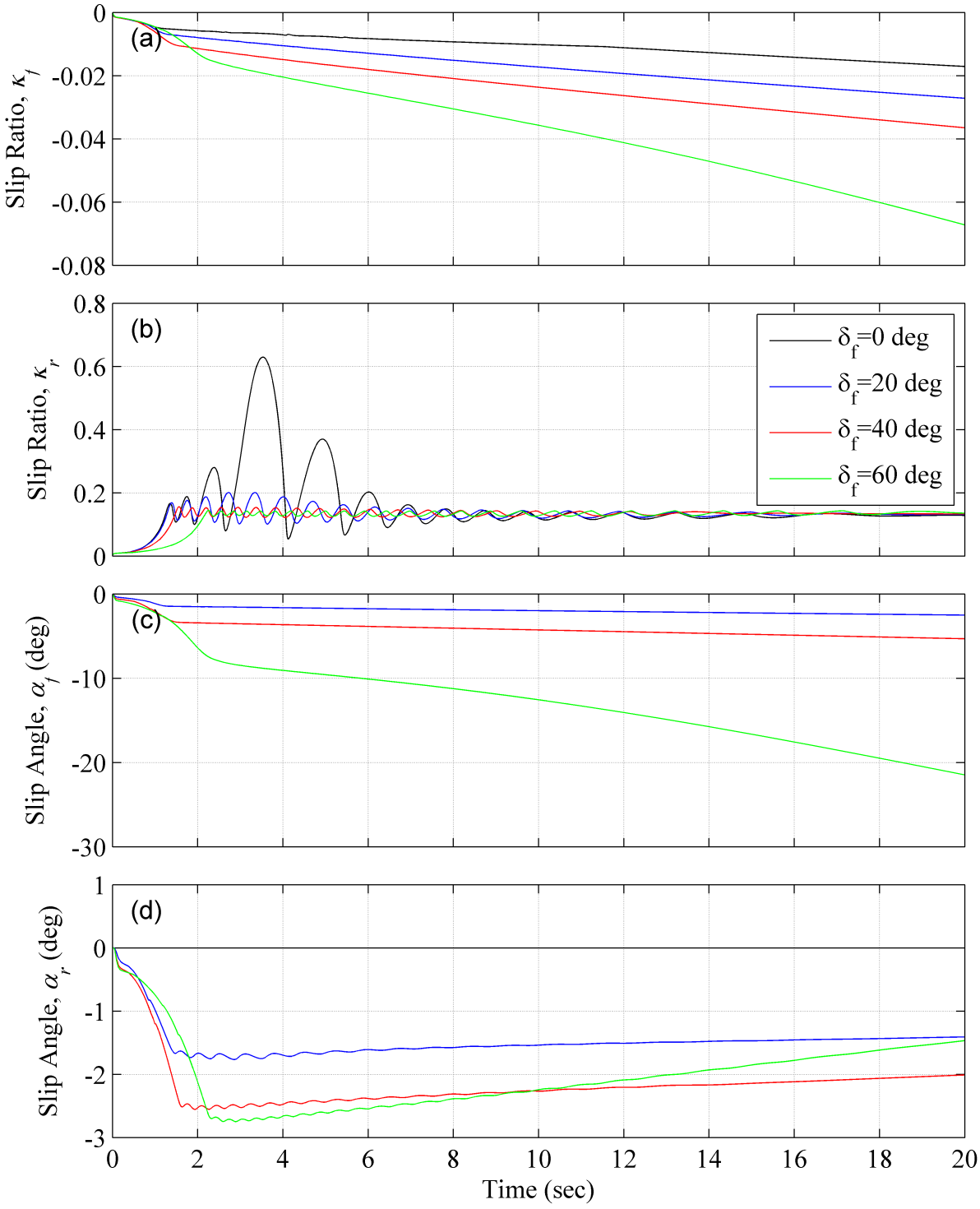

Figure 4.14: Slip ratio (κ) and slip angle (α) results for Scenarios 1-4 from Table 4.2 using the Indirect Adaptation Law.

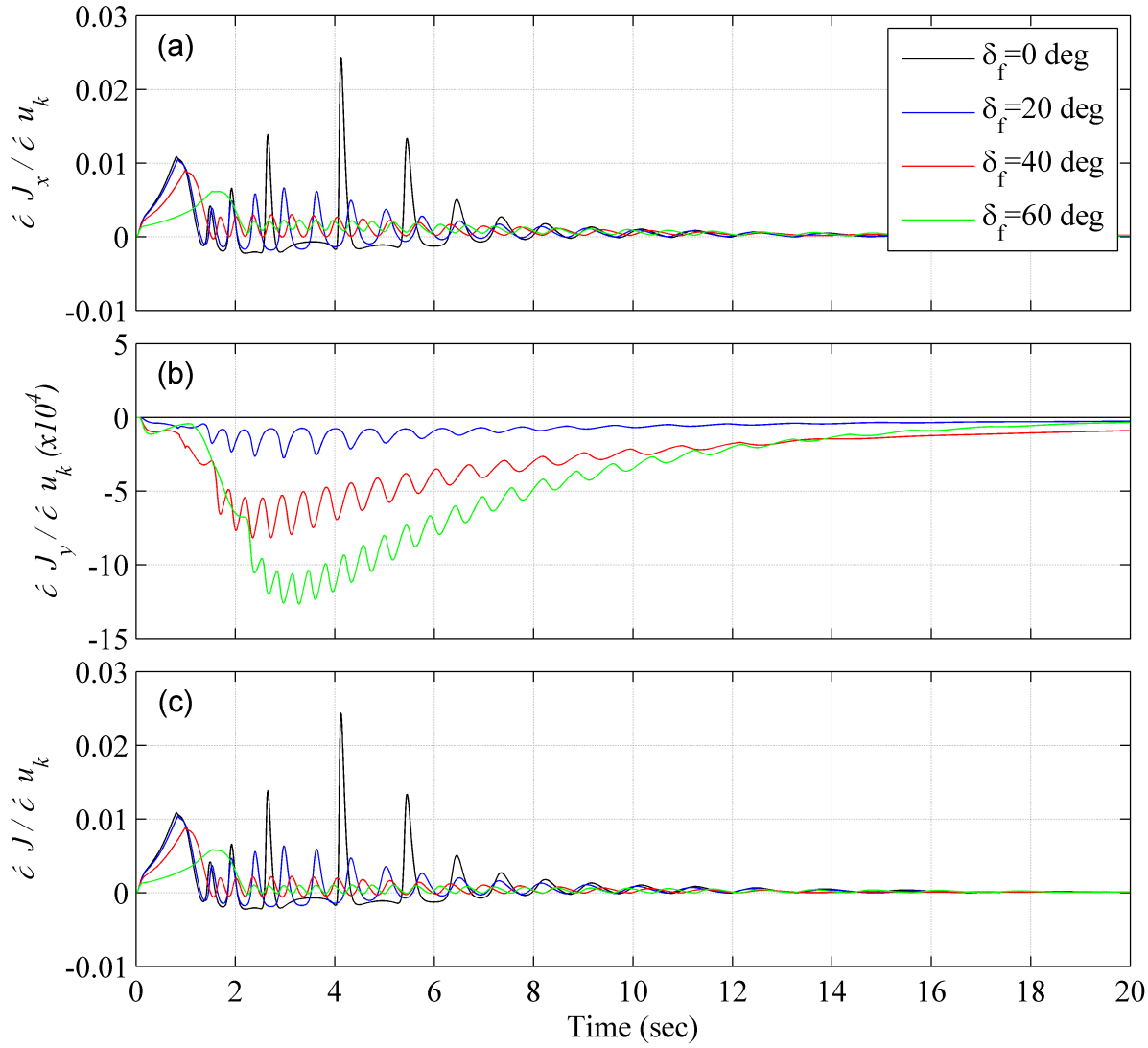

Figure 4.15: Gradient (∇_f, J_{fx} and J_{fy}) results for Scenarios 1-4 from Table 4.2 using the Indirect Adaptation Law.

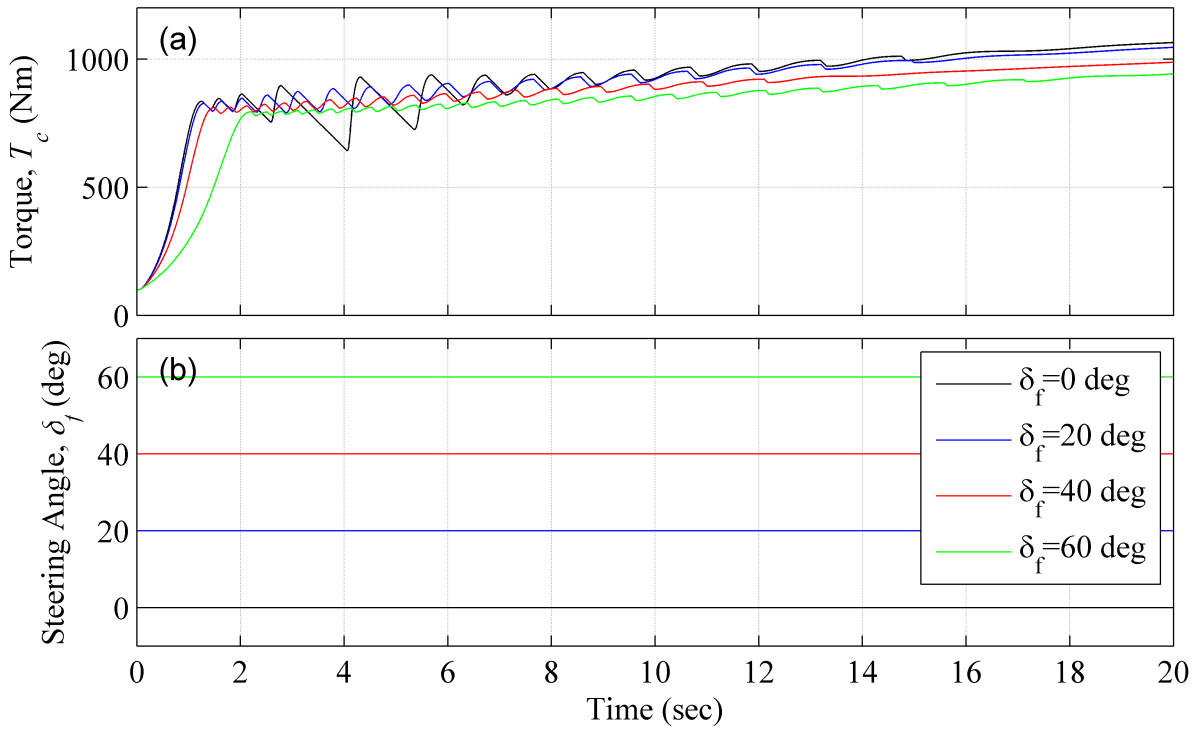

Figure 4.16: Throttle (T_c) and Steering Angle (δ_f) results for Scenarios 1-4 from Table 4.2 using the Indirect Adaptation Law.

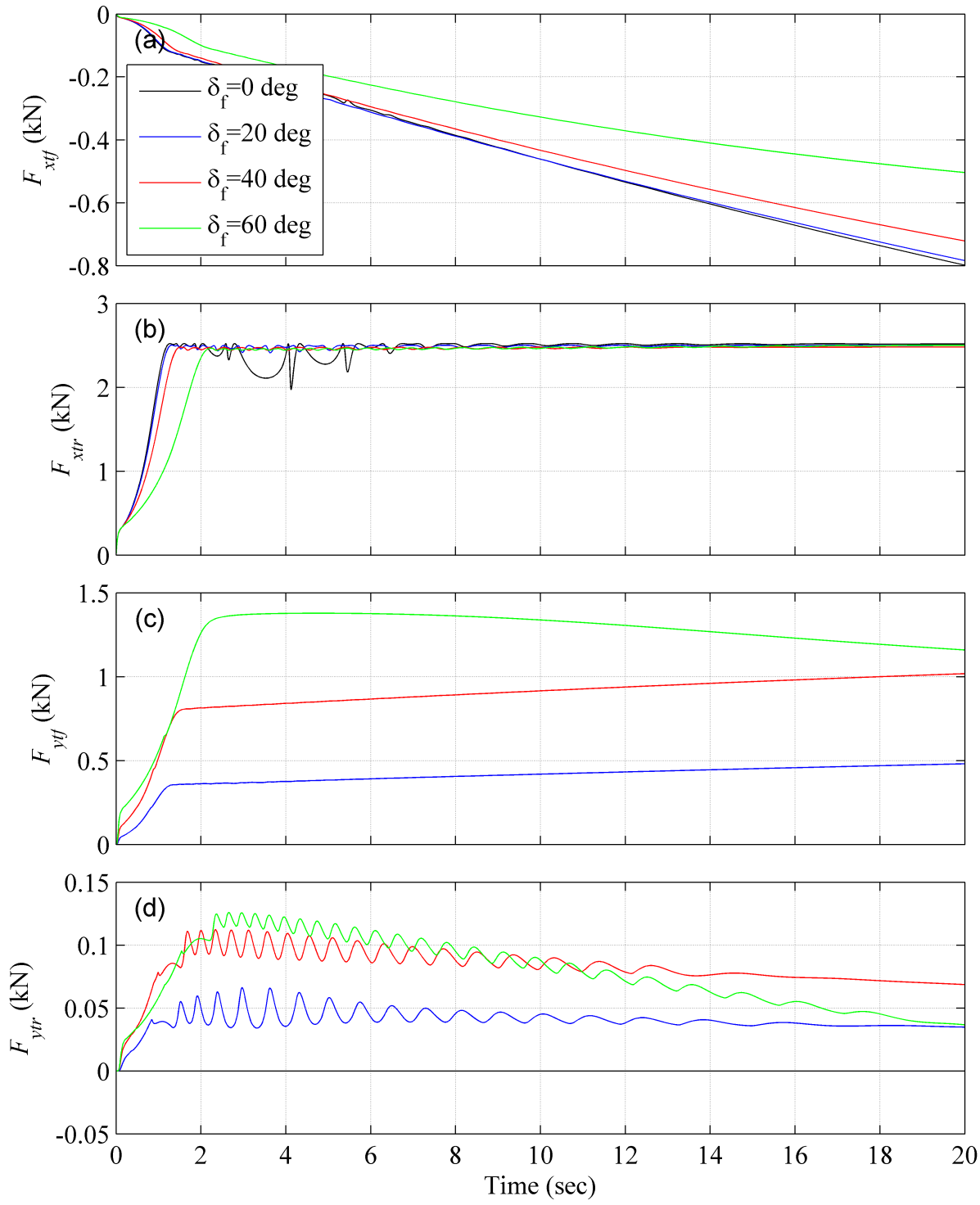

Figure 4.17: Tractive force (F_{xt} and F_{yt}) results for Scenarios 1-4 from Table 4.2 using the Indirect Adaptation Law.

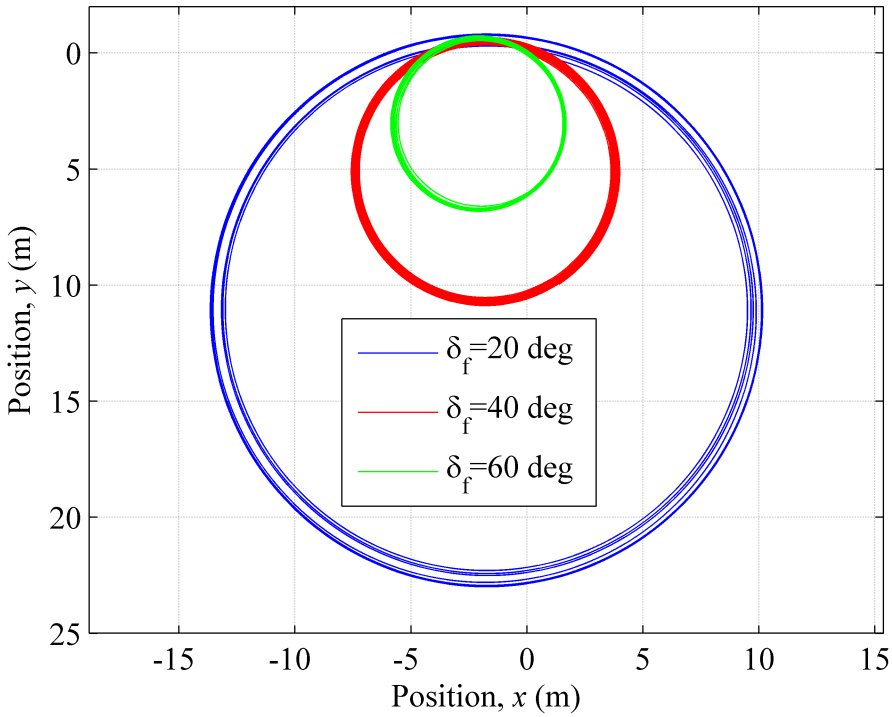

Figure 4.18: Position results for Scenarios 2-4 from Table 4.2 using the Direct Adaptation Law.

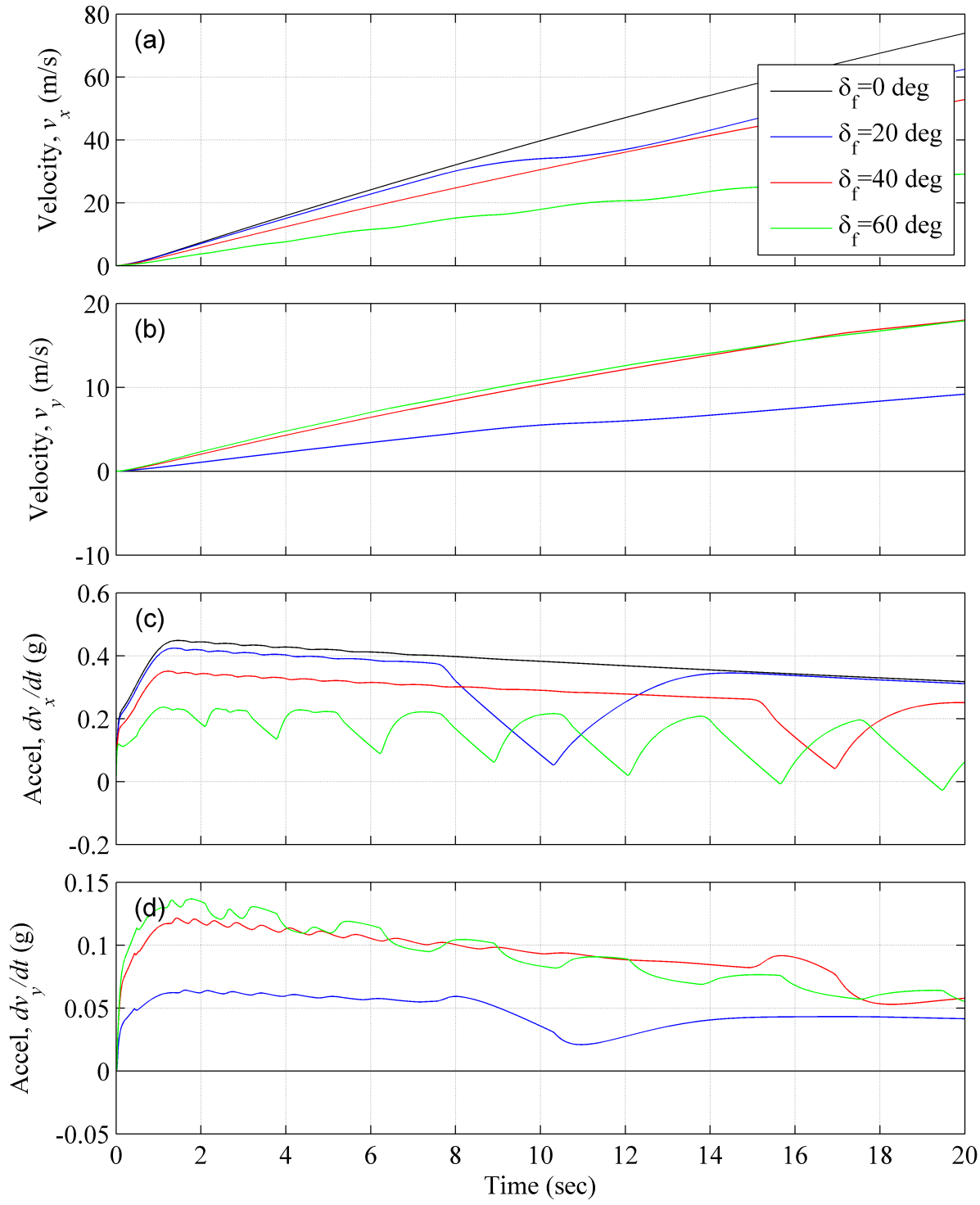

Figure 4.19: Velocity ($\mathbf{v}_k$) and acceleration ($\mathbf{a}_k$) results for Scenarios 1-4 from Table 4.2 using the Direct Adaptation Law.

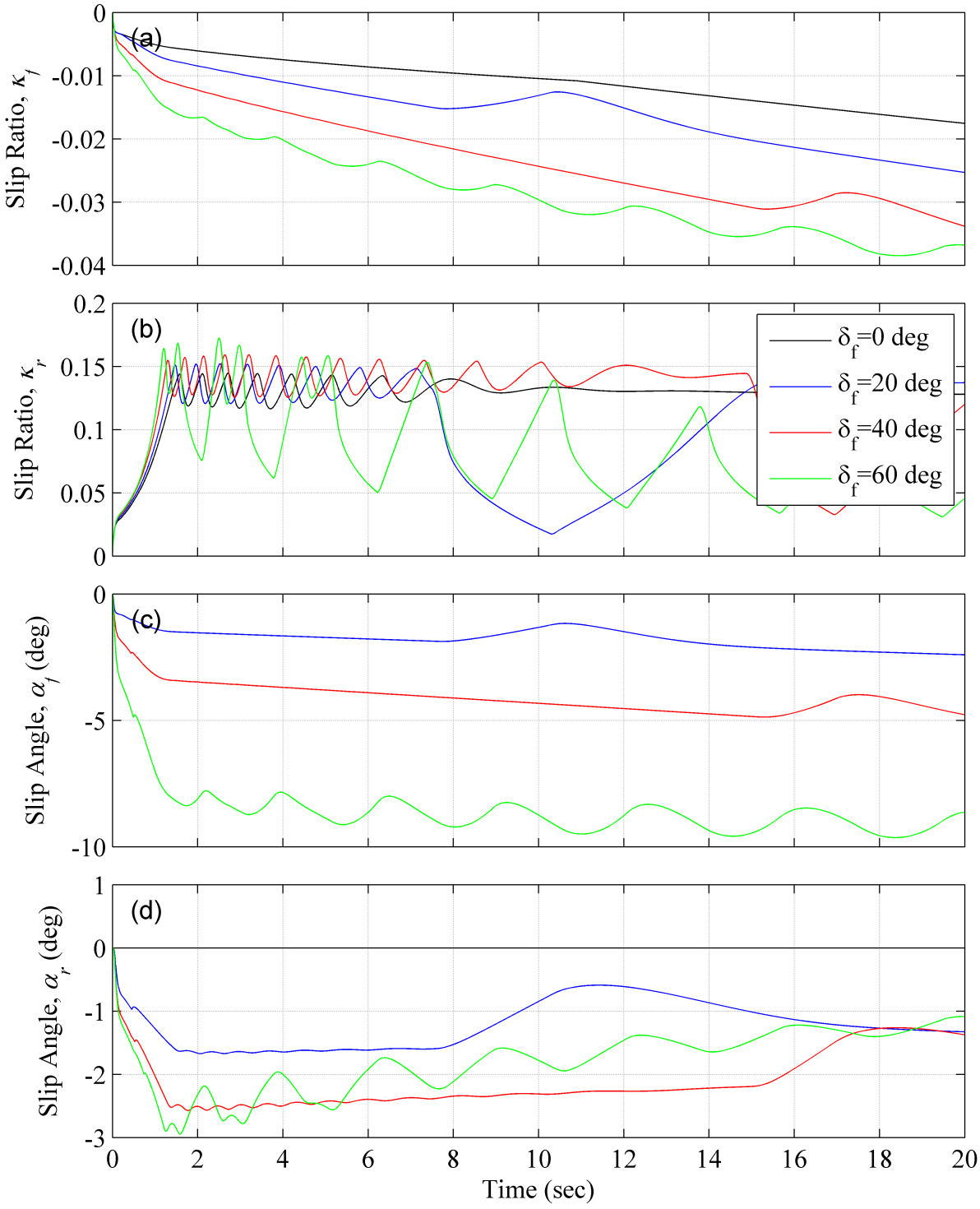

Figure 4.20: Slip ratio (κ) and slip angle (α) results for Scenarios 1-4 from Table 4.2 using the Direct Adaptation Law.

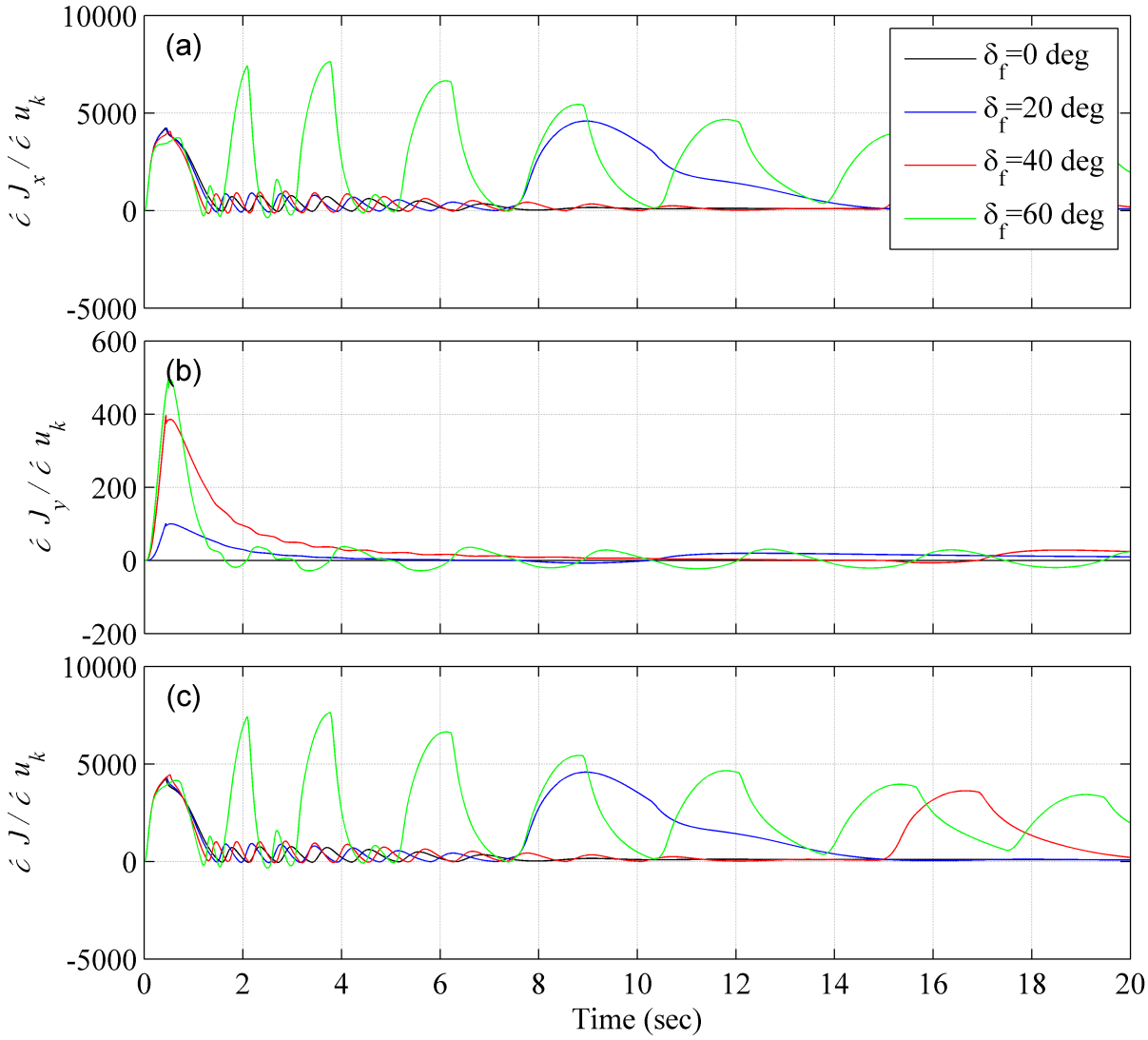

Figure 4.21: Gradient (∇_f, J_{fx} and J_{fy}) results for Scenarios 1-4 from Table 4.2 using the Direct Adaptation Law.

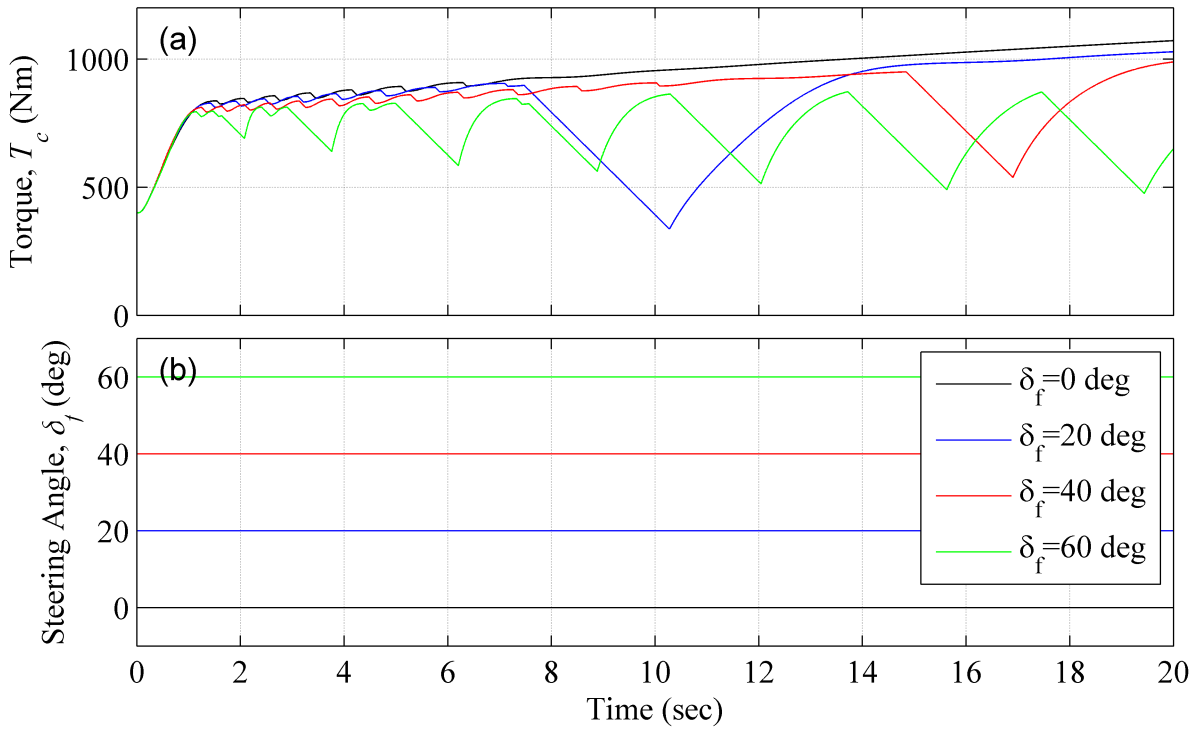

Figure 4.22: Throttle (T_c) and Steering Angle (δ_f) results for Scenarios 1-4 from Table 4.2 using the Direct Adaptation Law.

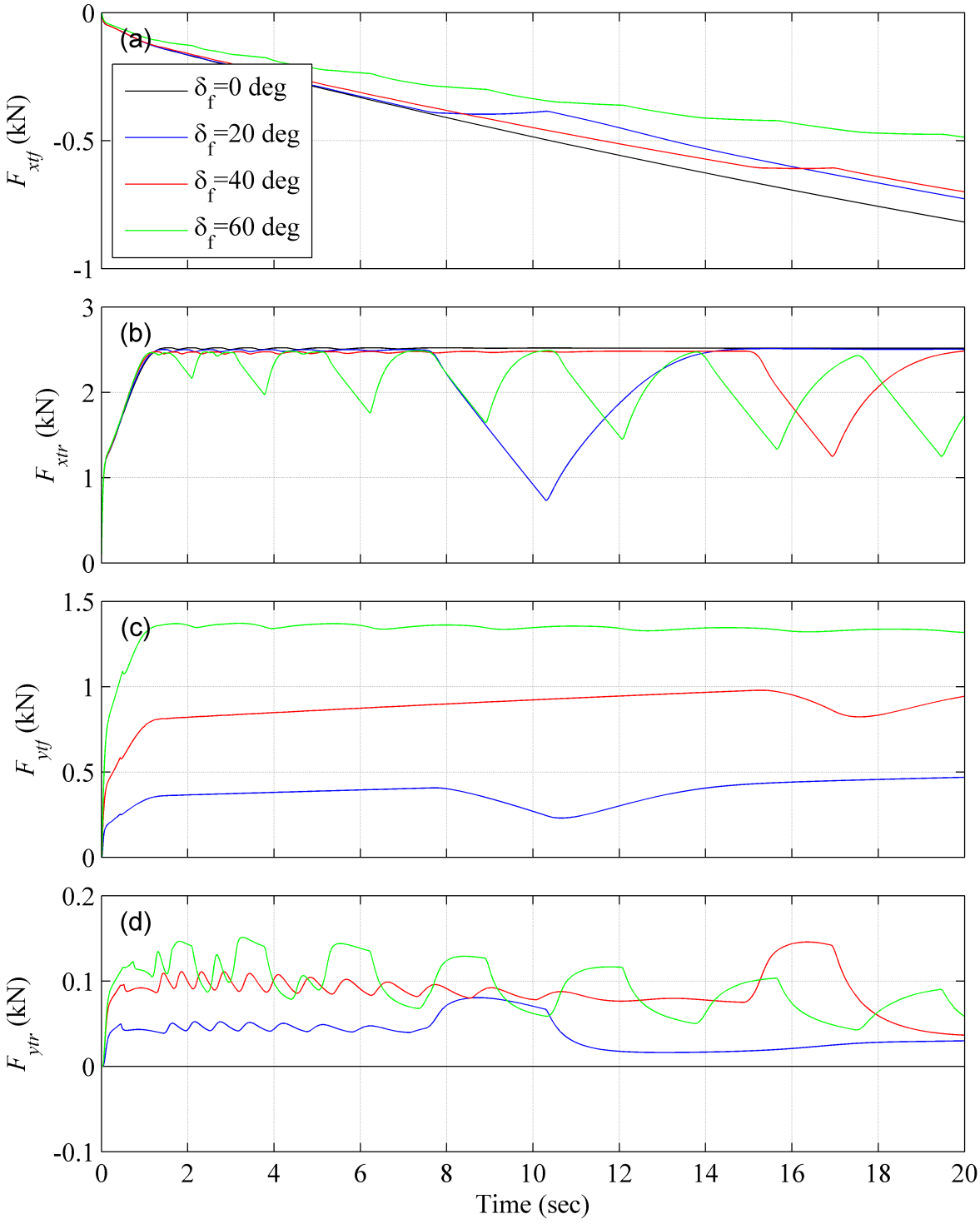

Figure 4.23: Tractive force (F_{xt} and F_{yt}) results for Scenarios 1-4 from Table 4.2 using the Direct Adaptation Law.

Chapter 5

Approximation of Gradient Filter

The second evolution of the controller uses an approximation of the gradient filter. The natural extension of the system shown in Figure 4.2 is the system presented in Figure 5.1. The block diagram of Figure 5.1 includes a more detailed version of the Gradient Estimation block in Figure 4.1. In this case, the gradient filter uses an approximation of the exact filter; using the gradient of the tractive forces with respect to slip to control the vehicle. While the vehicle model and tire-ground interface properties do effect the explicit pole and zero locations of the filter, the approximation enables the filter to be independent of these properties. Simulations using a 1-DOF model, similar to those in previous sections, are performed on a continuous segment of dry pavement as well as through a discrete transition from dry to wet pavement. The adaptive controller is shown to track the peak tractive force in both cases.

5.1 Gradient Filter Approximation

The complexity of the gradient filter defined by Equations 4.30 and 4.31 is somewhat cumbersome and requires knowledge of the vehicle dynamics and a high-fidelity longitudinal traction curve. An approximation to this filter, which captures the same general behavior, is desirable for both real-time efficiency and generality.

5.1.1 1-DOF Filter Approximation

In the case of the 1-DOF longitudinal vehicle model, it is helpful to define ξ to be the slope of the traction force with respect to the slip ratio, evaluated at the current operating point.

$$\xi(\kappa) = \frac{\partial F_x}{\partial \kappa} \tag{5.1}$$

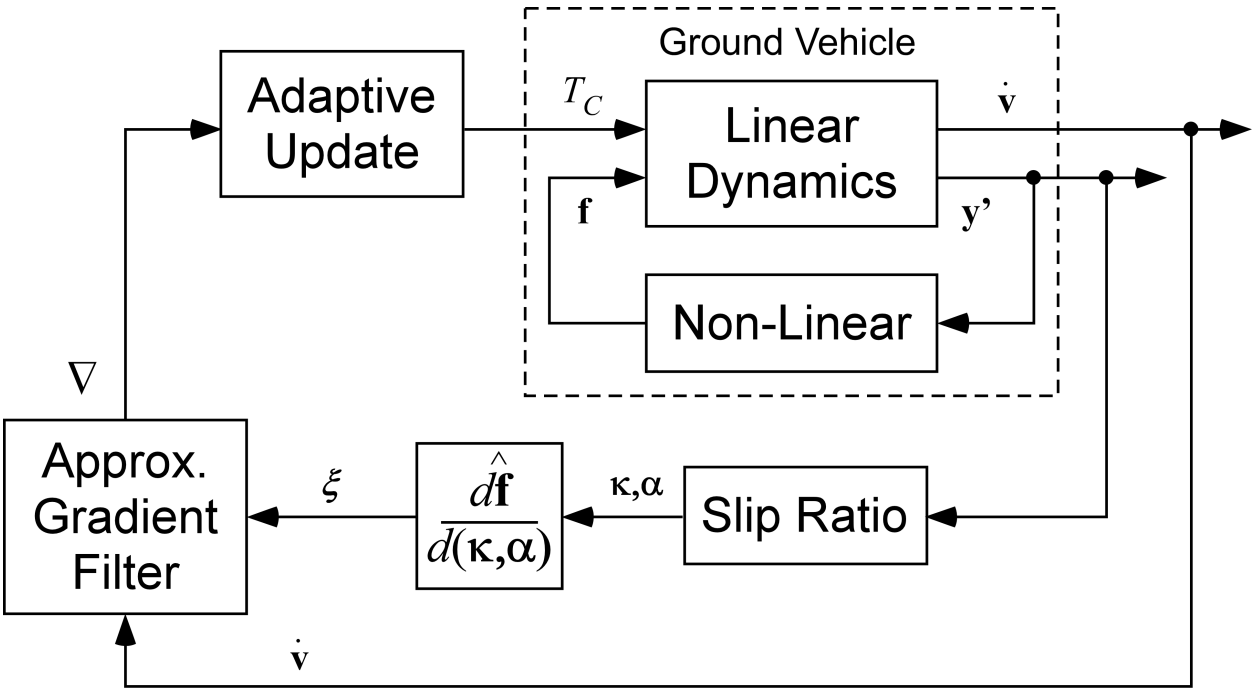

Figure 5.1: Detailed block diagram of control structure when using an approximation of the gradient filter for the 1-DOF Model.

Figure 5.2 shows snapshots of frequency response plots for the time-varying gradient filter given by Equations 4.30 and 4.31 evaluated at two different operating points. The frequency response of case A (in red) is associated with a relatively small slip ratio ($\kappa_A \approx 0.01$) which is far from the peak traction condition. The frequency response of case B (in blue) is associated with a slip ratio ($\kappa_B \approx 0.11$), which is closer to the peak traction condition. From the longitudinal traction curve on the right of Figure 5.2, it is clear that the slope $\xi(\kappa_A)$ is large compared to the slope $\xi(\kappa_B)$.

Several observations can be made from the example frequency response plots of Figure 5.2. First, both have a single zero at the origin, the same fixed first order pole (p_1) near 0.003 Hz and another fixed first order pole (p_2) near 4.0 Hz. The gradient filter has an overall bandpass characteristic frequency response. We also notice that the filter gain k is dependent on the slope ξ. The approximate gradient filter is given by Equation 5.2.

$$H(s,\xi) = k(\xi) \times s \times \left(\frac{p_1}{s+p_1}\right) \times \left(\frac{p_2}{s+p_2}\right) \tag{5.2}$$

The constant parameters p_1 and p_2 are considered to be application dependent tuning parameters. The term that is dependent on the slope ξ is also an application dependent function. For the example longitudinal traction problem previously studied [121, 122, 123], this dependence was determined using simulation results, and the functional form of the parameters was found to closely

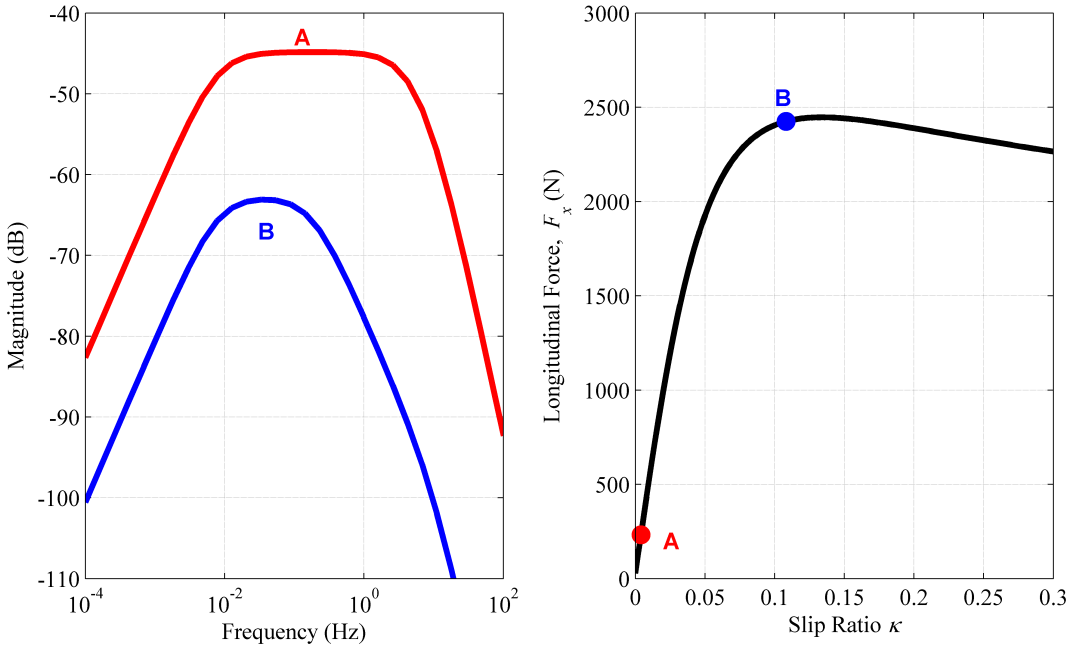

Figure 5.2: Gradient Filter frequency response at two characteristic operating points.

match Equation 5.3.

$$k(\xi) \quad = \quad k_0 \, arctan\,(k_1 \xi) \tag{5.3}$$

The plots in Figure 5.3 and 5.4 were generated with simulation data from Section 4.5.1, which was used to determine the coefficients of Equation 5.3. The most important characteristics of the filter approximation are the magnitude in the passband and the switching behavior of the phase. Using the coefficients in Table 5.1 it is possible to compare the exact filter solution to the approximate gradient filter using the simulation data from Section 4.5.1.

Table 5.1: 1-DOF Filter Approximation Parameters

Parameter	Value	Description
k_0	8.33×10^{-2}	Saturation Limit
k_1	1.25×10^{-4}	Scaling Parameter
p_1	$2\pi(0.003)$	Break Frequency (rad/s)
p_2	$2\pi(4)$	Break Frequency (rad/s)

The switching behavior of the phase can be completely captured as ξ changes sign while it passes through the peak of the traction curve, as seen in Figure 5.3(c). The magnitude plot, Figure 5.3(a)

is a bit more complex and while the approximation doesn't match perfectly, the important characteristics are captured, i.e. the slight change in the passband and relative difference in magnitude. While Figure 5.3(c) presents the functional dependence of k, Figure 5.3(a,b) present the magnitude and phase of the exact solution as well as the complete approximate gradient filter at a frequency in the passband ($f = 0.1\ Hz$). In reality the exact solution is a function of both ξ and the vehicle state x, where the approximate gradient filter has been simplified as only a function of ξ. This simplification manifests itself in the difference in magnitude between the Exact Solution and the Approximation presented in Figure 5.3(a,b) as well as Figure 5.5(a)

A plot of the magnitude and phase through time at the same frequency in the passband ($f = 0.01\ Hz$) is also informative when comparing the differences between the exact solution and the gradient filter approximation. This information is presented in Figure 5.5. From Figure 5.5(b) it is possible to conclude that the phase of the filter is approximated with a high degree of accuracy. While the magnitude, presented in Figure 5.5(a), is underestimated at high values of ξ and overestimated at small values of ξ.

More informative, however, is analyzing the complete frequency response function trough time using the 3D plots in Figures 5.7 and 5.8. Figures 5.7 and 5.8 were generated using the simulation data from Section 4.5.1 and should be considered a more complete comparison between the exact gradient filter solution and the gradient filter approximation.

5.2 Simulations with Approximate Gradient Filter

The exact same vehicle model for this simulation study, tire-ground interface model and simulation parameters used in Section 4.5 and 4.5.3 were used here. The only difference in the simulations presented in this Section from those of Section 4.5 and 4.5.3 is that the aforementioned approximation to the gradient filter(s) were used to calculate the gradient in real time, compared to the previous section in which the gradient filter was explicitly a function of the vehicle model which was assumed to be known. The control sample rate and sample rate for the approximate gradient filter remain unchanged at 200 Hz and 1000 Hz, respectively.

5.2.1 1-DOF Simulation: Uniform Surface

Figure 5.11(a) shows the position across time where it is evident that the response of the vehicle remains stable for the duration of the simulation. More interesting are the results in Figure 5.11(b-d), where torque, slip ratio and longitudinal acceleration are presented through time, respectively. The buildup to the optimal slip ratio on dry pavement can be seen for $t \in [0, 0.5]\ sec$. The anthropomimetic algorithm, using an approximate gradient filter, then tracks the optimal slip ratio as it decreases due to an increase in down force for $t \in [0.5, 5.0]\ sec$. The adaptive control algorithm when used with the approximate gradient filter displays the same, desirable, hunting behavior that the model based gradient filter displays.

5.2.2 1-DOF Simulation: Non-uniform Surface

The gradient filter approximation also proves to be successful when encountering a discrete surface change from dry pavement to wet pavement. It is evident from Figure 5.11(c) that the algorithm loses the peak of the tractive force at the pavement transition, but then recovers and tracks the peak tractive force on wet pavement by $t \approx 2.2\,sec$. The same hunting behavior is again visible in this simulation, albeit at a smaller magnitude. It is important to note that the same adaptive step size in Equation 4.47 was used for both simulations; continuous dry pavement, and the discrete change from dry to wet pavement.

5.3 Summary

In this chapter an approximation to the gradient filter was presented that was not a function of the vehicle model, but solely a function of the tire-ground interface properties. The filter approximation was used to perform the same simulations used in the previous chapter: one on uniform dry pavement, and one on a non-uniform surface that experienced a discrete change from dry pavement to wet pavement. Both simulations were performed using the same controller gains, and the controller was demonstrated to successfully track the peak tractive force in each simulation.

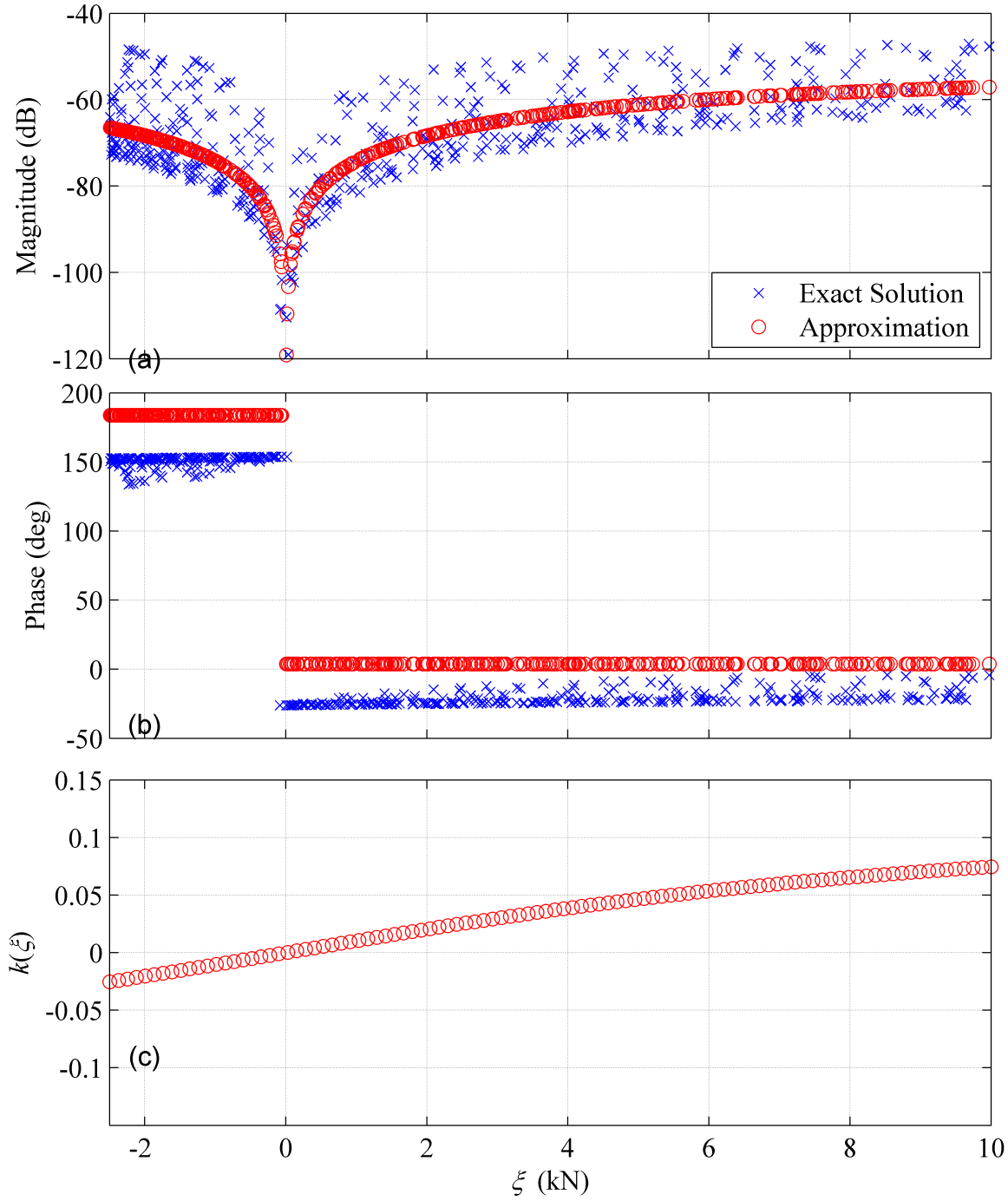

Figure 5.3: Simulation results at $f = 0.1\ Hz$, using data from a simulation on a flat uniform surface (Section 4.5.1), used to determine functional dependence of $k(\xi)$. Section 4.5.1 includes the simulation on a flat segment with uniform surface properties typical of dry pavement.

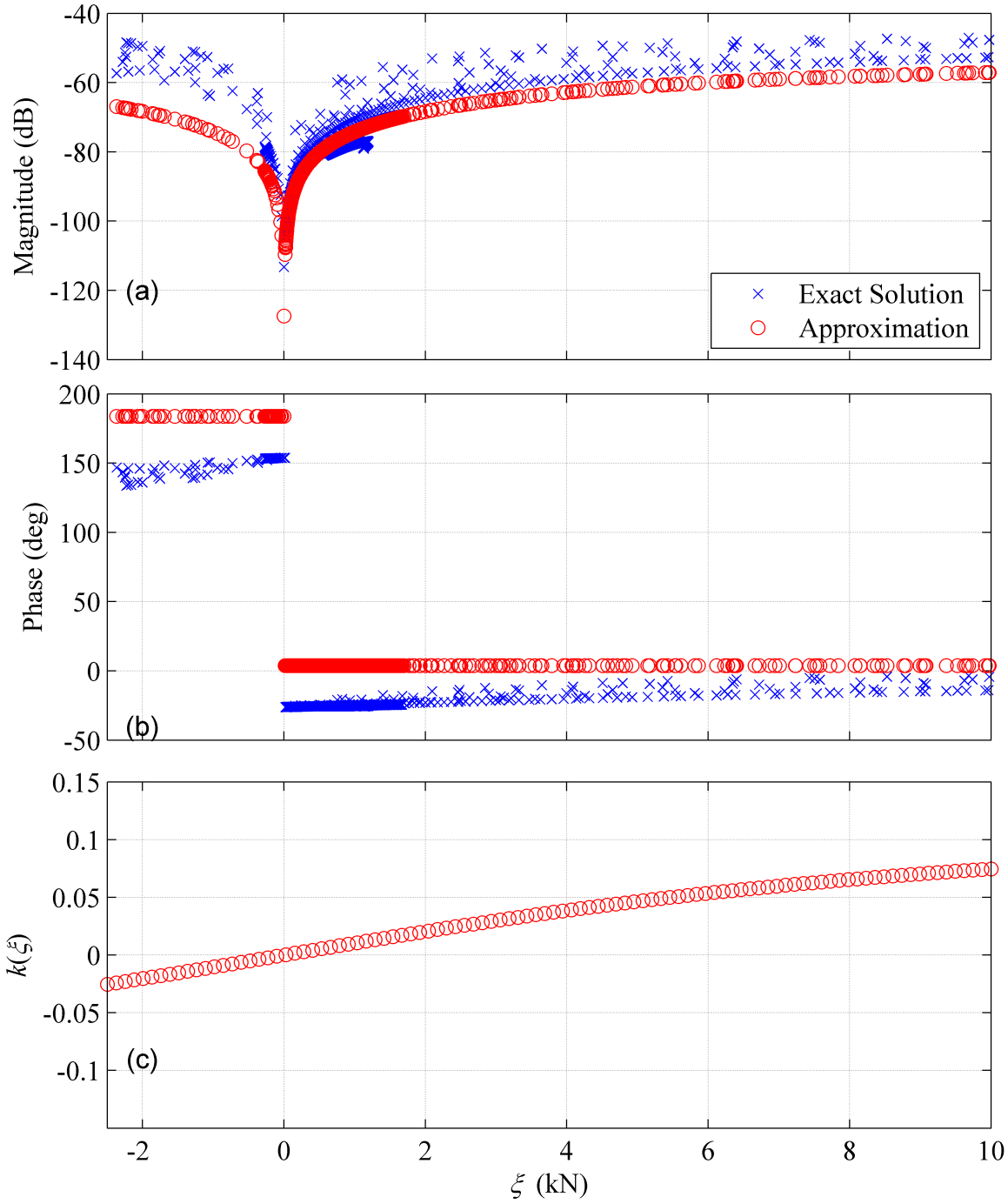

Figure 5.4: Simulation results at $f = 0.1\ Hz$, using data from a simulation on a flat non-uniform surface (Section 4.5.2), used to determine functional dependence of $k(\xi)$. Section 4.5.2 includes the simulation on a flat segment that transitions from surface properties typical of dry pavement to wet pavement at $x = 5\ m$

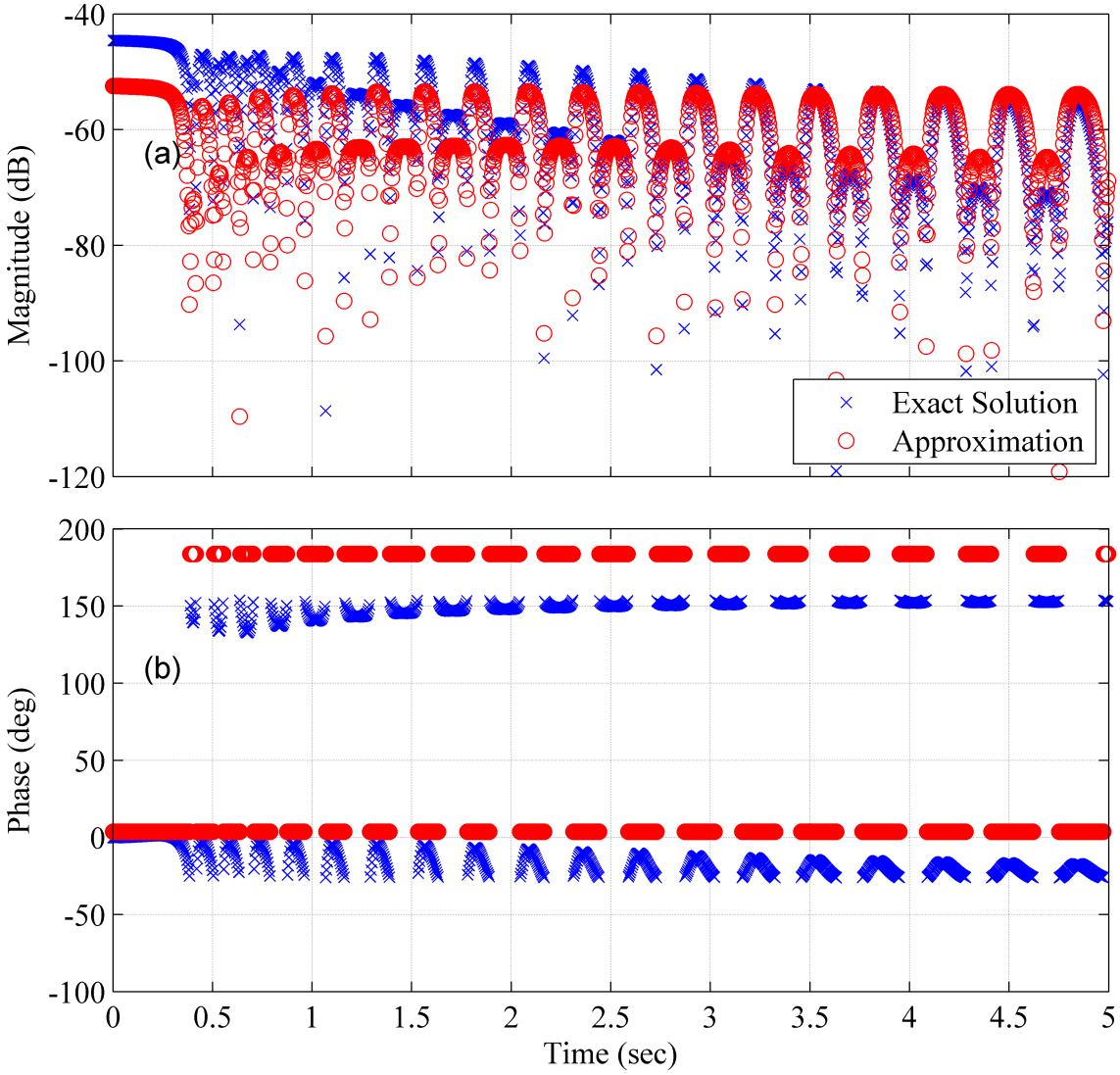

Figure 5.5: Comparison of gradient filter approximation and model based gradient filter through time at $f = 0.01\ Hz$, using data from a simulation on a flat uniform surface (Section 4.5.1).

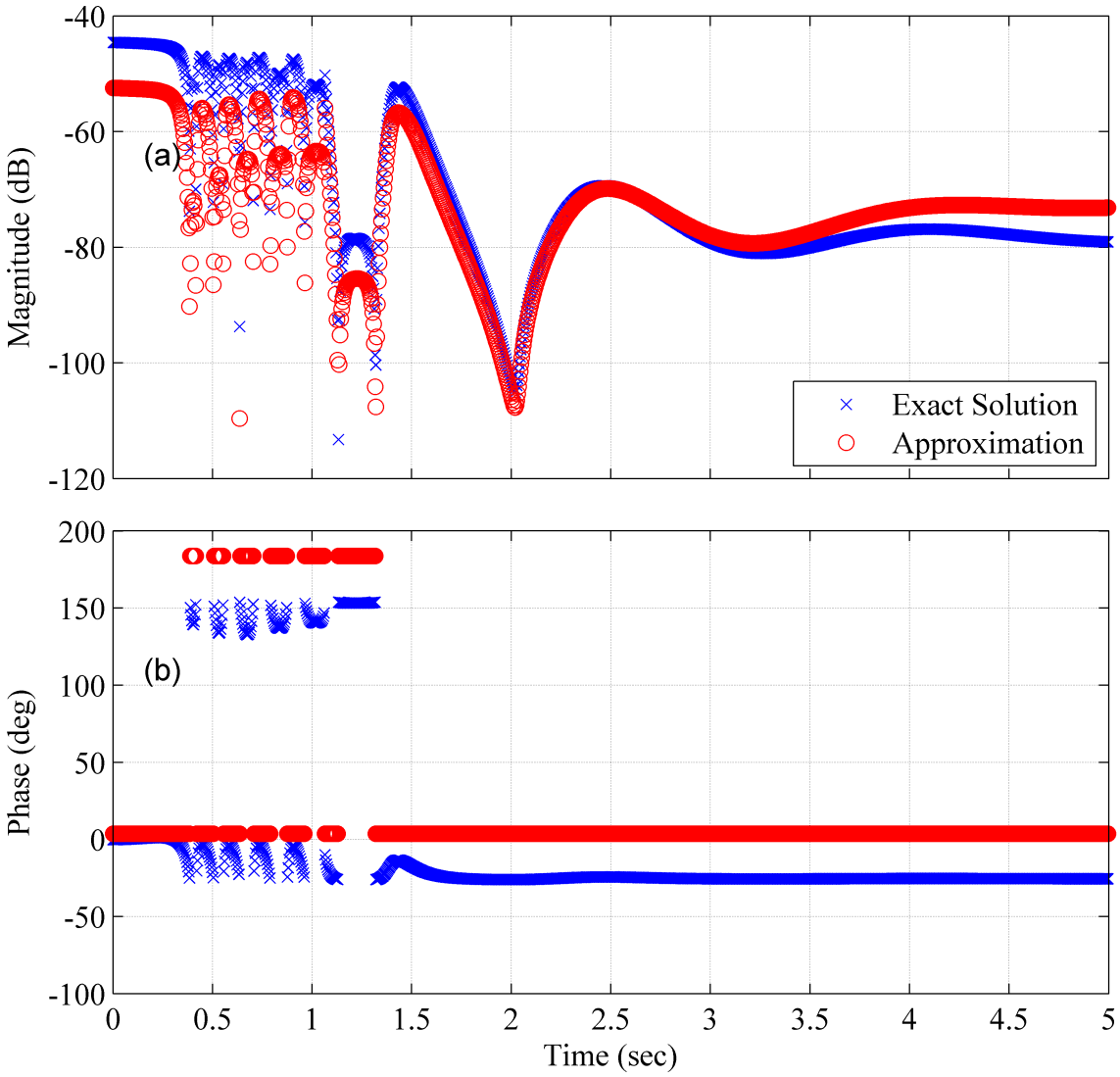

Figure 5.6: Comparison of gradient filter approximation and model based gradient filter through time at $f = 0.01\ Hz$, using data from a simulation on a flat non-uniform surface (Section 4.5.2).

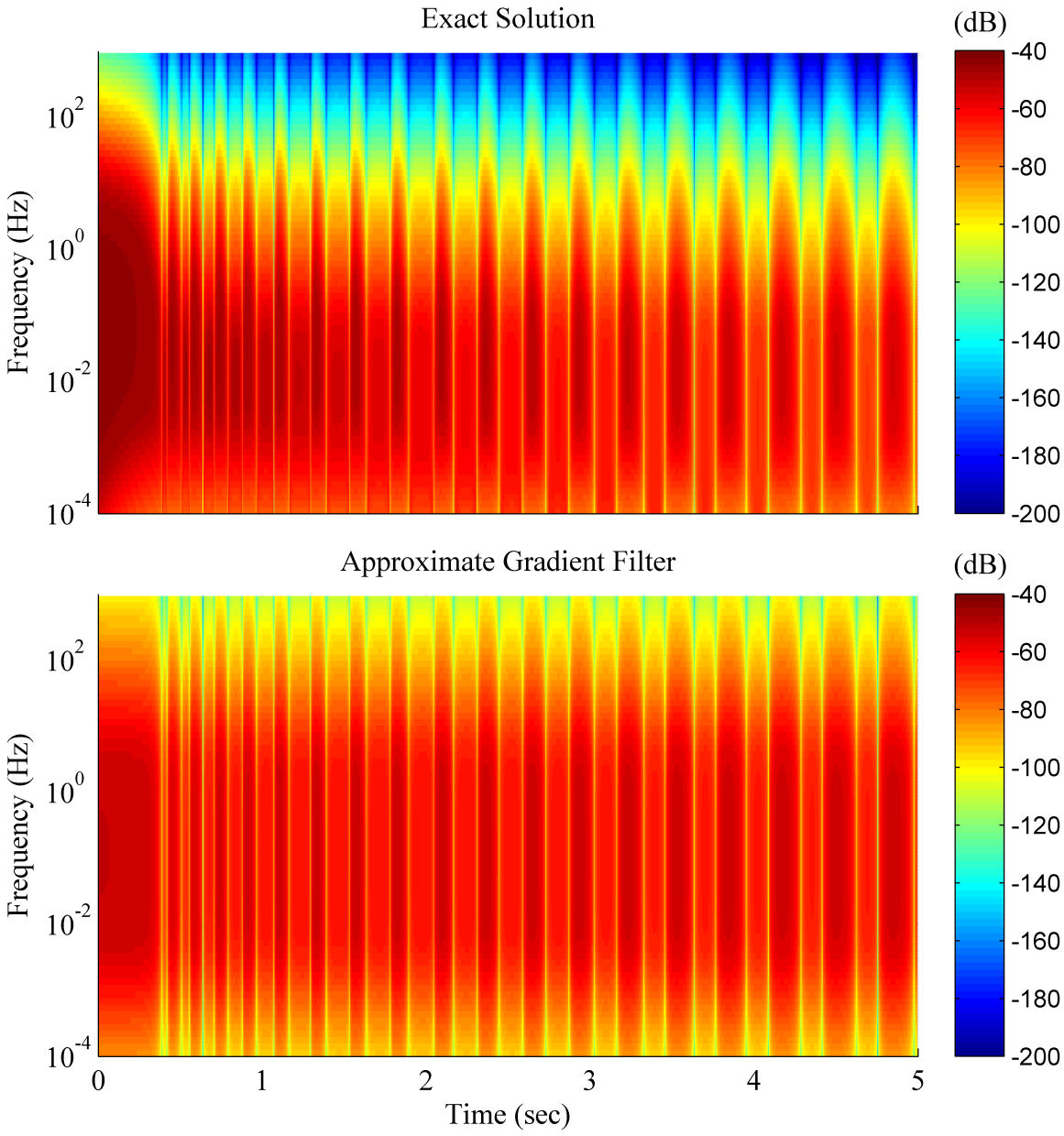

Figure 5.7: Comparison of frequency response (Magnitude) of exact gradient filter and the approximate gradient filter through time according to Equation 5.2 using data from a simulation on a flat uniform surface (Section 4.5.1).

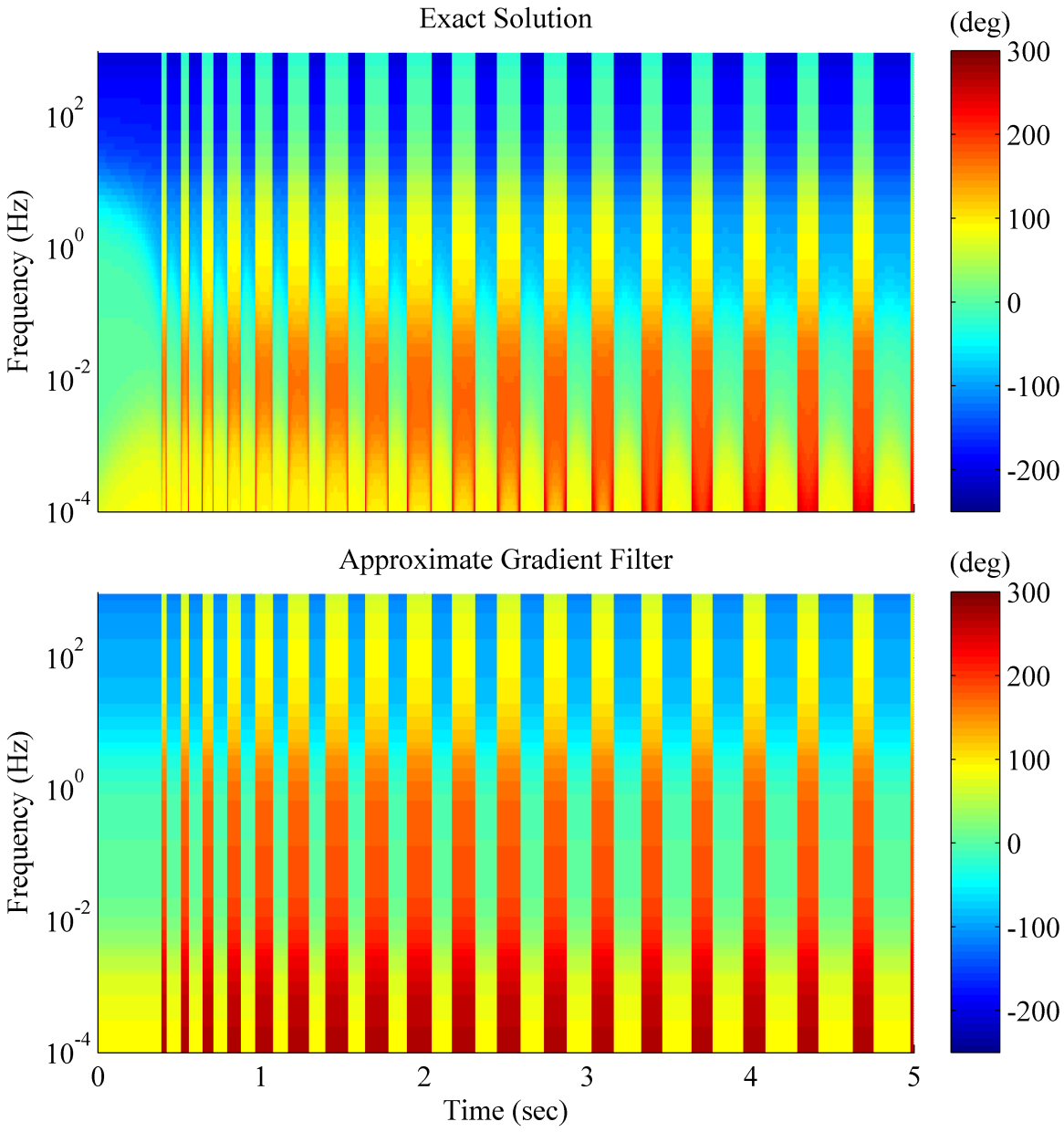

Figure 5.8: Comparison of frequency response (Phase) of exact gradient filter and the approximate gradient filter through time according to Equation 5.2 using data from a simulation on a flat uniform surface (Section 4.5.1).

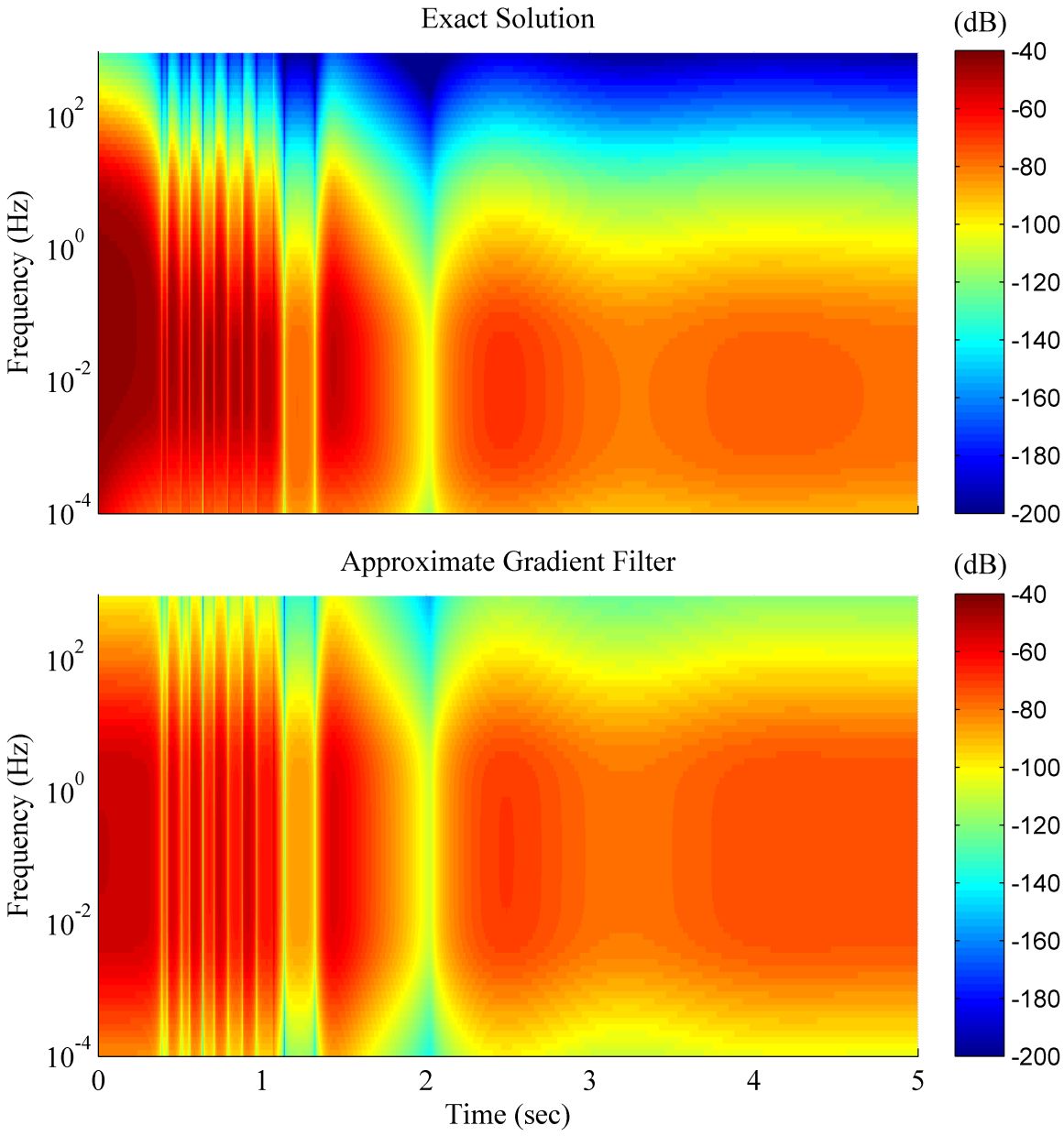

Figure 5.9: Comparison of frequency response (Magnitude) of exact gradient filter and the approximate gradient filter through time according to Equation 5.2 using data from a simulation on a flat non-uniform surface (Section 4.5.2).

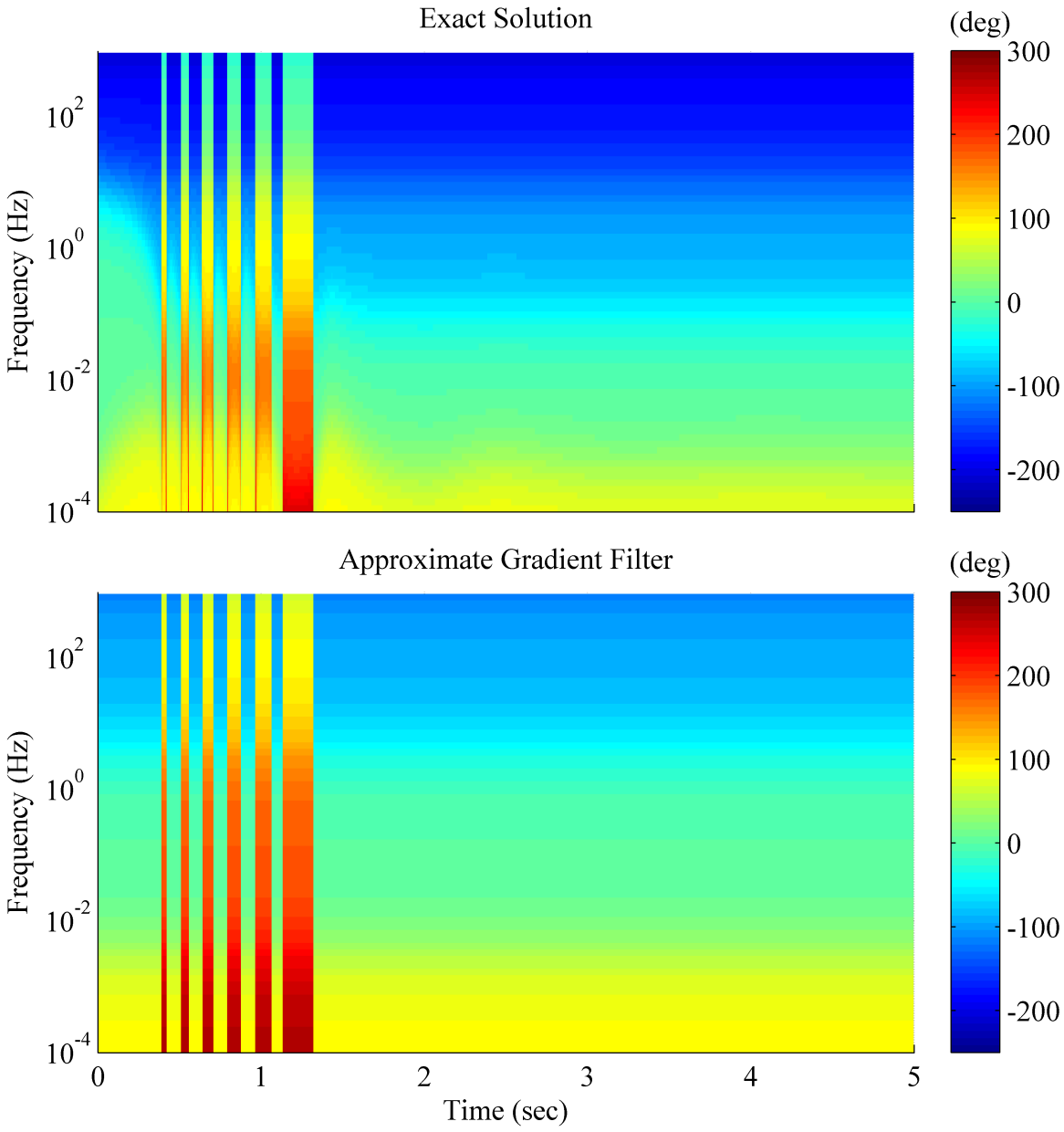

Figure 5.10: Comparison of frequency response (Phase) of exact gradient filter and the approximate gradient filter through time according to Equation 5.2 using data from a simulation on a flat non-uniform surface (Section 4.5.2).

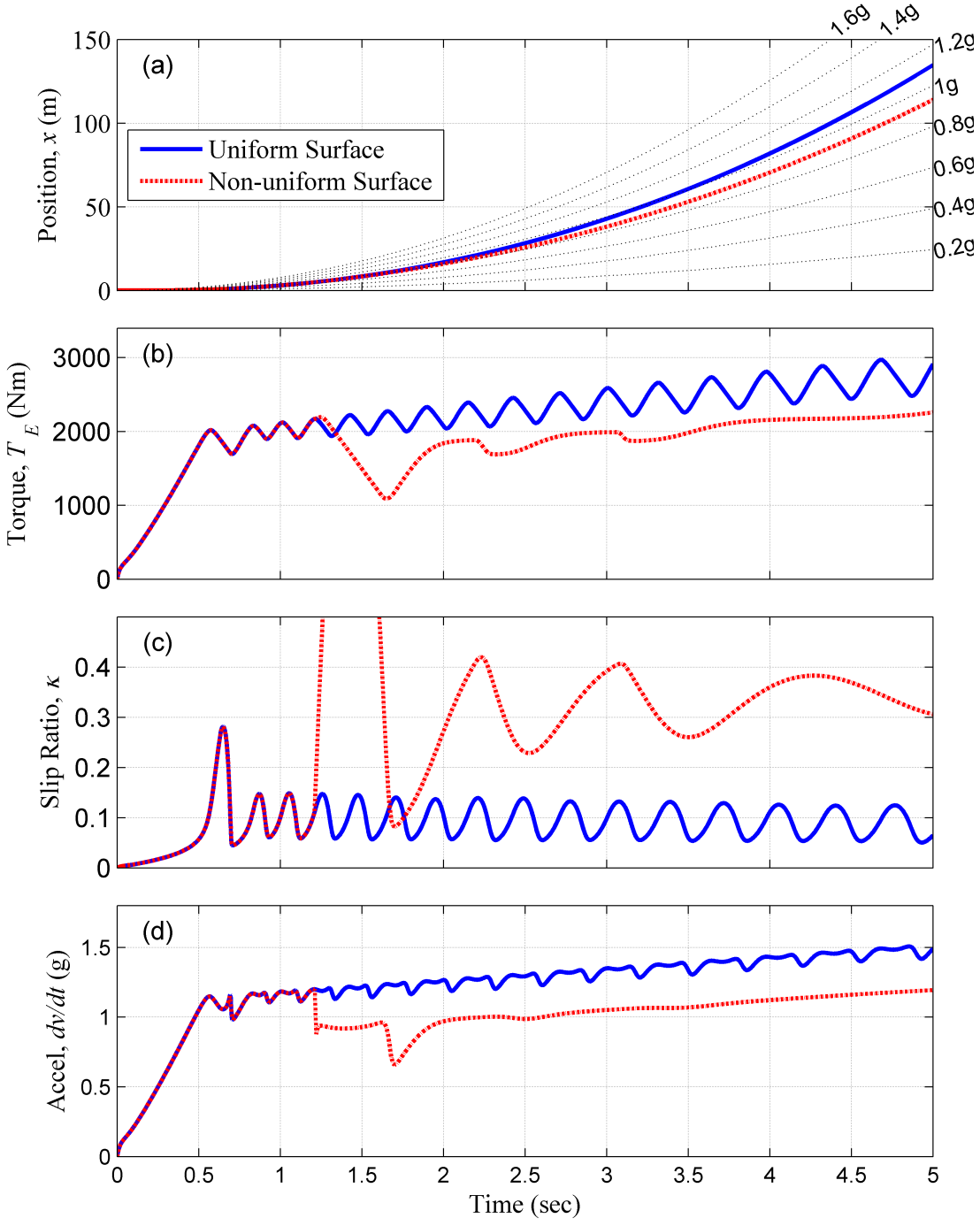

Figure 5.11: Control simulation results using approximation of gradient filter with explicit knowledge of the tire-ground interface for a uniform surface and non-uniform surface that changes from dry pavement to wet pavement at $x = 5\ m$.

Chapter 6

Estimation of Tire-Ground Interface

In order to estimate the pertinent properties of the tire-ground interface, the tractive force must be estimated and a subsequent friction model constructed. Recognizing the significant challenge associated with estimating a high fidelity model in real time, a method to estimate the traction curve using a simple constrained polynomial is developed in this chapter along with a method to estimate the tractive forces at the tire-ground interface. The method leverages a few key characteristics that all models display for the majority of all surfaces. The result is a method that only requires a model to estimate the tractive forces. Once the tractive forces are known, they can be used in a vehicle-independent and road-independent algorithm as a traction control solution.

6.1 Estimation of Instantaneous Traction Force

In order to implement the proposed adaptive traction control algorithm, knowledge of the instantaneous traction force(s) is required. Such knowledge can be obtained using a limited number of commercially available sensors such as Kistler RoaDyn wheel force transducers [62]. Although this and other similar tractive force sensing capability is possible, they are relatively expensive, making the use of such sensors highly impractical for the traction control application.

A more practical solution is to estimate the tractive forces of a vehicle using knowledge of the dynamic system (e.g. Equations 4.1 and 4.2) and key vehicle states measured with low-cost sensors. This kind of estimation approach is not new, and a number of public-domain solutions have been proposed specifically for estimating tractive forces [20, 3]. Although a variety of solutions exist, the preferred approach is similar to the method developed by Ray [20].

6.1.1 Kalman Filter (1-DOF Model)

In this approach, a Kalman filter is designed to estimate the tire forces as well as some relevant vehicle states in discrete time. Figure 6.1 is a block diagram representation of the preferred approach to instantaneous traction force estimation with a Kalman filter.

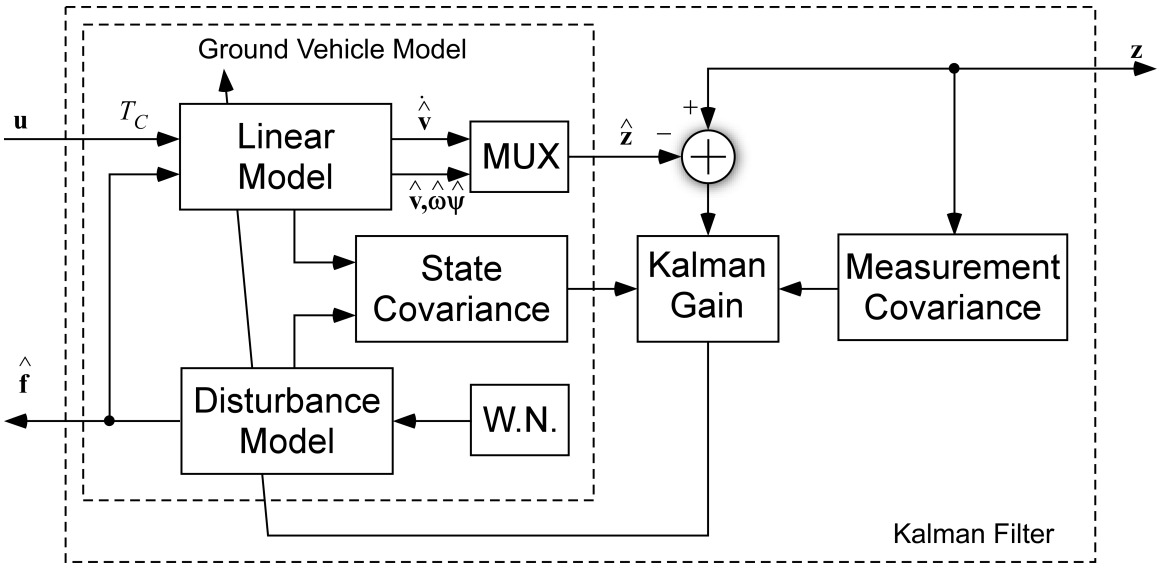

Figure 6.1: Kalman Filter with a Disturbance Model to estimate the traction force.

Notice from Figure 6.1 that the ground vehicle model parallels the assumed structure of the actual ground vehicle (compare to Figure 5.1) with a set of linear dynamics whose inputs are the commanded torque and the unmeasured tractive force. One key difference is that in the ground vehicle model, the estimated tractive force $\widehat{\mathbf{u}}' = \widehat{\mathbf{f}}$ is represented as the output of a linear disturbance model that is driven by a white noise process (W.N.). The disturbance model is preferentially chosen to have the structure proposed by Johnson [24]. This waveform generation model has been used in a number of applications to model the unmeasurable disturbances acting on a dynamic system [20, 44, 23]. This disturbance model is defined by the continuous-time equations 6.1 and 6.3.

$$\dot{\mathbf{q}} = \begin{bmatrix} \mathbf{0} & \mathbf{I} \\ \mathbf{0} & \mathbf{0} \end{bmatrix} \mathbf{q} + \mathbf{n}_q \tag{6.1}$$

$$\dot{\mathbf{q}} = \mathbf{\Lambda}_c \mathbf{q} + \mathbf{n}_q \tag{6.2}$$

$$\widehat{\mathbf{u}}' = \mathbf{\Gamma}\mathbf{q} \tag{6.3}$$

The quantity $\widehat{\mathbf{u}}'$ is the tire force to be estimated, $\mathbf{\Gamma} = \begin{bmatrix} 1 & \mathbf{0} \end{bmatrix}$ and $\mathbf{n}_q$ is assumed to be Gaussian white noise. A block diagram of the Kalman filter used to estimate $\widehat{\mathbf{u}}' = \widehat{F}_x$ is shown in Figure 6.1. The non-linear differential Equations that govern the state estimator can then be expressed, in continuous-time, according to Equations 6.8 and 6.9.

$$\dot{\boldsymbol{\rho}} = \begin{bmatrix} \mathbf{A}_c & \mathbf{F}_c\boldsymbol{\Gamma} \\ \mathbf{0} & \boldsymbol{\Lambda}_c \end{bmatrix} \boldsymbol{\rho} + \begin{bmatrix} \mathbf{B}_c \\ \mathbf{0} \end{bmatrix} \mathbf{u} + \mathbf{n}_w \tag{6.4}$$

$$= \overline{\mathbf{A}}_c \boldsymbol{\rho} + \overline{\mathbf{B}}_c \mathbf{u} + \mathbf{n}_w \tag{6.5}$$

$$\mathbf{v} = \begin{bmatrix} \mathbf{C}_c & \mathbf{G}_c\boldsymbol{\Gamma} \end{bmatrix} \boldsymbol{\rho} + \overline{\mathbf{D}}_c \mathbf{u} + \mathbf{n}_v \tag{6.6}$$

$$= \overline{\mathbf{C}}_c \boldsymbol{\rho} + \overline{\mathbf{D}}_c \mathbf{u} + \mathbf{n}_v \tag{6.7}$$

The state vector is defined as $\boldsymbol{\rho} = \begin{bmatrix} \mathbf{x} & \mathbf{q} \end{bmatrix}^T$, where $\mathbf{n}_w \in N(0, \sigma_w)$ and where $\mathbf{n}_v \in N(0, \sigma_v)$ or zero mean Gaussian noise with variances σ_w and σ_v. Assuming an acceptable method is chosen to discretize the system of Equations 6.5 and 6.7 it is possible to arrive at the system defined as Equations 6.8 and 6.9. In this work we use the Euler approximation to discretize the Kalman filter, according to Equations outlined in Appendix D.1.

$$\boldsymbol{\rho}_{k+1} = \overline{\mathbf{A}} \boldsymbol{\rho}_k + \overline{\mathbf{B}} \mathbf{u}_k + \mathbf{n}_w \tag{6.8}$$

$$\mathbf{v}_k = \overline{\mathbf{C}} \boldsymbol{\rho}_k + \overline{\mathbf{D}} \mathbf{u}_k + \mathbf{n}_v \tag{6.9}$$

The Kalman filter can then be implemented in discrete time in three steps [45]; the prediction step, updating of the Kalman gain, and the correction step. The prediction step begins by calculating state and covariance estimates according to Equations 6.10 and 6.11. The matrix $\boldsymbol{\Sigma}_w$ is an estimate of the covariance of the noise $\mathbf{n}_w$.

$$\overline{\boldsymbol{\rho}}_{k|k-1} = \overline{\mathbf{A}} \overline{\boldsymbol{\rho}}_{k-1|k-1} + \overline{\mathbf{B}} \mathbf{u}_{k-1} \tag{6.10}$$

$$\boldsymbol{\Sigma}_{\overline{\boldsymbol{\rho}}_{k|k-1}} = \overline{\mathbf{A}} \boldsymbol{\Sigma}_{\overline{\boldsymbol{\rho}}_{k-1|k-1}} \overline{\mathbf{A}}^T + \boldsymbol{\Sigma}_w \tag{6.11}$$

The Kalman Gain can then be computed based on the covariance prediction according to Equation 6.12.

$$\mathbf{K}_k = \boldsymbol{\Sigma}_{\overline{\boldsymbol{\rho}}_{k|k-1}} \overline{\mathbf{C}}^T \left(\overline{\mathbf{C}} \boldsymbol{\Sigma}_{\overline{\boldsymbol{\rho}}_{k|k-1}} \overline{\mathbf{C}}^T + \boldsymbol{\Sigma}_v \right)^{-1} \tag{6.12}$$

Once the Kalman gain has been calculated and the measurements $\mathbf{z}_k$ at the current time step have been taken it is possible to correct the state and covariance estimates according to Equations 6.13 and 6.14. The matrix $\boldsymbol{\Sigma}_v$ is the covariance of the measurement noise $\mathbf{n}_z = N(0, \sigma_v)$.

$$\overline{\boldsymbol{\rho}}_{k|k} = \overline{\boldsymbol{\rho}}_{k|k-1} + \mathbf{K}_k \left(\mathbf{z}_k - \overline{\mathbf{C}} \overline{\boldsymbol{\rho}}_{k|k-1} - \overline{\mathbf{D}} \mathbf{u}_k \right) \tag{6.13}$$

$$\boldsymbol{\Sigma}_{\overline{\boldsymbol{\rho}}_{k|k}} = \left(\mathbf{I} - \mathbf{K}_k \overline{\mathbf{C}} \right) \boldsymbol{\Sigma}_{\overline{\boldsymbol{\rho}}_{k|k-1}} \tag{6.14}$$

In the case of the 1-DOF model from Section 3.2 the measurement vector is defined as $\mathbf{z}_k = \begin{bmatrix} \dot{v} & \omega \end{bmatrix}^T$, where the state vector of the Kalman filter is exactly the same as the state vector of the 1-DOF model of Equation 4.1 augmented with the state vector of the disturbance, Equation 6.1. The tuning parameters of the Kalman Filter algorithm are the estimates of the covariances Σ_w and Σ_v. Using the simulation data from Section 4.5.1, where explicit knowledge of the gradient filter and tire-ground interface are assumed, it is possible to evaluate the performance of this estimation algorithm. The result of this comparison is shown in Figure 6.2, where the error in the tractive force F_x for the simulation of Section 4.5.1 is plotted. While this plot may be overly optimistic in the sense that we assume exact knowledge of the model, it is presented as validation of using the random walk of Equation 6.1 to estimate the tractive force for the 1-DOF model of Equations 3.15 and 3.16.

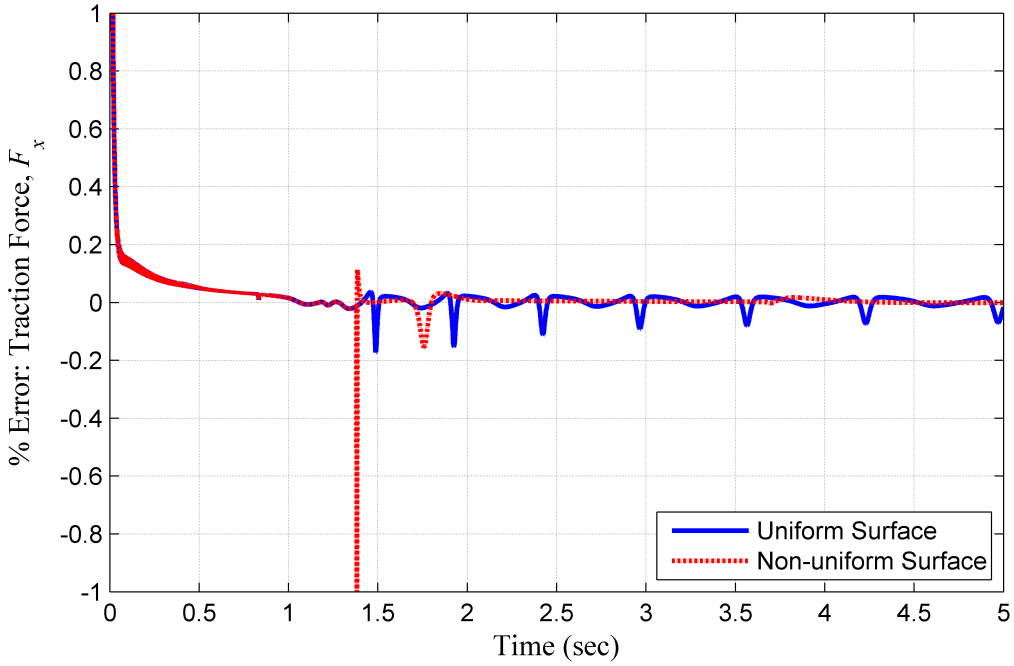

Figure 6.2: Error in $\widehat{\mathbf{u}}'$ between the Kalman filter and the true values using data from simulations on flat uniform and non-uniform surfaces (Sections 4.5.1 and 4.5.2)

The Kalman filter also performs well when estimating the tractive force F_x for the simulation in Section 4.5.2, where a discrete change from dry pavement to wet pavement occurs. The Estimation error through time in the simulation is shown in Figure 6.2, where the estimation error for F_x explodes at the point of the transition but recovers quickly and asymptotically approaches zero. The fact that the estimation error is so high at the transition, albeit briefly, is cause for concern. It is also the motivation for the subsequent use of a recursive least squares (RLS) algorithm with selective memory to estimate the traction force model, as will be shown below.

6.1.2 Kalman Filter (3-DOF Model)

In the case of the bicycle model (3-DOF) there are 4 forces to estimate. Therefore the disturbance model takes the form of Equation 6.16-6.18:

$$\mathbf{\Lambda} = \begin{bmatrix} \mathbf{0} & \mathbf{I} \\ \mathbf{0} & \mathbf{0} \end{bmatrix} \tag{6.15}$$

$$\dot{\mathbf{q}} = \begin{bmatrix} \mathbf{\Lambda} & \mathbf{0} & \mathbf{0} & \mathbf{0} \\ \mathbf{0} & \mathbf{\Lambda} & \mathbf{0} & \mathbf{0} \\ \mathbf{0} & \mathbf{0} & \mathbf{\Lambda} & \mathbf{0} \\ \mathbf{0} & \mathbf{0} & \mathbf{0} & \mathbf{\Lambda} \end{bmatrix} \mathbf{q} + \mathbf{n}_q \tag{6.16}$$

$$\dot{\mathbf{q}} = \mathbf{\Lambda}_c \mathbf{q} + \mathbf{n}_q \tag{6.17}$$

$$\widehat{\mathbf{u}}' = \mathbf{\Gamma q} \tag{6.18}$$

If we choose to use a third order random walk, then the quantities q_1, q_4, q_7 and q_{10} are the tire forces to be estimated. Therefore, $\mathbf{\Gamma}$ can be defined according to Equation 6.19, where $\mathbf{n}_q$ is assumed to be Gaussian white noise. The non-linear differential Equations that govern the state estimator can then be expressed as in Section 6.1.1, in continuous-time, according to Equations 6.8 and 6.9.

$$\mathbf{\Gamma} = \begin{bmatrix} 1 & 0 & 0 & 0 & 0 & 0 & 0 & 0 & 0 & 0 & 0 & 0 \\ 0 & 0 & 0 & 1 & 0 & 0 & 0 & 0 & 0 & 0 & 0 & 0 \\ 0 & 0 & 0 & 0 & 0 & 0 & 1 & 0 & 0 & 0 & 0 & 0 \\ 0 & 0 & 0 & 0 & 0 & 0 & 0 & 0 & 0 & 1 & 0 & 0 \end{bmatrix} \tag{6.19}$$

In the case of the 3-DOF model the measurement vector is defined as $\mathbf{z} = [\ v_x \quad v_y \quad \Psi \quad \omega_f \quad \omega_r\ ]$. The results of the Kalman filter when applied to the 3-DOF model are plotted in Figure 6.3, where it demonstrates the ability to successfully estimate all four forces for the four driving scenarios of Section 4.5.3.

6.2 Polynomial Approximation of Traction Force Curve

Many online and offline methods have been proposed for estimating high-fidelity traction force models such as the Pacejka Magic Tire formula. These methods work reasonably well for quasi-steady operating conditions and for uniform tire-ground interface properties. Unfortunately, these methods have great difficulty converging in real-time to a set of model parameters when the tire-ground interface is time-varying, yet this is exactly what is needed for high-performance traction control. The tire-ground interface is only uniform in very rare cases.

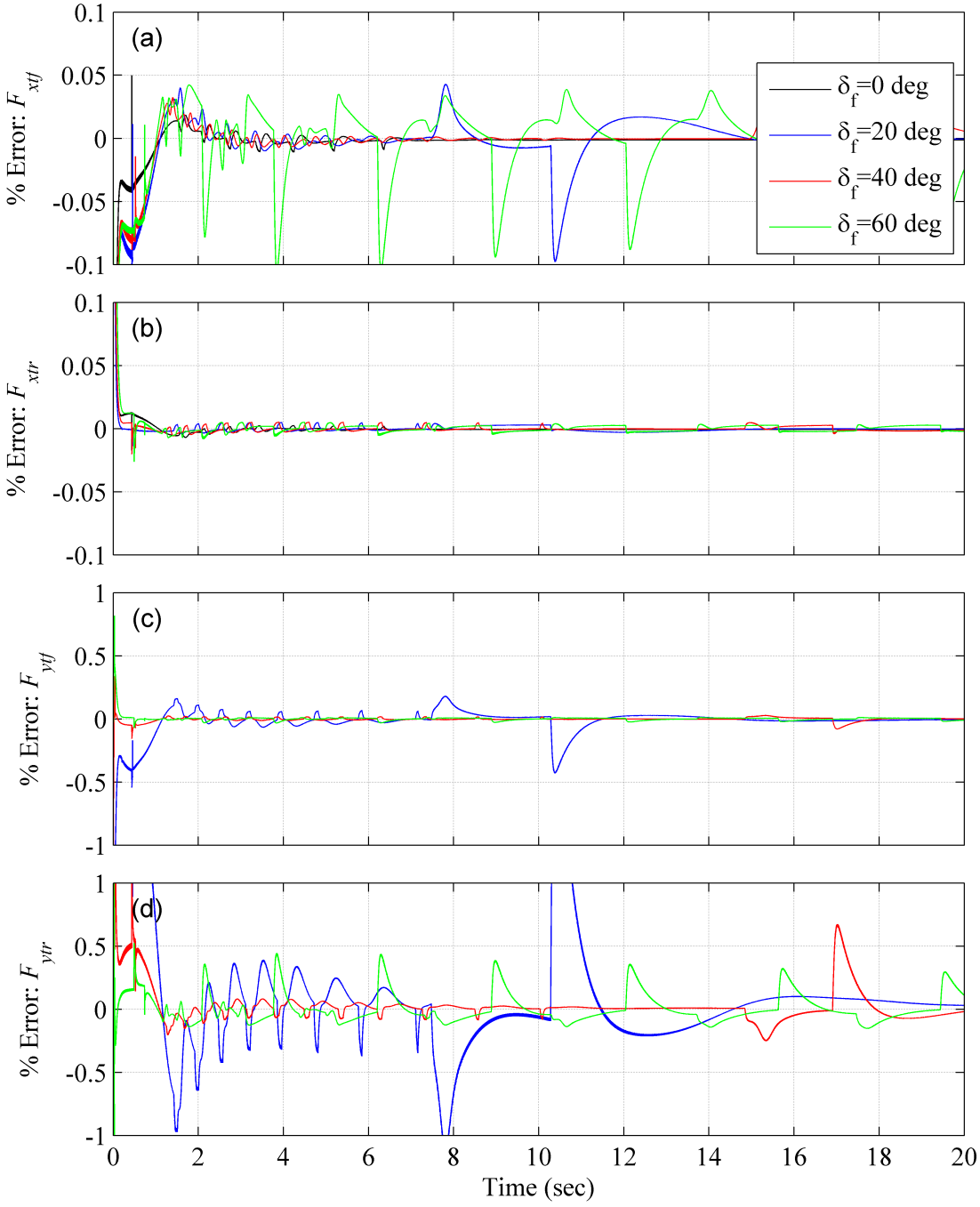

Figure 6.3: Error in $\widehat{\mathbf{u}}'$ between the Kalman filter and the true values using data from a simulation which includes four driving scenarios, each at a fixed steering angle δ_f on a flat uniform surface (Section 4.5.3).

The proposed solution does not attempt to generate a complete high-fidelity traction force model. Instead, a relatively simple but carefully designed model is identified in order to enable accurate real-time estimation of a limited set of characteristic features of the traction force curve that are pertinent to the proposed traction control strategy. Figure 6.4 is an illustration of a typical traction curve which is used to highlight the characteristic features.

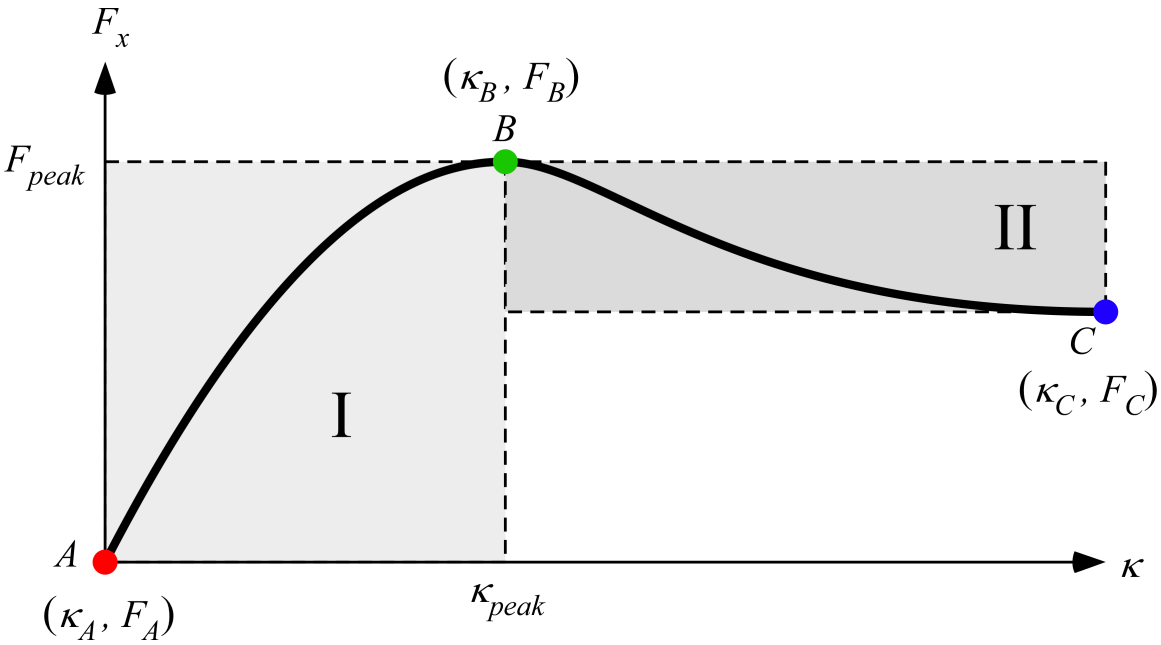

Figure 6.4: Characteristic features of the longitudinal traction curve.

The traction curve $F_x(\kappa)$ is contained within two adjoined rectangles, defined as Region I and Region II in Figure 6.4. Within Region I, the traction curve monotonically increases from the lower left corner (A) to the upper right corner (B), and is always concave-down in this interval. Within Region II, the traction curve monotonically decreases from the upper left corner (B) to the lower right corner (C). The portion of the curve in Region II nearest to point B is initially concave down; however, depending on the particular tire-ground interface condition, there may be an interior inflection point as indicated in Figure 6.4. Point A is usually at the origin (0,0), and point C typically represents the asymptotic burnout force. Point B is the most interesting and important part of the curve as it represents the peak traction force $(F_B = F_{peak})$ and the associated slip ratio $(\kappa_B = \kappa_{peak})$. The location of point B is time-varying since the peak force and the associated slip ratio vary as a function of the tire-ground interface condition and the normal force.

With regard to the proposed traction control elements previously discussed, we really only need to know the location of point B. Points A and C are interesting but not very useful for traction control purposes. From Equation 5.1, we know that the proposed gradient ascent algorithm uses the local slope ξ of the traction curve to push the resulting slip ratio toward the peak traction condition at κ_{peak}. With this in mind, it is clear that the existence of an inflection point in Region II is actually a significant drawback for the traction control objective because it serves to slow down

the convergence in the interval where the convergence should be increased.

6.2.1 Polynomial Approximation (1-DOF)

Given these characteristic features, the associated importance, and the implications for utility, we propose to use a strictly concave-down approximation function to fit only local portions of the traction curve using traction force data estimated from the Kalman filter. This approximation function is a concave-down parabola given by Equation 6.20; however, other similar functions may be substituted.

$$\widehat{F}_x(\kappa;\mathbf{a}) = a_1\kappa^2 + a_2\kappa + a_3 = \phi^T\mathbf{a} \tag{6.20}$$

$$\frac{\partial \widehat{F}_x}{\partial \kappa} = 2a_1\kappa + a_2 \tag{6.21}$$

Given these characteristic features, the associated importance, and the implications for utility, we propose to use a strictly concave-down approximation function to fit only local portions of the traction curve using traction force data estimated from the Kalman filter. This approximation function is a concave-down parabola given by Equation 6.20; however, other similar functions may be substituted. The slopes ξ obtained by substituting Equation 6.20 into Equation 5.1, while not precisely in agreement with the global behavior of the traction curve, will actually be more useful since they have the symmetric property that the slopes are larger further away from the estimated peak. Using traction force estimates from the Kalman filter $(\widehat{F}_{x,k})$ and current slip ratio (κ), the polynomial coefficients are estimated using the algorithm of Equation 6.24 that leverages the Fisher information to selectively update the coefficients at each iteration.

6.2.2 Polynomial Approximation (3-DOF)

When extending the gradient filter to a planar vehicle model (lateral and longitudinal dynamics) it is necessary to redefine the local polynomial approximation of the traction curve according to Equations 6.22 and 6.23.

$$\widehat{F}_xt(\kappa,\alpha;\mathbf{a}) = a_1\kappa^2 + a_2\alpha^2 + a_3\kappa\alpha + a_4\kappa + a_5\alpha + a_6 = \phi^T\mathbf{a} \tag{6.22}$$

$$\widehat{F}_yt(\kappa,\alpha;\mathbf{b}) = b_1\kappa^2 + b_2\alpha^2 + b_3\kappa\alpha + b_4\kappa + b_5\alpha + b_6 = \phi^T\mathbf{b} \tag{6.23}$$

Figure 6.5 shows the results of a traditional least squares performed on a specific region of the combined mode traction curves.

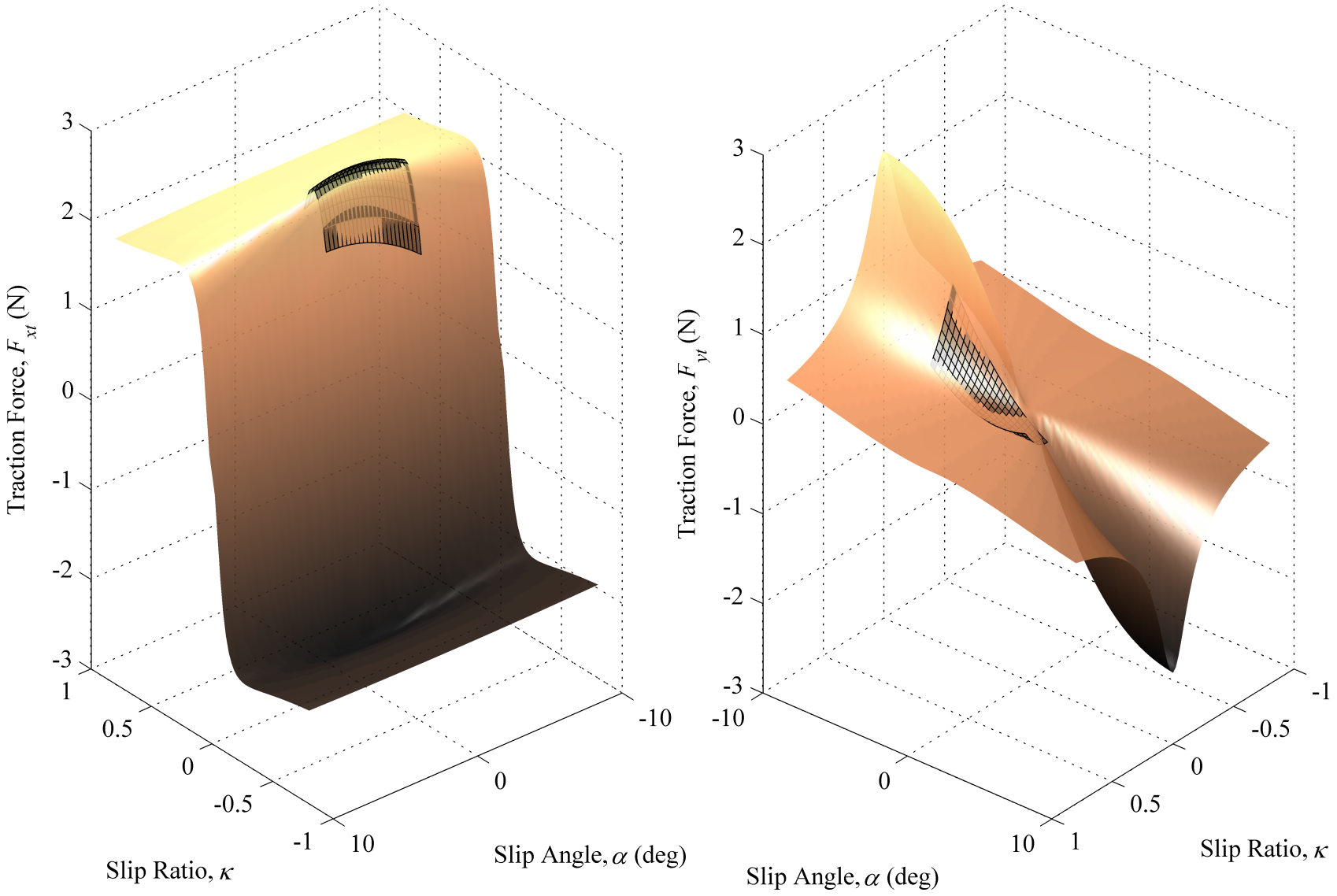

Figure 6.5: Illustration of local function estimation for 3-DOF combined (longitudinal and lateral) traction: (a) longitudinal force F_{xt}, and (b) lateral force F_{yt}.

6.2.3 Fisher Information Solution

One alternative to using a least squares fit with all the available data or a recursive least squares estimate, is to use the Fisher Information Matrix to select the data that is used to update parameter estimates of $\mathbf{a_i}$ just as Hill et. al. [46] did to learn the un-modelled dynamics of a generic non-linear system. The unknown parameters are arranged in a vector, where the parameter estimates are represented as $\widehat{\mathbf{a}} = [\widehat{a}_0, \widehat{a}_1, \cdots, \widehat{a}_n]$. The recursive least squares algorithm can then be represented as Equations 6.24 and 6.25 [47, 48]. While the aforementioned polynomial approximation is defined as being concave down there are no explicit constraints, with respect to concavity, imposed on the algorithm of Equations 6.24 and 6.25.

$$\widehat{\mathbf{a}}(t) = \widehat{\mathbf{a}}(t-1) + \Delta(t)\frac{\mathbf{P}(t-1)\phi(t-1)\mathbf{e}(t)}{r(t) + \phi(t-1)^T\mathbf{P}(t-1)\phi(t-1)} \tag{6.24}$$

$$\mathbf{P}(t) = \mathbf{P}(t-1) - \Delta(t)\frac{\mathbf{P}(t-1)\phi(t-1)\phi(t-1)^T\mathbf{P}(t-1)}{r(t) + \phi(t-1)^T\mathbf{P}(t-1)\phi(t-1)} \tag{6.25}$$

$$\phi(t) = \left[1,\ \kappa(t),\ \kappa(t)^2\right] \tag{6.26}$$

$$\mathbf{e}(t) = \widehat{\mathbf{u}}'(t) - \phi(t-1)^T\widehat{\mathbf{a}}(t-1) \tag{6.27}$$

$$r(t) = max\left\{\sigma r(t-1) + (1-\sigma)e(t)^2, r_0\right\} \tag{6.28}$$

$$\kappa(t-1) = \kappa_{t-1} \tag{6.29}$$

If $\Delta(t) = 1$, then the data is selected and inserted into the memory. If $\Delta(t) = 0$, then the data is discarded. The time constant for the variance estimate of Equation 6.28 is defined as Equation 6.30, where $\infty > M_0 > 1$ is the memory length.

$$\sigma = 1 - \frac{1}{M_0} \tag{6.30}$$

Following the work of Hill et. al. [46], the Fisher Information Matrix ($\mathbf{F}_I(t)$) can be used to select informative data. The Fisher Information Matrix in recursive form can be represented as Equation 6.31 [46].

$$\mathbf{F}_I(t) = \mathbf{F}_I(t-1) + \frac{\Delta(t)}{r(t)}\phi(t-1)\phi(t-1)^T \tag{6.31}$$

$$\mathbf{F}_I(t) = \mathbf{P}(t)^{-1} \tag{6.32}$$

The ratio between current and past information can be represented by Equations 6.33-6.35, where n is equal to the number of parameters to be estimated, or the length of $\phi(t)$.

$$
\begin{aligned}
c(t) &= \frac{1}{n} Trace\left\{\mathbf{F}_I(t)\mathbf{F}(t-1)^{-1}\right\} && (6.33)\\
&= \frac{1}{n} Trace\left\{\mathbf{I} + \frac{\Delta(t)}{r(t)}\phi(t-1)\phi(t-1)^T\mathbf{F}(t-1)^{-1}\right\} && (6.34)\\
&= 1 + \frac{\Delta(t)}{nr(t)}\phi(t-1)\mathbf{P}(t-1)\phi(t-1)^T && (6.35)
\end{aligned}
$$

If $c(t) = 1$ then the new data is no more accurate or reliable than the old and the parameters should not be updated. If $c(t) \geq 1 + \varepsilon_0/n$, which can be equivalently represented as Equation 6.36, then there is more accurate or reliable information available and the parameter estimates should be updated.

$$
\frac{\phi(t-1)\mathbf{P}(t-1)\phi(t-1)^T}{r(t)} \geq \varepsilon_0 \geq 0 \tag{6.36}
$$

As Hill et. al. [46] point out, the parameters should also be updated if the estimated variance is greater than the variance at the previous times such that Equation 6.37 is satisfied.

$$
r(t) \geq max_{0<i\leq t}\left\{r(t-i)\right\} \tag{6.37}
$$

If either Equation 6.36 or 6.37 is satisfied then $\Delta(t) = 1$ in Equations 6.24, 6.25, 6.31 and 6.35. If we consider the true vector that we are trying to estimate ($\mathbf{a}^*$) to be slowly time varying, there is the potential for the aforementioned method to break down. The algorithm itself is not adaptive in the long term as the parameters $\widehat{\mathbf{a}}$ eventually converge. To overcome this, the covariance $\mathbf{P}(t)$ can be periodically re-initialized. The challenge is to decide when this re-initialization occurs. One possible condition is when the error $\mathbf{e}(t)$ between the predicted force from the Kalman Filter $\widehat{\mathbf{u}}'(t)$ and the estimated force $\phi(t-1)^T\widehat{\mathbf{a}}(t-1)$, calculated according to Equation 6.27, exceeds a predetermined threshold. This is analogous to the control system learning a model, using that model in a control law, then at an arbitrary point in time decides that it no longer has a good understanding of the model and attempts to re-learn it. By re-initializing the covariance $\mathbf{P}(t)$ it is possible for the parameter estimates to drift, which in the case where a slowly time varying curve is being tracked, is desirable.

6.2.4 Cramer Rao Lower Bound

An estimator is said to be efficient if its covariance is equal to the Cramer Rao lower bound, or equivalently, the inverse of the Fisher Information matrix [47]. The covariance $\mathbf{P}$ of any unbiased estimator, provided certain regularity constraints are in place, can be expressed as Equation 6.38, where $\mathbf{F}_I$ is the Fisher Information Matrix.

$$\mathbf{P} \geq \mathbf{F}_I^{-1} \tag{6.38}$$

Provided an estimator is the maximum likelihood estimator than the covariance will achieve the Cramer-Rao lower bound and is said to be an efficient unbiased estimator. If $\mathbf{f}$ is distributed normally with a mean $\phi^T\mathbf{a}$ and variance $\sigma^2\mathbf{I}$ ($\mathbf{f} \sim N(\phi^T\mathbf{a}, \sigma^2\mathbf{I})$), then the least squares solution will achieve the Cramer-Rao lower bound and is considered a maximum likelihood estimator [47]. As we continue into the next section we assume that these normality conditions are satisfied.

6.2.5 Results: Polynomial Approximation (1-DOF)

Figure 6.6 shows the results of a verification simulation to demonstrate the ability of the Kalman filter solution and RLS algorithm to estimate the unmeasured traction forces and traction force curve. This plot shows a very small subset of actual longitudinal force estimates from the Kalman filter given by the red and blue circles. The red cluster of data corresponds to an early part of the simulation where the commanded torque is building up to get to the peak condition. The red curve, labeled Polynomial Estimation 1, is one polynomial that is estimated using the RLS algorithm and the cluster of red points and is characteristic of the traction curve when operating in Region 1 of Figure 6.4. The blue cluster of data corresponds to a later part of the simulation where the commanded torque has reached a level such that the traction force is at or near the peak level. The blue curve, labeled Polynomial Estimation 2, is a polynomial that is estimated using the RLS algorithm from the cluster of blue points and would be characteristic of the traction curve when operating in Region 2 of Figure 6.4.

Again, we explicitly note that neither the red polynomial estimate or the blue polynomial estimate matches the black Pacejka curve over the entire slip ratio range, and they are not expected to. All that matters is for the polynomial curves to be concave down and that they fit the local shape of the traction curve as provided by traction force estimates from the Kalman Filter. A simple illustration to show how curves for a variety of surfaces can be locally fit according to Equation 6.20 using a polynomial is presented in Figure 6.7, where the traditional least squares algorithm is used on a finite region that is local to the maximum of each curve.

The results of this estimation algorithm when using the simulation data from Sections 4.5.1 and 4.5.2 is presented in Figure 6.8. It is important to note the tendency of the algorithm to overestimate the magnitude of negative values of $\partial\widehat{F}_x/\partial\kappa$. It is also important to note that sufficient richness in

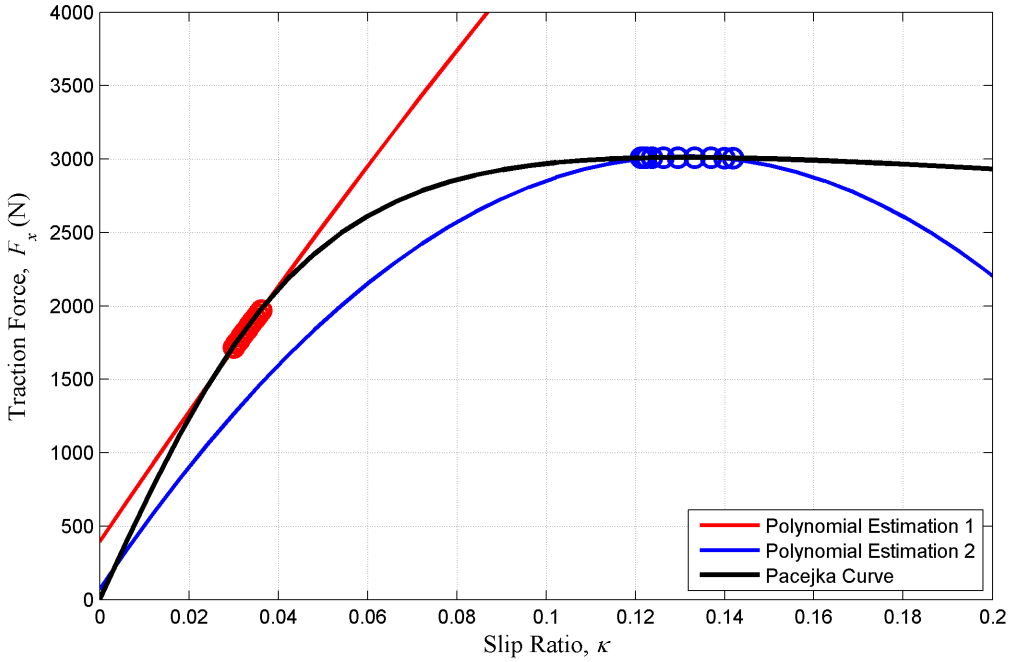

Figure 6.6: Illustration of local function estimation for 1-DOF longitudinal traction.

the excitation signal is required. This fact becomes evident after analyzing Figure 6.8(a), where the algorithm tracks the true value quite nicely. Meanwhile, Figure 6.8(b) shows the results from the simulation that encounters a discrete transition from a dry surface to a wet surface at $t \approx 1.1$ *sec*, the algorithm initially tracks the true values in but starts to suffer from a lack of sufficient richness in the excitation signal towards the end of the simulation and the estimation of $\partial \widehat{F}_x / \partial \kappa$ suffers as a result.

6.2.6 Results: Polynomial Approximation (3-DOF)

The vector quantities **a** and **b** include the polynomial coefficients, and $\phi = \begin{bmatrix} \kappa^2 & \alpha^2 & \kappa\alpha & \kappa & \alpha & 1 \end{bmatrix}^T$. The slopes of the traction curves, defined according to Equations 6.39-6.42, while not precisely in agreement with the global behavior of the traction curve, will again be more useful since they have the symmetric property that the slopes are larger further away from the estimated peak. The results for the RLS algorithm when estimating these partial derivatives using simulation data for a flat uniform surface from Section 4.5.3 is presented in Figure 6.9.

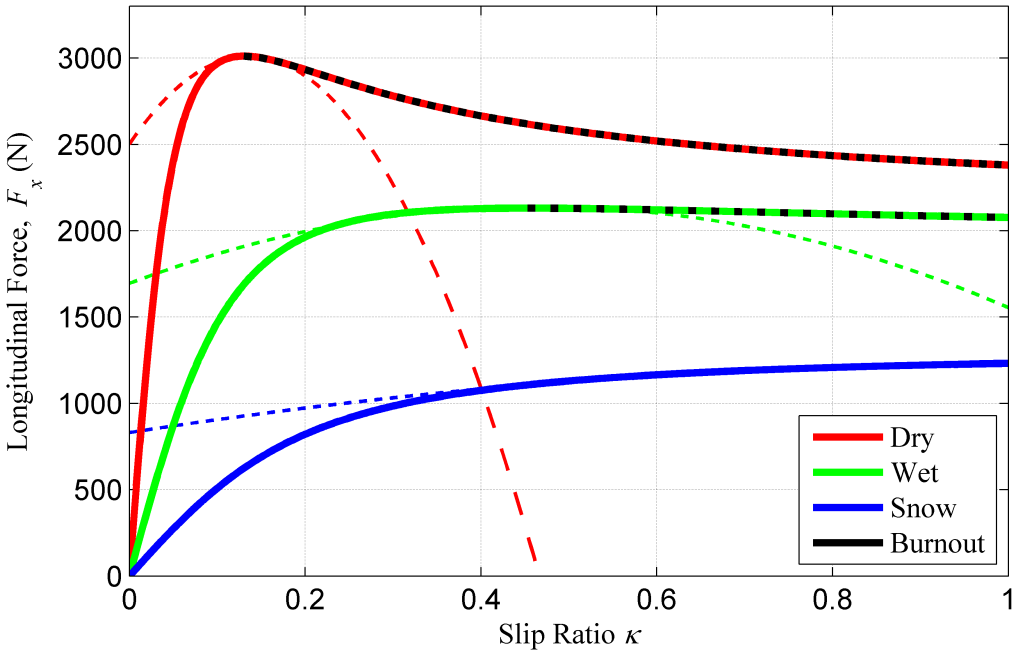

Figure 6.7: Example traction curves from the Pacejka Magic Formula

$$\frac{\partial \widehat{F}_{xt}}{\partial \kappa} = 2a_1\kappa + a_3\alpha + a_4 \tag{6.39}$$

$$\frac{\partial \widehat{F}_{xt}}{\partial \alpha} = 2a_2\alpha + a_3\kappa + a_5 \tag{6.40}$$

$$\frac{\partial \widehat{F}_{yt}}{\partial \kappa} = 2b_1\kappa + b_3\alpha + b_4 \tag{6.41}$$

$$\frac{\partial \widehat{F}_{yt}}{\partial \alpha} = 2b_2\alpha + b_3\kappa + b_5 \tag{6.42}$$

6.3 Simulations using Estimation Algorithms and Approximate Gradient Filter

The third generation of the control architecture, presented in Figure 6.10, uses a Kalman filter to calculate the tractive force(s) in real time, build an estimate of the friction model(s) and uses the approximation of the gradient filter outlined in the previous Chapter to perform traction control. The block diagram of Figure 6.10 is a more detailed version of the Gradient Filter block in Figure 4.1.

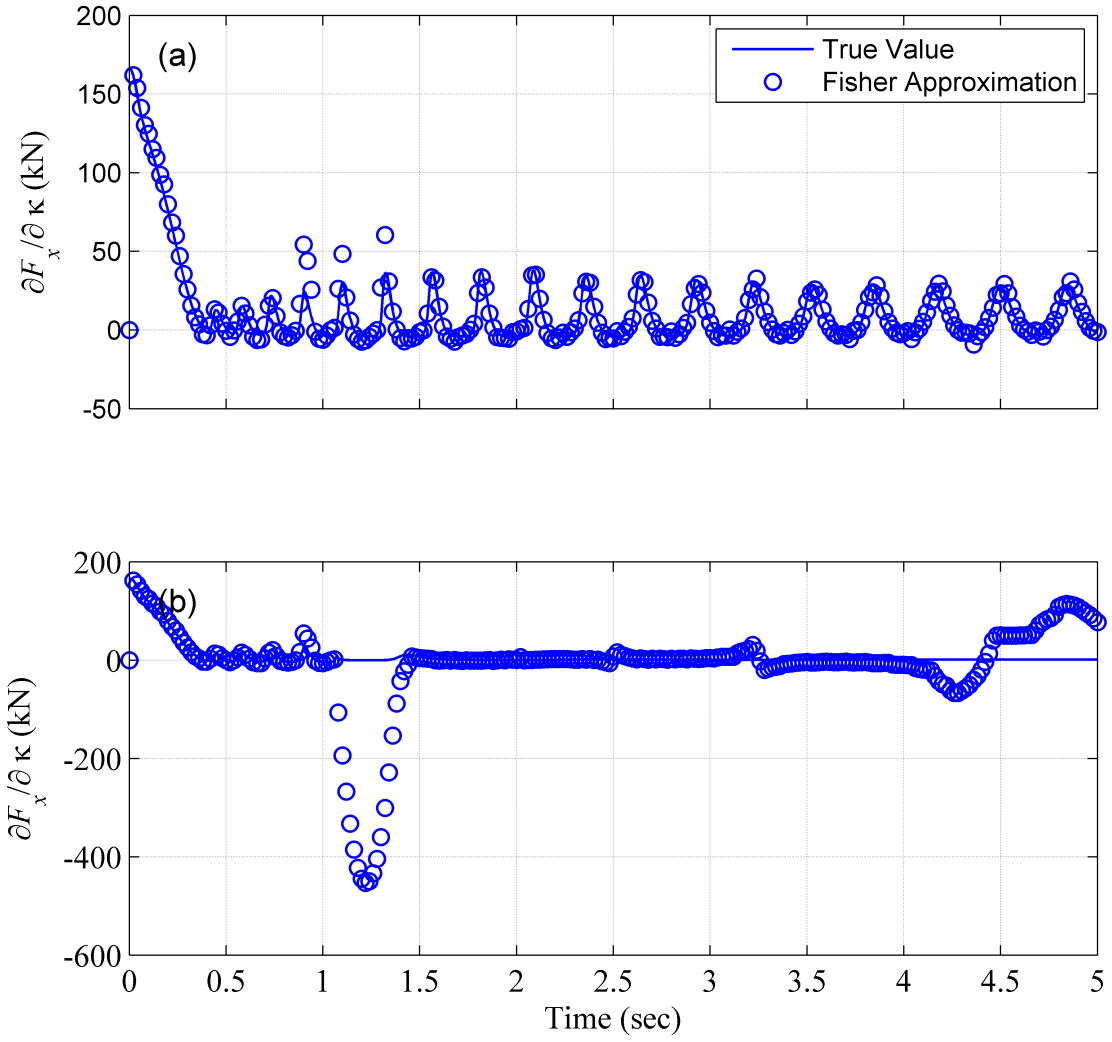

Figure 6.8: Comparison between the Fisher approximation and the true values using simulation data from the 1-DOF vehicle model on a flat (a) uniform surface and (b) non-uniform surface (Sections 4.5.1 and Section 4.5.2)

s

The exact same vehicle model, tire-ground interface model, and simulation parameters used in Sections 4.5 and 5.2 were used here. The only difference in the simulations presented in this Section from those of Sections 4.5 and 5.2 is that the force estimation using the Kalman filter and selective memory solution building a friction model are added to the algorithm according to Figure 6.10.

6.3.1 1-DOF Simulation: Uniform Surface

Figure 6.11(a) shows the position across time where it is evident that the response of the vehicle remains stable for the duration of the simulation. More interesting are the results in Figure 6.11(b-d), where torque, slip ratio and longitudinal acceleration are presented through time, respectively. The buildup to the optimal slip ratio on dry pavement has an additional delay, compared to the exact solution of Section 4.5.1, in the first 1.3 seconds of the simulation result due to the transient convergence of the Kalman Filter. This transient can significantly be reduced through pre-convergence. The anthropomimetic algorithm, using an approximate gradient filter, then tracks the optimal slip ratio as it decreases as a function of down force for $t \in [1.3, 5.0]\,sec$. The adaptive control algorithm when used with the approximate gradient filter displays the same, desirable, hunting behavior that the model based gradient filter displays.

6.3.2 1-DOF Simulation: Non-uniform Surfaces

The estimation algorithms also prove to be successful when encountering a discrete surface change from dry pavement to wet pavement. It is evident from Figure 6.11(c) that the algorithm loses the peak of the tractive force at the instance of change, but then recovers and is tracking the peak tractive force on wet pavement by $t \approx 3.3\,sec$, which is also slightly slower than the exact solution presented in Section 4.5.2, and again can be attributed to the convergence of the Kalman filter. The same hunting behavior is again visible in this simulation, albeit at a smaller magnitude. It is important to note that the same controller gain in Equation 4.47 was used for both simulations; continuous dry pavement, and the discrete change from dry to wet pavement.

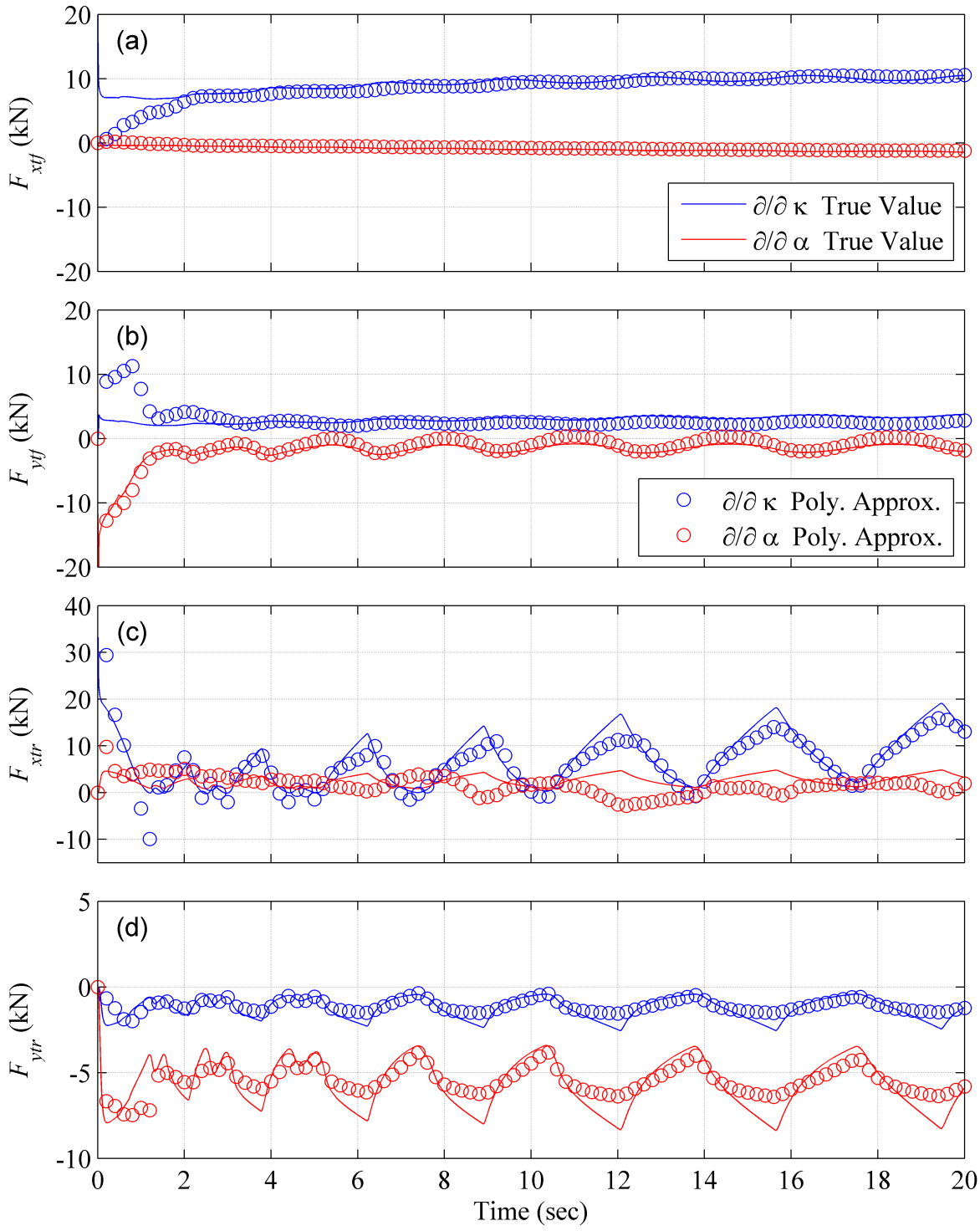

Figure 6.9: Comparison between the Fisher approximation and the true values using simulation data from the 3-DOF vehicle model on a flat uniform surface (Section 4.5.3) at $\delta_f = 60\,deg$

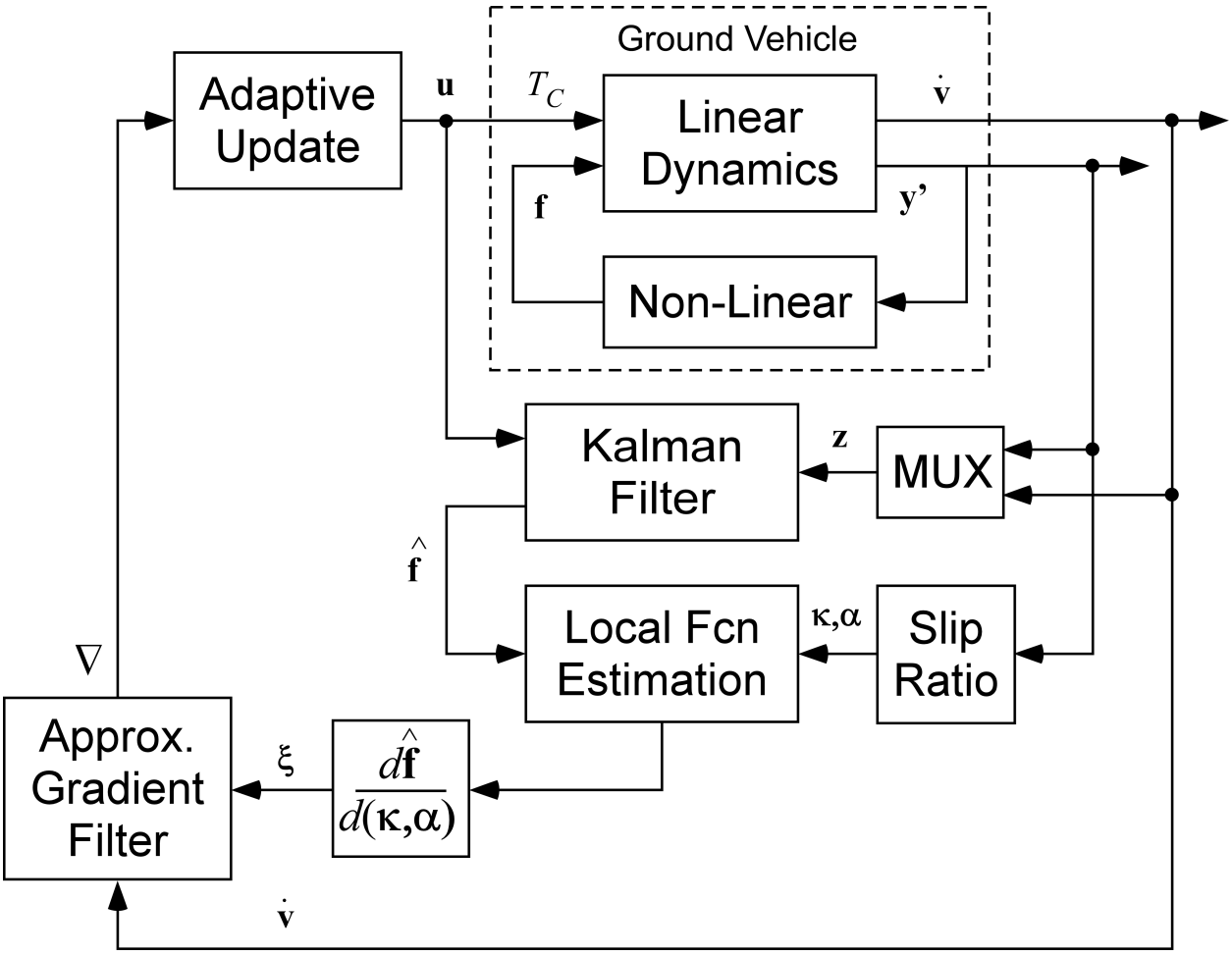

Figure 6.10: Detailed block diagram of control structure when using approximation of gradient filter and a combination of estimation algorithms to learn the tire-ground interface properties.

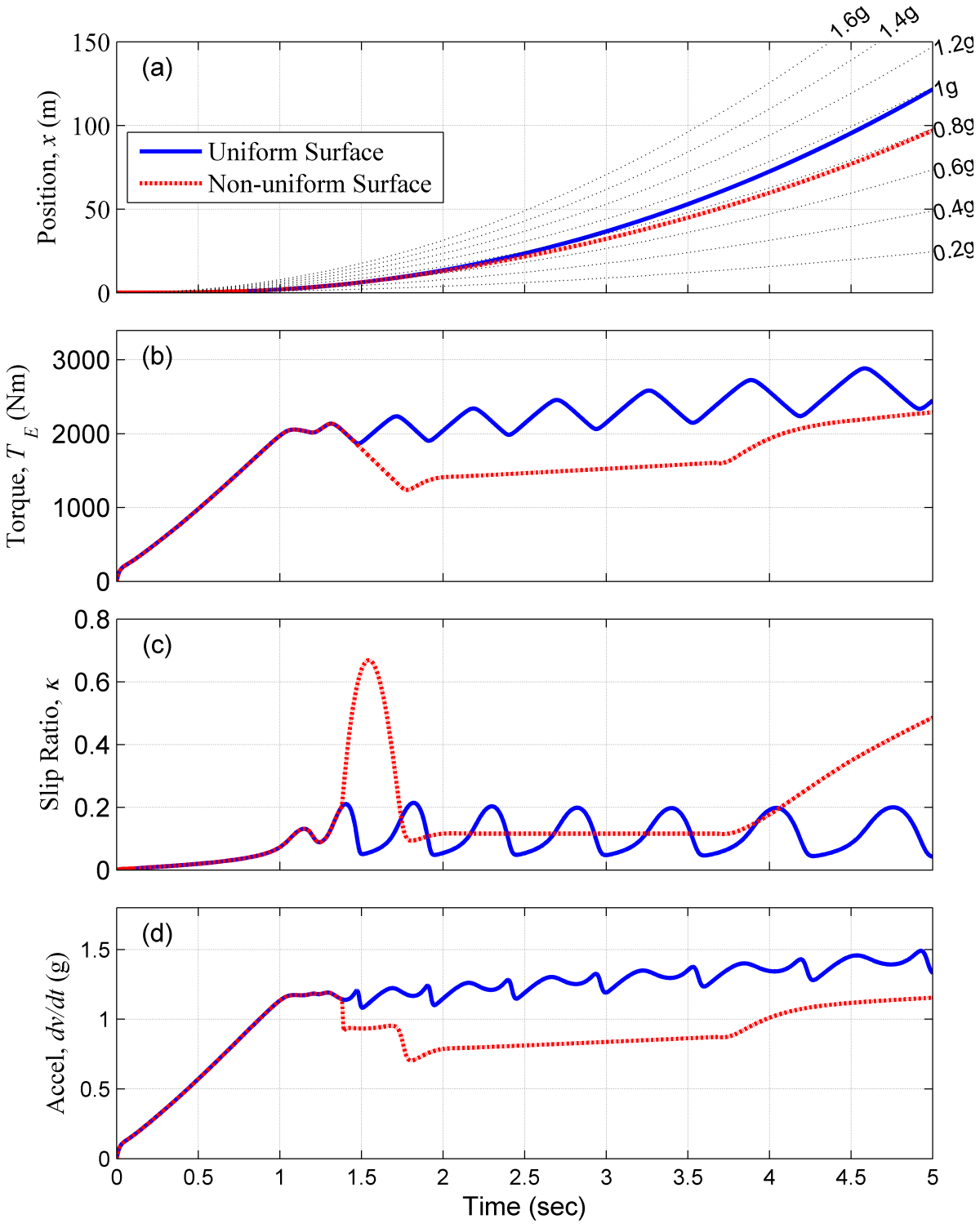

Figure 6.11: Verification of complete control system; approximate gradient filter, Kalman filter and selective memory estimation of the tractive forces. Control simulation results for a uniform surface and non-uniform surface that changes from dry pavement to wet pavement at $x = 5$ m (Sections 4.5.1 and Section 4.5.2).

6.4 Summary

In this chapter, algorithms were presented for estimating the tractive force in real time and a selective memory approach to building a tractive force model were presented. The selective memory approach to identifying the tractive force assumes a novel polynomial model, which differs greatly from previous work related to friction modeling [14, 1, 4]. The model retains key features that the majority of friction models have: the curve monotonically increases to a unique maximum at which point the curve decreases and then asymptotically approaches a level that is less than the maximum. The estimation algorithms were used in combination with the filter approximation described in the previous chapter to perform the same simulations used in previous chapters: one on uniform dry pavement, and one on a non-uniform surface that experienced a discrete change from dry pavement to wet pavement. Both simulations were performed using the same controller gains, and the controller was shown to successfully track the peak tractive force in each simulation.

Chapter 7

Implementation of Control Architecture on HIL Simulator

A model similar to the 3-DOF model presented in Section 3.4 was implemented on the Cruden 6-DOF full-motion driving simulator located at SoVa Motion Labs [61]. A few key modifications to the model presented in Section 3.4 were utilized to overcome the singularity that exists in the slip calculations of Equations 3.2 and 3.1, as well as the fact that braking torques at each wheel are only applied when $\omega_r \neq 0$ or $\omega_f \neq 0$, respectively. The singularity in the slip at v_{xt} was addressed using a method similar to the Stretched String Model for transient tire behavior used by Pacejka [31]. This method, in which a first order lag is introduced in the slip calculations, was implemented according to Equations 7.1 and 7.2, where the relaxation lengths σ_α and σ_κ used in this particular work can be found in Table F.1. It is important to note that Equations 7.1 and 7.2 are used for both front and rear wheels independently and $v_{sx} = \omega R - v_{xt}$ or the slip velocity of each wheel.

$$\sigma_\alpha \frac{\partial \alpha}{\partial t} = v_{yt} - |v_{xt}|\alpha \tag{7.1}$$

$$\sigma_\kappa \frac{\partial \kappa}{\partial t} = -v_{sx} - |v_{xt}|\kappa \tag{7.2}$$

Once the slip speeds are calculated, the slip ratios and slip angles for each tire are calculated in a similar manner to Equations 3.1 and 3.2, but using Equations 7.3 and 7.4

$$\alpha(v_{xt}, v_{yt}) = \arctan\left(\frac{v_{yt}}{|v_{xt}|}\right) \tag{7.3}$$

$$\kappa(\omega, v_{xt}) = \left(\frac{\omega R - v_{xt}}{v_{xt}}\right) \tag{7.4}$$

Equations 7.5 and 7.6 are used to accommodate the physical reality that braking torque is only applied to the front and rear wheels when $\omega_f \neq 0$ and $\omega_r \neq 0$, respectively.

$$T_{b,f} = \begin{cases} 0 & \omega_f = 0\ rad/s \\ T_b & \omega_f \neq 0\ m/s \end{cases} \tag{7.5}$$

$$T_{b,r} = \begin{cases} 0 & \omega_r = 0\ rad/s \\ T_b & \omega_r \neq 0\ m/s \end{cases} \tag{7.6}$$

7.1 Controller - Longitudinal Model (1-DOF)

In a driver assist application, control authority is only given to the traction control algorithm outlined in this work during certain prescribed times. As with commercially available traction control systems, a set of criteria must be met before the algorithm is given control authority. In many systems this criteria can be and often is fairly complex [6]. In this work, a much simpler criteria is used to determine who has full control authority of the input, i.e. the commanded torque T_c. The criteria is outlined in Equation 7.7, and is quite simple. When the slip ratio has exceeded the given threshold and the commanded torque provided by the driver $T_{c,driver}$ is greater than that of the algorithm, the algorithm is given full control authority and in all other cases the driver is given full control authority.

$$T_c = \begin{cases} T_{c,control} & \kappa_r \geq 0.05 \ \ and \ \ T_{c,driver} > T_c \\ T_{c,driver} & \kappa_r \leq 0.05 \ \ or \ \ T_{c,driver} < T_c \end{cases} \tag{7.7}$$

The controller was implemented on the driving simulator using this modification along with the control algorithm from Section 5.1.1. A photo taken while testing the control algorithm on the Cruden 6-DOF full-motion driving simulator is presented in Figure 7.1.

7.2 Results: 1-DOF Controller

A series of HIL tests were performed on a uniform and relatively flat surface where the objective was the same as in Chapter 2, to travel the maximum distance in a specified time, considered analogous to traveling a specified distance in the minimum amount of time. A series of six runs were performed to analyze the performance of the algorithm on the Cruden 6-DOF driving simulator. The results of the sequential runs with the application of the algorithm in this Chapter are presented in Figure 7.2. The desirable traits that the algorithm was designed to include are evident in Figure 7.2(b) and (c) where it is evident that the optimal or near optimal slip ratio is being tracked by the algorithm. It is also evident that the algorithm shows a small amount of variability and almost no

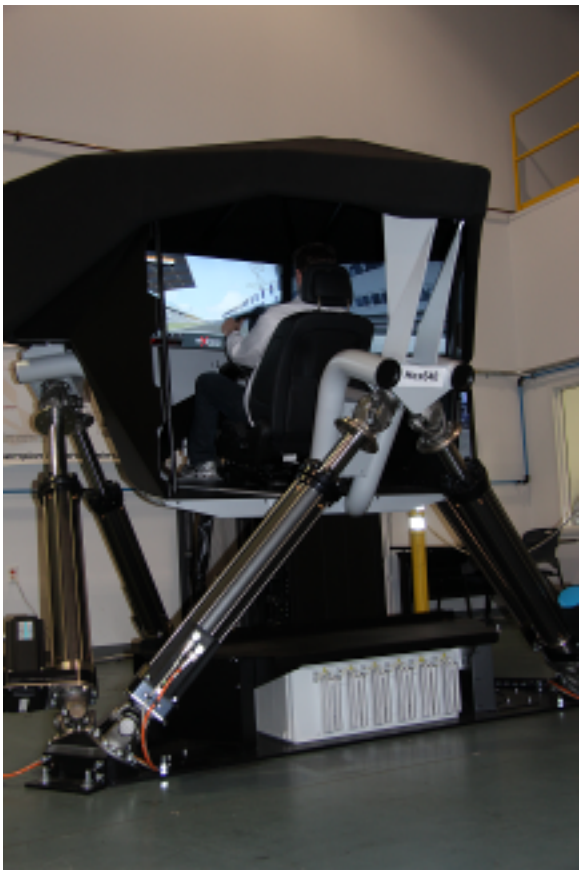

Figure 7.1: HIL experimental test on the SoVA Motion Labs 6-DOF Driving Simulator

oscillation in the input torque T_e shown in Figure 7.2. It should be noted here that a rather poor estimate of the surface was used for the first run in this experiment for the specific purpose of distilling the general trends the algorithm displays when a new (analogous to different) surface is encountered. As eluded to before, while there is little of the desirable hunting behavior visible in Figure 7.2(b), the algorithm shows little variability in Figure 7.2(a). The algorithm does successfully converge to the slip ratio at which peak traction is achieved in Figure 7.2(c,d). It should be noted here that the gain $\mu = 300$ used in the implementation of the controller from Section 5.1.1 can be tuned for faster/slower convergence or more/less oscillation in the control torques T_c and T_e.

The estimation results using the Extended Kalman filter are presented in Figure 7.3(a) and show reasonable accuracy, despite being implemented using the rather crude Euler approximation to discretize the filter, the equations used to implement the Euler approximation are included in Appendix D.1.

The polynomial approximation at an arbitrary point during run 6 is presented in Figure 7.4. This estimate, as discussed in Sections 6.2-6.2.2 is local to the current area of operation on the traction

curve that is used to ultimately estimate $\partial F_{xtr}/\partial \kappa_r$. The estimates of the partial derivative pertinent to the 1-DOF controller, $\partial F_{xtr}/\partial \kappa_r$, for each run are presented in Figure 7.3. As mentioned in Sections 6.2-6.2.2, this particular algorithm tends to overestimate negative values of the partial derivatives but captures the changes in sign quite successfully. This is allowable and can occasionally prove beneficial since the further away from the peak of the traction curve the operating point becomes the partial derivative is guaranteed to increase in magnitude. This is not the case with the true curve as there is an additional inflection point that occurs after its peak.

7.3 Summary

This Chapter has outlined the additions and changes required of models defined in previous Chapters to allow for real-time implementation of the 1-DOF control algorithm on a Cruden 6-DOF full-motion driving simulator. The complete 1-DOF algorithm from Section 5.1.1 was implemented successfully using Matlab, Simulink's, Real-Time Workshop. The complete 1-DOF algorithm that was implemented includes the approximate gradient filter outlined in Section 5.1.1, the instantaneous force estimation method outlined in Section 6.1, and the estimation of the maximum tractive force outlined in Section 6.2. During HIL testing on the simulator, the algorithm displayed behaviour similar to what was displayed in numerical simulations with the exception of there being less oscillation or hunting behavior in the control torque. This is, however, tunable using the adaptive step size μ.

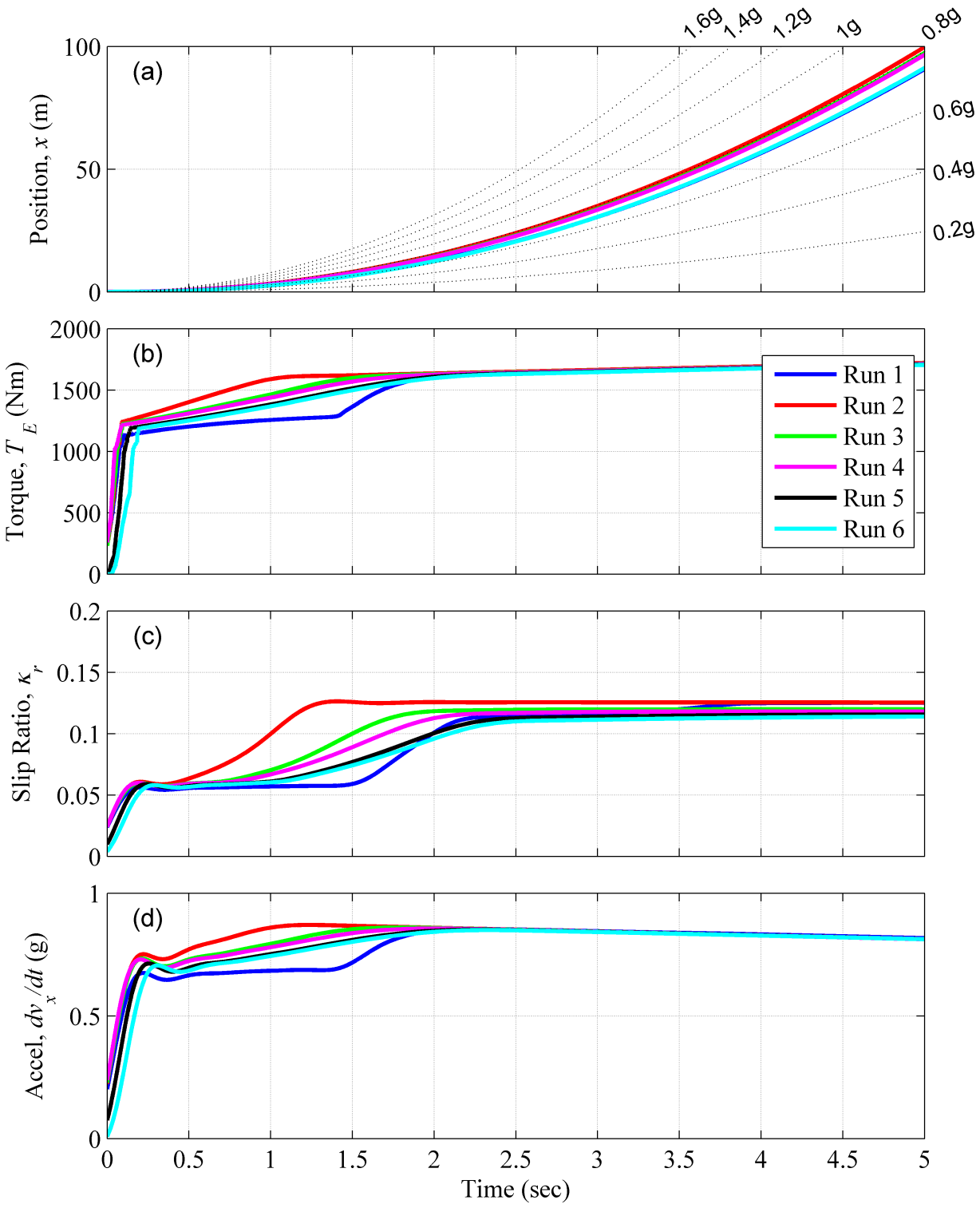

Figure 7.2: HIL experimental data with control; (a) position, (b) wheel torque, (c) slip ratio, and (d) acceleration.

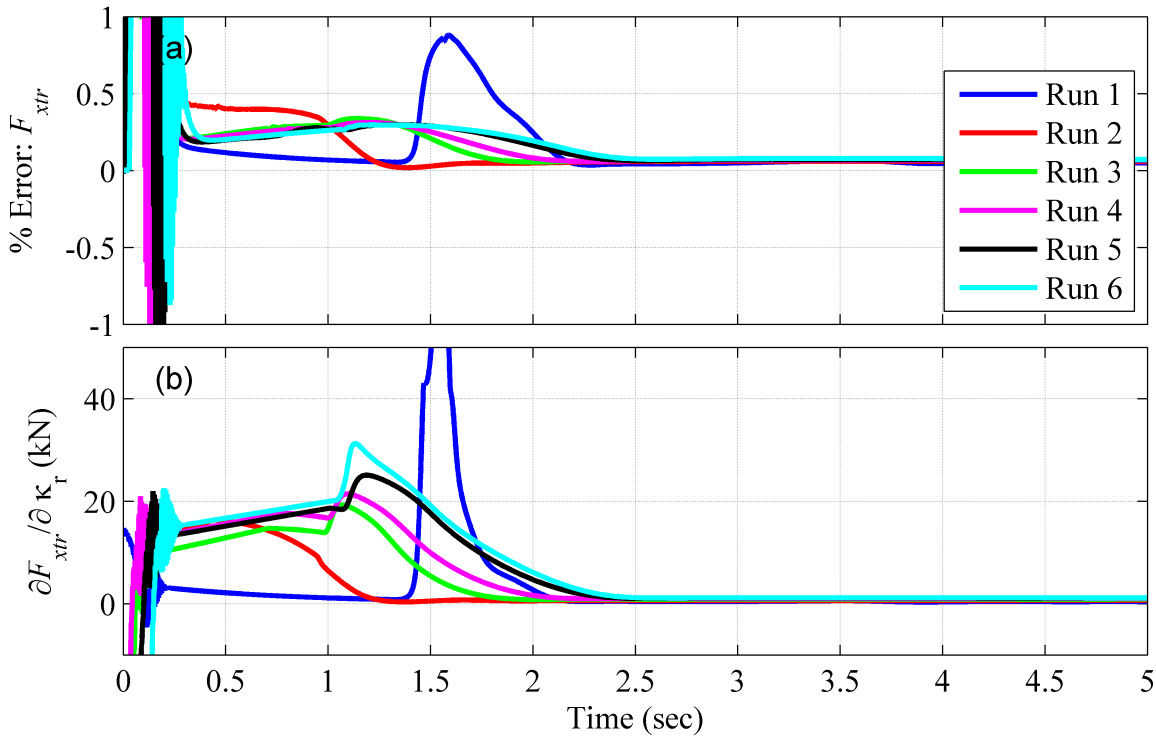

Figure 7.3: HIL experimental results for the Kalman Filter and Fisher Information estimation of traction curve.

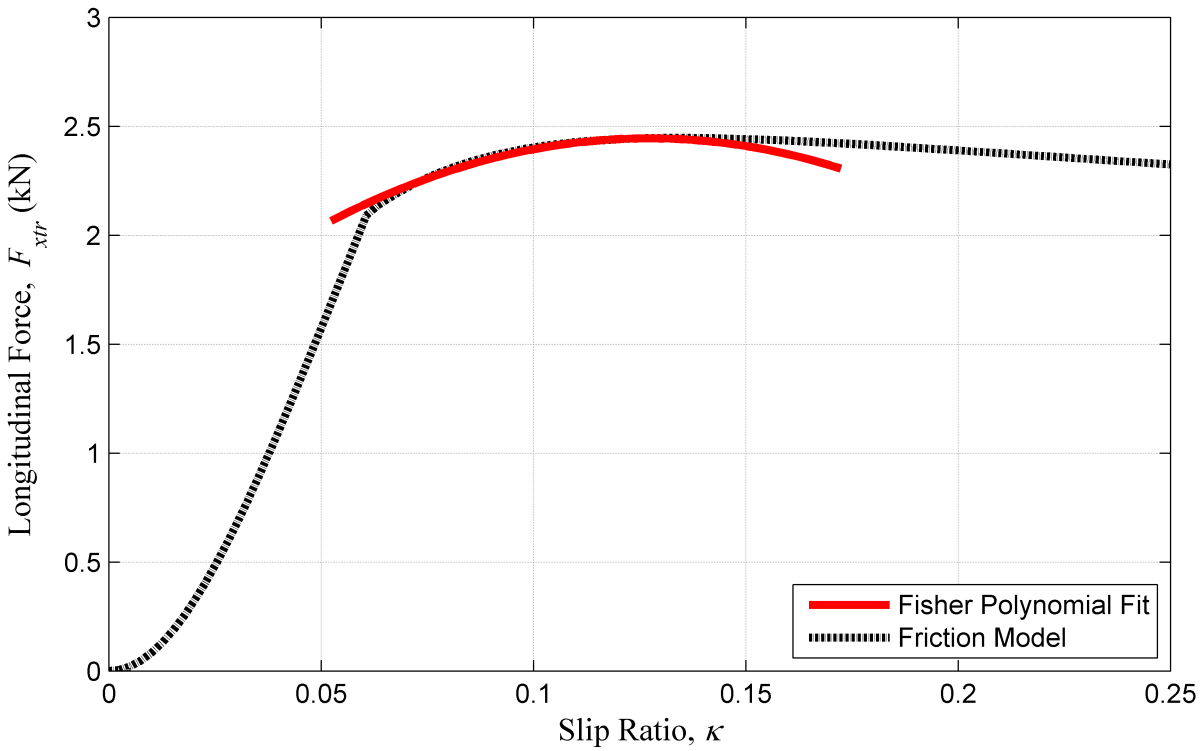

Figure 7.4: HIL experimental results for the selective memory algorithm.

Chapter 8

Novel Contributions

This Chapter outlines the five significant contributions of this work. The contributions include the algorithms and experimental data associated with an anthropomimetic control strategy to perform traction control for a ground vehicle.

Synthesized a novel traction control law which is capable of adapting to changing environmental conditions, based on an analysis of expert human behavioral response

A series of HIL tests were conducted in which an expert driver was given the objective to travel a specified distance in the minimum amount of time, which is considered to be analogous to traveling a maximum distance in the minimum amount of time. Using the HIL response data, an anthropomimetic control strategy was synthesised from the same set of correlated sensory inputs and outputs. To study this problem, representative vehicle and tire-ground interface models were introduced. Key features were distilled from the HIL behavioral responses, and were integrated in a simulation study and the resulting control algorithm. At the heart of this architecture is a novel filter that was used to successfully calculate the gradient of the outputs of a certain class of nonlinear dynamic system with respect to its inputs. This nonlinear filter was developed using dynamic systems theory for a general class of MIMO systems and is considered generally applicable to any nonlinear dynamic system where the nonlinearities are quasi-static.

Developed a novel and efficient traction force estimation algorithm that is capable of selectively eliminating data which will not be useful

The Kalman Filter and Extended Kalman Filter with a random walk disturbance model to estimate disturbances is known, but specific design requirements were developed for the application of estimating unmeasurable or unknown inputs. The approach to model the traction forces as the outputs of a dynamic system that consisted of a series of random walks was shown to be a successful and necessary tool when implementing the control architecture developed in this work. The work in this area shows great promise not only in the area of ground vehicles but also to a broader class of problems concerned with estimating disturbances, and unmeasurable or unknown inputs.

Developed a novel and efficient algorithm for estimating and tracking the local time-varying behavior of traction curves without the need for a high fidelity tire or tire-ground interface model

A simple polynomial approximation was introduced to locally model the traction force curve(s). A constrained Recursive Least Squares algorithm was designed to identify the polynomial coefficients in real time. This polynomial approximation was subsequently used to successfully estimate an approximation the partial derivatives of the traction force curve for use in the gradient filter. This method greatly decreases the computational burden associated with fitting the empirical tire models that are widely used in literature.

Extended conventional traction control strategies to simultaneously control both longitudinal and lateral traction

Traditional traction control algorithms are only capable of maximizing longitudinal traction forces. This work developed the necessary gradient filter to allow for successfully maximizing both longitudinal and lateral accelerations simultaneously. The simulations performed using two different adaptation laws for the MIMO system were shown to display different but desirable behavior due to differences in how the accelerations and forces had been weighted.

Validated the adaptive traction control algorithm using a human-in-the-loop driving simulator

The proposed traction control architecture consisting of the gradient filter, Extended Kalman Filter and polynomial approximation were implemented on the Cruden 6-DOF driving simulator in a series of HIL validation experiments. The control architecture was shown to successfully estimate the instantaneous traction forces (Extended Kalman Filter), approximate the traction force curve (RLS) and regulate the control torque (Gradient Filter and Adaptive Update) to maximize longitudinal acceleration. The results of this testing displayed a consistent repeatability, despite the fact that rather simple methods were used to discretize the Extended Kalman Filter and Gradient Filter. The Cruden 6-DOF driving simulator proved to be a useful and necessary asset in synthesizing a control strategy as well as an exceptional platform for prototyping and testing vehicle control algorithms.

Chapter 9

Future Work and Direction of Research

This Chapter is devoted to discussing the future direction of this research. It includes discussions on certain areas that have arisen in previous chapters as well as items that have not been discussed previously, but are natural extensions of the algorithms used and developed in this work.

9.1 Real-time Force and Moment Estimation

While the Kalman filter approach to disturbance estimation was successfully used in this work, it as an estimation algorithm that could prove to be invaluable to the ground vehicle community. It is conceivable that this algorithm could estimate the forces and moments of each individual wheel of a ground vehicle in real-time. However it is known that there exist singularities in the vehicle operating conditions that cause the states representing the forces and moments to become unobservable. One only needs to consider the case of a four wheeled ground vehicle where we have ten measurements and four inputs used to estimate eight tractive forces and potentially 4-8 moments. The estimation process would become statically indeterminate in certain cases, which suggests that there may be some type of test to check the observability of the tractive forces and moments through a range of state trajectories.

9.2 Stability Analysis

It would seem that there exists a finite limit on the partial derivative(s) $\partial\mathbf{f}/\partial\mathbf{x}$ and $\partial\mathbf{f}/\partial\mathbf{u}$ for which the gradient filter derived in Chapter 4 is guaranteed to remain stable, assuming the plant dynamics are also naturally stable. Empirical evidence collected when qualitatively investigating the sensitivity of the algorithm to changes in the tire-ground interface properties would also suggest that this limit exists, although evidence of its existence is not included in this work. It is the authors belief and hope that this limit will be derived analytically in future work.

9.3 Driving Scenarios and Optimality

The driving scenarios presented in this work were relatively simple in the sense that there was one single objective, maximizing acceleration. A more thorough analysis of the algorithms effect on yaw stability with respect to combined mode friction (longitudinal and lateral) would be insightful, providing a more robust set of results to judge both the estimation algorithm (Kalman Filter) as well as the adaptation algorithm (Gradient Ascent). The control gains used in this work also do not guarantee optimality with respect to acceleration of the vehicle on a specified path or unconstrained path, and an analytical study of maximum realizable acceleration for the vehicle operating conditions would provide a useful comparison to the results in this work.

References

[1] H. B. Pacejka and I. J. M. Besselink, "Magic formula tyre model with transient properties," *Vehicle System Dynamics International Journal of Vehicle Mechanics and Mobility*, vol. 27, no. 1, pp. 234–249, 1997. (document)

[2] D. G. Straitiff, J. S. Freeman, and S. A. Velinsky, "Simple methodology for evaluating and imlementing vehicle anti-lock brake systems," in *Trends in Vehicle Design Research - 1987. Presented at the Winter Annual Meeting of the American Society of Mechanical Engineers.*, vol. 11 of *American Society of Mechanical Engineers, Design Engineering Division (Publication) DE*, (Boston, MA, USA), pp. 35–43, ASME, 1987. (document), 1.2.1

[3] K. Li, J. A. Misener, and K. Hedrick, "On-board road condition monitoring system using slip-based tyre-road friction estimation and wheel speed signal analysis," *Proceedings of the Institution of Mechanical Engineers, Part K: Journal of Multi-body Dynamics*, vol. 221, pp. 129–146, 2007. 1.2.1

[4] W. F. Milliken and D. L. Milliken, *Race Car Vehicle Dynamics*. Warrendale, PA: SAE International, 1995. 1.2.1

[5] G. K. Instrell, "Anti-lock brake systems - field experience on passenger cars," *Proceedings of the Institution of Mechanical Engineers. Part D, Transport engineering*, vol. 200, pp. 283–286, 1986. 1.2.1

[6] A. Benny, A. Nauman, and M. McCoy, *Technical Note: Traction Control TNAU0001*. Motec, 2003.

[7] Y. H. J. Hsu, S. M. Laws, and J. C. Gerdes, "Estimation of tire slip angle and friction limits using steering torque," *IEEE Transactions on Control Systems Technology*, vol. 18, no. Copyright 2010, The Institution of Engineering and Technology, pp. 896–907, 2010.

[8] R. Kazemi, B. Hamedi, and B. Javadi, "A new sliding mode controller for four wheel anti-lock braking system (abs)," *Proceedings of the Automotive Dynamics and Stability Conference*, p. 354, 2000.

[9] H. Lee and M. Tomizuka, "Adaptive vehicle traction force control for intelligent vehicle highway systems (ivhss)," *IEEE Transactions on Industrial Electronics*, vol. 50, pp. 37–47, 2003.

[10] V. Colli, G. Tomassi, and M. Scarano, ""single wheel" longitudinal traction control for electric vehicles," *IEEE Transactions on Power Electronics*, vol. 21, no. Copyright 2006, The Institution of Engineering and Technology, pp. 799–808, 2006.

[11] S. K. Clark and A. United States. National Highway Traffic Safety, *Mechanics of pneumatic tires*. Washington, D.C.: U.S. Dept. of Transportation, National Highway Traffic Safety Administration : For sale by the Supt. of Docs., U.S. G.P.O., 1981.

[12] K. Lyon, M. Philipp, and E. Grommes, "Traction control for a formula 1 race car: Conceptual design, algorithm development, and calibration methodology," *SAE Motorsports Engineering Conference & Expostion, December 1994, Dearborn, MI, USA*, 1994.

[13] T. H. Tran and Q. P. Ha, "Fast algorithm for ugv wheel-terrain interaction analysis," in *10th International Conference on Control, Automation, Robotics and Vision (ICARCV 2008), 17-20 Dec.*, (Piscataway, NJ, USA), pp. 674–80, IEEE, 2008.

[14] H. B. Pacejka and E. Bakker, "Magic formula tyre model," *Vehicle System Dynamics*, vol. 21, pp. 1–18, 1993.

[15] X. Peng, C. Chen, J. Zhang, and L. Wang, "Optimal slip ratio estimation using local polynomial fitting," in *Computer Application and System Modeling (ICCASM), 2010 International Conference on*, vol. 12, pp. V12–319–V12–323, 2010.

[16] M. Bian, K. Li, D. Jin, and X. Lian, "Road condition estimation for automotive anti-skid control system based on bp neural network," in *IEEE International Conference on Mechatronics and Automation, ICMA 2005, July 29, 2005 - August 1, 2005*, IEEE International Conference on Mechatronics and Automation, ICMA 2005, (Niagara Falls, ON, Canada), pp. 1017–1022, IEEE, 2005.

[17] W. R. Pasterkamp and H. B. Pacejka, "Application of neural networks in the estimation of tire/road friction using the tire as sensor," in *Proceedings of the 1997 International Congress and Exposition, Febrary 24-27*, vol. 1228 of *SAE Special Publications*, (Detroit, MI, USA), pp. 1–7, SAE, 1997.

[18] R. Rajamani, N. Piyabongkarn, J. Lew, K. Yi, and G. Phanomchoeng, "Tire-road friction-coefficient estimation," *Control Systems Magazine, IEEE*, vol. 30, no. 4, pp. 54–69, 2010.

[19] R. Rajamani, D. Piyabongkarn, J. Y. Lew, and J. A. Grogg, "Algorithms for real-time estimation of individual wheel tire-road friction coefficients," in *American Control Conference, 2006*, p. 6 pp., 2006.

[20] L. R. Ray, "Nonlinear state and tire force estimation for advanced vehicle control," *Control Systems Technology, IEEE Transactions on*, vol. 3, no. 1, pp. 117–124, 1995.

[21] L. R. Ray, "Nonlinear tire force estimation and road friction identification: Simulation and experiments," *Automatica*, vol. 33, no. 10, pp. 1819–1833, 1997.

[22] M. A. Wilkin, W. J. Manning, D. A. Crolla, and M. C. Levesley, "Use of an extended kalman filter as a robust tyre force estimator," *Vehicle System Dynamics*, vol. 44, no. Copyright 2007, The Institution of Engineering and Technology, pp. 50–9, 2006.

[23] C. T. Leondes, "Control and dynamic systems : advances in theory and applications," *Control and dynamic systems : advances in theory and applications.*, 1973.

[24] C. Johnson, "Accomodation of external disturbances in linear regulator and servomechanism problems," *Automatic Control, IEEE Transactions on*, vol. 16, pp. 635 – 644, Dec 1971.

[25] D. R. Morgan and C. Sanford, "A control theory approach to the stability and transient analysis of the filtered-x lms adaptive notch filter," *IEEE Transactions on Signal Processing*, vol. 40, no. 9, pp. 2341–2346, 1992.

[26] B. Widrow and S. Stearns, *Adaptive Signal Processing*. Englewood Cliffs, New Jersey: Prentice-Hall, 1985.

[27] J. R. Treichler, C. R. Johnson, and M. G. Larimore, *Theory and design of adaptive filters*. Upper Saddle River, NJ: Prentice Hall, 2001.

[28] J. Burki-Cohen, N. N. Soja, and T. Longridge, "Simulator platform motion-the need revisited," *The International Journal of Aviation Psychology*, vol. 8, no. 3, pp. 293 – 317, 1998.

[29] G. Reymond and A. Kemeny, "Motion cueing in the renault driving simulator," *Vehicle System Dynamics*, vol. 34, no. Copyright 2001, IEE, pp. 249–59, 2000.

[30] E. Bakker, L. Nyborg, and H. B. Pacejka, "Tyre modelling for use in vehicle dynamics studies," *SAE Technical Paper Series*, vol. 870421, 1987.

[31] TNO, *MF-Tyre User Manual Version 5.2*. TNO, 2001.

[32] G. Genta, *Motor Vehicle Dynamics: modeling and simulation*. New Jersey: World Scientific, series on advances in mathematics for applied sciences - vol. 43 ed., 1997.

[33] B. J. Olson, S. W. Shaw, and G. Stepan, "Nonlinear dynamics of vehicle traction," *Vehicle System Dynamics*, vol. 40, pp. 377–399, 2003.

[34] B. J. Olson, S. W. Shaw, and G. Stepan, "Stability and bifurcation of longitudinal vehicle braking," *Nonlinear Dynamics*, vol. 40, pp. 339–65, 2006.

[35] K. Cheok, F. Hoogterp, and W. Fales, "Fuzzy logic approach to traction control design," *SAE International Congress & Exposition, February 1996, Detroit, MI, USA*, 1996.

[36] H. S. Tan and M. Tomizuka, "Discrete-time controller design for robust vehicle traction," *IEEE Control Systems Magazine*, vol. 10, pp. 107–13, 1990.

[37] H. Chen, J. Yang, Z. Du, and W. Wang, "Adhesion control method based on fuzzy logic control for four-wheel driven electric vehicle," *SAE 2010 World Congress & Exhibition, April 2010, Detroit, MI, USA*, 2010.

[38] R. Rajamani, *Vehicle Dynamics and Control*. New York, NY: Springer, 2006.

[39] S. Taheri and E. H. Law, "Investigation of a combined slip control braking and closed loop four wheel steering system for an automobile during combined hard braking and severe steering," in *American Control Conference, 1990*, pp. 1862–1867, 1990.

[40] H. Wang, "Hardware-in-the-loop simulation for traction control and the debugs of its electric control unit," *SAE Technical Paper Series*, vol. 2004-01-2056, 2004.

[41] F. Zhejun, K. Yoram, and D. Wehe, "A simple traction control for tracked vehicles," in *Proceedings of 1995 American Control Conference - ACC'95, 21-23 June 1995*, vol. vol.2 of *Proceedings of the 1995 American Control Conference (IEEE Cat. No.95CH35736)*, (Evanston, IL, USA), pp. 1176–7, American Autom Control Council, 1995.

[42] T. D. Day and S. G. Roberts, "A simulation model for vehicle braking systems fitted with abs," *SAE 2002 World Congress & Exhibition, March 2002, Detroit, MI, USA*, 2002.

[43] P. Clarkson, *Optimal and Adaptive Signal Processing*. CRC Press, 1993.

[44] M. Sri-Jayantha and R. F. Stengel, "Determination of nonlinear aerodynamic coefficients using the estimation-before-modeling method," *Journal of Aircraft*, vol. 25, no. Compendex, pp. 796–804, 1988.

[45] H. Durrant-Whyte, "Introduction to decentralised data fusion," The Australian Center for Field Robotics, (The University of Sydney, Australia), 2004.

[46] J. H. Hill and B. E. Ydstie, "Adaptive control with selective memory," *International Journal of Adaptive Control and Signal Processing*, vol. 18, no. 7, pp. 571–587, 2004.

[47] G. C. Goodwin and R. L. Payne, *Dynamic system identification : experiment design and data analysis*. New York: Academic Press, 1977.

[48] H. Sado, S.-i. Sakai, and Y. Hori, "Road condition estimation for traction control in electric vehicle," in *Proceedings of the 1999 IEEE International Symposium on Industrial Electronics (ISIE'99), July 12, 1999 - July 16, 1999*, vol. 2 of *IEEE International Symposium on Industrial Electronics*, (Bled, Slovenia), pp. 973–978, IEEE, 1999.

[49] Y. Shao-zhi, L. Jing, and L. You-de, "Traction control system with consideration of road surface roughness," *Journal of Jilin University (Engineering and Technology Edition)*, p. 05, 2007.

[50] Y. Hori, Y. Toyoda, and Y. Tsuruoka, "Traction control of electric vehicle: Basic experimental results using the test ev uot electric march," *Industry Applications, IEEE Transactions on*, vol. 34, no. 5, pp. 1131–1138, 1998.

[51] C. Canudas de Wit and P. Tsiotras, "Dynamic tire friction models for vehicle traction control," in *Decision and Control, 1999. Proceedings of the 38th IEEE Conference on*, vol. 4, pp. 3746–3751, IEEE, 1999.

[52] S. Sreenivasan and B. Wilcox, "Stability and traction control of an actively actuated micro-rover," *Journal of Robotic Systems*, vol. 11, no. 6, pp. 487–502, 1994.

[53] K. Iagnemma and S. Dubowsky, "Traction control of wheeled robotic vehicles in rough terrain with application to planetary rovers," *The International Journal of Robotics Research*, vol. 23, no. 10-11, p. 1029, 2004.

[54] F. Borrelli, A. Bemporad, M. Fodor, and D. Hrovat, "An mpc/hybrid system approach to traction control," *Control Systems Technology, IEEE Transactions on*, vol. 14, no. 3, pp. 541–552, 2006.

[55] H. Tan and Y. Chin, "Vehicle traction control: variable-structure control approach," *Journal of dynamic systems, measurement, and control*, vol. 113, p. 223, 1991.

[56] F. Borrelli, A. Bemporad, M. Fodor, and D. Hrovat, "A hybrid approach to traction control," *Hybrid Systems: Computation and Control*, pp. 162–174, 2001.

[57] H. Sado, S. Sakai, and Y. Hori, "Road condition estimation for traction control in electric vehicle," in *Industrial Electronics, 1999. ISIE'99. Proceedings of the IEEE International Symposium on*, vol. 2, pp. 973–978, IEEE, 1999.

Websites

[58] "MOTEC," May 2011. http://www.motec.com.au/home.

[59] "EFI technology," May 2011. http://www.efitechnology.com/X3.html.

[60] "Pectel Engine Controllers," May 2011. http://www.cosworth.com/Default.aspx?id=1089651.

[61] "SoVa Motion," March 2012. http://www.sovamotion.com/.

[62] "Kistler RoaDyn," June 2011. http://www.kistler.com/MX_en-us/vehicles_1_2_1_roadyn/RoaDyn-Wheel-Force-Transducers.html.

Patents

[63] D. Kabasin, "Adaptive vehicle traction control system," Feb. 25 1992. US Patent 5,090,511.

[64] R. Matsumoto, "Vehicle traction control system for preventing vehicle turnover on curves and turns," Dec. 11 1990. US Patent 4,976,330.

[65] H. Horner Jr, M. Zenner, D. Nowack, and H. Christopherson, "Lawn mower traction control system," Dec. 17 1985. US Patent 4,558,558.

[66] L. Brooks and K. Kidston, "Electric vehicle with traction control," Feb. 20 1996. US Patent 5,492,192.

[67] D. Kabasin and D. Stoltman, "Vehicle traction control system," Jan. 26 1988. US Patent 4,721,176.

[68] Y. Akuta, T. Ikeda, and T. Nishihara, "Vehicle traction control system," Dec. 6 1994. US Patent 5,370,199.

[69] H. Leiber, "All-wheel drive automotive vehicle traction control system," May 20 1986. US Patent 4,589,511.

[70] S. Cikanek, "Electric vehicle regenerative antiskid braking and traction control system," Sept. 12 1995. US Patent 5,450,324.

[71] K. Hosomi and A. Nagae, "Vehicle traction control apparatus and method of traction control," June 22 2001. US Patent App. 09/885,938.

[72] S. Rees, R. Milunas, L. Nitz, and W. Bolander, "Integrated traction control system," Nov. 30 1993. US Patent 5,265,693.

[73] K. Nakamura, I. Kobayashi, T. Nogami, A. Shirai, Y. Nomura, and K. Ohashi, "Traction control device of a motor vehicle," Jan. 20 1987. US Patent 4,637,487.

[74] G. Naito, "Traction control system for four-wheel drive vehicle," Dec. 8 1992. US Patent 5,168,955.

[75] R. Rudolph, T. Hoffman, J. Cage, and M. Gatt, "Brake vacuum modulator traction control with pressure source variable as function of engine load during incipient wheel spin conditions," Oct. 18 1988. US Patent 4,778,225.

[76] S. Cikanek, "Fuzzy logic electric vehicle regenerative antiskid braking and traction control system," Oct. 25 1994. US Patent 5,358,317.

[77] E. Browalski and P. Nimmo IV, "Vehicle traction control system," Aug. 7 1990. US Patent 4,946,015.

[78] T. Iwata, T. Murakami, M. Tamura, and T. Fukumura, "Traction control for automotive vehicle," Jan. 9 1996. US Patent 5,482,133.

[79] D. Poirier, M. Matheny, G. Mitchell, S. Swantick, G. Wroblewski, D. Menck, and R. Simon Jr, "Vehicle traction control system with fuel control," June 25 1991. US Patent 5,025,881.

[80] H. Pueschel, G. Schmidt, and M. Gerdes, "Method and device for controlling an abs antilock braking/asr traction control system," Mar. 17 1998. US Patent 5,727,852.

[81] J. McEnnan, "Method for estimating reference speed and acceleration for traction and antiskid braking control," Apr. 4 1989. US Patent 4,818,037.

[82] W. Seibert and K. Blum, "Method and brake system for traction control," Oct. 27 1987. US Patent 4,702,336.

[83] Y. Imoto, H. Uno, T. Takei, H. Wakata, and Y. Hattori, "Braking system with power brake, braking force proportioning, anti-skid, and traction control functions," July 5 1988. US Patent 4,755,008.

[84] R. Diaz, "Guidance control system for a traction vehicle," Aug. 5 1980. US Patent 4,215,759.

[85] Y. Ghoneim and Y. Chin, "Vehicle traction control system," June 25 1991. US Patent 5,025,882.

[86] J. Polidan and D. Harnack, "Traction control system with fuel and spark control," May 25 1993. US Patent 5,213,178.

[87] K. Matsuno, Y. Hiwatashi, A. Takahashi, and M. Matsuura, "Traction control system for four wheel drive vehicle and the method thereof," Dec. 15 1998. US Patent 5,850,616.

[88] K. Matsuno and S. Oshita, "Traction control system for fourwheel drive vehicle," Apr. 7 1998. US Patent 5,737,714.

[89] G. Naito, "Control system for limited-slip differential gear unit associated with wheel-spinning preventive traction control system," Dec. 13 1988. US Patent 4,790,404.

[90] M. Kollers, G. Wolff, and G. Kaes, "Hydraulic brake system with anti-skid system and traction control for a vehicle," July 21 1992. US Patent 5,131,730.

[91] T. Yamashita and K. Hirai, "Traction control system for vehicle," Sept. 10 1996. US Patent 5,555,499.

[92] T. Tsuyama, T. Onaka, K. Nobumoto, and M. Kawamura, "Traction control system for motor vehicle," June 28 1994. US Patent 5,325,300.

[93] M. Kawamura, T. Tsuyama, K. Nobumoto, and H. Okazaki, "Traction control system for motor vehicle," Jan. 25 1994. US Patent 5,281,008.

[94] Y. Etoh, "System for automatically controlling vehicle speed to desired cruise speed whose control function is inhibited when system for controlling a vehicular traction operates and method therefor," Aug. 21 1990. US Patent 4,951,208.

[95] M. Hashiguchi, K. Yamada, S. Nishikawa, S. Ikeda, M. Shimada, and T. Dogahara, "Traction control apparatus for vehicle engine," June 12 1990. US Patent 4,933,857.

[96] K. May and R. Holzwarth, "Hybrid traction control system," July 11 1995. US Patent 5,431,241.

[97] M. Kawamura, T. Tsuyama, M. Hideshima, and K. Hayafuchi, "Vehicle traction control device," June 29 1993. US Patent 5,222,570.

[98] S. Katayose, M. Tamura, and T. Iwata, "Traction control system for controlling engine output and brake for maintaining optimum wheel traction with road friction level dependent brake control," Oct. 19 1993. US Patent 5,255,193.

[99] F. Porter, "Active control of a hydra-mechanical traction control device," Mar. 30 2001. US Patent App. 09/822,612.

[100] F. Kageyama, H. Kanazawa, S. Takahara, and T. Morita, "Suspension-traction total control system," Feb. 2 1993. US Patent 5,183,127.

[101] S. Watanabe, "Integral anti-lock brake/traction control system," June 8 1993. US Patent 5,217,283.

[102] K. Tezuka and H. Fujiki, "Traction control system for a four-wheel drive motor vehicle," Apr. 2 1991. US Patent 5,004,064.

[103] J. Hughes, L. Christensen, W. Wade, P. Grutter, and M. Weyburne, "Torque managed traction control for the drive wheels of an automotive vehicle," May 21 1996. US Patent 5,519,617.

[104] T. Tsuyama, T. Onaka, K. Nobumoto, and M. Kawamura, "Traction control system using estimated road surface friction coefficient," Oct. 4 1994. US Patent 5,353,225.

[105] D. Poirier, M. Matheny, H. Martin, G. Wroblewski, and R. Simon Jr, "Vehicle traction control system with fuel control," Aug. 28 1990. US Patent 4,951,773.

[106] T. Sugiura, S. Kitamura, M. Tsujino, and M. Yasuda, "Throttle valve operating device with traction control function," Dec. 8 1992. US Patent 5,168,951.

[107] W. Jonner, "Method and apparatus for traction control (asr)," Nov. 20 1990. US Patent 4,971,400.

[108] R. Rodgers and N. Luo, "Electronic traction control system," June 25 2002. US Patent 6,408,972.

[109] T. Matsuda, "Automotive traction control system with feature of enabling and disabling control depending upon vehicle speed," Sept. 20 1988. US Patent 4,771,850.

[110] G. Villec, "Integrated anti-lock braking and traction control system," Aug. 27 1991. US Patent 5,042,885.

[111] M. Hashiguchi, K. Yamada, M. Ito, A. Kawano, S. Nishikawa, T. Funakoshi, and S. Ikeda, "Traction control apparatus," Nov. 13 1990. US Patent 4,970,650.

[112] M. Hara, S. Kamio, M. Takao, K. Sakita, and T. Abe, "Traction control system," May 28 1991. US Patent 5,018,595.

[113] W. Jonner and L. Kirstein, "Anti-skid and traction control system," Feb. 13 1990. US Patent 4,900,102.

[114] T. Tsuyama, T. Onaka, K. Nobumoto, F. Kageyama, and M. Kawamura, "Traction control system for vehicle," Mar. 29 1994. US Patent 5,297,662.

[115] K. May, "Traction control system responsive to wheel speed fluctuations," May 25 1993. US Patent 5,213,177.

[116] T. Matsuda, "Automotive traction control system with feature of adjusting wheel slippage detecting threshold level depending upon vehicle speed," Aug. 16 1988. US Patent 4,763,912.

[117] M. Sato, S. Shiraishi, and T. Muto, "Traction control system for controlling slip of a driving wheel of a vehicle," Oct. 10 1989. US Patent 4,873,639.

[118] C. Johnson, "Traction control system and a method for remedying wheel-slippage," Jan. 4 2000. US Patent 6,012,011.

[119] D. Hrovat, "Traction control system with active suspension," May 14 1996. US Patent 5,517,414.

[120] G. Fischle, M. Baumann, R. Klingel, and C. Pfister, "Traction control method for stabilizing motor vehicle motion in the event of increased driving wheel slip," Oct. 15 1996. US Patent 5,564,800.

Relevant Publications

[121] W. Kirchner and S. Southward, "An anthropomimetic approach to high performance traction control," *(Paladyn) Journal of Behavioral Robotics (Paladyn)*, vol. 2, pp. 25–35, 2011. doi: 10.2478/s13230-011-0013-9.

[122] W. Kirchner and S. Southward, "Traction control using an anthropomimetic approach," in *ASME International Design Engineering Technical Conference and Computers and Information in Engineering Conference, August 28-31*, (Washington, DC, USA), ASME, 2011.

[123] W. Kirchner and S. Southward, "Anthropomimetic traction control: Quarter car model," in *SAE Commercial Vehicle Engineering Congress, September 13-14*, (Rosemont, IL, USA), SAE, 2011.

[124] W. Kirchner and S. Southward, "Anthropomimetic traction control: Quarter car model," *SAE International Journal of Commercial Vehicles*, vol. 4, no. 1, pp. 127–134, 2011. doi: 10.4271/2011-01-2178.

[125] W. Kirchner and S. Southward, "Method for poly-functional adaptive traction control," *Invention Disclosure Submitted to VTIP (11-138)*, June 2011.

Appendix A

Vehicle Models

$$\begin{aligned} \dot{\mathbf{x}} &= \mathbf{A_c x} + \mathbf{B_c u} + \mathbf{F_c u'} \\ \mathbf{y} &= \mathbf{C_c x} + \mathbf{D_c u} + \mathbf{G_c u'} \end{aligned}$$

A.1 1-DOF Longitudinal Model

$$\begin{aligned} \mathbf{u'} &= [F_x] \\ \mathbf{u} &= [T_C] \\ \mathbf{x} &= \begin{bmatrix} v & \omega & T_E \end{bmatrix}^T \\ \mathbf{y} &= [\dot{v}] \end{aligned}$$

$$\begin{bmatrix} \dot{v} \\ \dot{\omega} \\ \dot{T}_E \end{bmatrix} = \begin{bmatrix} -\left(\frac{\alpha}{m}\right) & 0 & 0 \\ 0 & -\left(\frac{\beta}{J_W}\right) & \left(\frac{1}{J_W}\right) \\ 0 & 0 & -(2\pi f_E) \end{bmatrix} \begin{bmatrix} v \\ \omega \\ T_E \end{bmatrix} + \begin{bmatrix} 0 & \left(\frac{1}{m}\right) \\ 0 & -\left(\frac{R}{J_W}\right) \\ (2\pi f_E) & 0 \end{bmatrix} \begin{bmatrix} T_C \\ F_x \end{bmatrix}$$

A.2 3-DOF Bicycle Model

$$
\begin{aligned}
\mathbf{y}' &= \begin{bmatrix} \mathbf{I}_N \\ \mathbf{0} \end{bmatrix} \mathbf{x} + \begin{bmatrix} \mathbf{0} \\ \mathbf{I}_M \end{bmatrix} \mathbf{u} = \begin{bmatrix} \mathbf{x} \\ \mathbf{u} \end{bmatrix} \\
\mathbf{u}' &= \begin{bmatrix} f_1(\mathbf{y}') \\ \vdots \\ f_Q(\mathbf{y}') \end{bmatrix} = \mathbf{f}(\mathbf{y}') \\
\mathbf{A_c} &= \begin{bmatrix}
\frac{-\gamma_x}{m} & 0 & 0 & 0 & 0 & 0 \\
0 & \frac{-\gamma_y}{m} & 0 & 0 & 0 & 0 \\
0 & 0 & 0 & 0 & 0 & 0 \\
0 & 0 & 0 & \frac{-\beta}{J_w} & 0 & 0 \\
0 & 0 & 0 & 0 & \frac{-\beta}{J_w} & \frac{1}{J_w} \\
0 & 0 & 0 & 0 & 0 & -2\pi f_e
\end{bmatrix} \\
\mathbf{B_c} &= \begin{bmatrix} 0 & 0 & 0 & 0 & 0 & 2\pi f_e \end{bmatrix}^T \quad (acceleration) \\
\mathbf{B_c} &= \begin{bmatrix}
0 & 0 & 0 & \frac{-1}{J_w} & 0 & 0 \\
0 & 0 & 0 & 0 & \frac{-1}{J_w} & 0
\end{bmatrix}^T \quad (braking) \\
\mathbf{F_c} &= \begin{bmatrix}
\frac{1}{m}\cos(\delta_f) & \frac{1}{m} & \frac{-1}{m}\cos(90-\delta_f) & 0 \\
\frac{1}{m}\sin(\delta_f) & 0 & \frac{1}{m}\sin(90-\delta_f) & \frac{1}{m} \\
\frac{L_f}{J_m}\sin(\delta_f) & 0 & \frac{L_f}{J_m}\sin(90-\delta_f) & -\frac{L_r}{J_m} \\
\frac{-R}{J_w} & 0 & 0 & 0 \\
0 & \frac{-R}{J_w} & 0 & 0 \\
0 & 0 & 0 & 0
\end{bmatrix} \\
\mathbf{C_c} &= \begin{bmatrix}
\frac{-\gamma_x}{m} & 0 & 0 & 0 & 0 & 0 \\
0 & \frac{-\gamma_y}{m} & 0 & 0 & 0 & 0
\end{bmatrix} \\
\mathbf{D_c} &= \begin{bmatrix} 0 \\ 0 \end{bmatrix}^T \quad (acceleration) \\
\mathbf{D_c} &= \begin{bmatrix} 0 & 0 \\ 0 & 0 \end{bmatrix}^T \quad (braking) \\
\mathbf{G_c} &= \begin{bmatrix}
\frac{1}{m}\cos(\delta_f) & \frac{1}{m} & \frac{-1}{m}\cos(90-\delta_f) & 0 \\
\frac{1}{m}\sin(\delta_f) & 0 & \frac{1}{m}\sin(90-\delta_f) & \frac{1}{m}
\end{bmatrix}
\end{aligned}
$$

$$
\begin{aligned}
\mathbf{x} &= \begin{bmatrix} v_x & v_y & \dot{\psi} & \omega_f & \omega_r & T_e \end{bmatrix}^T \\
\mathbf{y} &= \begin{bmatrix} \dot{v}_x & \dot{v}_y \end{bmatrix}^T \\
\mathbf{u} &= \begin{bmatrix} T_c \end{bmatrix} \quad (acceleration) \\
\mathbf{u} &= \begin{bmatrix} T_{b,f} & T_{b,r} \end{bmatrix} \quad (braking) \\
\mathbf{u}' &= \begin{bmatrix} F_{xtf} & F_{xtr} & F_{ytf} & F_{ytr} \end{bmatrix}^T
\end{aligned}
$$

Appendix B

Indirect Gradient Filter

B.1 1-DOF Longitudinal Model

$$
\begin{aligned}
A_f &= \begin{bmatrix}
-\gamma_x/m & 0 & 0 & \frac{\partial F_{xtr}}{\partial v_x}/m & \frac{\partial F_{xtr}}{\partial w_r}/m & 0 & 0 & 0 & 0 \\
0 & -\beta/J_w & 1/J_w & -(R\frac{\partial F_{xtr}}{\partial v_x})/J_w & -(R\frac{\partial F_{xtr}}{\partial w_r})/J_w & 0 & 0 & 0 & 0 \\
0 & 0 & -2\pi f_e & 0 & 0 & 0 & 0 & 0 & 0 \\
0 & 0 & 0 & \frac{\partial F_{xtr}}{\partial v_x}/m - \gamma_x/m & \frac{\partial F_{xtr}}{\partial w_r}/m & 0 & 0 & 0 & 0 \\
0 & 0 & 0 & -(R\frac{\partial F_{xtr}}{\partial v_x})/J_w & -\beta/J_w - (R\frac{\partial F_{xtr}}{\partial w_r})/J_w & 1/J_w & 0 & 0 & 0 \\
0 & 0 & 0 & 0 & 0 & -2\pi f_e & 0 & 0 & 0 \\
0 & 0 & 0 & 0 & 0 & 0 & -\gamma_x/m & 0 & 0 \\
0 & 0 & 0 & 0 & 0 & 0 & 0 & -\beta/J_w & 1/J_w \\
0 & 0 & 0 & 0 & 0 & 0 & 0 & 0 & -2\pi f_e
\end{bmatrix} \\
B_f &= \begin{bmatrix} 0 & 0 & 0 & 0 & 0 & 2\pi f_e & 0 & 0 & 2\pi f_e \end{bmatrix}^T \\
C_f &= \begin{bmatrix} -\gamma_x/m & 0 & 0 & \frac{\partial F_{xtr}}{\partial v_x}/m & \frac{\partial F_{xtr}}{\partial w_r}/m & 0 & -\gamma_x/m & 0 & 0 \end{bmatrix} \\
D_f &= \begin{bmatrix} 0 \end{bmatrix}
\end{aligned}
$$

B.2 3-DOF Bicycle Model

$$
A_f = \begin{bmatrix}
-\gamma_x/m & 0 & 0 & 0 & 0 & 0 & \#1 & \#2 & \#3 & \#4 & \frac{\partial F_{xtr}}{\partial \omega_r}/m & 0 & 0 & 0 & 0 & 0 & 0 & 0 \\
0 & -\gamma_y/m & 0 & 0 & 0 & 0 & \#5 & \#6 & \#7 & \#8 & \frac{\partial F_{ytr}}{\partial \omega_r}/m & 0 & 0 & 0 & 0 & 0 & 0 & 0 \\
0 & 0 & 0 & 0 & 0 & 0 & \#9 & \#10 & \#11 & \#12 & -(L_r\frac{\partial F_{ytr}}{\partial \omega_r})/J_m & 0 & 0 & 0 & 0 & 0 & 0 & 0 \\
0 & 0 & 0 & -\beta/J_w & 0 & 0 & -(R\frac{\partial F_{xtf}}{\partial v_x})/J_w & -(R\frac{\partial F_{xtf}}{\partial v_y})/J_w & -(R\frac{\partial F_{xtf}}{\partial \psi})/J_w & -(R\frac{\partial F_{xtf}}{\partial \omega_f})/J_w & 0 & 0 & 0 & 0 & 0 & 0 & 0 & 0 \\
0 & 0 & 0 & 0 & -\beta/J_w & 1/J_w & -(R\frac{\partial F_{xtr}}{\partial v_x})/J_w & -(R\frac{\partial F_{xtr}}{\partial v_y})/J_w & -(R\frac{\partial F_{xtr}}{\partial \psi})/J_w & 0 & -(R\frac{\partial F_{xtr}}{\partial \omega_r})/J_w & 0 & 0 & 0 & 0 & 0 & 0 & 0 \\
0 & 0 & 0 & 0 & 0 & -2\pi f_e & 0 & 0 & 0 & 0 & 0 & 0 & 0 & 0 & 0 & 0 & 0 & 0 \\
0 & 0 & 0 & 0 & 0 & 0 & \#13 & \#14 & \#15 & \#16 & \frac{\partial F_{xtr}}{\partial \omega_r}/m & 0 & 0 & 0 & 0 & 0 & 0 & 0 \\
0 & 0 & 0 & 0 & 0 & 0 & \#17 & \#18 & \#19 & \#20 & \frac{\partial F_{ytr}}{\partial \omega_r}/m & 0 & 0 & 0 & 0 & 0 & 0 & 0 \\
0 & 0 & 0 & 0 & 0 & 0 & \#21 & \#22 & \#23 & \#24 & -(L_r\frac{\partial F_{ytr}}{\partial \omega_r})/J_m & 0 & 0 & 0 & 0 & 0 & 0 & 0 \\
0 & 0 & 0 & 0 & 0 & 0 & -(R\frac{\partial F_{xtf}}{\partial v_x})/J_w & -(R\frac{\partial F_{xtf}}{\partial v_y})/J_w & -(R\frac{\partial F_{xtf}}{\partial \psi})/J_w & -\beta/J_w-(R\frac{\partial F_{xtf}}{\partial \omega_f})/J_w & 0 & 0 & 0 & 0 & 0 & 0 & 0 & 0 \\
0 & 0 & 0 & 0 & 0 & 0 & -(R\frac{\partial F_{xtr}}{\partial v_x})/J_w & -(R\frac{\partial F_{xtr}}{\partial v_y})/J_w & -(R\frac{\partial F_{xtr}}{\partial \psi})/J_w & 0 & -\beta/J_w-(R\frac{\partial F_{xtr}}{\partial \omega_r})/J_w & 1/J_w & 0 & 0 & 0 & 0 & 0 & 0 \\
0 & 0 & 0 & 0 & 0 & 0 & 0 & 0 & 0 & 0 & 0 & -2\pi f_e & 0 & 0 & 0 & 0 & 0 & 0 \\
0 & 0 & 0 & 0 & 0 & 0 & 0 & 0 & 0 & 0 & 0 & 0 & -\gamma_x/m & 0 & 0 & 0 & 0 & 0 \\
0 & 0 & 0 & 0 & 0 & 0 & 0 & 0 & 0 & 0 & 0 & 0 & 0 & -\gamma_y/m & 0 & 0 & 0 & 0 \\
0 & 0 & 0 & 0 & 0 & 0 & 0 & 0 & 0 & 0 & 0 & 0 & 0 & 0 & 0 & 0 & 0 & 0 \\
0 & 0 & 0 & 0 & 0 & 0 & 0 & 0 & 0 & 0 & 0 & 0 & 0 & 0 & 0 & -\beta/J_w & 0 & 0 \\
0 & 0 & 0 & 0 & 0 & 0 & 0 & 0 & 0 & 0 & 0 & 0 & 0 & 0 & 0 & 0 & -\beta/J_w & 1/J_w \\
0 & 0 & 0 & 0 & 0 & 0 & 0 & 0 & 0 & 0 & 0 & 0 & 0 & 0 & 0 & 0 & 0 & -2\pi f_e
\end{bmatrix}
$$

$$
B_f = \begin{bmatrix} 0 & 0 & 0 & 0 & 0 & 0 & 0 & 0 & 0 & 0 & 2\pi f_e & 0 & 0 & 0 & 0 & 0 & 2\pi f_e \end{bmatrix}^T
$$

$$
C_{f,x} = \begin{bmatrix} -\gamma_x/m & 0 & 0 & 0 & 0 & 0 & \#1 & \#2 & \#3 & \#4 & \frac{\partial F_{xtr}}{\partial \omega_r}/m & 0 & -\gamma_x/m & 0 & 0 & 0 & 0 & 0 \end{bmatrix}
$$

$$
C_{f,y} = \begin{bmatrix} 0 & -\gamma_y/m & 0 & 0 & 0 & 0 & \#5 & \#6 & \#7 & \#8 & \frac{\partial F_{ytr}}{\partial \omega_r}/m & 0 & 0 & -\gamma_y/m & 0 & 0 & 0 & 0 \end{bmatrix}
$$

$$
D_{f,x} = [0]
$$

$$
D_{f,y} = [0]
$$

$$
\begin{aligned}
\#1 &= \frac{\partial F_{xtr}}{\partial v_x}/m + (\frac{\partial F_{xtf}}{\partial v_x}cos(\delta_f))/m - (\frac{\partial F_{ytf}}{\partial v_x}cos(\delta_f - \pi/2))/m \\
\#2 &= \frac{\partial F_{xtr}}{\partial v_y}/m + (\frac{\partial F_{xtf}}{\partial v_y}cos(\delta_f))/m - (\frac{\partial F_{ytf}}{\partial v_y}cos(\delta_f - \pi/2))/m \\
\#3 &= \frac{\partial F_{xtr}}{\partial \dot{\psi}}/m + (\frac{\partial F_{xtf}}{\partial \dot{\psi}}cos(\delta_f))/m - (\frac{\partial F_{ytf}}{\partial \dot{\psi}}cos(\delta_f - \pi/2))/m \\
\#4 &= (\frac{\partial F_{xtf}}{\partial \omega_f}cos(\delta_f))/m - (\frac{\partial F_{ytf}}{\partial \omega_f}cos(\delta_f - \pi/2))/m \\
\#5 &= \frac{\partial F_{ytr}}{\partial v_x}/m + (\frac{\partial F_{xtf}}{\partial v_x}sin(\delta_f))/m - (\frac{\partial F_{ytf}}{\partial v_x}sin(\delta_f - \pi/2))/m \\
\#6 &= \frac{\partial F_{ytr}}{\partial v_y}/m + (\frac{\partial F_{xtf}}{\partial v_y}sin(\delta_f))/m - (\frac{\partial F_{ytf}}{\partial v_y}sin(\delta_f - \pi/2))/m \\
\#7 &= \frac{\partial F_{ytr}}{\partial \dot{\psi}}/m + (\frac{\partial F_{xtf}}{\partial \dot{\psi}}sin(\delta_f))/m - (\frac{\partial F_{ytf}}{\partial \dot{\psi}}sin(\delta_f - \pi/2))/m \\
\#8 &= (\frac{\partial F_{xtf}}{\partial \omega_f}sin(\delta_f))/m - (\frac{\partial F_{ytf}}{\partial \omega_f}sin(\delta_f - \pi/2))/m \\
\#9 &= (L_f\frac{\partial F_{xtf}}{\partial v_x}sin(\delta_f))/J_m - (L_r\frac{\partial F_{ytr}}{\partial v_x})/J_m - (L_f\frac{\partial F_{ytf}}{\partial v_x}sin(\delta_f - \pi/2))/J_m \\
\#10 &= (L_f\frac{\partial F_{xtf}}{\partial v_y}sin(\delta_f))/J_m - (L_r\frac{\partial F_{ytr}}{\partial v_y})/J_m - (L_f\frac{\partial F_{ytf}}{\partial v_y}sin(\delta_f - \pi/2))/J_m \\
\#11 &= (L_f\frac{\partial F_{xtf}}{\partial \dot{\psi}}sin(\delta_f))/J_m - (L_r\frac{\partial F_{ytr}}{\partial \dot{\psi}})/J_m - (L_f\frac{\partial F_{ytf}}{\partial \dot{\psi}}sin(\delta_f - \pi/2))/J_m \\
\#12 &= (L_f\frac{\partial F_{xtf}}{\partial \omega_f}sin(\delta_f))/J_m - (L_f\frac{\partial F_{ytf}}{\partial \omega_f}sin(\delta_f - \pi/2))/J_m \\
\#13 &= \frac{\partial F_{xtr}}{\partial v_x}/m - \gamma_x/m + (\frac{\partial F_{xtf}}{\partial v_x}cos(\delta_f))/m - (\frac{\partial F_{ytf}}{\partial v_x}cos(\delta_f - \pi/2))/m \\
\#14 &= \frac{\partial F_{xtr}}{\partial v_y}/m + (\frac{\partial F_{xtf}}{\partial v_y}cos(\delta_f))/m - (\frac{\partial F_{ytf}}{\partial v_y}cos(\delta_f - \pi/2))/m \\
\#15 &= \frac{\partial F_{xtr}}{\partial \dot{\psi}}/m + (\frac{\partial F_{xtf}}{\partial \dot{\psi}}cos(\delta_f))/m - (\frac{\partial F_{ytf}}{\partial \dot{\psi}}cos(\delta_f - \pi/2))/m \\
\#16 &= (\frac{\partial F_{xtf}}{\partial \omega_f}cos(\delta_f))/m - (\frac{\partial F_{ytf}}{\partial \omega_f}cos(\delta_f - \pi/2))/m \\
\#17 &= \frac{\partial F_{ytr}}{\partial v_x}/m + (\frac{\partial F_{xtf}}{\partial v_x}sin(\delta_f))/m - (\frac{\partial F_{ytf}}{\partial v_x}sin(\delta_f - \pi/2))/m
\end{aligned}
$$

$$
\begin{aligned}
\#18 &= \frac{\partial F_{ytr}}{\partial v_y}/m - \gamma_y/m + (\frac{\partial F_{xtf}}{\partial v_y} sin(\delta_f))/m - (\frac{\partial F_{ytf}}{\partial v_y} sin(\delta_f - \pi/2))/m \\
\#19 &= \frac{\partial F_{ytr}}{\partial \dot{\psi}}/m + (\frac{\partial F_{xtf}}{\partial \dot{\psi}} sin(\delta_f))/m - (\frac{\partial F_{ytf}}{\partial \dot{\psi}} sin(\delta_f - \pi/2))/m \\
\#20 &= (\frac{\partial F_{xtf}}{\partial \omega_f} sin(\delta_f))/m - (\frac{\partial F_{ytf}}{\partial \omega_f} sin(\delta_f - \pi/2))/m \\
\#21 &= (L_f \frac{\partial F_{xtf}}{\partial v_x} sin(\delta_f))/J_m - (L_r \frac{\partial F_{ytr}}{\partial v_x})/J_m - (L_f \frac{\partial F_{ytf}}{\partial v_x} sin(\delta_f - \pi/2))/J_m \\
\#22 &= (L_f \frac{\partial F_{xtf}}{\partial v_y} sin(\delta_f))/J_m - (L_r \frac{\partial F_{ytr}}{\partial v_y})/J_m - (L_f \frac{\partial F_{ytf}}{\partial v_y} sin(\delta_f - \pi/2))/J_m \\
\#23 &= (L_f \frac{\partial F_{xtf}}{\partial \dot{\psi}} sin(\delta_f))/J_m - (L_r \frac{\partial F_{ytr}}{\partial \dot{\psi}})/J_m - (L_f \frac{\partial F_{ytf}}{\partial \dot{\psi}} sin(\delta_f - \pi/2))/J_m \\
\#24 &= (L_f \frac{\partial F_{xtf}}{\partial \omega_f} sin(\delta_f))/J_m - (L_f \frac{\partial F_{ytf}}{\partial \omega_f} sin(\delta_f - \pi/2))/J_m
\end{aligned}
$$

Appendix C

Direct Gradient Filter

C.1 1-DOF Longitudinal Model

$$
\begin{aligned}
A_f &= \begin{bmatrix} \frac{\partial F_{xtr}}{\partial v_x}/m - \gamma_x/m & \frac{\partial F_{xtr}}{\partial w_r}/m & 0 \\ -(R\frac{\partial F_{xtr}}{\partial v_x})/J_w & -\beta/J_w - (R\frac{\partial F_{xtr}}{\partial w_r})/J_w & 1/J_w \\ 0 & 0 & -2\pi f_e \end{bmatrix} \\
B_f &= \begin{bmatrix} 0 & 0 & 2\pi f_e \end{bmatrix}^T \\
C_f &= \begin{bmatrix} \frac{\partial F_{xtr}}{\partial v_x} & \frac{\partial F_{xtr}}{\partial w_r} & 0 \end{bmatrix} \\
D_f &= \begin{bmatrix} 0 \end{bmatrix}
\end{aligned}
$$

C.2 3-DOF Bicycle Model

$$
\begin{aligned}
A_f &= \begin{bmatrix}
\#13 & \#14 & \#15 & \#16 & \frac{\partial F_{xtr}}{\partial \omega_r}/m & 0 \\
\#17 & \#18 & \#19 & \#20 & \frac{\partial F_{ytr}}{\partial \omega_r}/m & 0 \\
\#21 & \#22 & \#23 & \#24 & -(L_r \frac{\partial F_{ytr}}{\partial \omega_r})/J_m & 0 \\
-(R\frac{\partial F_{xtf}}{\partial v_x})/J_w & -(R\frac{\partial F_{xtf}}{\partial v_y})/J_w & -(R\frac{\partial F_{xtf}}{\partial \dot{\psi}})/J_w & -\beta/J_w - (R\frac{\partial F_{xtf}}{\partial \omega_f})/J_w & 0 & 0 \\
-(R\frac{\partial F_{xtr}}{\partial v_x})/J_w & -(R\frac{\partial F_{xtr}}{\partial v_y})/J_w & -(R\frac{\partial F_{xtr}}{\partial \dot{\psi}})/J_w & 0 & -\beta/J_w - (R\frac{\partial F_{xtr}}{\partial \omega_r})/J_w & 1/J_w \\
0 & 0 & 0 & 0 & 0 & -2\pi f_e
\end{bmatrix} \\
B_f &= \begin{bmatrix} 0 & 0 & 0 & 0 & 0 & 2\pi f_e \end{bmatrix}^T \\
C_{f,1} &= \begin{bmatrix} \frac{\partial F_{xtf}}{\partial v_x} & \frac{\partial F_{xtf}}{\partial v_y} & \frac{\partial F_{xtf}}{\partial \dot{\psi}} & \frac{\partial F_{xtf}}{\partial \omega_f} & 0 & 0 \end{bmatrix} \\
C_{f,2} &= \begin{bmatrix} \frac{\partial F_{xtr}}{\partial v_x} & \frac{\partial F_{xtr}}{\partial v_y} & \frac{\partial F_{xtr}}{\partial \dot{\psi}} & 0 & \frac{\partial F_{xtr}}{\partial \omega_r} & 0 \end{bmatrix} \\
C_{f,3} &= \begin{bmatrix} \frac{\partial F_{ytf}}{\partial v_x} & \frac{\partial F_{ytf}}{\partial v_y} & \frac{\partial F_{ytf}}{\partial \dot{\psi}} & \frac{\partial F_{ytf}}{\partial \omega_f} & 0 & 0 \end{bmatrix} \\
C_{f,4} &= \begin{bmatrix} \frac{\partial F_{ytr}}{\partial v_x} & \frac{\partial F_{ytr}}{\partial v_y} & \frac{\partial F_{ytr}}{\partial \dot{\psi}} & 0 & \frac{\partial F_{ytr}}{\partial \omega_r} & 0 \end{bmatrix} \\
D_{f,1} &= [0] \\
D_{f,2} &= [0] \\
D_{f,3} &= [0] \\
D_{f,4} &= [0]
\end{aligned}
$$

$$
\begin{aligned}
\#13 &= \frac{\partial F_{xtr}}{\partial v_x}/m - \gamma_x/m + (\frac{\partial F_{xtf}}{\partial v_x}cos(\delta_f))/m - (\frac{\partial F_{ytf}}{\partial v_x}cos(\delta_f - \pi/2))/m \\
\#14 &= \frac{\partial F_{xtr}}{\partial v_y}/m + (\frac{\partial F_{xtf}}{\partial v_y}cos(\delta_f))/m - (\frac{\partial F_{ytf}}{\partial v_y}cos(\delta_f - \pi/2))/m \\
\#15 &= \frac{\partial F_{xtr}}{\partial \dot{\psi}}/m + (\frac{\partial F_{xtf}}{\partial \dot{\psi}}cos(\delta_f))/m - (\frac{\partial F_{ytf}}{\partial \dot{\psi}}cos(\delta_f - \pi/2))/m \\
\#16 &= (\frac{\partial F_{xtf}}{\partial \omega_f}cos(\delta_f))/m - (\frac{\partial F_{ytf}}{\partial \omega_f}cos(\delta_f - \pi/2))/m \\
\#17 &= \frac{\partial F_{ytr}}{\partial v_x}/m + (\frac{\partial F_{xtf}}{\partial v_x}sin(\delta_f))/m - (\frac{\partial F_{ytf}}{\partial v_x}sin(\delta_f - \pi/2))/m \\
\#18 &= \frac{\partial F_{ytr}}{\partial v_y}/m - \gamma_y/m + (\frac{\partial F_{xtf}}{\partial v_y}sin(\delta_f))/m - (\frac{\partial F_{ytf}}{\partial v_y}sin(\delta_f - \pi/2))/m \\
\#19 &= \frac{\partial F_{ytr}}{\partial \dot{\psi}}/m + (\frac{\partial F_{xtf}}{\partial \dot{\psi}}sin(\delta_f))/m - (\frac{\partial F_{ytf}}{\partial \dot{\psi}}sin(\delta_f - \pi/2))/m \\
\#20 &= (\frac{\partial F_{xtf}}{\partial \omega_f}sin(\delta_f))/m - (\frac{\partial F_{ytf}}{\partial \omega_f}sin(\delta_f - \pi/2))/m \\
\#21 &= (L_f\frac{\partial F_{xtf}}{\partial v_x}sin(\delta_f))/J_m - (L_r\frac{\partial F_{ytr}}{\partial v_x})/J_m - (L_f\frac{\partial F_{ytf}}{\partial v_x}sin(\delta_f - \pi/2))/J_m \\
\#22 &= (L_f\frac{\partial F_{xtf}}{\partial v_y}sin(\delta_f))/J_m - (L_r\frac{\partial F_{ytr}}{\partial v_y})/J_m - (L_f\frac{\partial F_{ytf}}{\partial v_y}sin(\delta_f - \pi/2))/J_m \\
\#23 &= (L_f\frac{\partial F_{xtf}}{\partial \dot{\psi}}sin(\delta_f))/J_m - (L_r\frac{\partial F_{ytr}}{\partial \dot{\psi}})/J_m - (L_f\frac{\partial F_{ytf}}{\partial \dot{\psi}}sin(\delta_f - \pi/2))/J_m \\
\#24 &= (L_f\frac{\partial F_{xtf}}{\partial \omega_f}sin(\delta_f))/J_m - (L_f\frac{\partial F_{ytf}}{\partial \omega_f}sin(\delta_f - \pi/2))/J_m
\end{aligned}
$$

Appendix D

Kalman Filter

$$\dot{\rho} = \overline{\mathbf{A}}_c\rho + \overline{\mathbf{B}}_c\mathbf{u} + \mathbf{n}_w \tag{D.1}$$
$$\mathbf{v} = \overline{\mathbf{C}}_c\rho + \overline{\mathbf{D}}_c\mathbf{u} + \mathbf{n}_v \tag{D.2}$$

D.1 Euler Approximation

The Euler approximation can be expressed as either Equation D.3 or D.4, where $h = \Delta t$.

$$\mathbf{x}_{k+1} = \mathbf{x}_k + \frac{d\mathbf{x}}{dt}h \tag{D.3}$$
$$\dot{\mathbf{x}} = \frac{\mathbf{x}_{k+1} - \mathbf{x}_k}{\Delta t} \tag{D.4}$$

Using either expression will approximate the system of Equations D.1 and D.2 as Equations D.5-D.10.

$$\rho_{k+1} = \overline{\mathbf{A}}\rho_k + \overline{\mathbf{B}}\mathbf{u}_k + \mathbf{n}_w \tag{D.5}$$
$$\mathbf{v}_k = \overline{\mathbf{C}}\rho_k + \overline{\mathbf{D}}\mathbf{u}_k + \mathbf{n}_v \tag{D.6}$$
$$\overline{\mathbf{A}} = \Delta t\overline{\mathbf{A}}_c + \mathbf{I} \tag{D.7}$$
$$\overline{\mathbf{B}} = \Delta t\overline{\mathbf{B}}_c \tag{D.8}$$
$$\overline{\mathbf{C}} = \overline{\mathbf{C}}_c \tag{D.9}$$
$$\overline{\mathbf{D}} = \overline{\mathbf{D}}_c \tag{D.10}$$

D.2 1-DOF Longitudinal Model

$$\begin{bmatrix} \dot{v} \\ \dot{\omega} \\ \dot{T}_E \\ \dot{F}_x \\ \ddot{F}_x \\ \dddot{F}_x \end{bmatrix} = \begin{bmatrix} -\left(\frac{\alpha}{m}\right) & 0 & 0 & \left(\frac{1}{m}\right) & 0 & 0 \\ 0 & -\left(\frac{\beta}{J_W}\right) & \left(\frac{1}{J_W}\right) & -\left(\frac{R}{J_W}\right) & 0 & 0 \\ 0 & 0 & -(2\pi f_E) & 0 & 0 & 0 \\ 0 & 0 & 0 & 0 & 1 & 0 \\ 0 & 0 & 0 & 0 & 0 & 1 \\ 0 & 0 & 0 & 0 & 0 & 0 \end{bmatrix} \begin{bmatrix} v \\ \omega \\ T_E \\ F_x \\ \dot{F}_x \\ \ddot{F}_x \end{bmatrix} + \begin{bmatrix} 0 \\ 0 \\ (2\pi f_E) \\ 0 \\ 0 \\ 0 \end{bmatrix} \begin{bmatrix} T_C \end{bmatrix}$$

$$\begin{bmatrix} \dot{v} \\ \dot{\omega} \end{bmatrix} = \begin{bmatrix} -\left(\frac{\alpha}{m}\right) & 0 & 0 & \left(\frac{1}{m}\right) & 0 & 0 \\ 0 & 1 & 0 & 0 & 0 & 0 \end{bmatrix} \begin{bmatrix} v \\ \omega \\ T_E \\ F_x \\ \dot{F}_x \\ \ddot{F}_x \end{bmatrix} + \begin{bmatrix} 0 \\ 0 \end{bmatrix} \begin{bmatrix} T_C \end{bmatrix}$$

$$\begin{aligned} \Sigma_v &= \mathbf{I} \\ \sigma_d &= 4e4 \\ \Sigma_w &= \begin{bmatrix} 10 & 0 & 0 & 0 & 0 & 0 \\ 0 & 1 & 0 & 0 & 0 & 0 \\ 0 & 0 & 10 & 0 & 0 & 0 \\ 0 & 0 & 0 & \sigma_d & 0 & 0 \\ 0 & 0 & 0 & 0 & \sigma_d & 0 \\ 0 & 0 & 0 & 0 & 0 & \sigma_d \end{bmatrix} \end{aligned}$$

D.3 3-DOF Bicycle Model

$$
\overline{\mathbf{A}}_c = \begin{bmatrix}
\frac{-\gamma_x}{m} & 0 & 0 & 0 & 0 & 0 & \frac{1}{m}\cos(\delta_f) & 0 & 0 & \frac{1}{m} & 0 & 0 & \frac{-1}{m}\cos(90-\delta_f) & 0 & 0 & 0 & 0 & 0 \\
0 & \frac{-\gamma_y}{m} & 0 & 0 & 0 & 0 & \frac{1}{m}\sin(\delta_f) & 0 & 0 & 0 & 0 & 0 & \frac{1}{m}\sin(90-\delta_f) & 0 & 0 & \frac{1}{m} & 0 & 0 \\
0 & 0 & 0 & 0 & 0 & 0 & \frac{L_f}{J_m}\sin(\delta_f) & 0 & 0 & 0 & 0 & 0 & \frac{L_f}{J_m}\sin(90-\delta_f) & 0 & 0 & -\frac{L_r}{J_m} & 0 & 0 \\
0 & 0 & 0 & \frac{-\beta}{J_w} & 0 & 0 & \frac{-R}{J_w} & 0 & 0 & 0 & 0 & 0 & 0 & 0 & 0 & 0 & 0 & 0 \\
0 & 0 & 0 & 0 & \frac{-\beta}{J_w} & \frac{1}{J_w} & 0 & 0 & 0 & \frac{-R}{J_w} & 0 & 0 & 0 & 0 & 0 & 0 & 0 & 0 \\
0 & 0 & 0 & 0 & 0 & -2\pi f_e & 0 & 0 & 0 & 0 & 0 & 0 & 0 & 0 & 0 & 0 & 0 & 0 \\
0 & 0 & 0 & 0 & 0 & 0 & 0 & 1 & 0 & 0 & 0 & 0 & 0 & 0 & 0 & 0 & 0 & 0 \\
0 & 0 & 0 & 0 & 0 & 0 & 0 & 0 & 1 & 0 & 0 & 0 & 0 & 0 & 0 & 0 & 0 & 0 \\
0 & 0 & 0 & 0 & 0 & 0 & 0 & 0 & 0 & 0 & 0 & 0 & 0 & 0 & 0 & 0 & 0 & 0 \\
0 & 0 & 0 & 0 & 0 & 0 & 0 & 0 & 0 & 0 & 1 & 0 & 0 & 0 & 0 & 0 & 0 & 0 \\
0 & 0 & 0 & 0 & 0 & 0 & 0 & 0 & 0 & 0 & 0 & 1 & 0 & 0 & 0 & 0 & 0 & 0 \\
0 & 0 & 0 & 0 & 0 & 0 & 0 & 0 & 0 & 0 & 0 & 0 & 0 & 0 & 0 & 0 & 0 & 0 \\
0 & 0 & 0 & 0 & 0 & 0 & 0 & 0 & 0 & 0 & 0 & 0 & 0 & 1 & 0 & 0 & 0 & 0 \\
0 & 0 & 0 & 0 & 0 & 0 & 0 & 0 & 0 & 0 & 0 & 0 & 0 & 0 & 1 & 0 & 0 & 0 \\
0 & 0 & 0 & 0 & 0 & 0 & 0 & 0 & 0 & 0 & 0 & 0 & 0 & 0 & 0 & 0 & 0 & 0 \\
0 & 0 & 0 & 0 & 0 & 0 & 0 & 0 & 0 & 0 & 0 & 0 & 0 & 0 & 0 & 1 & 0 & 0 \\
0 & 0 & 0 & 0 & 0 & 0 & 0 & 0 & 0 & 0 & 0 & 0 & 0 & 0 & 0 & 0 & 1 & 0 \\
0 & 0 & 0 & 0 & 0 & 0 & 0 & 0 & 0 & 0 & 0 & 0 & 0 & 0 & 0 & 0 & 0 & 0
\end{bmatrix}
$$

$$
\overline{\mathbf{B}}_c = \begin{bmatrix} 0 & 0 & 0 & 0 & 0 & 2\pi f_e & 0 & 0 & 0 & 0 & 0 & 0 & 0 & 0 & 0 & 0 & 0 & 0 \end{bmatrix}^T \quad (acceleration)
$$

$$
\overline{\mathbf{B}}_c = \begin{bmatrix} 0 & 0 & 0 & \frac{-1}{J_w} & 0 & 0 & 0 & 0 & 0 & 0 & 0 & 0 & 0 & 0 & 0 & 0 & 0 & 0 \\ 0 & 0 & 0 & 0 & \frac{-1}{J_w} & 0 & 0 & 0 & 0 & 0 & 0 & 0 & 0 & 0 & 0 & 0 & 0 & 0 \end{bmatrix}^T \quad (braking)
$$

$$
\overline{\mathbf{C}}_c = \begin{bmatrix}
\frac{-\gamma_x}{m} & 0 & 0 & 0 & 0 & 0 & \frac{1}{m}\cos(\delta_f) & 0 & 0 & \frac{1}{m} & 0 & 0 & \frac{-1}{m}\cos(90-\delta_f) & 0 & 0 & 0 & 0 & 0 \\
0 & \frac{-\gamma_y}{m} & 0 & 0 & 0 & 0 & \frac{1}{m}\sin(\delta_f) & 0 & 0 & 0 & 0 & 0 & \frac{1}{m}\sin(90-\delta_f) & 0 & 0 & \frac{1}{m} & 0 & 0 \\
0 & 0 & 0 & 0 & 0 & 0 & \frac{L_f}{J_m}\sin(\delta_f) & 0 & 0 & 0 & 0 & 0 & \frac{L_f}{J_m}\sin(90-\delta_f) & 0 & 0 & -\frac{L_r}{J_m} & 0 & 0 \\
0 & 0 & 0 & 1 & 0 & 0 & 0 & 0 & 0 & 0 & 0 & 0 & 0 & 0 & 0 & 0 & 0 & 0 \\
0 & 0 & 0 & 0 & 1 & 0 & 0 & 0 & 0 & 0 & 0 & 0 & 0 & 0 & 0 & 0 & 0 & 0
\end{bmatrix}
$$

$$
\overline{\mathbf{D}}_c = \begin{bmatrix} 0 & 0 & 0 & 0 & 0 \end{bmatrix}^T \quad (acceleration)
$$

$$
\overline{\mathbf{D}}_c = \begin{bmatrix} 0 & 0 & 0 & 0 & 0 \\ 0 & 0 & 0 & 0 & 0 \end{bmatrix}^T \quad (braking)
$$

$$
\boldsymbol{\rho} = \begin{bmatrix} v_x & v_y & \dot{\psi} & \omega_f & \omega_r & T_e & F_{xtf} & \dot{F}_{xtf} & \ddot{F}_{xtf} & F_{xtr} & \dot{F}_{xtr} & \ddot{F}_{xtr} & F_{ytf} & \dot{F}_{ytf} & \ddot{F}_{ytf} & F_{ytr} & \dot{F}_{ytr} & \ddot{F}_{ytr} \end{bmatrix}^T
$$

$$
\mathbf{v} = \begin{bmatrix} \dot{v}_x & \dot{v}_y & \dot{\psi} & \omega_f & \omega_r \end{bmatrix}^T
$$

$$
\mathbf{u} = \begin{bmatrix} T_c \end{bmatrix} \quad (acceleration)
$$

$$
\mathbf{u} = \begin{bmatrix} T_{b,f} & T_{b,r} \end{bmatrix} \quad (braking)
$$

$$
\begin{aligned}
\boldsymbol{\Sigma}_v &= 2\mathbf{I} \\
\sigma_d &= 1e10 \\
\boldsymbol{\Sigma}_w &= \begin{bmatrix}
10 & 0 & 0 & 0 & 0 & 0 & 0 & 0 & 0 & 0 & 0 & 0 & 0 & 0 & 0 & 0 & 0 & 0 \\
0 & 10 & 0 & 0 & 0 & 0 & 0 & 0 & 0 & 0 & 0 & 0 & 0 & 0 & 0 & 0 & 0 & 0 \\
0 & 0 & 10 & 0 & 0 & 0 & 0 & 0 & 0 & 0 & 0 & 0 & 0 & 0 & 0 & 0 & 0 & 0 \\
0 & 0 & 0 & 10 & 0 & 0 & 0 & 0 & 0 & 0 & 0 & 0 & 0 & 0 & 0 & 0 & 0 & 0 \\
0 & 0 & 0 & 0 & 10 & 0 & 0 & 0 & 0 & 0 & 0 & 0 & 0 & 0 & 0 & 0 & 0 & 0 \\
0 & 0 & 0 & 0 & 0 & 10 & 0 & 0 & 0 & 0 & 0 & 0 & 0 & 0 & 0 & 0 & 0 & 0 \\
0 & 0 & 0 & 0 & 0 & 0 & \sigma_d & 0 & 0 & 0 & 0 & 0 & 0 & 0 & 0 & 0 & 0 & 0 \\
0 & 0 & 0 & 0 & 0 & 0 & 0 & \sigma_d & 0 & 0 & 0 & 0 & 0 & 0 & 0 & 0 & 0 & 0 \\
0 & 0 & 0 & 0 & 0 & 0 & 0 & 0 & \sigma_d & 0 & 0 & 0 & 0 & 0 & 0 & 0 & 0 & 0 \\
0 & 0 & 0 & 0 & 0 & 0 & 0 & 0 & 0 & \sigma_d & 0 & 0 & 0 & 0 & 0 & 0 & 0 & 0 \\
0 & 0 & 0 & 0 & 0 & 0 & 0 & 0 & 0 & 0 & \sigma_d & 0 & 0 & 0 & 0 & 0 & 0 & 0 \\
0 & 0 & 0 & 0 & 0 & 0 & 0 & 0 & 0 & 0 & 0 & \sigma_d & 0 & 0 & 0 & 0 & 0 & 0 \\
0 & 0 & 0 & 0 & 0 & 0 & 0 & 0 & 0 & 0 & 0 & 0 & \sigma_d & 0 & 0 & 0 & 0 & 0 \\
0 & 0 & 0 & 0 & 0 & 0 & 0 & 0 & 0 & 0 & 0 & 0 & 0 & \sigma_d & 0 & 0 & 0 & 0 \\
0 & 0 & 0 & 0 & 0 & 0 & 0 & 0 & 0 & 0 & 0 & 0 & 0 & 0 & \sigma_d & 0 & 0 & 0 \\
0 & 0 & 0 & 0 & 0 & 0 & 0 & 0 & 0 & 0 & 0 & 0 & 0 & 0 & 0 & \sigma_d & 0 & 0 \\
0 & 0 & 0 & 0 & 0 & 0 & 0 & 0 & 0 & 0 & 0 & 0 & 0 & 0 & 0 & 0 & \sigma_d & 0 \\
0 & 0 & 0 & 0 & 0 & 0 & 0 & 0 & 0 & 0 & 0 & 0 & 0 & 0 & 0 & 0 & 0 & \sigma_d
\end{bmatrix}
\end{aligned}
$$

Appendix E

Fisher Estimation

E.1 1-DOF Longitudinal Model

$$
\begin{aligned}
\sigma_f &= 1e3 \\
r_0 &= 1 \\
M_0 &= 100 \\
\varepsilon_0 &= 1e-1 \\
\mathbf{P}_0 &= \sigma_f \begin{bmatrix} 200000 & 0 & 0 \\ 0 & 2 & 0 \\ 0 & 0 & 50 \end{bmatrix}
\end{aligned}
$$

E.2 3-DOF Bicycle Model

$$
\begin{aligned}
\sigma_f &= 1e4 \\
r_0 &= 1 \\
M_0 &= 10000 \\
\varepsilon_0 &= 1e-4 \\
\mathbf{P}_{0,xtf} &= \sigma_f \begin{bmatrix} 1000 & 0 & 0 & 0 & 0 & 0 \\ 0 & 10 & 0 & 0 & 0 & 0 \\ 0 & 0 & 10 & 0 & 0 & 0 \\ 0 & 0 & 0 & 10 & 0 & 0 \\ 0 & 0 & 0 & 0 & 10 & 0 \\ 0 & 0 & 0 & 0 & 0 & 1 \end{bmatrix} \\
\mathbf{P}_{0,ytf} &= \sigma_f \begin{bmatrix} 10 & 0 & 0 & 0 & 0 & 0 \\ 0 & 1000 & 0 & 0 & 0 & 0 \\ 0 & 0 & 10 & 0 & 0 & 0 \\ 0 & 0 & 0 & 10 & 0 & 0 \\ 0 & 0 & 0 & 0 & 10 & 0 \\ 0 & 0 & 0 & 0 & 0 & 1000 \end{bmatrix} \\
\mathbf{P}_{0,xtr} &= \sigma_f \begin{bmatrix} 1000 & 0 & 0 & 0 & 0 & 0 \\ 0 & 10 & 0 & 0 & 0 & 0 \\ 0 & 0 & 10 & 0 & 0 & 0 \\ 0 & 0 & 0 & 10 & 0 & 0 \\ 0 & 0 & 0 & 0 & 10 & 0 \\ 0 & 0 & 0 & 0 & 0 & 1 \end{bmatrix} \\
\mathbf{P}_{0,ytr} &= \sigma_f \begin{bmatrix} 10 & 0 & 0 & 0 & 0 & 0 \\ 0 & 1000 & 0 & 0 & 0 & 0 \\ 0 & 0 & 10 & 0 & 0 & 0 \\ 0 & 0 & 0 & 10 & 0 & 0 \\ 0 & 0 & 0 & 0 & 10 & 0 \\ 0 & 0 & 0 & 0 & 0 & 1000 \end{bmatrix}
\end{aligned}
$$

Appendix F

Tire Model - Pacejka

F.1 Pure Longitudinal and Lateral Slip

$$
\begin{aligned}
C_x &= b_0 && \text{(F.1)}\\
D_x &= (b_1 F_z + b_2) F_z && \text{(F.2)}\\
B_x &= ((b_3 F_z^2 + b_4 F_z)\exp(-b_5 F_z))/(C_x D_x) && \text{(F.3)}\\
S_{hx} &= b_9 F_z + b_{10} && \text{(F.4)}\\
S_{vx} &= b_{11} F_z + b_{12} && \text{(F.5)}\\
E_x &= b_6 F_z^2 + b_7 F_z + b_8 && \text{(F.6)}\\
X_x &= 100\kappa + S_{hx} && \text{(F.7)}\\
Y(\kappa,\gamma,F_z;\mathbf{p_x}) &= D_x sin(C_x(atan(B_x(1-E_x)X_x + E_x atan(B_x X_x)))) + S_{vx} && \text{(F.8)}\\
\frac{\partial Y(\kappa,\gamma,F_z;\mathbf{p_x})}{\partial \kappa} &= -\big(C_x * D_x * cos\,(C_x * atan\,(E_x * atan(100 * B_x * \kappa)\\
&\quad - 100 * B_x * \kappa * (E_x - 1))) * (100 * B_x * (E_x - 1)\\
&\quad - (100 * B_x * E_x)/(10000 * B_x^2 * \kappa^2 + 1))\big) / ((E_x * atan(100 * B_x * \kappa)\\
&\quad - 100 * B_x * \kappa * (E_x - 1))^2 + 1\Big) && \text{(F.9)}\\
\frac{\partial Y(\kappa,\gamma,F_z;\mathbf{p_x})}{\partial \alpha} &= 0 && \text{(F.10)}\\
Fx_0 &= Y(\kappa,\gamma,F_z;\mathbf{p_x}) && \text{(F.11)}\\
\frac{\partial F_{x0}}{\partial \kappa} &= \frac{\partial Y(\kappa,\gamma,F_z;\mathbf{p_x})}{\partial \kappa} && \text{(F.12)}\\
\frac{\partial F_{x0}}{\partial \alpha} &= \frac{\partial Y(\kappa,\gamma,F_z;\mathbf{p_x})}{\partial \alpha} && \text{(F.13)}\\
& && \text{(F.14)}
\end{aligned}
$$

$$
\begin{aligned}
C_y &= a_0 && \text{(F.15)}\\
D_y &= (a_1 F_z + a_2) F_z && \text{(F.16)}\\
B_y &= (a_3 sin(2atan(F_z/a_4))(1 - a_5 * camber))/(C_y D_y) && \text{(F.17)}\\
E_y &= a_6 F_z + a_7 && \text{(F.18)}\\
S_{hy} &= a_8 F_z + a_9 + a_{10} camber && \text{(F.19)}\\
S_{vy} &= a_{11} F_z + a_{12} + (a_{13} Fz^2) * camber && \text{(F.20)}\\
X_y &= 100\alpha + S_{hy} && \text{(F.21)}\\
Y(\alpha, \gamma, F_z; \mathbf{p_x}) &= D_y sin(C_y atan(B_y(1 - E_y)X_y + E_y atan(B_y X_y))) + S_{vy} && \text{(F.22)}\\
\frac{\partial Y(\alpha, \gamma, F_z; \mathbf{p_x})}{\partial \kappa} &= 0 && \text{(F.23)}\\
\frac{\partial Y(\alpha, \gamma, F_z; \mathbf{p_x})}{\partial \alpha} &= -\big(C_y * D_y * cos(C_y * atan(E_y * atan(100 * B_y * \alpha)\\
&\quad - 100 * B_y * \alpha * (E_y - 1))) * (100 * B_y * (E_y - 1)\\
&\quad - (100 * B_y * E_y)/(10000 * B_y^2 * \alpha^2 + 1))\big) / ((E_y * atan(100 * B_y * \alpha)\\
&\quad - 100 * B_y * \alpha * (E_y - 1))^2 + 1\Big) && \text{(F.24)}\\
Fy0 &= Y(\alpha, \gamma, F_z; \mathbf{p_x}) && \text{(F.25)}\\
\frac{\partial F_{y0}}{\partial \alpha} &= \frac{\partial Y(\alpha, \gamma, F_z; \mathbf{p_x})}{\partial \alpha} && \text{(F.26)}
\end{aligned}
$$

F.2 Combined Slip

$$
\begin{aligned}
F_{xo}(\kappa, \gamma, F_z) &= Y(\kappa, \gamma, F_z; \mathbf{p_x}) && \text{(F.27)}\\
F_{yo}(\alpha, \gamma, F_z) &= -Y(\alpha, \gamma, F_z; \mathbf{p_y}) && \text{(F.28)}\\
\sigma_x^* &= \kappa/\kappa^* && \text{(F.29)}\\
\sigma_y^* &= \alpha/\alpha^* && \text{(F.30)}\\
\sigma^* &= \sqrt{(\sigma_x^*)^2 + (\sigma_y^*)^2} && \text{(F.31)}\\
F_x(\alpha, \kappa, \gamma, F_z) &= \frac{\sigma_x^*}{\sigma^*} |F_{xo}(\kappa, \gamma, F_z)| && \text{(F.32)}\\
F_y(\alpha, \kappa, \gamma, F_z) &= \frac{\sigma_y^*}{\sigma^*} \left|F_{yo}(\alpha, \gamma, F_z)\right| && \text{(F.33)}
\end{aligned}
$$

F.3 Model Parameters

Table F.1: Tire Model Parameters

	Dry Pavement		Wet Pavement	
Parameter	Front Tire	Rear Tire	Front Tire	Rear Tire
a_0	1.6	1.7	1.3	1.1
a_1	-120	-90	-50	-50
a_2	2200	1800	1400	1400
a_3	1600	1500	1200	1100
a_4	14	17	14	14
a_5	0.05	0.05	0.05	0.05
a_6	-0.2	-0.2	-0.2	-0.2
a_7	-1	0	-1	-1
a_8	0	0	0	0
a_9	0	0	0	0
a_{10}	0	0	0	0
a_{11}	0	0	0	0
a_{12}	0	0	0	0
a_{13}	0	0	0	0
b_0	1.5	1.5	1.28000	1.28000
b_1	-100	-85	-7.61180	-7.61180
b_2	2000	1960	1300	1300
b_3	-0.00736	-0.00736	-0.00736	-0.00736
b_4	350	350	100	100
b_5	-0.07661	-0.07661	-0.07661	-0.07661
b_6	-0.00386	-0.00386	-0.003	-0.003
b_7	0.08506	0.08506	0.07	0.07
b_8	0.07572	0.07572	0.07	0.07
b_9	0	0	0	0
b_{10}	0	0	0	0
b_{11}	0	0	0	0
b_{12}	0	0	0	0
c_0	2	2.23	2	2.23
c_1	3.67	3.67	3.67	3.67
c_2	0.18	0.18	0.18	0.18
c_3	0.2	0.42	0.2	0.42
c_4	-2.4	-3.6	-2.4	-3.6
c_5	-0.228	-0.25964	-0.228	-0.25964
c_6	0.092	-0.0013	0.092	-0.0013
c_7	-0.35835	-0.35835	-0.35835	-0.35835
c_8	3.74476	3.74476	3.74476	3.74476
c_9	-15.1566	-15.1566	-15.1566	-15.1566
c_{10}	0.00212	0.00212	0.00212	0.00212
c_{11}	0.00035	0.00035	0.00035	0.00035
c_{12}	0.00914	0.00914	0.00914	0.00914
c_{13}	-0.094	-0.094	-0.094	-0.094
c_{14}	0.10069	0.10069	0.10069	0.10069
c_{15}	0	0	0	0
c_{16}	0.44441	0.44441	0.44441	0.44441
c_{17}	2.23	2.23	2.23	2.23
κ^*	0.1080	0.1217	0.4340	0.4550
α^*	0.1515	0.1822	0.1980	0.4050
σ_α	0.25	0.25	0.25	0.25
σ_κ	0.091	0.091	0.091	0.091

Appendix G

Partial Derivatives

G.1 1-DOF Longitudinal Model

In the case of the Longitudinal Vehicle Model of Section 3.2, Equation 3.14 , the partial derivatives are defined according to Equations G.1 and G.2.

$$\frac{\partial \mathbf{f}}{\partial \mathbf{u}} = [0] \tag{G.1}$$

$$\frac{\partial \mathbf{f}}{\partial \mathbf{x}} = \left[\frac{\partial F_x(v,\omega)}{\partial \kappa}\frac{\partial \kappa}{\partial v}, \quad \frac{\partial F_x(v,\omega)}{\partial \kappa}\frac{\partial \kappa}{\partial \omega}, \quad \frac{\partial F_x(v,\omega)}{\partial \kappa}\frac{\partial \kappa}{\partial T_C} \right] \tag{G.2}$$

G.2 3-DOF Bicycle Model

In the case of dynamic bicycle model of Section 3.4, Equations 3.32-3.44, the partial derivatives are defined according to Equations G.3 and G.4.

$$\frac{\partial \mathbf{f}}{\partial \mathbf{u}} = \begin{bmatrix} \frac{\partial F_{xtf}}{\partial T_c} \\ \frac{\partial F_{xtr}}{\partial T_c} \\ \frac{\partial F_{ytf}}{\partial T_c} \\ \frac{\partial F_{ytr}}{\partial T_c} \end{bmatrix} \tag{G.3}$$

$$\frac{\partial \mathbf{f}}{\partial \mathbf{x}} = \begin{bmatrix} \frac{\partial F_{xtf}}{\partial v_x} & \frac{\partial F_{xtf}}{\partial v_y} & \frac{\partial F_{xtf}}{\partial \dot{\psi}} & \frac{\partial F_{xtf}}{\partial \omega_f} & \frac{\partial F_{xtf}}{\partial \omega_r} & \frac{\partial F_{xtf}}{\partial T_e} \\ \frac{\partial F_{xtr}}{\partial v_x} & \frac{\partial F_{xtr}}{\partial v_y} & \frac{\partial F_{xtr}}{\partial \dot{\psi}} & \frac{\partial F_{xtr}}{\partial \omega_f} & \frac{\partial F_{xtr}}{\partial \omega_r} & \frac{\partial F_{xtr}}{\partial T_e} \\ \frac{\partial F_{ytf}}{\partial v_x} & \frac{\partial F_{ytf}}{\partial v_y} & \frac{\partial F_{ytf}}{\partial \dot{\psi}} & \frac{\partial F_{ytf}}{\partial \omega_f} & \frac{\partial F_{ytf}}{\partial \omega_r} & \frac{\partial F_{ytf}}{\partial T_e} \\ \frac{\partial F_{ytr}}{\partial v_x} & \frac{\partial F_{ytr}}{\partial v_y} & \frac{\partial F_{ytr}}{\partial \dot{\psi}} & \frac{\partial F_{ytr}}{\partial \omega_f} & \frac{\partial F_{ytr}}{\partial \omega_r} & \frac{\partial F_{ytr}}{\partial T_e} \end{bmatrix} \tag{G.4}$$

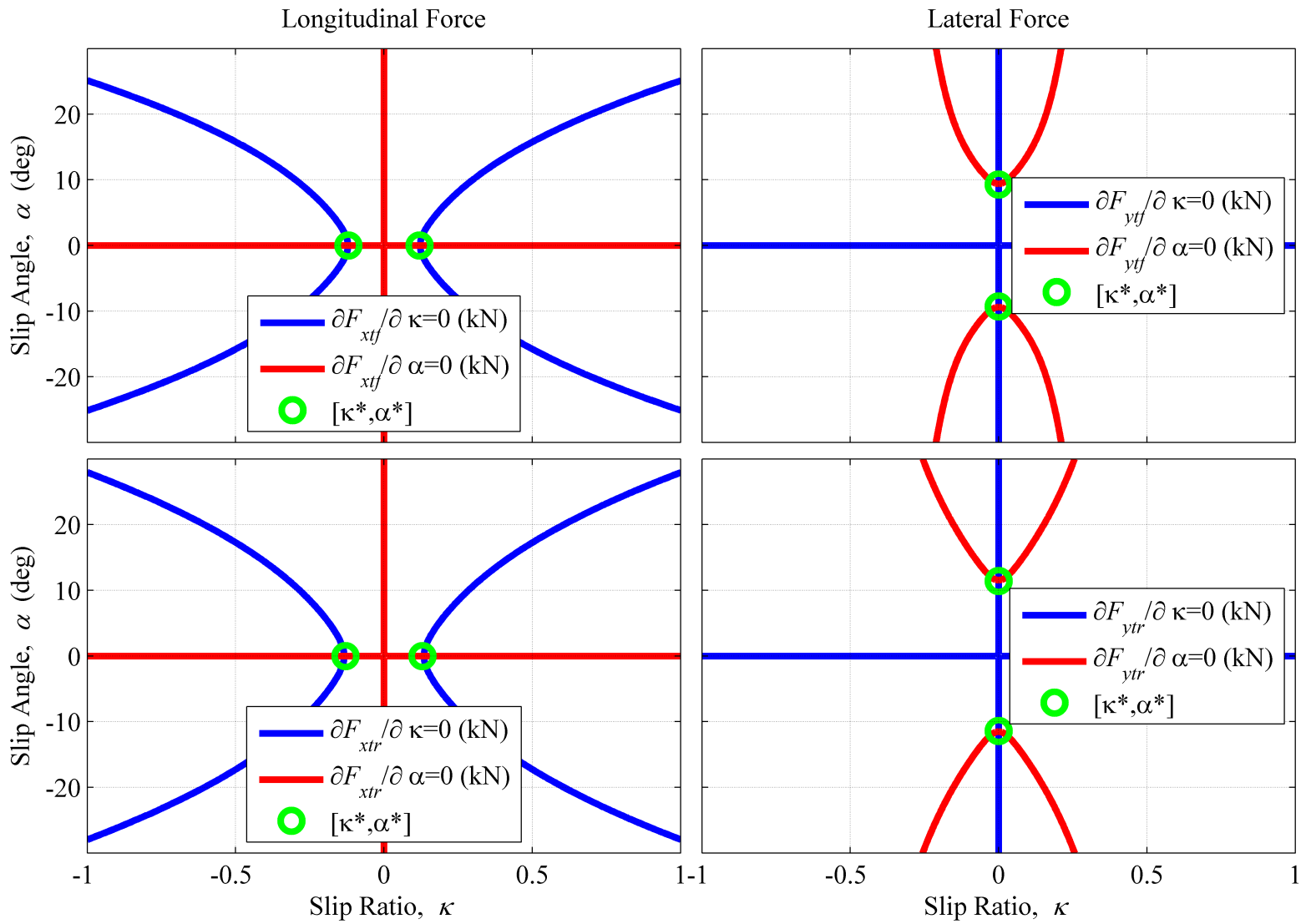

Figure G.1: Regions of interest of partial derivatives for F_{xt} and F_{yt} with respect to slip ratio κ and slip angle α when operating in the combined mode friction regime

Appendix H

Cruden 6-DOF Simulator Implementation

H.1 Dynamic Bicycle Model

$$\dot{v}_x = -\frac{\gamma_x}{m}v_x + \frac{F_{xtf}}{m}\cos(\delta_f) - \frac{F_{ytf}}{m}\cos(90-\delta_f) + \frac{F_{xtr}}{m}\cos(\delta_r) - \frac{F_{ytr}}{m}\cos(90-\delta_r) \quad \text{(H.1)}$$

$$\dot{v}_y = -\frac{\gamma_y}{m}v_y + \frac{F_{xtf}}{m}\sin(\delta_f) + \frac{F_{ytf}}{m}\sin(90-\delta_f) + \frac{F_{xtr}}{m}\sin(\delta_r) + \frac{F_{ytr}}{m}\sin(90-\delta_r) \quad \text{(H.2)}$$

$$\ddot{\psi} = \frac{L_f}{J_m}\left[F_{xtf}\sin(\delta_f) + F_{ytf}\sin(90-\delta_f)\right] - \frac{L_r}{J_m}\left[F_{xtr}\sin(\delta_r) + F_{ytr}\sin(90-\delta_r)\right] \quad \text{(H.3)}$$

$$\dot{\omega}_f = \frac{-\beta}{J_w}\omega_f - \frac{R}{J_w}F_{xtf} - \frac{1}{J_w}T_{b,f} \quad \text{(H.4)}$$

$$\dot{\omega}_r = \frac{-\beta}{J_w}\omega_r - \frac{R}{J_w}F_{xtr} - \frac{1}{J_w}T_{b,r} + \frac{1}{J_w}T_e \quad \text{(H.5)}$$

$$\dot{T}_e = -2\pi f_e T_e + 2\pi f_e T_c \quad \text{(H.6)}$$